

Extrusion-based 3D printing of biodegradable porous iron for bone substitution

Putra, N.E.

DOI

[10.4233/uuid:a4d2f3d3-74bc-4dcd-9e5a-71deb5f74a38](https://doi.org/10.4233/uuid:a4d2f3d3-74bc-4dcd-9e5a-71deb5f74a38)

Publication date

2023

Document Version

Final published version

Citation (APA)

Putra, N. E. (2023). *Extrusion-based 3D printing of biodegradable porous iron for bone substitution*. [Dissertation (TU Delft), Delft University of Technology]. <https://doi.org/10.4233/uuid:a4d2f3d3-74bc-4dcd-9e5a-71deb5f74a38>

Important note

To cite this publication, please use the final published version (if applicable).
Please check the document version above.

Copyright

Other than for strictly personal use, it is not permitted to download, forward or distribute the text or part of it, without the consent of the author(s) and/or copyright holder(s), unless the work is under an open content license such as Creative Commons.

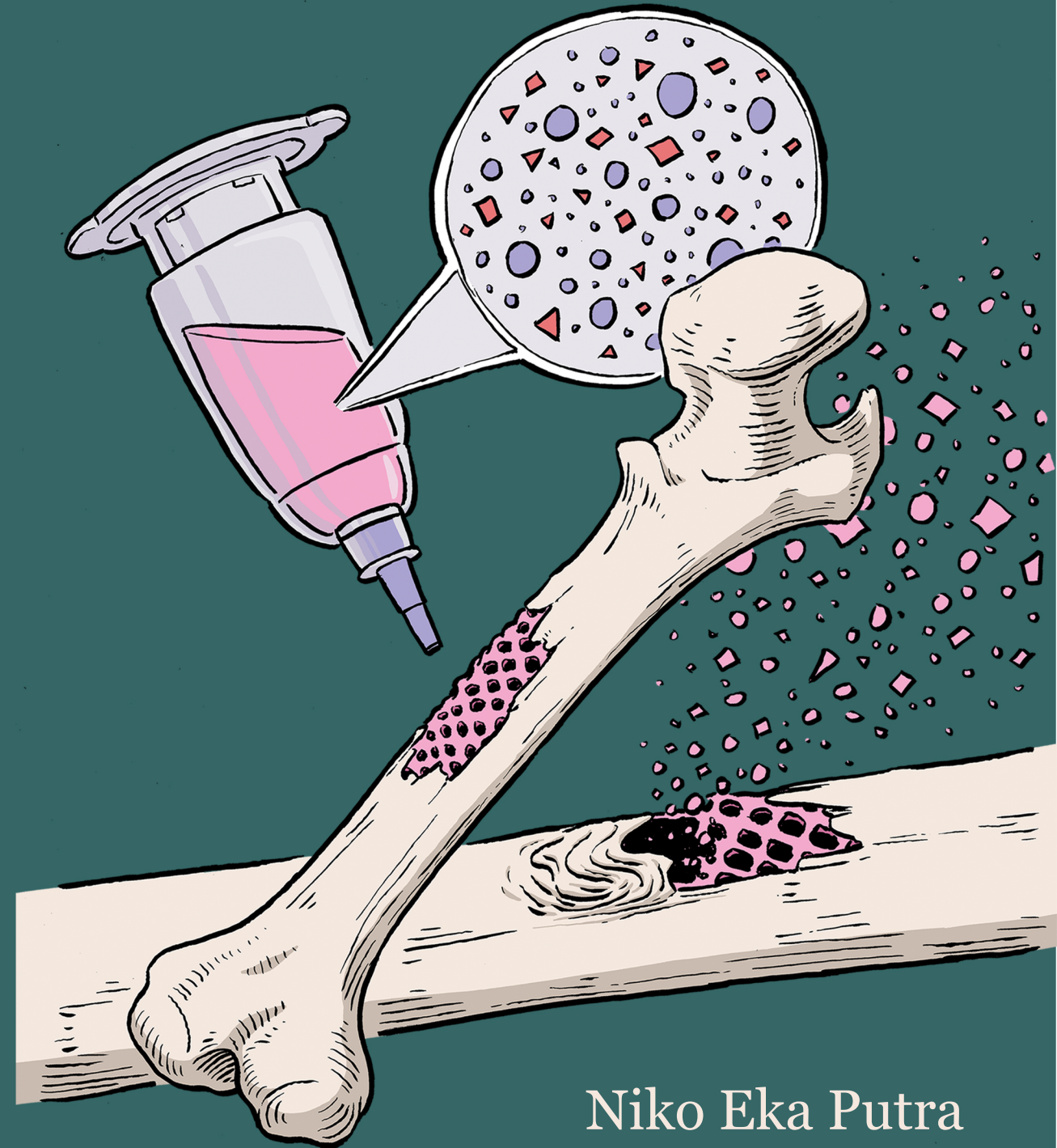
Takedown policy

Please contact us and provide details if you believe this document breaches copyrights.
We will remove access to the work immediately and investigate your claim.

Extrusion-based 3D printing of biodegradable porous iron for bone substitution

Extrusion-based 3D printing of biodegradable porous iron for bone substitution

Niko Eka Putra



Extrusion-based 3D printing of biodegradable porous iron for bone substitution

Extrusion-based 3D printing of biodegradable porous iron for bone substitution

Proefschrift

ter verkrijging van de graad van doctor
aan de Technische Universiteit Delft,
op gezag van de Rector Magnificus, Prof.dr.ir. T.H.J.J. van der Hagen,
voorzitter van het College voor Promoties,
in het openbaar te verdedigen op dinsdag 14 maart 2023 om 10:00 uur.

door

Niko Eka PUTRA

Ingenieur in de Biomedische Techniek,
Technische Universiteit Delft, Nederland,
geboren te Medan, Indonesia.

Dit proefschrift is goedgekeurd door de promotoren.

Samenstelling promotiecommissie bestaat uit:

Rector magnificus,	Voorzitter
Prof. dr. A.A. Zadpoor,	Technische Universiteit Delft, promotor
Dr. J. Zhou,	Technische Universiteit Delft, promotor
Dr. ir. I. Apachitei,	Technische Universiteit Delft, copromotor

Onafhankelijke leden:

Prof. dr. ir. J. Sietsma	Technische Universiteit Delft, Nederland
Prof. dr. ir. H.A. Terry	Vrije Universiteit Brussels, Belgium
Prof. dr. G.J.V.M. van Osch	Erasmus Medical Center Rotterdam, Nederland
Prof. dr. H.E.J. Veeger	Technische Universiteit Delft, Nederland

Reserve lid:

Prof. dr. ir. P. Breedveld	Technische Universiteit Delft, Nederland
----------------------------	--



The research leading to these results was part of the 3DMed project that received funding from the Interreg 2 Seas program 2014 – 2020, co-funded by the European Regional Development Fund under subsidy contract No. 2S04-014.

Keywords: extrusion-based 3D printing; biodegradable; iron; bone substitution

Cover illustration: Niek van Ooijen | www.niekvanooijen.nl

Printed by: Gildeprint | www.gildeprint.nl

Copyright © 2023 by N.E. Putra

ISBN 978-94-6384-416-1

An electronic version of this dissertation is available at <http://repository.tudelft.nl/>

Summary

The treatment of large bone injuries continues to be challenging partially due to the limited quantity and quality of bone-replacing materials. Iron (Fe) and its alloys have been developed as a group of load-bearing biomaterials. Recent advances in additive manufacturing (AM) have enhanced the potential of Fe-based biomaterials as biodegradable bone substitutes. Firstly, AM Fe-based implants can now be personalized to exactly match the geometry of bony defects. Secondly, AM Fe-based implants with macro- and micro-scale porosities can mimic the mechanical properties of the native bony tissue. The mechanical properties can also be tuned to sustain over the biodegradation period until the new bone tissue takes over their biomechanical function. Finally, AM offers a pathway for *in situ* or *ex situ* alloying as well as for other types of multi-material printing to achieve multiple functionalities, such as paramagnetic properties, high rates of biodegradation, and, most importantly, bioactivity (*e.g.*, to induce the osteogenic differentiation of stem cells or to ward off implant-associated infections).

This thesis presents the results of multiple attempts at leveraging the advantages of extrusion-based AM for the fabrication of effective, multi-functional biodegradable bone substitutes. It begins with identifying the most straightforward AM technology for the fabrication of multi-functional Fe-based biomaterials for bone implants. In Chapter 2, we review the currently available AM technologies to realize multi-material orthopedic biomaterials. For each category of AM technologies, our treatment of the topic is accompanied by a critical assessment of the properties of the presented material category in comparison with the requirements of ideal bone substitutes. Of these technologies, extrusion-based 3D printing is identified to have the greatest potential to not only allow for the fabrication of complex porous structures, but also to adjust the material types and compositions within the implant.

In Chapter 3, we report on the development of an ink formulation containing Fe powder particles for extrusion-based 3D printing of porous Fe, and optimized debinding and sintering as post-AM processes. The Fe scaffolds were designed in a laydown pattern with a strut size of 410 μm , topologically ordered macropores

with a size of 400 μm , and random micropores in the struts, to achieve a final absolute porosity of 67%. The extrusion-based 3D printed porous Fe demonstrated an improved biodegradation rate (*i.e.*, 0.05 mm/y) as compared to traditionally cast iron (*i.e.*, 0.02 mm/y). The mechanical properties of the scaffolds remained within the range of the cancellous bone for 4 weeks of *in vitro* biodegradation. Such a biodegradation rate is, however, still too low for the porous Fe to function as a biodegradable implant. The dense coverage of the scaffold struts by the Fe-based biodegradation products and their passivation behavior hampered the further biodegradation of Fe. Another issue was the cytotoxicity towards preosteoblasts MC3T3-E1 bone cells.

In the subsequent research presented in Chapter 4, we improved the biodegradation profile and cytocompatibility of our AM porous Fe by applying a non-biodegradable coating made of poly(2-ethyl-2-oxazoline) (PEtOx) on the extrusion-based 3D printed porous Fe scaffolds. We comprehensively studied the coated specimens in terms of the biodegradation behavior, electrochemical responses, the mechanical properties before and after *in vitro* biodegradation, and cytocompatibility with preosteoblasts. A thin layer of PEtOx coating transformed the morphology and chemical compositions of the Fe-based biodegradation products to be more porous and less passivating, which improved the biodegradation profile of Fe. The presence of the PEtOx layer also supported the viability of the preosteoblasts. However, these improvements were not sufficient to push the biodegradation rate high enough and into the range of the desired values (*i.e.*, 0.2-0.5 mm/y). Moreover, cytocompatibility, while improved, was not accompanied by an osteogenic behavior for improved bone regeneration. Moreover, the inherent incompatibility of pure Fe with MRI was identified as an extra impediment to the clinical adoption of the developed biomaterials.

To further develop multi-functional Fe-based bone implants, we utilized the multi-material AM capability of extrusion-based 3D printing. We chose Mn as the alloying element for its antiferromagnetic property to create paramagnetic FeMn alloys that are MRI-friendly. Moreover, Mn having a lower standard electrode potential, was expected to increase the biodegradation rate of the alloy. We also chose akermanite as the reinforcement component for its bioactivity and osteogenic potential, as well as its higher solubility in the body fluid that would aid in the biodegradation profile of the composite.

In Chapter 5 and 6, we describe the ink formulations containing Fe-Mn powder mixtures (with 25, 30 and 35 wt% Mn) and Fe-akermanite powder mixtures (with 5, 10, 15 and 20 vol% akermanite) for the fabrication of porous FeMn alloy scaffolds and Fe-akermanite composite scaffolds using extrusion-based 3D printing. With the same porous geometrical design as porous Fe, the

FeMn alloys and Fe-akermanite composites exhibited similar values of absolute porosities (i.e., 69% and 69–71%, respectively). The Fe₂₅Mn alloy contained the ϵ -FeMn and γ -FeMn phases, while the Fe₃₀Mn and Fe₃₅Mn alloys had only the γ -FeMn phase. The Fe-akermanite composites maintained the individual α -Fe and akermanite phases. The γ -FeMn phase in the FeMn alloys made them paramagnetic, and thus, MRI-friendly. The biodegradation rates of the FeMn alloys (with 35 wt% Mn = 0.23 mm/y) were also enhanced by up to 4.6 times (as compared to porous Fe). The enhanced values were in the range of the ideal values for biodegradable implants. The biodegradation rates of the Fe-akermanite composites (with 20 vol% akermanite = 0.13 mm/y) increased as well to the values that were up to 2.6 times higher than the porous Fe. However, they did not reach the desired range of biodegradation rates. As for the mechanical properties, the yield strengths and elastic moduli of porous FeMn and Fe-akermanite decreased over 4 weeks of *in vitro* biodegradation. Nevertheless, they remained within the range of values reported for the cancellous bone. Regarding cytocompatibility, the FeMn alloys were cytotoxic against preosteoblasts. On the other hand, the Fe-akermanite composites (with 10 vol% akermanite or more) improved the adhesion of bone cells, encouraged their proliferation, and facilitated cell differentiation as evidenced by increased secretion of collagen type-1, and alkaline phosphatase activity over time. The biocompatibility of the Fe-akermanite composites did not differ from the commonly used Ti6Al4V bone implants.

In Chapter 7, we took a step forward, combining the best of FeMn and Fe-akermanite composites to create FeMn-akermanite. We developed an Fe-based ink containing 35 wt% Mn and 20 or 30 vol% akermanite powder mixtures. For the same geometrical porous design, the FeMn-akermanite composites exhibited an absolute porosity of 69–70%. The metal matrix composite contained the γ -FeMn phase and nesosilicate phases. The former provided the composites with a paramagnetic behavior, making the composites MR-friendly. The biodegradation rates of the composites were enhanced up to 0.27 mm/y, which is within the desired range for biodegradable bone substitutes. The yield strengths and elastic moduli of the FeMn-akermanite composites remained similar to those of the cancellous bone, despite 4 weeks of *in vitro* biodegradation. The nesosilicate phases present in the developed composites made them compatible with preosteoblasts as well as osteogenic (as confirmed by Runx2 immunostaining). Moreover, osteopontin immunostaining indicated the initiation of *in vitro* biomineralization.

Chapter 8 concludes this thesis by drawing up several general conclusions and presenting some recommendations regarding the promising avenues for future research. Extrusion-based 3D printing technology has opened an

unprecedented opportunity for porous AM Fe-based biomaterials to be fabricated and functionalized for bone substitution. Our experimental results demonstrate the remarkable potential of the FeMn-akermanite composites in fulfilling all the requirements of porous biodegradable bone substitutes, motivating future research to evaluate their performance *in vivo*.

Contents

Summary.....	xvii
1. Introduction	2
1.1 Background	3
1.2 Metallic biomaterials for load-bearing bone substitution.....	3
1.3 Progress in the development of Fe-based bone substitutes	5
1.4 Thesis aim and outline.....	9
Bibliography	11
2. Multi-material additive manufacturing technologies for Ti-, Mg-, and Fe-based biomaterials for bone substitution	16
2.1 Fabrication technologies for metallic biomaterials as bone substitutes	17
2.2 Multi-material metallic AM technologies	19
2.3 Selection of multi-material AM technologies for the fabrication of multi-functional Fe-based bone substitutes	25
2.4 Concluding remarks and future perspective	27
Bibliography	29
3. Biodegradable porous Fe.....	34
3.1 Introduction	35
3.2 Materials and methods	36
3.3 Results.....	43
3.4 Discussion.....	53
3.5 Conclusion.....	59
3.6 Supplementary material	60
Bibliography	62
4. Poly(2-ethyl-2-oxazoline) coating on biodegradable porous Fe	68
4.1 Introduction	69

4.2 Materials and methods	70
4.3 Results.....	76
4.4 Discussion.....	83
4.5 Conclusion.....	90
4.6 Supplementary material	91
Bibliography	93
5. <i>Ex situ</i>-alloy highly biodegradable MRI-friendly porous Fe-Mn	98
5.1 Introduction	99
5.2 Materials and methods	100
5.3 Results.....	105
5.4 Discussion.....	115
5.5 Conclusion.....	125
5.6 Supplementary material	126
Bibliography	131
6. <i>Ex situ</i>-composite bioactive and biodegradable porous Fe-Akermanite.....	136
6.1 Introduction	137
6.2 Materials and methods	138
6.3 Results.....	143
6.4 Discussion.....	158
6.5 Conclusion.....	165
6.6 Supplementary material	167
Bibliography	176
7. Highly biodegradable MRI-friendly osteogenic porous Fe-Mn-Akermanite.....	182
7.1 Introduction	183
7.2 Materials and methods	184
7.3 Results.....	190
7.4 Discussion.....	200
7.5 Conclusion.....	208
7.6 Supplementary material	209
Bibliography	213

8. Concluding remarks	218
8.1 Main findings	219
8.2 General discussion	221
8.3 Recommendations and outlook of future research	227
Bibliography	230
Acknowledgements	233
List of publications	237
Curriculum Vitae	239

1

Introduction

“Breathing in, I calm body and mind.

Breathing out, I smile.

Dwelling in the present moment, I know this is the only moment.”

Thích Nhất Hạnh

This chapter is partly based on
Putra, N.E., Mirzaali, M.J., Apachitei, I., Zhou, J. and Zadpoor, A.A., 2020. Multi-material additive manufacturing technologies for Ti-, Mg-, and Fe-based biomaterials for bone substitution. *Acta Biomaterialia*, 109, pp.1-20.

1.1 Background

With the ever-increasing human population, the demands for bone grafts has dramatically increased, challenging the healthcare systems worldwide [1]. Bone is the second most grafted tissue [2]. Bone has two basic structures (Figure 1): the inner part (*i.e.*, the cancellous bone) with 50 – 90% porosity and the outer part (*i.e.*, the cortical bone) with only ~10% porosity [3]. Due to the structural complexity of bone at different length scales, its mechanical properties vary over wide ranges, with the compressive yield strengths varying between 0.5 and 200 MPa and the Young's moduli between 0.5 and 20 GPa [4]. Bone adapts to mechanical loading and heals itself when damaged at a small scale through a dynamic process of remodeling, through which old, microcracked bone is resorbed and replaced by new bone [5].

Despite being able to regenerate, bone loss from traumas or diseases often leads to non-unions and critical-size bone lesions (*i.e.*, > 5 cm, *e.g.*, in the femur and tibia [6]). A critical-size bony lesion is defined as a lesion that cannot be healed naturally during the patient's lifetime [7]. In such cases, bone replacements are necessary. Until today, autografts, or bone replacements collected from and implanted in the same person, remain the gold standard clinical treatments for critical-size bony lesions [8]. However, the volume of autografts that can be harvested to replace critical-size bony lesions, for example, from the posterior iliac crest, is limited to 33.82 cm³ [9], while the volume of, say, tibia defects may amount to 122 cm³ [10]. Although allografts (*i.e.*, bone replacements from donors) can compensate for the shortage of autografts, the risks of disease transmission as well as immunogenic incompatibility pose other types of challenges. Driven by the need to provide an alternative bone replacement approach, bone tissue engineering, which focuses on regenerating bone tissue using synthetic biomaterials, has shown promising progress in the reconstruction of large-scale bony lesions [11].

1.2 Metallic biomaterials for load-bearing bone substitution

Ideal synthetic biomaterials for bone substitution must be biocompatible and designed to mimic the extracellular matrix of the natural bone. They should provide bone regeneration environment, facilitate complete bone regeneration, withstand dynamic mechanical loading, and degrade along with the formation of new bone [12]. A successful bone substitute first allows mesenchymal stem cells (MSCs) to adhere onto its surface and differentiate into bone cells, followed by inward mineralization [13]. In the design of an ideal bone substitute, the mechanical properties, pore sizes, pore distribution, porosity, surface

characteristics, and biodegradability of the biomaterial should all be taken into consideration.

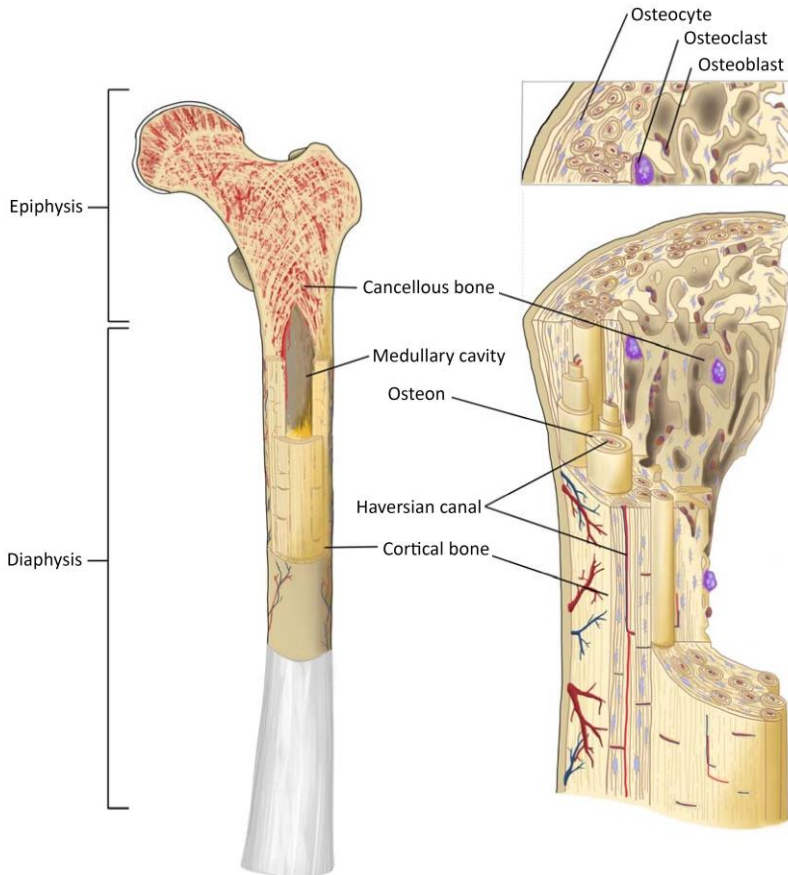


Figure 1.1. The anatomy of bone (Reprinted with permission from [2]).

Synthetic bone substitutes can be made using metallic biomaterials, bioceramics, biopolymers, or composite biomaterials. Metallic biomaterials have been widely used for functional and load-bearing bone substitutes due to their mechanical properties that are superior to those of bioceramics, biopolymers and composite biomaterials. Most of bulk metals, however, are much stiffer than the native bone, which could cause bone tissue resorption after implantation as a result of stress shielding [14]. However, the excessively high mechanical properties of metals can be tuned by increasing their porosity. Increasing the porosity of metallic biomaterials not only can reduce their mechanical properties but can also improve their permeability for cells and nutrients and facilitate angiogenesis and bone ingrowth [15]. The porosity of metallic biomaterials

should be at least 50%, while pore sizes $> 300 \mu\text{m}$ are recommended to ensure better progress of the bone tissue regeneration process [16,17]. The porous design of metallic biomaterials should be tailored to ensure an optimum trade-off between the mechanical properties for load bearing and the porous structure needed for vascularization.

At the early stage of bone defect regeneration, the entire mechanical support relies on the implanted biomaterial. The mechanical integrity of the biomaterial should be sustained for about 3 to 12 weeks to support the upper limb healing process, while the lower limb requires approximately 12 to 24 weeks [18]. As the newly regenerated bone slowly regains its strength, the biomaterial is allowed to degrade gradually. Therefore, the biodegradation rate of metallic bone substitutes should be adjusted such that the loss in the load-bearing capacity of the implanted biomaterial is balanced by the gain in the structural integrity of the bone. Furthermore, the biodegradation products must be delivered in acceptable quantities to make sure that they are well tolerated by the body.

If all the requirements for ideal bone substitutes are fulfilled, the regeneration of bony lesions assisted by metallic biomaterials could result in healthy and functional bone. To obtain such ideal biomaterials, advanced fabrication technologies that enable the precise arrangement and control of complex geometries *i.e.*, multi-material additive manufacturing (AM) are required.

1.3 Progress in the development of Fe-based bone substitutes

Fe and its alloys have been studied for temporary load-bearing bone replacements. They combine biodegradable behavior with high mechanical strength and ductility [19]. As compared to Mg-based materials, Fe-based biomaterials have the advantage of not releasing hydrogen as they degrade. Their biodegradation products, being not completely dissolvable in physiological solutions, have been found to hinder the release of iron ions and slow down the biodegradation process [20]. In addition, the ferromagnetic nature of iron may need to be altered prior to using it for the fabrication of imaging-friendly implantable devices.

Alloying Fe with Mn or noble metals and reinforcing Fe with bioceramics through powder metallurgy techniques have been investigated to increase the biodegradation rate [20]. Noble metals, such as Ag, Au, Pd, and Pt [21–23] have been used to create second phases in Fe-based alloys (*e.g.*, Fe-Ag, Fe-Au, Fe-Pd and Fe-Pt), which can induce micro-galvanic coupling to stimulate Fe degradation. Among the possible alloying elements, Mn is considered a promising one because it can not only improve the biodegradation rate of Fe [24–

26], but also lead to anti-ferromagnetic Fe-Mn alloys [27]. For implanted medical devices, such as bone implants, the magnetic properties of the biomaterials are of importance. Fe is ferromagnetic and strongly attracted to a magnetic field. Therefore, alloying Fe with 28 wt% or more Mn to create paramagnetic Fe-Mn alloys is necessary [28]. This will ensure the magnetic resonance imaging (MRI) compatibility of the bone implants for the patients who may need the use of MRI scan during their treatment.

Biofunctionalization of the surface of Fe with polymeric coating is another strategy to enhance the biodegradation of iron [29,30]. Polymers, such as polylactic acid or PLA [31–33], poly(lactic-co-glycolic acid) or PLGA [34], polyethylene glycol or PEG [35], and polyethyleneimine or PEI [36], have been studied as coating materials on Fe. These polymer coatings enhanced biodegradation of Fe by creating an acidic environment during the hydrolyzation of the polymer chains. Although this concept is promising, it leaves the question open as to whether the Fe substrate will still biodegrade fast enough, once the whole polymer coating layer dissolves.

In addition to alloying Fe with Mn and coating Fe surface with polymers, reinforcing Fe with bioceramic materials has been taken as another strategy to improve the biodegradation rate, while providing the biocompatibility of Fe-based materials. To date, various Fe-based bioceramic composites with the addition of hydroxyapatite [37–39], tricalcium phosphate [40–42], calcium silicate (CaSiO_3) [43,44], magnesium silicide (Mg_2Si) [45–47], and bredigite ($\text{Ca}_7\text{Mg}(\text{SiO}_4)_4$) [48,49] have been manufactured. The faster biodegradation rates of these bioceramic materials in the Fe matrix are expected to increase the biodegradation rates of the composite materials. At the same time, the early dissolution of the bioceramic components in the body fluids can promote surface mineralization to stimulate cell adhesion, proliferation, and differentiation. Overall, the benefits from adding bioceramics to Fe have been well acknowledged in improving both biodegradation and bioactivity of Fe-based biomaterials. More research is still needed to determine the appropriate choice of the bioceramics and their optimum concentrations in the composites.

Even though alloying pure Fe can speed up its biodegradation in in vitro tests, such improvements have not been observed in vivo (Figure 1.2a-c) [50]. The inadequate biodegradation rate was explained by insufficient oxygen transport to the biomaterial surface, due to a dense layer of biodegradation products that wrap around the surface and hinder further degradation of iron. These findings suggest that Fe based biomaterials should be designed to be highly porous and highly permeable to enable accelerated biodegradation. As for biocompatibility, in vivo studies on bulk Fe based biomaterials (i.e., Fe-10Mn-1Pd, Fe-21Mn-0.7C-1Pd, Fe-

30Mn, Fe-Mn-Si, and Fe-bioceramics composites) have reported no systemic toxicities [19,50–52].

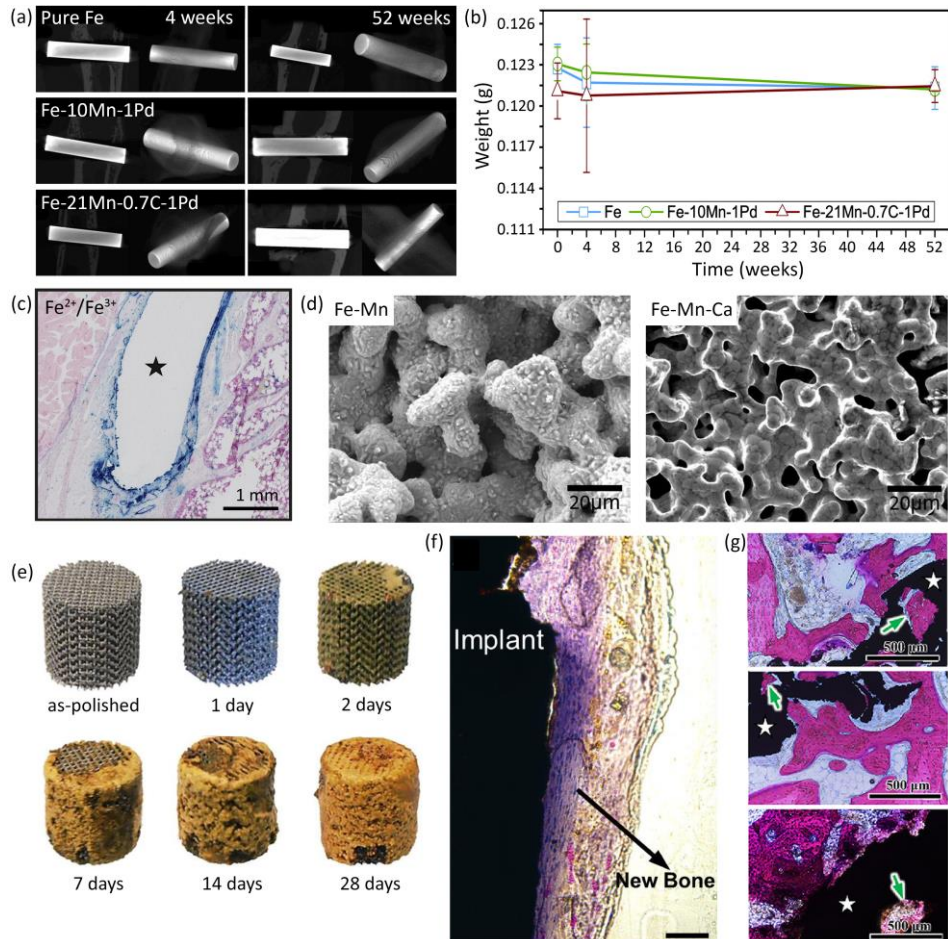


Figure 1.2. Progress of Fe-based bone substitutes. (a, b) *In vivo* biodegradation of bulk Fe-based biomaterials [50] (c) Diffusion of Fe ions *in vivo* [50]. (d) Binder jetted Fe-30Mn [53] and Fe-35Mn-1Ca [54]. (e) *In vitro* biodegradation of SLM porous Fe [55]. (f) *In vivo* osseointegration of SLM Fe-35Mn [56]. (g) Histological images of new bone formation in SLM Fe-30Mn after 48 weeks *in vivo* [57].

The advances in AM technologies (*e.g.*, binder jetting, selective laser melting (SLM), and extrusion-based 3D printing) have opened new possibilities to improve the biodegradation profiles of Fe-based biomaterials through porous topological and multi-material designs. The Fe-30Mn alloy with an open porosity of 36.3% (Figure 1.2d) has been shown to exhibit an electrochemical corrosion

rate that is ~11 times higher than that of pure iron with the same exposed surface area [53]. Moreover, Fe-35Mn-1Ca has been found to almost doubled the biodegradation rate of Fe-35Mn [54]. Furthermore, topologically ordered AM porous pure Fe with 80% porosity (Figure 1.2e) has demonstrated an electrochemical corrosion rate that is ~12 times higher than that of cold-rolled iron [55]. Although the electrochemical corrosion values of AM porous Fe-based biomaterials have been generally found to increase, their *in vitro* biodegradation rates validated *via* immersion tests are low. This may be due to inadequate *in vitro* fluid flow, different atmospheric conditions from those occurring *in vivo*, as well as the absence of blood cells and macrophages, which could have contributed to the faster biodegradation of biomaterials and the removal of the corrosion products. Performing long-term *in vivo* biodegradation studies on porous AM Fe-based biomaterials is, therefore, of critical importance. To date, only two *in vivo* studies on AM porous Fe-based biomaterials intended for the application of bone substitution have been performed. A 4-week *in vivo* study of SLM Fe-35Mn, having a 43% porosity, demonstrated good bone-implant integration [56]. Moreover, SLM Fe-30Mn with 37.8–47.2% porosity exhibited a scaffold volume reduction of 10.1–20.9%, and decreases in the elastic modulus and yield strength of up to 42.3% and 23.3%, respectively, after 48 weeks *in vivo* [57].

In addition to the improved rates of electrochemical biodegradation, the progress in multi-material AM has introduced other functionalities to Fe-based biomaterials including anti-ferromagnetic properties, improved osteosynthesis properties, and assistance in bone cancer treatment. Binder jetted Fe-30Mn [53] and Fe-35Mn-1Ca [54] exhibited the ϵ -martensite and γ -austenite Fe-Mn phases. The ϵ and γ -Fe-Mn phases possessed the intrinsic anti-ferromagnetic properties [58]. Furthermore, the Fe-30CaSiO₃ composites fabricated using material extrusion not only improved the *in vivo* osteosynthesis significantly as compared to pure iron but also demonstrated the potential for bone cancer therapy. In the synergy with laser and reactive oxygen species, the Fe-30CaSiO₃ biomaterial enhanced the therapeutic effects of tumor treatment *in vivo* [44].

In summary, Fe-based biomaterials have shown their potential as temporary load-bearing bone implants. Still, more research employing (multiple materials) AM technologies for Fe-based bone substitutes is required to solve all the challenges of such biomaterial at once: speed up the biodegradation profile, alter the ferromagnetic behavior, enhance the bioactivity for bone regeneration, all while maintaining the bone-mimicking mechanical properties.

1.4 Thesis aim and outline

This thesis contains six chapters to tackle the abovementioned challenges of Fe-based biomaterials as bone substitutes by answering the following research questions:

What is the best multi-material 3D printing option for the fabrication of multi-functional Fe-based materials intended for bone substitution?

In **Chapter 2**, we present a literature study on the additive manufacturing technologies, concerning their capabilities and limitations in performing multi-material 3D printing of metallic biomaterials, not only Fe-based, but also Ti-based and Mg-based. We made choice of extrusion-based 3D printing, which is the most straightforward multi-material fabrication method to achieve biofunctionalized bone-substituting biomaterials.

*Can we use extrusion-based 3D printing to fabricate porous Fe?
What is the performance of the material?*

In the research presented in **Chapter 3**, we developed extrusion-based 3D printed porous Fe and comprehensively studied the *in vitro* biofunctionalities of the material, including the biodegradation and electrochemical responses in simulated body fluid, the changes in its mechanical properties over time due to *in vitro* biodegradation and its cytocompatibility towards a mouse preosteoblast cell line.

Although the extrusion-based 3D printed porous Fe showed somewhat improved biodegradability and bone-mimicking mechanical properties, relative to solid Fe, the overall biofunctionality of the materials needed improvements, which led us to the next research question:

Can a polymer coating improve the biofunctionality of the extrusion-based 3D printed porous Fe?

In **Chapter 4**, we applied poly(2-ethyl-2-oxazoline) coating onto the extrusion-based 3D printed porous Fe and comprehensively studied the *in vitro* characteristics. This chapter shows that such a coating can improve the biofunctionality of AM porous Fe, but only to a limited extent.

This led to the idea that a major biofunctional improvement of AM porous Fe can perhaps only be achieved by altering the natural characteristics of Fe (*i.e.*, by alloying Fe with Mn or reinforcing Fe with akermanite), hence the research questions:

Can we use extrusion-based 3D printing to fabricate porous FeMn alloys and porous Fe-akermanite composites?

What are the performances of these materials?

In the research presented in **Chapters 5** and **6**, we successfully developed *ex situ*-alloyed porous FeMn scaffolds and *ex situ*-composited porous Fe-akermanite scaffolds. The scaffolds tackled one or two challenges in developing Fe-based biomaterials as bone implants, but not all of them at once. With understanding the benefits of adding Mn and akermanite for the biofunctionalities of Fe gained, we moved forward to the final research questions:

Can we use extrusion-based 3D printing to fabricate porous FeMn-akermanite composite scaffolds?

Do alloying Fe with Mn and combining the alloy with akermanite address all the challenges associated with Fe-based biomaterials intended for bone tissue substitution?

In the research presented in **Chapter 7**, we developed *ex situ* porous FeMn-akermanite composite scaffolds and demonstrated that all the major challenges of Fe-based biomaterials can be addressed through this new material configuration.

Bibliography

- [1] M.M. Stevens, Biomaterials for bone tissue engineering, *Mater. Today*. 11 (2008) 18–25. [https://doi.org/10.1016/S1369-7021\(08\)70086-5](https://doi.org/10.1016/S1369-7021(08)70086-5).
- [2] J. Scheinpflug, M. Pfeiffenberger, A. Damerau, F. Schwarz, M. Textor, A. Lang, F. Schulze, Journey into bone models: A review, *Genes (Basel)*. 9 (2018) 247. <https://doi.org/10.3390/genes9050247>.
- [3] B.Q. Le, V. Nurcombe, S.M.K. Cool, C.A. van Blitterswijk, J. de Boer, V.L.S. LaPointe, The components of bone and what they can teach us about regeneration, *Materials (Basel)*. 11 (2017) 1–16. <https://doi.org/10.3390/ma11010014>.
- [4] T.M. Keaveny, W.C. Hayes, Mechanical properties of cortical and trabecular bone, *Bone*. 7 (1993) 285–344.
- [5] R. Florencio-silva, G. Rodrigues, E. Sasso-cerri, M.J. Simões, P.S. Cerri, B. Cells, Biology of bone tissue: Structure, function, and factors that influence bone cells, *Biomed Res. Int*. 2015 (2015) 1–17. <https://doi.org/10.1155/2015/421746>.
- [6] G.M. Calori, E. Mazza, M. Colombo, C. Ripamonti, The use of bone-graft substitutes in large bone defects: Any specific needs?, *Injury*. 42 (2011) S56–S63. <https://doi.org/10.1016/j.injury.2011.06.011>.
- [7] E. Roddy, M.R. DeBaun, A. Daoud-Gray, Y.P. Yang, M.J. Gardner, Treatment of critical-sized bone defects: clinical and tissue engineering perspectives, *Eur. J. Orthop. Surg. Traumatol*. 28 (2018) 351–362. <https://doi.org/10.1007/s00590-017-2063-0>.
- [8] K.S. Griffin, K.M. Davis, T.O. McKinley, J.O. Anglen, T.M.G. Chu, J.D. Boerckel, M.A. Kacena, Evolution of bone grafting: Bone grafts and tissue engineering strategies for vascularized bone regeneration, *Clin. Rev. Bone Miner. Metab*. 13 (2015) 232–244. <https://doi.org/10.1007/s12018-015-9194-9>.
- [9] T. Burk, J. Del Valle, R.A. Finn, C. Phillips, Maximum quantity of bone available for harvest from the anterior iliac crest, posterior iliac crest, and proximal tibia using a standardized surgical approach: A cadaveric study, *J. Oral Maxillofac. Surg*. 74 (2016) 2532–2548. <https://doi.org/10.1016/j.joms.2016.06.191>.
- [10] J.K. McEwan, H.C. Tribe, N. Jacobs, N. Hancock, A.A. Qureshi, D.G. Dunlop, R.O.C. Oreffo, Regenerative medicine in lower limb reconstruction, *Regen. Med*. 13 (2018) 477–490. <https://doi.org/10.2217/rme-2018-0011>.
- [11] J.J. Li, M. Ebied, J. Xu, H. Zreiqat, Current approaches to bone tissue engineering: The interface between biology and engineering, *Adv. Healthc. Mater*. 7 (2018) 1–8. <https://doi.org/10.1002/adhm.201701061>.
- [12] L. Polo-Corrales, M. Latorre-Estevés, J.E. Ramirez-Vick, Scaffold design for bone regeneration, *J. Nanosci. Nanotechnol*. 14 (2014) 15–56. <https://doi.org/10.1166/jnn.2014.9127>.
- [13] A. Kolk, J. Handschel, W. Drescher, D. Rothamel, F. Kloss, M. Blessmann, M. Heiland, K.D. Wolff, R. Smeets, Current trends and future perspectives of bone substitute materials - From space holders to innovative biomaterials, *J. Cranio-Maxillofacial Surg*. 40 (2012) 706–718. <https://doi.org/10.1016/j.jcms.2012.01.002>.
- [14] L. Roseti, V. Parisi, M. Petretta, C. Cavallo, G. Desando, I. Bartolotti, B. Grigolo, Scaffolds for Bone Tissue Engineering: State of the art and new perspectives, *Mater. Sci. Eng. C*. 78 (2017) 1246–1262. <https://doi.org/10.1016/j.msec.2017.05.017>.
- [15] S. Wu, X. Liu, K.W.K. Yeung, C. Liu, X. Yang, Biomimetic porous scaffolds for bone tissue engineering, *Mater. Sci. Eng. R Reports*. 80 (2014) 1–36. <https://doi.org/10.1016/j.mser.2014.04.001>.
- [16] S. Arabnejad, R. Burnett Johnston, J.A. Pura, B. Singh, M. Tanzer, D. Pasini, High-strength porous biomaterials for bone replacement: A strategy to assess the interplay between cell morphology, mechanical properties, bone ingrowth and manufacturing constraints, *Acta Biomater*. 30 (2016) 345–356. <https://doi.org/10.1016/j.actbio.2015.10.048>.
- [17] V. Karageorgiou, D. Kaplan, Porosity of 3D biomaterial scaffolds and osteogenesis, *Biomaterials*. 26 (2005) 5474–5491. <https://doi.org/10.1016/j.biomaterials.2005.02.002>.
- [18] Y.F. Zheng, X.N. Gu, F. Witte, Biodegradable metals, *Mater. Sci. Eng. R Reports*. 77 (2014) 1–34. <https://doi.org/10.1016/j.mser.2014.01.001>.

- [19] R. Gorejová, L. Haverová, R. Oriňáková, A. Oriňák, M. Oriňák, Recent advancements in Fe-based biodegradable materials for bone repair, *J. Mater. Sci.* 54 (2019) 1913–1947. <https://doi.org/10.1007/s10853-018-3011-z>.
- [20] J. He, F.L. He, D.W. Li, Y.L. Liu, Y.Y. Liu, Y.J. Ye, D.C. Yin, Advances in Fe-based biodegradable metallic materials, *RSC Adv.* 6 (2016) 112819–112838. <https://doi.org/10.1039/C6RA20594A>.
- [21] J. Čapek, K. Stehlíková, A. Michalcová, Š. Msallamová, D. Vojtěch, Microstructure, mechanical and corrosion properties of biodegradable powder metallurgical Fe-2 wt% X (X = Pd, Ag and C) alloys, *Mater. Chem. Phys.* 181 (2016) 501–511. <https://doi.org/10.1016/j.matchemphys.2016.06.087>.
- [22] T. Huang, J. Cheng, D. Bian, Y. Zheng, Fe-Au and Fe-Ag composites as candidates for biodegradable stent materials, *J. Biomed. Mater. Res. - Part B Appl. Biomater.* 104 (2016) 225–240. <https://doi.org/10.1002/jbm.b.33389>.
- [23] T. Huang, J. Cheng, Y.F. Zheng, In vitro degradation and biocompatibility of Fe-Pd and Fe-Pt composites fabricated by spark plasma sintering, *Mater. Sci. Eng. C* 35 (2014) 43–53. <https://doi.org/10.1016/j.msec.2013.10.023>.
- [24] Q. Zhang, P. Cao, Degradable porous Fe-35wt.% Mn produced via powder sintering from NH_4HCO_3 porogen, *Mater. Chem. Phys.* 163 (2015) 394–401. <https://doi.org/10.1016/j.matchemphys.2015.07.056>.
- [25] M. Kupková, M. Hrubovčáková, M. Kupka, R. Oriňáková, A.M. Turonová, Sintering behaviour, graded microstructure and corrosion performance of sintered Fe-Mn biomaterials, *Int. J. Electrochem. Sci.* 10 (2015) 9256–9268.
- [26] M. Heiden, E. Walker, E. Nauman, L. Stanciu, Evolution of novel bioresorbable iron-manganese implant surfaces and their degradation behaviors in vitro, *J. Biomed. Mater. Res. - Part A* 103 (2015) 185–193. <https://doi.org/10.1002/jbm.a.35155>.
- [27] H. Hermawan, H. Alamdari, D. Mantovani, D. Dubé, Iron-manganese: New class of metallic degradable biomaterials prepared by powder metallurgy, *Powder Metall.* 51 (2008) 38–45. <https://doi.org/10.1179/174329008X284868>.
- [28] Y. Ishikawa, Y. Endoh, Antiferromagnetism of γ -FeMn alloys, *J. Appl. Phys.* 39 (1968) 1318–1319. <https://doi.org/10.1063/1.1656274>.
- [29] R. Oriňáková, M. Gorejová, Z. Orságová Králová, A. Oriňák, Surface modifications of biodegradable metallic foams for medical applications, *Coatings* 10 (2020) 819. <https://doi.org/10.3390/coatings10090819>.
- [30] A.H. Md Yusop, A. Al Sakka, H. Nur, Modifications on porous absorbable Fe-based scaffolds for bone applications: A review from corrosion and biocompatibility viewpoints, *J. Biomed. Mater. Res. - Part B Appl. Biomater.* 110 (2022) 18–44. <https://doi.org/10.1002/jbm.b.34893>.
- [31] M. Hrubovčáková, M. Kupková, M. Džupon, M. Giretová, L. Medvecký, R. Džunda, Biodegradable polylactic acid and polylactic acid/hydroxyapatite coated iron foams for bone replacement materials, *Int. J. Electrochem. Sci.* 12 (2017) 11122–11136. <https://doi.org/10.20964/2017.12.53>.
- [32] Y. Qi, H. Qi, Y. He, W. Lin, P. Li, L. Qin, Y. Hu, L. Chen, Q. Liu, H. Sun, Q. Liu, G. Zhang, S. Cui, J. Hu, L. Yu, D. Zhang, J. Ding, Strategy of Metal-Polymer Composite Stent to Accelerate Biodegradation of Iron-Based Biomaterials, *ACS Appl. Mater. Interfaces* 10 (2018) 182–192. <https://doi.org/10.1021/acsami.7b15206>.
- [33] X. Li, W. Zhang, W. Lin, H. Qiu, Y. Qi, X. Ma, H. Qi, Y. He, H. Zhang, J. Qian, G. Zhang, R. Gao, D. Zhang, J. Ding, Long-term efficacy of biodegradable metal-polymer composite stents after the first and the second implantations into porcine coronary arteries, *ACS Appl. Mater. Interfaces* 12 (2020) 15703–15715. <https://doi.org/10.1021/acsami.0c00971>.
- [34] A.H.M. Yusop, N.M. Daud, H. Nur, M.R.A. Kadir, H. Hermawan, Controlling the degradation kinetics of porous iron by poly(lactic-co-glycolic acid) infiltration for use as temporary medical implants, *Sci. Rep.* 5 (2015) 1–17. <https://doi.org/10.1038/srep11194>.
- [35] L. Haverová, R. Oriňáková, A. Oriňák, R. Gorejová, M. Baláž, P. Vanýsek, M. Kupková, M. Hrubovčáková, P. Mudroň, J. Radoňák, Z.O. Králová, A.M. Turoňová, An in vitro corrosion study of open cell iron structures with PEG coating for bone replacement applications, *Metals (Basel)* 8 (2018) 1–21. <https://doi.org/10.3390/met8070499>.
- [36] R. Gorejová, R. Oriňáková, Z. Orságová Králová, M. Baláž, M. Kupková, M. Hrubovčáková,

- L. Haverová, M. Džupon, A. Oriňák, F. Kaľavský, K. Kovaľ, In vitro corrosion behavior of biodegradable iron foams with polymeric coating, *Materials (Basel)*. 13 (2020) 1–17.
- [37] M.F. Ullum, A. Arafat, D. Noviana, A.H. Yusop, A.K. Nasution, M.R. Abdul Kadir, H. Hermawan, In vitro and in vivo degradation evaluation of novel iron-bioceramic composites for bone implant applications, *Mater. Sci. Eng. C*. 36 (2014) 336–344. <https://doi.org/10.1016/j.msec.2013.12.022>.
- [38] M.F. Ullum, A.K. Nasution, A.H. Yusop, A. Arafat, M.R.A. Kadir, V. Juniantito, D. Noviana, H. Hermawan, Evidences of in vivo bioactivity of Fe-bioceramic composites for temporary bone implants, *J. Biomed. Mater. Res. - Part B Appl. Biomater.* 103 (2015) 1354–1365. <https://doi.org/10.1002/jbm.b.33315>.
- [39] M. Dehestani, E. Adolfsson, L.A. Stanciu, Mechanical properties and corrosion behavior of powder metallurgy iron-hydroxyapatite composites for biodegradable implant applications, *Mater. Des.* 109 (2016) 556–569. <https://doi.org/10.1016/j.matdes.2016.07.092>.
- [40] A. Reindl, R. Borowsky, S.B. Hein, J. Geis-Gerstorfer, P. Imgrund, F. Petzoldt, Degradation behavior of novel Fe/ β -TCP composites produced by powder injection molding for cortical bone replacement, *J. Mater. Sci.* 49 (2014) 8234–8243. <https://doi.org/10.1007/s10853-014-8532-5>.
- [41] F. He, G. Qian, W. Ren, J. Ke, P. Fan, X. Shi, Y. Cheng, S. Wu, X. Deng, J. Ye, Preparation and characterization of iron/ β -tricalcium phosphate bio-cermet for load-bearing bone substitutes, *Ceram. Int.* 43 (2017) 8348–8355. <https://doi.org/10.1016/j.ceramint.2017.03.173>.
- [42] E.B. Montufar, M. Casas-Luna, M. Horynová, S. Tkachenko, Z. Fohlerová, S. Diaz-de-la-Torre, K. Dvořák, L. Čelko, J. Kaiser, High strength, biodegradable and cytocompatible alpha tricalcium phosphate-iron composites for temporal reduction of bone fractures, *Acta Biomater.* 70 (2018) 293–303. <https://doi.org/10.1016/j.actbio.2018.02.002>.
- [43] S. Wang, Y. Xu, J. Zhou, H. Li, J. Chang, Z. Huan, In vitro degradation and surface bioactivity of iron-matrix composites containing silicate-based bioceramic, *Bioact. Mater.* 2 (2017) 10–18. <https://doi.org/10.1016/j.bioactmat.2016.12.001>.
- [44] H. Ma, T. Li, Z. Huan, M. Zhang, Z. Yang, J. Wang, J. Chang, C. Wu, 3D printing of high-strength bioscaffolds for the synergistic treatment of bone cancer, *NPG Asia Mater.* 10 (2018) 31–44. <https://doi.org/10.1038/s41427-018-0015-8>.
- [45] M. Sikora-Jasinska, C. Paternoster, E. Mostaed, R. Tolouei, R. Casati, M. Vedani, D. Mantovani, Synthesis, mechanical properties and corrosion behavior of powder metallurgy processed Fe/Mg₂Si composites for biodegradable implant applications, *Mater. Sci. Eng. C*. 81 (2017) 511–521. <https://doi.org/10.1016/j.msec.2017.07.049>.
- [46] M. Sikora-Jasinska, P. Chevallier, S. Turgeon, C. Paternoster, E. Mostaed, M. Vedani, D. Mantovani, Long-term in vitro degradation behaviour of Fe and Fe/Mg₂Si composites for biodegradable implant applications, *RSC Adv.* 8 (2018) 9627–9639. <https://doi.org/10.1039/c8ra00404h>.
- [47] M. Sikora-Jasinska, P. Chevallier, S. Turgeon, C. Paternoster, E. Mostaed, M. Vedani, D. Mantovani, Understanding the effect of the reinforcement addition on corrosion behavior of Fe/Mg₂Si composites for biodegradable implant applications, *Mater. Chem. Phys.* 223 (2019) 771–778. <https://doi.org/10.1016/j.matchemphys.2018.11.068>.
- [48] C. Shuai, Y. Li, Y. Yang, S. Peng, W. Yang, F. Qi, S. Xiong, H. Liang, L. Shen, Bioceramic enhances the degradation and bioactivity of iron bone implant, *Mater. Res. Express*. 6 (2019) 115401. <https://doi.org/10.1088/2053-1591/ab45b9>.
- [49] C. Gao, M. Yao, S. Li, P. Feng, S. Peng, C. Shuai, Highly biodegradable and bioactive Fe-Pd-bredigite biocomposites prepared by selective laser melting, *J. Adv. Res.* 20 (2019) 91–104. <https://doi.org/10.1016/j.jare.2019.06.001>.
- [50] T. Kraus, F. Moszner, S. Fischerauer, M. Fiedler, E. Martinelli, J. Eichler, F. Witte, E. Willbold, M. Schinhammer, M. Meischel, P.J. Uggowitzer, J.F. Löffler, A. Weinberg, Biodegradable Fe-based alloys for use in osteosynthesis: Outcome of an in vivo study after 52 weeks, *Acta Biomater.* 10 (2014) 3346–3353. <https://doi.org/10.1016/j.actbio.2014.04.007>.
- [51] M. Traverson, M. Heiden, L.A. Stanciu, E.A. Nauman, Y. Jones-Hall, G.J. Breur, In vivo evaluation of biodegradability and biocompatibility of Fe₃₀Mn alloy, *Vet. Comp. Orthop. Traumatol.* 31 (2018) 10–16. <https://doi.org/10.3415/VCOT-17-06-0080>.

-
- [52] M. Fântânariu, L.C. Trinca, C. Solcan, A. Trofin, Ș. Strungaru, E.V. Șindilar, G. Plavan, S. Stanciu, A new Fe-Mn-Si alloplastic biomaterial as bone grafting material: In vivo study, *Appl. Surf. Sci.* 352 (2015) 129–139. <https://doi.org/10.1016/j.apsusc.2015.04.197>.
- [53] D.T. Chou, D. Wells, D. Hong, B. Lee, H. Kuhn, P.N. Kumta, Novel processing of iron-manganese alloy-based biomaterials by inkjet 3-D printing, *Acta Biomater.* 9 (2013) 8593–8603. <https://doi.org/10.1016/j.actbio.2013.04.016>.
- [54] D. Hong, D.T. Chou, O.I. Velikokhatnyi, A. Roy, B. Lee, I. Swink, I. Issaev, H.A. Kuhn, P.N. Kumta, Binder-jetting 3D printing and alloy development of new biodegradable Fe-Mn-Ca/Mg alloys, *Acta Biomater.* 45 (2016) 375–386. <https://doi.org/10.1016/j.actbio.2016.08.032>.
- [55] Y. Li, H. Jahr, K. Lietaert, P. Pavanram, A. Yilmaz, L.I. Fockaert, M.A. Leeftang, B. Pouran, Y. Gonzalez-Garcia, H. Weinans, J.M.C. Mol, J. Zhou, A.A. Zadpoor, Additively manufactured biodegradable porous iron, *Acta Biomater.* 77 (2018) 380–393. <https://doi.org/10.1016/j.actbio.2018.07.011>.
- [56] D. Carluccio, C. Xu, J. Venezuela, Y. Cao, D. Kent, M. Bermingham, A.G. Demir, B. Previtali, Q. Ye, M. Dargusch, Additively manufactured iron-manganese for biodegradable porous load-bearing bone scaffold applications, *Acta Biomater.* 103 (2020) 346–360. <https://doi.org/10.1016/j.actbio.2019.12.018>.
- [57] Y. Nie, G. Chen, H. Peng, S. Tang, Z. Zhou, F. Pei, B. Shen, In vitro and 48 weeks in vivo performances of 3D printed porous Fe-30Mn biodegradable scaffolds, *Acta Biomater.* 121 (2021) 724–740. <https://doi.org/10.1016/j.actbio.2020.12.028>.
- [58] Y.P. Feng, A. Blanquer, J. Fornell, H. Zhang, P. Solsona, M.D. Baró, S. Suriñach, E. Ibáñez, E. García-Lecina, X. Wei, R. Li, L. Barrios, E. Pellicer, C. Nogués, J. Sort, Novel Fe-Mn-Si-Pd alloys: Insights into mechanical, magnetic, corrosion resistance and biocompatibility performances, *J. Mater. Chem. B.* 4 (2016) 6402–6412. <https://doi.org/10.1039/c6tb01951j>.

Multi-material additive manufacturing technologies for Ti-, Mg-, and Fe-based biomaterials for bone substitution

The growing interest in multi-functional metallic biomaterials for bone substitutes challenges the current additive manufacturing (AM, =3D printing) technologies. It is foreseeable that advances in multi-material AM for metallic biomaterials will not only allow for complex geometrical designs, but also improve their multi-functionalities by tuning the types or compositions of the underlying base materials, thereby presenting unprecedented opportunities for advanced orthopedic treatments. AM technologies are yet to be extensively explored for the fabrication of multi-functional metallic biomaterials, especially for bone substitutes. Here, we present the viable options of the state-of-the-art multi-material AM for metallic biomaterials to be used as bone substitutes. The fabrication technologies for metallic biomaterials were discussed to highlight the advantages of using AM over conventional fabrication methods. Five AM technologies suitable for metal 3D printing are compared against the requirements for multi-material AM. Of these AM technologies, extrusion-based multi-material AM is shown to have the greatest potential to meet the requirements for the fabrication of multi-functional metallic biomaterials.

2.1 Fabrication technologies for metallic biomaterials as bone substitutes

Over the years, porous metallic biomaterials have been produced using conventional fabrication technologies, mostly based on powder metallurgy, such as metal injection molding [1] or the space-holder method [2,3]. Even with the remarkable progress made in these fabrication technologies, certain limitations, such as the impossibility to control the geometry and distribution of pores precisely, as well as dimensional inaccuracies, remain.

Additive manufacturing (AM) has recently emerged as a powerful method for the fabrication of biomaterials, including metallic biomaterials aimed for bone tissue regeneration [4]. AM technologies enable high-precision fabrication with high flexibility in the internal and external macro- and micro-architecture of orthopedic implants [5]. Through controlled AM fabrication processes, geometrical and topological porous characteristics of metallic biomaterials can be precisely tuned, leading to improved bone-mimicking mechanical properties [6,7], altered biodegradation kinetics [8,9], enhanced bone tissue regeneration rates [10–12] and the formation of an extensive, interconnected osteocyte lacuno-canalicular network [13,14]. However, some other properties, including hardness, wear resistance, anti-ferromagnetic properties, or antibacterial properties, cannot be simply adjusted through geometrical design, as they require the adjustments of the properties of the underlying base material(s) prior to AM processing.

As for the biocompatibility, most metallic biomaterials have a relatively low intrinsic osteogenic and osteoimmunomodulation potential as compared with, for example, Ca-P-based bioceramics [15]. Their presence as foreign body objects is often a risk factor for prolonged chronic inflammation [16]. The high surface area to volume ratio of porous AM metallic biomaterials raises another challenge in preventing bacteria colonization. These issues are currently being addressed by taking an additional post-AM step of surface biofunctionalization to add bioactive agents to the porous surfaces in order to improve the performance of AM biomaterials including their osteogenic properties, and to prevent infection [17].

The existing technologies for the fabrication of multi-functional porous AM metallic biomaterials strongly rely on the availability of pre-alloyed materials and the post-AM surface biofunctionalization, thus, being a two-step process. There is a strong need to upgrade the AM technologies so that they can realize the desired spatial distribution and bonding of multiple materials, thereby enabling the *in situ* synthesis of multiple materials in one single AM process.

Utilizing multi-material AM technologies will enable the fabrication of multi-functional porous AM metallic biomaterials with region-specific performance such that the material types and compositions can be specifically placed at different scales within the biomaterials design. The mechanical properties of porous AM metallic biomaterials, including hardness, can be realized, in accordance with those of cortical and cancellous bone by changing not only the porosity but also the material types or compositions. Enhanced osteoconductivity and antibacterial properties with appropriate inflammatory responses can be obtained through the right compositions and distributions of bioactive agents on the metallic surfaces. Varying the compositions and types of materials that have distinct biodegradation properties, for example, from bio-inert or slowly biodegrading biomaterials to fast biodegrading materials, will create complex profiles of biomaterials properties over time, as clinically required.

Despite the fact that numerous properties of porous AM metallic biomaterials can be improved by using multi-material metallic AM technologies, the currently available literature on these technologies is relatively scarce [18]. Recent literature on the AM technologies for bone tissue engineering is mainly focused on the commercially available AM processes and the choices of existing biomaterials, including biocompatible metals [19–23], and geometrical and topological designs of porous AM metallic biomaterials [24–28] in relation to their mechanical and biological performance. Regarding the multi-material AM technologies, multi-material polymers are advancing the frontiers of multi-material AM concepts due to the relative simplicity of the involved processes and the compatibility of those materials with multiple AM technologies [29]. *In situ* multi-material AM for metals and metal-ceramic composites has been mainly reviewed for industrial applications, such as in aerospace and automotive applications [30–32], but not specifically for biomedical applications.

In this review, we present the prospects of using the currently available metallic AM technologies for *in situ* or *ex situ* multi-material fabrication of multi-functional Ti-, Mg-, Fe-based bone-substituting biomaterials. The key principle of each of the AM technologies and its advantages and limitations for multi-material fabrication are described, analyzed, and compared. Recent research on Ti-, Mg-, and Fe-based biomaterials and the (multi-material) AM technologies for these biomaterials is also reviewed. Finally, the current challenges and future perspectives in metallic multi-material AM technologies are provided.

2.2 Multi-material metallic AM technologies

To build multi-functional porous AM metallic biomaterials using multi-material AM technologies, multiple materials must be delivered during the fabrication processes, and strong bonding between biomaterials of different types or compositions must be ensured. Multiple material delivery systems and their bonding processes vary, depending on the particular AM technology used. Meeting these two requirements is essential for successful multi-material fabrication, as they strongly influence the performance of the resulting multi-materials, especially at the interfaces. Some AM technologies only allow the interchange (and bonding) of different materials between layers to lead to the generation of planar multi-material interfaces, while others can deliver and bond any materials throughout the build to achieve complex multi-material interfaces.

There are five AM technologies, according to the ASTM F2792–12a standard [33], that are suitable for the fabrication of metallic biomaterials, including powder bed fusion, directed energy deposition, sheet lamination, binder jetting, and material extrusion. Each of these AM technologies has its own capabilities and limitations, and may or may not meet the requirements for multi-material fabrication.

2.2.1 Powder bed fusion

Powder bed fusion works by delivering a layer of metal powder and then selectively melting or sintering the desired area by using laser or electron beam. The process iteratively continues by lowering the build plate, spreading another metal powder layer over the previous layer, and selectively melting or sintering this layer and the layer(s) beneath. Selective laser melting (SLM) is the most common powder bed fusion technology for fabricating metallic biomaterials. This technology usually utilizes only one powder bed dispensing system for one single metal powder, which makes the fabrication process challenging to accommodate the *in situ* delivery of multiple materials, unless a multi-material powder mixture is prepared beforehand. By using blended metal or metal-ceramic powder mixtures in the powder bed (Figure 2.1a), multi-material SLM has been applied for the multi-material fabrication of Ti-based [53–64] and Mg-based [46–49] biomaterials.

In situ multi-material SLM for Ti-based biomaterials enhanced the hardness and wear resistance through the *in situ* reinforcement of titanium with SiC [34], Si₃N₄ [35], TiB₂ [36,37], or hydroxyapatite (HA) [38,39]. In addition, the *in situ* SLM of titanium with Mo [40], Nb [41,42], and Ta [43], improved biomechanical compatibility with bone in terms of elastic modulus, in comparison with the elastic moduli of pure Ti and Ti-6Al-4V. Moreover, the *in situ* alloying of

Ti-6Al-4V with Cu [44,45] has been shown to upregulate the angiogenesis-related genes and demonstrate antibacterial properties.

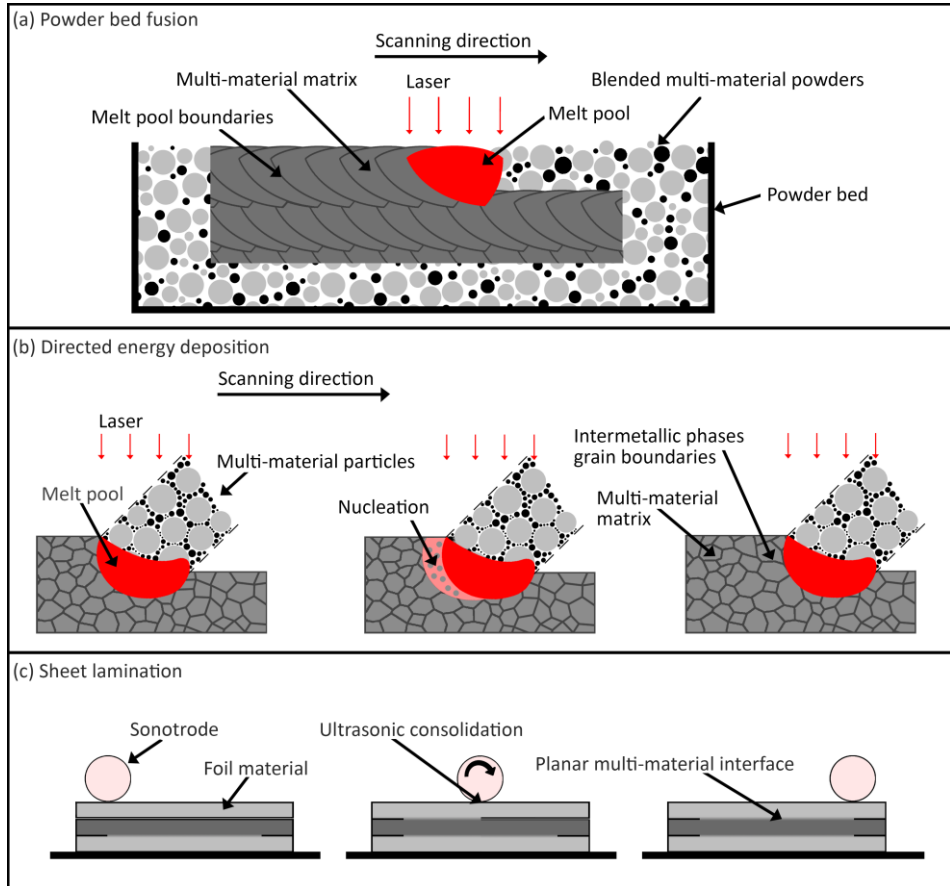


Figure 2.1. Laser and ultrasonic multi-material AM for metals according to the process classifications of ASTM F2792–12a [33]: (a) powder bed fusion, (b) directed energy deposition, and (c) sheet lamination.

For Mg-based biomaterials, the *in situ* alloying of Mg with Zn during SLM [46] has been explored and the relationships between Mg-Zn composition, defects, and mechanical characteristics have been studied. In addition, pre-alloyed Mg-based biomaterials (*e.g.*, ZK60 and Mg-3Zn) have been *in situ* alloyed with rare earth elements (*e.g.*, Nd [47] and Dy [48]) during SLM, for improved corrosion resistance and prolonged biomaterials integrity. Furthermore, the *in situ* alloying of ZK60 with Cu [49] has been found to provide the base alloy with antibacterial properties and improved the compressive

strength. Furthermore, for Fe-based biomaterials, SLM of pre-milled Fe and Mn powders enhanced the biodegradation rate and mechanical properties of the iron [50,51].

To obtain the intended multi-functionality for the biomaterials, optimum SLM processing parameters must be selected to allow for sufficient diffusion of alloying elements into the base materials [34,35]. Tuning laser energy density, while avoiding the formation of undesirable internal pores and excessive melting, is challenging due to the distinctly different thermal properties of multiple materials. Some alloying elements have very high melting points and cannot be completely melted and diffused, and as a result partially melted material remains next to the matrix [41,43]. To bridge the gap in thermal properties, the particle size distributions of multi-material powders can be varied, with a higher melting point material having smaller particle sizes [42]. In addition, post-AM heat treatment may be necessary to improve the multi-material diffusion and homogeneity in chemical composition [41]. Furthermore, the delivery of multi-material powders to the powder bed is an equally important aspect to ensure a uniform multi-material distribution within the resultant biomaterial [43]. Since powder bed fusion operates with high thermal energies, this AM process is also prone to high temperature gradients, which can cause cracks and distortions in the multi-material structure.

Using powder bed fusion for building *in situ* multi-functional AM metals or metal-ceramic composites requires complex and comprehensive process optimization to ensure proper selection of the laser power and the other process parameters that have to be aligned with the physical properties and powder characteristics of each of the materials. In addition, the steps required for the recycling and reuse of the leftover materials in the powder bed need to be considered.

2.2.2 Directed energy deposition

In directed energy deposition, a metallic material is delivered in the form of powder or wire through a nozzle, which is then melted by using thermal energy. Laser engineered net shaping (LENS) is the most common commercial process used for directed energy deposition. This technology offers a straightforward multi-material delivery system through multiple nozzles and the capability of *in situ* deposition and synthesis of different materials to obtain multi-material gradients in the structure (Figure 2.1b). In addition, compositionally graded structures can be produced by depositing one material and gradually replacing that material with another. Using multi-material LENS, Ti-based biomaterials have been *in situ* alloyed with boron [52,53] or reinforced with HA (under a N₂ atmosphere) [54], CaP [55], Nb-Zr-Ta elemental powders [56], and Zr-BN [57] to

improve the hardness and wear resistance of the base biomaterial. Compositionally graded Co-Cr-Mo coating on Ti-6Al-4V surface [58] and TiO₂ coating on Ti surface [59] have been fabricated to minimize the wear-induced loosening of metal-on-metal implants.

Similar to the laser-based multi-material AM processes based on powder bed fusion, the vast differences in the thermal properties of multiple materials have to be comprehensively investigated, in order to match these with the laser parameters and process parameters to create multi-functional structures with no structural or metallurgical defects. Despite the fact that directed energy deposition has the ability of *in situ* deposition of multiple materials, this AM process is less suitable for fabricating structures with fine geometries or hollow passages, which are often required for complex porous biomaterials designs [60]. Apart from that, this technology suffers from the common drawbacks of laser-based AM processes, *i.e.*, high thermal gradients, which can induce residual stresses and metallurgical defects.

2.2.3 Sheet lamination

Sheet lamination is performed by stacking, bonding, and cutting foil materials into a 3D structure, after which an additional machining or milling process is required to make a specific structure. Ultrasonic consolidation is the most commonly used technique for bonding metallic foils [61–63]. Although the main advantages of this technology lie in the low operating temperature and the capability of producing large-scale structures at low costs, this technology has not yet been reported for the fabrication of multi-materials for bone substitutes.

Although sheet lamination accommodates simultaneous multiple foil feeding, due to the stacking and bonding of foils (Figure 2.1c), multi-material interfaces occur only in the planar direction. The major drawback of this technology concerns the voids occurring along the foil interfaces due to excessive and/or insufficient welding, surface roughness, or inaccuracy in the manual positioning of the foils. Such defects create a low bonding strength between the layers and increase the possibility of delamination, which leads to poor mechanical properties of the resulting structure under shear and tensile loading. Considering the capabilities of this technology, the sheet lamination technology is more suitable for an embedded application, rather than multi-material AM for porous bone-substituting biomaterials, where mechanical integrity is one of the most important criteria.

2.2.4 Binder jetting

Binder jetting operates in a similar manner to powder bed fusion, but instead of applying thermal energy to fuse metal powder feedstock, an adhesive

liquid is dispensed on the surface of the powder bed, bonding powder particles to form a desired structure. Since an adhesive liquid is delivered, the compatibility of the binder with metal powders, as well as the bonding properties are of great importance. Several types of adhesives are available, such as polymer binders, particle suspension inks, metallic salt compounds, and organometallic inks [64].

For multi-material binder jetting, a powder bed similar to the one required in powder bed fusion processes is utilized, meaning that this technology requires a carefully designed multi-material powder handling system for the preparation of blended multi-material powder prior to AM, as well as the systems for recycling and reusing the leftover powders after AM. Multi-material binder jetting with blended multi-material metal powders (Figure 2.2a) has been studied for porous Fe-Mn [65] and Fe-Mn-Ca [66] biomaterials to enhance the biodegradation rate of iron and to develop anti-ferromagnetic properties.

Porous binder-jetted biomaterials (*e.g.*, Fe-Mn [65] and Fe-Mn-Ca [66]) are composed of adhesive-bound powders. As such, post-AM debinding and sintering are needed to remove the binder and subsequently fuse multi-material powder particles together. Since the binder-jetted adhesive-bound porous structure is built inside a powder bed, it is required to remove loose powder particles from pores before post-AM heat-treatment, without damaging the structural integrity of the biomaterial. If loose powder particles inside pores are not completely removed, they will fuse into the structure during sintering, compromising the interconnectivity of the pores and reducing the fidelity of the morphological properties of the final biomaterial. The as-printed structure is usually cured to strengthen the adhesive bonding [65], then high-pressure air is applied to remove loose powder particles before sintering [65].

Although removing loose particles in a green structure is demanding, there are no residual stresses created during the binder jetting process, due to the absence of direct laser heating and rapid cooling during fabrication. However, post-AM sintering causes structural shrinkage, as a consequence of binder decomposition and powder particle rearrangement and integration. As an example, Fe-Mn-Ca biomaterials shrank about 11.7% in all directions [66].

In summary, the application of binder jetting for the fabrication of multi-functional porous AM metals or metal-ceramic composite biomaterials not only requires intricate multi-material powder handling systems before and after AM, but also necessitates some steps to remove loose powder particles from the adhesive-bound porous structure and to sinter the particles through a subsequent post-AM heat treatment.

2.2.5 Material extrusion

Extrusion-based AM technology works by continuously pushing metal or ceramic powder-based feedstock through a nozzle or nozzles to build a 3D structure layer by layer. The feedstock materials should have viscoelastic properties that enable them to flow through the nozzle, solidify immediately upon extrusion, and maintain the shape even when they are stretched over the space of the underlying layers [67]. The feedstock materials can be designed to comprise powdered materials of various compositions mixed with a polymer binder. The compatibility of the feedstock material with the binder should avoid undesired interactions during mixing, extrusion, debinding, and even sintering. For multi-material AM purposes, more than one nozzle can be integrated to deliver different feedstock materials and achieve complex multi-material interfaces within the structure. Alternatively, one feedstock of multi-material can be prepared and delivered through one single nozzle.

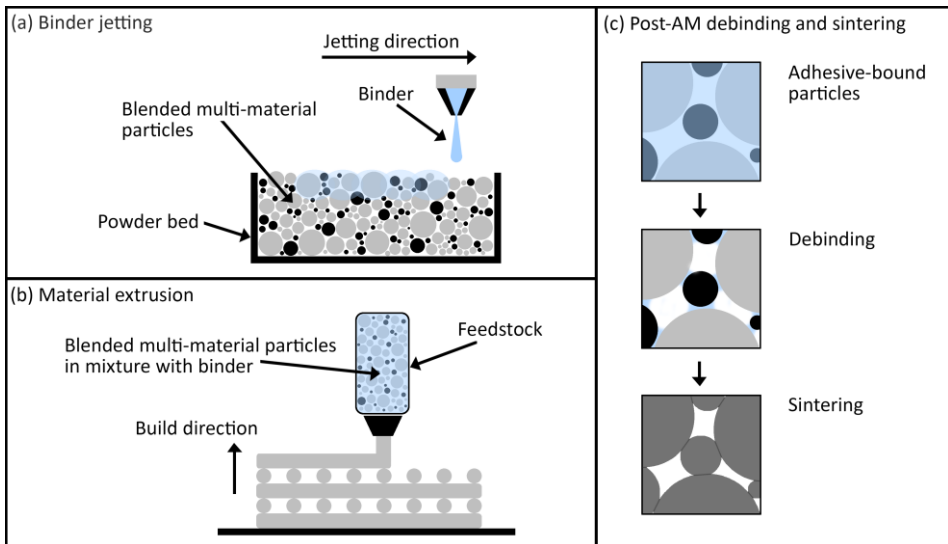


Figure 2.2. Adhesive multi-material AM for metals according to the process classifications of ASTM F2792–12a [33]: (a) binder jetting and (b) material extrusion.

Material extrusion with blended multi-material powder-based feedstock (Figure 2.2b) has been pursued [68–70], since it has no drawbacks inherent to the laser-based AM technologies that were described earlier, such as residual stresses, cracks, distortions, and even metallurgical defects. Using this technique, Fe-based biomaterials (*e.g.*, Fe-CaSiO₃) has been realized for bone cancer treatment as well as for regenerating cortical bone defects [68]. The extruded

Fe-CaSiO₃ composite is composed of an adhesive-bound multi-material powder mixture, which requires post-AM debinding and sintering. Since the adhesive-bound structure is not built in the powder bed, it saves the powder handling steps of recycling and reusing multi-material powder, as well as the post-AM step to remove loose powder particles.

The main limitation of this technology lies in the printing resolution, which is strongly dependent on the powder particle size and the nozzle diameter. In addition, building a part with a large aspect ratio and an overhanging structure can only be achieved by controlling the composition of the feedstock and its rheological properties in order to ensure consistent flow and fast solidification. Designing suitable multi-material feedstock is the most crucial step to achieve complex structures with multi-material interfaces.

2.3 Selection of multi-material AM technologies for the fabrication of multi-functional Fe-based bone substitutes

Choosing a suitable multi-material AM technology for fabricating multi-functional porous metallic biomaterials requires a comprehensive knowledge of the capabilities and limitations of each of the processes described earlier. The basic requirements for a multi-material AM technology concern the capabilities of delivering multiple materials, achieving complex multi-material interfaces, and ensuring strong bonding between the materials of different types and compositions.

With respect to the material delivery systems that influence the multi-material interaction, three systems have been implemented in AM technologies, namely powder bed dispensers, nozzles, and foil material delivery systems. The AM processes based on powder bed fusion, binder jetting, directed energy deposition, and material extrusion allow for the building of complex multi-material interfaces, while sheet lamination can only create planar multi-material interfaces.

Moreover, the cost effectiveness in relation to the material delivery system is another issue to address. Using a powder bed dispensing system to build complex multi-material interfaces requires an advanced powder handling system to allow for the recycling and reuse of multi-material powder mixtures. A post-AM step is needed to remove the unbound or unmolten powder particles entrapped in the pores of structures. This step is demanding, especially for binder jetting, as the as-built structure is bound only by an adhesive material and is, thus, vulnerable. Multi-material deposition using nozzles in material extrusion and directed energy deposition processes is capable of controlling the quantity of the materials needed, while recycling and reusing the powder or a post-AM step

of removing loose powder particles are not required. Nozzles are, therefore, a more suitable material delivery means for multi-material AM.

In addition to the material delivery system, bonding between multiple materials is of critical importance for the performance of multi-functional porous AM metallic biomaterials. Two material bonding approaches are usually used in multi-material AM technologies including direct heating by laser or adhesive bonding by using a binder, followed by post-AM heat treatment. The chosen type of bonding also determines the final microstructure of the multi-material. Using direct heating in powder bed fusion and directed energy deposition processes enables the *in situ* AM of multi-materials. This approach, however, requires advanced process control and management, due to the integration of laser energy into the AM machine and the vast differences in thermal properties between multiple materials. Adhesive bonding in binder jetting and material extrusion, on the other hand, is only capable of the *ex situ* AM of multi-materials and requires post-AM debinding and sintering. The biocompatibility of the residual binder entrapped inside the multi-material structure may be an important issue to consider.

AM using direct heating usually produces mechanically stable structures. However, there is a risk of having high thermal gradients and metallurgical mismatch, which may induce residual stresses or structural defects. Furthermore, this is a challenging approach for fabricating metals with low boiling points and high vapor pressures. On the other hand, the post-processing of adhesive-bound AM structures is usually conducted in a homogeneously heated furnace, which allows the materials to diffuse slowly and bond strongly through sintering. Although sintering leads to the shrinkage of the structure, this can be compensated for during the design phase and minimized during fabrication. In addition, the parameters of the sintering processing can be optimized to yield high-density structures, which presents an opportunity to fabricate not only porous but also fully dense biomaterials for bone substitutes. Based on the advantages and disadvantages of each of bonding approaches, adhesive bonding followed by sintering seems to be a better choice for multi-material bonding.

Comparing the five available multi-material AM technologies, material extrusion appears to be the most straightforward option for multi-material fabrication of multi-functional bone substituting biomaterials [68]. Material extrusion is capable of building multi-material interfaces. Moreover, material extrusion does not directly heat the feedstock materials to fuse the multiple materials, making it less probable to create metallurgical defects in the structure. In addition to Fe-CaSiO₃ scaffolds that were aimed for bone substitutes [68], multi-material extrusion AM has been applied to fabricate materials for other types of application including hydroxyapatite-based surgical biomaterials,

graphene-based materials for biomedical electronic devices, and other multi-element materials systems such as Fe-Ni-Cr, Al-Mg-Cr-Fe and Ag-Cu for various applications [69–73].

2.4 Concluding remarks and future perspective

The initial efforts of the bone tissue engineering community were mainly focused on fabricating biomaterials that mimic the macrostructure of the natural bone. Recent efforts have been mobilized to produce biomaterials using the AM technologies that allow for the realization of micro-architecture porous geometries and the placement of the right biomaterial at the right place for bone regeneration. Given the possibility of high-precision manufacturing of complex macro- and micro-architecture porous biomaterials, the AM technologies are undoubtedly linked to the future of metallic biomaterials for bone implants.

Clearly, AM technologies intrinsically provide the potential for multi-material fabrication that have not yet been extensively explored for bone implant applications. Using multi-material AM technologies, the functional requirements of biomaterials for bone implants, such as long-term mechanical properties for permanent use, short-term mechanical integrity, and biodegradation for temporary replacements, as well as biocompatibility, can be tailored not only through structural design but also via adjustment of material types or compositions.

Among the available multi-material AM technologies, extrusion-based AM, using multi-material powder-based feedstock, appears to be the most straightforward option due to its capability of fabricating complex multi-material interfaces with a simple manufacturing process. For the multi-material extrusion-based AM to be successful in fabricating metallic bone substitutes, the fabrication processes, implant design, and material choice need to be properly selected. Understanding the chemistry of multiple materials in the feedstock, which may or may not affect the AM process, structure, and material properties, is essential. In addition, ensuring a homogenous distribution of multiple materials in the feedstock prior to AM and in the fabricated biomaterials is equally important in order to achieve near-isotropic material properties. Together with appropriate AM processing parameters, the multi-material feedstock with shear-thinning behavior and free-standing characteristics should allow continuous, stable deposition of structures even when the aspect ratios are high. Post-AM debinding and sintering need to be adjusted with respect to temperature, time, and atmosphere in order to achieve specific microstructures and biomaterial functionalities. Even though the multi-material extrusion-based technology has been so far primarily applied to Fe-based bone-substituting [68], it can, in principle, be applied to a wide range of powdered feedstock materials

for various multi-functionalities, including metallic biomaterials, such as tantalum-based alloys and shape memory alloys.

The future research on the multi-material extrusion-based AM for metallic biomaterials should be directed towards enhanced abilities to introduce materials of different types or compositions locally at a few micrometer scale within the structure. This will advance the technology towards improved control over the resulting implant properties. Additionally, fabricating geometrically complex multi-functional biomaterials should involve easily dissolvable or decomposable sacrificial support materials that will pose no adverse effects on the performance and biocompatibility of the resultant biomaterials. Finally, combining multi-material extrusion-based AM with two-dimensional nanopatterning on each layer [74–76] during the fabrication process could further improve the functionalities of the final biomaterials through the optimization of surface nanotopography. Overall, multi-material extrusion-based AM technologies hold a great promise for advancing the state of the art in the fabrication of metallic multi-functional bone substitutes.

Bibliography

- [1] M.F.F.A. Hamidi, W.S.W. Harun, M. Samykano, S.A.C. Ghani, Z. Ghazalli, F. Ahmad, A.B. Sulong, A review of biocompatible metal injection moulding process parameters for biomedical applications, *Mater. Sci. Eng. C*. 78 (2017) 1263–1276. <https://doi.org/10.1016/j.msec.2017.05.016>.
- [2] B. Arifvianto, J. Zhou, Fabrication of metallic biomedical scaffolds with the space holder method: A review, *Materials* (Basel). 7 (2014) 3588–3622. <https://doi.org/10.3390/ma7053588>.
- [3] Y. Chen, D. Kent, M. Bermingham, A. Dehghan-Manshadi, G. Wang, C. Wen, M. Dargusch, Manufacturing of graded titanium scaffolds using a novel space holder technique, *Bioact. Mater.* 2 (2017) 248–252. <https://doi.org/10.1016/j.bioactmat.2017.07.001>.
- [4] A.A. Zadpoor, J. Malda, Additive manufacturing of biomaterials, tissues, and organs, *Ann. Biomed. Eng.* 45 (2017) 1–11. <https://doi.org/10.1007/s10439-016-1719-y>.
- [5] S. Bose, S. Vahabzadeh, A. Bandyopadhyay, Bone tissue engineering using 3D printing, *Mater. Today*. 16 (2013) 496–504. <https://doi.org/10.1016/j.mattod.2013.11.017>.
- [6] G. Campoli, M.S. Borleffs, S. Amin Yavari, R. Wauthle, H. Weinans, A.A. Zadpoor, Mechanical properties of open-cell metallic biomaterials manufactured using additive manufacturing, *Mater. Des.* 49 (2013) 957–965. <https://doi.org/10.1016/j.matdes.2013.01.071>.
- [7] S. Amin Yavari, R. Wauthle, J. Van Der Stok, A.C. Riemsdijk, M. Janssen, M. Mulier, J.P. Kruth, J. Schrooten, H. Weinans, A.A. Zadpoor, Fatigue behavior of porous biomaterials manufactured using selective laser melting, *Mater. Sci. Eng. C*. 33 (2013) 4849–4858. <https://doi.org/10.1016/j.msec.2013.08.006>.
- [8] Y. Li, J. Zhou, P. Pavanram, M.A. Leeftang, L.I. Fockaert, B. Pouran, N. Tümer, K.U. Schröder, J.M.C. Mol, H. Weinans, H. Jahr, A.A. Zadpoor, Additively manufactured biodegradable porous magnesium, *Acta Biomater.* 67 (2018) 378–392. <https://doi.org/10.1016/j.actbio.2017.12.008>.
- [9] Y. Li, H. Jahr, K. Lietaert, P. Pavanram, A. Yilmaz, L.I. Fockaert, M.A. Leeftang, B. Pouran, Y. Gonzalez-Garcia, H. Weinans, J.M.C. Mol, J. Zhou, A.A. Zadpoor, Additively manufactured biodegradable porous iron, *Acta Biomater.* 77 (2018) 380–393. <https://doi.org/10.1016/j.actbio.2018.07.011>.
- [10] A. Fukuda, M. Takemoto, T. Saito, S. Fujibayashi, M. Neo, D.K. Pattanayak, T. Matsushita, K. Sasaki, N. Nishida, T. Kokubo, T. Nakamura, Osteoinduction of porous Ti implants with a channel structure fabricated by selective laser melting, *Acta Biomater.* 7 (2011) 2327–2336. <https://doi.org/10.1016/j.actbio.2011.01.037>.
- [11] S. Van Bael, Y.C. Chai, S. Truscetto, M. Moesen, G. Kerckhofs, H. Van Oosterwyck, J.P. Kruth, J. Schrooten, The effect of pore geometry on the *in vitro* biological behavior of human periosteum-derived cells seeded on selective laser-melted Ti6Al4V bone scaffolds, *Acta Biomater.* 8 (2012) 2824–2834. <https://doi.org/10.1016/j.actbio.2012.04.001>.
- [12] N. Taniguchi, S. Fujibayashi, M. Takemoto, K. Sasaki, B. Otsuki, T. Nakamura, T. Matsushita, T. Kokubo, S. Matsuda, Effect of pore size on bone ingrowth into porous titanium implants fabricated by additive manufacturing: An *in vivo* experiment, *Mater. Sci. Eng. C*. 59 (2016) 690–701. <https://doi.org/10.1016/j.msec.2015.10.069>.
- [13] F.A. Shah, A. Snis, A. Matic, P. Thomsen, A. Palmquist, 3D printed Ti6Al4V implant surface promotes bone maturation and retains a higher density of less aged osteocytes at the bone-implant interface, *Acta Biomater.* 30 (2016) 357–367. <https://doi.org/10.1016/j.actbio.2015.11.013>.
- [14] F.A. Shah, O. Omar, F. Suska, A. Snis, A. Matic, L. Emanuelsson, B. Norlindh, J. Lausmaa, P. Thomsen, A. Palmquist, Long-term osseointegration of 3D printed CoCr constructs with an interconnected open-pore architecture prepared by electron beam melting, *Acta Biomater.* 36 (2016) 296–309. <https://doi.org/10.1016/j.actbio.2016.03.033>.
- [15] D. Xiao, J. Zhang, C. Zhang, D. Barbieri, H. Yuan, L. Moroni, G. Feng, The role of calcium phosphate surface structure in osteogenesis and the mechanism involved, *Acta Biomater.* 106 (2019) 22–33. <https://doi.org/10.1016/j.actbio.2019.12.034>.
- [16] P.H. Wooley, N.J. Hallab, Wound healing, chronic inflammation, and immune responses, in: *Metal-on-Metal Bearings*, Springer, New York, NY, 2014: pp. 109–133.
- [17] I.A.J. van Hengel, M. Riool, L.E. Fratila-Apachitei, J. Witte-Bouma, E. Farrell, A.A. Zadpoor, S.A.J. Zaai, I. Apachitei, Selective laser melting porous metallic implants with immobilized silver nanoparticles kill and prevent biofilm formation by methicillin-resistant

- Staphylococcus aureus, *Biomaterials*. 140 (2017) 1–15.
<https://doi.org/10.1016/j.biomaterials.2017.02.030>.
- [18] A. Bandyopadhyay, B. Heer, Additive manufacturing of multi-material structures, *Mater. Sci. Eng. R Reports*. 129 (2018) 1–16. <https://doi.org/10.1016/j.mser.2018.04.001>.
- [19] S. Bose, D. Ke, H. Sahasrabudhe, A. Bandyopadhyay, Additive manufacturing of biomaterials, *Prog. Mater. Sci.* 93 (2018) 45–111.
<https://doi.org/10.1016/j.pmatsci.2017.08.003>.
- [20] W.S.W. Harun, M.S.I.N. Kamariah, N. Muhamad, S.A.C. Ghani, F. Ahmad, Z. Mohamed, A review of powder additive manufacturing processes for metallic biomaterials, *Powder Technol.* 327 (2018) 128–151. <https://doi.org/10.1016/j.powtec.2017.12.058>.
- [21] A. Wubneh, E.K. Tsekoura, C. Ayranci, H. Uludağ, Current state of fabrication technologies and materials for bone tissue engineering, *Acta Biomater.* 80 (2018) 1–30.
<https://doi.org/10.1016/j.actbio.2018.09.031>.
- [22] A.P. Moreno Madrid, S.M. Vrech, M.A. Sanchez, A.P. Rodriguez, Advances in additive manufacturing for bone tissue engineering scaffolds, *Mater. Sci. Eng. C*. 100 (2019) 631–644. <https://doi.org/10.1016/j.msec.2019.03.037>.
- [23] L. Zhang, G. Yang, B.N. Johnson, X. Jia, Three-dimensional (3D) printed scaffold and material selection for bone repair, *Acta Biomater.* 84 (2019) 16–33.
<https://doi.org/10.1016/j.actbio.2018.11.039>.
- [24] X. Wang, S. Xu, S. Zhou, W. Xu, M. Leary, P. Choong, M. Qian, M. Brandt, Y.M. Xie, Topological design and additive manufacturing of porous metals for bone scaffolds and orthopaedic implants: A review, *Biomaterials*. 83 (2016) 127–141.
<https://doi.org/10.1016/j.biomaterials.2016.01.012>.
- [25] X.P. Tan, Y.J. Tan, C.S.L. Chow, S.B. Tor, W.Y. Yeong, Metallic powder-bed based 3D printing of cellular scaffolds for orthopaedic implants: A state-of-the-art review on manufacturing, topological design, mechanical properties and biocompatibility, *Mater. Sci. Eng. C*. 76 (2017) 1328–1343. <https://doi.org/10.1016/j.msec.2017.02.094>.
- [26] X.Y. Zhang, G. Fang, J. Zhou, Additively manufactured scaffolds for bone tissue engineering and the prediction of their mechanical behavior: A review, *Materials (Basel)*. 10 (2017) 50.
<https://doi.org/10.3390/ma10010050>.
- [27] A.A. Zadpoor, Additively manufactured porous metallic biomaterials, *J. Mater. Chem. B*. 7 (2019) 4088–4117. <https://doi.org/10.1039/c9tb00420c>.
- [28] L. Yuan, S. Ding, C. Wen, Additive manufacturing technology for porous metal implant applications and triple minimal surface structures: A review, *Bioact. Mater.* 4 (2019) 56–70.
<https://doi.org/10.1016/j.bioactmat.2018.12.003>.
- [29] R. Singh, R. Kumar, I. Farina, F. Colangelo, L. Feo, F. Fraternali, Multi-material additive manufacturing of sustainable innovative materials and structures, *Polymers (Basel)*. 11 (2019) 1–14. <https://doi.org/10.3390/polym11010062>.
- [30] S. Dadbakhsh, R. Mertens, L. Hao, J. Van Humbeeck, J.P. Kruth, Selective laser melting to manufacture “*in situ*” metal matrix composites: A review, *Adv. Eng. Mater.* 21 (2019) 1–18.
<https://doi.org/10.1002/adem.201801244>.
- [31] E. Fereiduni, M. Yakout, M. Elbestawi, Laser-based additive manufacturing of lightweight metal matrix composites, in: *Additive Manufacturing of Emerging Materials*, Springer, Cham, 2019; pp. 55–109.
- [32] T. Larimian, T. Borkar, Additive manufacturing of *in situ* metal matrix composites, in: *Additive Manufacturing of Emerging Materials*, Springer, Cham, 2019; pp. 1–28.
- [33] ASTM F2792-12, Standard Terminology for Additive Manufacturing Technologies, ASTM International, (2012).
- [34] D. Gu, Y.C. Hagedorn, W. Meiners, K. Wissenbach, R. Poprawe, Selective Laser Melting of in-situ TiC/Ti₅Si₃ composites with novel reinforcement architecture and elevated performance, *Surf. Coatings Technol.* 205 (2011) 3285–3292.
<https://doi.org/10.1016/j.surfcoat.2010.11.051>.
- [35] D. Gu, C. Hong, G. Meng, Densification, microstructure, and wear property of in situ titanium nitride-reinforced titanium silicide matrix composites prepared by a novel selective laser melting process, *Metall. Mater. Trans. A Phys. Metall. Mater. Sci.* 43 (2012) 697–708.
<https://doi.org/10.1007/s11661-011-0876-8>.
- [36] L. Liu, M. He, X. Xu, C. Zhao, Y. Gan, J. Lin, J. Luo, Preliminary study on the corrosion resistance, antibacterial activity and cytotoxicity of selective-laser-melted Ti6Al4V-xCu alloys, *Mater. Sci. Eng. C*. 72 (2017) 631–640.
<https://doi.org/10.1016/j.msec.2016.11.126>.

- [37] X. Xu, Y. Lu, S. Li, S. Guo, M. He, K. Luo, J. Lin, Copper-modified Ti6Al4V alloy fabricated by selective laser melting with pro-angiogenic and anti-inflammatory properties for potential guided bone regeneration applications, *Mater. Sci. Eng. C* 90 (2018) 198–210. <https://doi.org/10.1016/j.msec.2018.04.046>.
- [38] C. Cai, C. Radoslaw, J. Zhang, Q. Yan, S. Wen, B. Song, Y. Shi, In-situ preparation and formation of TiB/Ti-6Al-4V nanocomposite via laser additive manufacturing: Microstructure evolution and tribological behavior, *Powder Technol.* 342 (2019) 73–84. <https://doi.org/10.1016/j.powtec.2018.09.088>.
- [39] H. Attar, M. Bönisch, M. Calin, L.C. Zhang, S. Scudino, J. Eckert, Selective laser melting of in situ titanium-titanium boride composites: Processing, microstructure and mechanical properties, *Acta Mater.* 76 (2014) 13–22. <https://doi.org/10.1016/j.actamat.2014.05.022>.
- [40] C. Han, Q. Wang, B. Song, W. Li, Q. Wei, S. Wen, J. Liu, Y. Shi, Microstructure and property evolutions of titanium/nano-hydroxyapatite composites in-situ prepared by selective laser melting, *J. Mech. Behav. Biomed. Mater.* 71 (2017) 85–94. <https://doi.org/10.1016/j.jmbbm.2017.02.021>.
- [41] C. Han, Y. Li, Q. Wang, D. Cai, Q. Wei, L. Yang, S. Wen, J. Liu, Y. Shi, Titanium/hydroxyapatite (Ti/HA) gradient materials with quasi-continuous ratios fabricated by SLM: Material interface and fracture toughness, *Mater. Des.* 141 (2018) 256–266. <https://doi.org/10.1016/j.matdes.2017.12.037>.
- [42] B. Vrancken, L. Thijs, J.P. Kruth, J. Van Humbeeck, Microstructure and mechanical properties of a novel β titanium metallic composite by selective laser melting, *Acta Mater.* 68 (2014) 150–158. <https://doi.org/10.1016/j.actamat.2014.01.018>.
- [43] J.C. Wang, Y.J. Liu, P. Qin, S.X. Liang, T.B. Sercombe, L.C. Zhang, Selective laser melting of Ti–35Nb composite from elemental powder mixture: Microstructure, mechanical behavior and corrosion behavior, *Mater. Sci. Eng. A* 760 (2019) 214–224. <https://doi.org/10.1016/j.msea.2019.06.001>.
- [44] M. Fischer, D. Joguet, G. Robin, L. Peltier, P. Laheurte, In situ elaboration of a binary Ti–26Nb alloy by selective laser melting of elemental titanium and niobium mixed powders, *Mater. Sci. Eng. C* 62 (2016) 852–859. <https://doi.org/10.1016/j.msec.2016.02.033>.
- [45] S.L. Sing, W.Y. Yeong, F.E. Wiria, Selective laser melting of titanium alloy with 50 wt% tantalum: Microstructure and mechanical properties, *J. Alloys Compd.* 660 (2016) 461–470. <https://doi.org/10.1016/j.jallcom.2015.11.141>.
- [46] K. Wei, X. Zeng, Z. Zhang, J. Deng, M. Liu, G. Huang, X. Yuan, Selective laser melting of Mg–Zn binary alloys: Effects of Zn content on densification behavior, microstructure, and mechanical property, *Mater. Sci. Eng. A* 756 (2019) 226–236. <https://doi.org/10.1016/j.msea.2019.04.067>.
- [47] C. Shuai, Y. Yang, S. Peng, C. Gao, P. Feng, J. Chen, Y. Liu, X. Lin, S. Yang, F. Yuan, Nd-induced honeycomb structure of intermetallic phase enhances the corrosion resistance of Mg alloys for bone implants, *J. Mater. Sci. Mater. Med.* 28 (2017) 1–12. <https://doi.org/10.1007/s10856-017-5945-0>.
- [48] T. Long, X. Zhang, Q. Huang, L. Liu, Y. Liu, J. Ren, Y. Yin, D. Wu, H. Wu, Novel Mg-based alloys by selective laser melting for biomedical applications: microstructure evolution, microhardness and *in vitro* degradation behaviour, *Virtual Phys. Prototyp.* 13 (2018) 71–81. <https://doi.org/10.1080/17452759.2017.1411662>.
- [49] C. Shuai, L. Liu, M. Zhao, P. Feng, Y. Yang, W. Guo, C. Gao, F. Yuan, Microstructure, biodegradation, antibacterial and mechanical properties of ZK60–Cu alloys prepared by selective laser melting technique, *J. Mater. Sci. Technol.* 34 (2018) 1944–1952. <https://doi.org/10.1016/j.jmst.2018.02.006>.
- [50] D. Carlucci, C. Xu, J. Venezuela, Y. Cao, D. Kent, M. Birmingham, A.G. Demir, B. Previtali, Q. Ye, M. Dargusch, Additively manufactured iron-manganese for biodegradable porous load-bearing bone scaffold applications, *Acta Biomater.* 103 (2020) 346–360. <https://doi.org/10.1016/j.actbio.2019.12.018>.
- [51] C. Shuai, W. Yang, Y. Yang, H. Pan, C. He, F. Qi, D. Xie, H. Liang, Selective laser melted Fe–Mn bone scaffold: Microstructure, corrosion behavior and cell response, *Mater. Res. Express* 7 (2019) 015404. <https://doi.org/10.1088/2053-1591/ab62f5>.
- [52] Y. Hu, B. Zhao, F. Ning, H. Wang, W. Cong, In-situ ultrafine three-dimensional quasi-continuous network microstructural TiB reinforced titanium matrix composites fabrication using laser engineered net shaping, *Mater. Lett.* 195 (2017) 116–119. <https://doi.org/10.1016/j.matlet.2017.02.112>.
- [53] Y. Hu, F. Ning, H. Wang, W. Cong, B. Zhao, Laser engineered net shaping of quasi-

- continuous network microstructural TiB reinforced titanium matrix bulk composites: Microstructure and wear performance, *Opt. Laser Technol.* 99 (2018) 174–183. <https://doi.org/10.1016/j.optlastec.2017.08.032>.
- [54] H. Sahasrabudhe, A. Bandyopadhyay, In situ reactive multi-material Ti6Al4V-calcium phosphate-nitride coatings for bio-tribological applications, *J. Mech. Behav. Biomed. Mater.* 85 (2018) 1–11. <https://doi.org/10.1016/j.jmbbm.2018.05.020>.
- [55] A. Bandyopadhyay, S. Ditttrick, T. Gualtieri, J. Wu, W.M.K. Biomedical, M. Engineering, Calcium phosphate–titanium composites for articulating surfaces of load-bearing implants, *J. Mech. Behav. Biomed. Mater.* 57 (2016) 280–288. <https://doi.org/10.1016/j.jmbbm.2015.11.022>.
- [56] S. Samuel, S. Nag, S. Nasrazadani, V. Ukirde, M. El Bouanani, A. Mohandas, K. Nguyen, R. Banerjee, Corrosion resistance and in vitro response of laser-deposited Ti-Nb-Zr-Ta alloys for orthopedic implant applications, *J. Biomed. Mater. Res. - Part A*. 94 (2010) 1251–1256. <https://doi.org/10.1002/jbm.a.32782>.
- [57] K.D. Traxel, A. Bandyopadhyay, Reactive-deposition-based additive manufacturing of Ti-Zr-BN composites, *Addit. Manuf.* 24 (2018) 353–363. <https://doi.org/10.1016/j.addma.2018.10.005>.
- [58] B. Vamsi Krishna, W. Xue, S. Bose, A. Bandyopadhyay, Functionally graded Co-Cr-Mo coating on Ti-6Al-4V alloy structures, *Acta Biomater.* 4 (2008) 697–706. <https://doi.org/10.1016/j.actbio.2007.10.005>.
- [59] V.K. Balla, P.D. DeVasConCellos, W. Xue, S. Bose, A. Bandyopadhyay, Fabrication of compositionally and structurally graded Ti-TiO₂ structures using laser engineered net shaping (LENS), *Acta Biomater.* 5 (2009) 1831–1837. <https://doi.org/10.1016/j.actbio.2009.01.011>.
- [60] F.H. Froes, B. Dutta, The additive manufacturing (AM) of titanium alloys, *Adv. Mater. Res.* 1019 (2014) 19–25. <https://doi.org/10.1016/B978-0-12-800054-0.00024-1>.
- [61] G.D.J. Ram, C. Robinson, Y. Yang, B.E. Stucker, Use of ultrasonic consolidation for fabrication of multi-material structures, *Rapid Prototyp. J.* 13 (2007) 226–235. <https://doi.org/10.1108/13552540710776179>.
- [62] B.E. Stucker, J.O. Obielodan, A. Ceylan, L.E. Murr, Multi-material bonding in ultrasonic consolidation, *Rapid Prototyp. J.* 16 (2010) 180–188. <https://doi.org/10.1108/13552541011034843>.
- [63] J. Obielodan, B. Stucker, A fabrication methodology for dual-material engineering structures using ultrasonic additive manufacturing, *Int. J. Adv. Manuf. Technol.* 70 (2014) 277–284. <https://doi.org/10.1007/s00170-013-5266-5>.
- [64] Y. Bai, C.B. Williams, Binder jetting additive manufacturing with a particle-free metal ink as a binder precursor, *Mater. Des.* 147 (2018) 146–156. <https://doi.org/10.1016/j.matdes.2018.03.027>.
- [65] D.T. Chou, D. Wells, D. Hong, B. Lee, H. Kuhn, P.N. Kumta, Novel processing of iron-manganese alloy-based biomaterials by inkjet 3-D printing, *Acta Biomater.* 9 (2013) 8593–8603. <https://doi.org/10.1016/j.actbio.2013.04.016>.
- [66] D. Hong, D.T. Chou, O.I. Velikokhatnyi, A. Roy, B. Lee, I. Swink, I. Issaev, H.A. Kuhn, P.N. Kumta, Binder-jetting 3D printing and alloy development of new biodegradable Fe-Mn-Ca/Mg alloys, *Acta Biomater.* 45 (2016) 375–386. <https://doi.org/10.1016/j.actbio.2016.08.032>.
- [67] J.A. Lewis, Direct ink writing of 3D functional materials, *Adv. Funct. Mater.* 16 (2006) 2193–2204. <https://doi.org/10.1002/adfm.200600434>.
- [68] H. Ma, T. Li, Z. Huan, M. Zhang, Z. Yang, J. Wang, J. Chang, C. Wu, 3D printing of high-strength bioscaffolds for the synergistic treatment of bone cancer, *NPG Asia Mater.* 10 (2018) 31–44. <https://doi.org/10.1038/s41427-018-0015-8>.
- [69] A.E. Jakus, S.L. Taylor, N.R. Geisendorfer, D.C. Dunand, R.N. Shah, Metallic architectures from 3D-printed powder-based liquid inks, *Adv. Funct. Mater.* 25 (2015) 6985–6995. <https://doi.org/10.1002/adfm.201503921>.
- [70] A.E. Jakus, A.L. Rutz, S.W. Jordan, A. Kannan, S.M. Mitchell, C. Yun, K.D. Koube, S.C. Yoo, H.E. Whiteley, C.P. Richter, R.D. Galiano, W.K. Hsu, S.R. Stock, E.L. Hsu, R.N. Shah, Hyperelastic “bone”: A highly versatile, growth factor-free, osteoregenerative, scalable, and surgically friendly biomaterial, *Sci. Transl. Med.* 8 (2016) 1–16. <https://doi.org/10.1126/scitranslmed.aaf7704>.
- [71] S.L. Taylor, A.E. Jakus, R.N. Shah, D.C. Dunand, Iron and Nickel Cellular Structures by Sintering of 3D-Printed Oxide or Metallic Particle Inks, *Adv. Eng. Mater.* 19 (2017) 1–8.

- <https://doi.org/10.1002/adem.201600365>.
- [72] A.E. Jakus, K.D. Koube, N.R. Geisendorfer, R.N. Shah, Robust and elastic lunar and martian structures from 3D-printed regolith inks, *Sci. Rep.* 7 (2017) 1–8. <https://doi.org/10.1038/srep44931>.
- [73] A.E. Jakus, E.B. Secor, A.L. Rutz, S.W. Jordan, M.C. Hersam, R.N. Shah, Three-dimensional printing of high-content graphene scaffolds for electronic and biomedical applications, *ACS Nano*. 9 (2015) 4636–4648. <https://doi.org/10.1021/acs.nano.5b01179>.
- [74] H. Do Cha, J.M. Hong, T.Y. Kang, J.W. Jung, D.H. Ha, D.W. Cho, Effects of micro-patterns in three-dimensional scaffolds for tissue engineering applications, *J. Micromechanics Microengineering*. 22 (2012) 125002. <https://doi.org/10.1088/0960-1317/22/12/125002>.
- [75] T. Sjöström, L.E. Mcnamara, R.M.D. Meek, M.J. Dalby, B. Su, 2D and 3D nanopatterning of titanium for enhancing osteoinduction of stem cells at implant surfaces, *Adv. Healthc. Mater.* 2 (2013) 1285–1293. <https://doi.org/10.1002/adhm.201200353>.
- [76] D.S. Widyaratih, P.L. Hagedoorn, L.G. Otten, M. Ganjian, N. Tümer, I. Apachitei, C.W. Hagen, L.E. Fratila-Apachitei, A.A. Zadpoor, Towards osteogenic and bactericidal nanopatterns?, *Nanotechnology*. 30 (2019) 20LT01. <https://doi.org/10.1088/1361-6528/ab0a3a>.

Biodegradable porous Fe

No extensive evaluation of the biodegradation behavior and properties of porous iron scaffolds made by extrusion-based 3D printing has been reported. Here, we studied the *in vitro* biodegradation behavior, electrochemical response, evolution of mechanical properties along with biodegradation, and responses of an osteoblastic cell line to the 3D printed iron scaffolds. An ink formulation, as well as matching 3D printing, debinding and sintering conditions, was developed to create iron scaffolds with a porosity of 67%, a pore interconnectivity of 96%, and a strut density of 89% after sintering. X-ray diffractometry confirmed the presence of the α -iron phase in the scaffolds without any residuals from the rest of the ink. Owing to the presence of geometrically designed macropores and random micropores in the struts, the *in vitro* corrosion rate of the scaffolds was much improved as compared to the bulk counterpart, with 7% mass loss after 28 days. The mechanical properties of the scaffolds remained in the range of those of cancellous bone despite 28 days of *in vitro* biodegradation. The direct culture of MC3T3-E1 preosteoblasts on the scaffolds led to a substantial reduction in living cell count, caused by a high concentration of iron ions, as revealed by the indirect assays. On the other hand, the ability of the cells to spread and form filopodia indicated the cytocompatibility of the corrosion products. Taken together, this study shows the great potential of extrusion-based 3D printed porous iron to be further developed as a biodegradable bone substituting biomaterial.

3.1 Introduction

Owing to its abundance in nature, ease of manufacturing, and high mechanical performance, iron-based materials have been extensively used as structural materials and potentially to be used as biodegradable materials for bone substitution [1]. Iron is an essential element in the human metabolism for transporting oxygen, mediating electron transfers, and accelerating enzyme reactions. It plays a role in immune function [2]. Moreover, the homeostasis of iron is essential for optimal bone regeneration [3]. Iron acts as a catalyst for the formation of reactive oxygen species (ROS) and an appropriate ROS level has been reported to regulate a pathway in osteoblast differentiation [4]. Adequate iron uptake *in vivo* can assist in the development of osteoblasts [5,6] and induce platelet activation [7], which is important for the initial healing stage of bone recovery. On the one hand, there is evidence that iron ions exhibit cytotoxicity when the rate of ion release exceeds a certain threshold [8]. On the other hand, long-term *in vivo* studies on iron-based bone substitutes have shown that the corrosion products are biocompatible [9,10]. It is important to note that the reported *in vivo* corrosion rates are extremely low with no significant changes in the mass of iron-based materials implanted in the bulk (after 52 weeks) [9] and foam (after 6 weeks) forms [10], which may lead to the longer-than-expected longevity of such iron-based implants (within a few years [11]). It is still an open research question whether the biocompatibility of iron-based materials remains favorable enough when their biodegradation rates are enhanced to match the rate of bone tissue healing.

To address the first issue, *i.e.*, too slow biodegradation of iron, recent research has been focused on developing new types of iron-based alloys [12,13], modifying the surface properties through sandblasting [14] and bio-functionalizing the surface using polymers [15–17] or bioceramics [18,19] to accelerate biodegradation. In addition, porous structures have been fabricated using various techniques, including both traditional techniques, such as electrodeposition [20], space holder method [21–25], powder molding onto porous template [26], and 3D printing techniques, such as binder/ink-jetting [27,28], material extrusion [29–33], and selective laser melting [34–37].

3D printing has recently emerged as the most promising approach to the fabrication of porous biodegradable metals [38,39]. Using this approach, tailor-made designs of biodegradable scaffolds can be realized to meet the specific requirements of various treatment conditions. Examples include tailor-made solutions to the treatment of critical bony defects and osteosynthesis as well as site-specific drug delivery for cancer patients [39]. 3D printed implants with a geometrically ordered pore network provide tissue-mimicking mechanical

properties, facilitate osseointegration, and greatly increase the surface area to volume ratio, thereby increasing the rate of biodegradation. Extrusion-based 3D printing provides a straightforward approach to the *ex situ* fabrication of porous structures using metallic materials (or material mixtures), which would otherwise be challenging for other 3D printing techniques [40], such as powder bed fusion 3D printing processes [41,42].

In the last few years, 3D printing techniques, including material extrusion and selective laser melting (SLM), have been used to fabricate porous pure iron for bone substitution. Extrusion-based 3D-printed topologically ordered porous iron scaffolds with cubic unit cell (31% porosity) and hexagonal unit cell (60% porosity) have been evaluated in terms of their mechanical behavior [31–33]. The surface of lay-down patterned iron scaffolds has been biofunctionalized by applying hydroxyapatite coating for enhanced cell-material interaction [29]. A few in-depth studies on the material properties and biocompatibility of SLM porous iron have appeared in the literature too [34,35]. However, no extensive evaluation of porous iron made by extrusion-based 3D printing is available yet. We, therefore, studied the early-stage *in vitro* biodegradation behavior, electrochemical response, time-dependent mechanical properties, and cytocompatibility of lay-down patterned porous iron scaffolds made by means of extrusion-based 3D printing.

3.2 Materials and methods

3.2.1 Scaffold design, 3D printing, and post-processing

In this research, pure iron was chosen to understand the *in vitro* biodegradation behavior, electrochemical response, evolution of mechanical properties, and cytocompatibility of 3D printed scaffolds so as to build up a solid base, on which further endeavors could be made to address the other issues related to iron-based materials for biomedical applications, for example, by adding alloying elements or functional agents. Iron powder with 99.88 wt% purity, minor impurities (Cu, Ni, Mo, Al, Mn, Si, and Cr), and spherical particle morphology (Figure 3.1a) produced through nitrogen gas atomization (Material Technology Innovations Co., Ltd., China) was sieved to reach a particle size distribution of $D_{10} = 25.85 \mu\text{m}$, $D_{50} = 39.93 \mu\text{m}$ and $D_{90} = 53.73 \mu\text{m}$. A printable ink with iron powder loading was prepared by manually mixing the iron powder with a 5 wt% hydroxypropyl methylcellulose (hypromellose) polymer ($M_w \sim 86$ kDa, Sigma Aldrich, Germany) aqueous solution [29] at a mass ratio of 7:1 (corresponding to a volume ratio of 49:50), based on the preliminary experiments with different powder-to-binder (mass) ratios in order to choose a 3D printable ink. Then, the shear-thinning properties of the chosen ink were studied using an

MCR302 rheometer (Anton Paar GmbH, Germany). In addition, thermogravimetric analysis (TGA) of hypromellose was performed using an SDT Q600 v20.9 thermogravimetric analyzer (TA Instruments, USA).

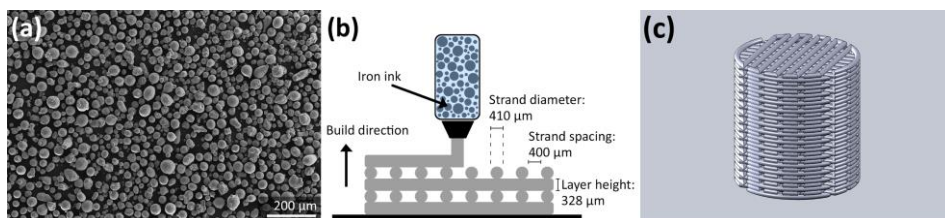


Figure 3.1. The starting material, extrusion-based 3D printing, and scaffold design: (a) iron powder particle morphology, (b) an illustration of extrusion-based 3D printing, and (c) the scaffold with the 0° and 90° lay-down pattern design.

Porous iron scaffolds (10.5 mm in height and 10 mm in diameter) were designed with the GeSiM Robotics software (GeSiM Bioinstruments and Microfluidics, Germany) to have a strut width of 410 µm, a strut spacing of 400 µm, a layer thickness of 328 µm, a designed porosity of 50%, and an initial design surface area of 40.4 cm² (Figure 3.1b). The iron ink was extruded into 3D porous iron scaffolds through a 410 µm tapered nozzle tip using 3D BioScaffolder 3.2 (GeSiM Bioinstruments and Microfluidics, Germany) with angles of 0° and 90° that interchanged every layer (Figure 3.1c). The printing pressure and printing speed were set at 200 kPa and 5 mm/s, respectively. After 3D printing, the as-printed iron scaffolds were allowed to dry for at least 30 min in a desiccator, before being loaded into a tube furnace STF16/180 (Carbolite Gero Ltd., UK) under a highly pure argon atmosphere (purity: 99.9999%; inlet pressure: 1 bar) and held at 350 °C for 1 h for debinding and at 1200 °C for 6 h for sintering. Finally, the as-sintered iron scaffolds were ultrasonically cleaned in isopropyl alcohol for 15 min prior to characterization and investigation.

3.2.2 Characterization of macrostructure and microstructure

The height and diameter of the porous iron scaffolds were measured before and after sintering to determine the shrinkage. The micro-architecture of the iron scaffolds was observed using a scanning electron microscope (SEM, JEOL JSM-IT100, Japan). From SEM images, the strut width and strut spacing of the scaffolds were measured. The cross sections of the as-sintered iron scaffolds, after polishing up to 1 µm, were observed using SEM. The regions of interest on the cross section of the struts were defined and analyzed with color threshold in ImageJ (NIH, USA) to select the porous area. The solid fractions of the struts (X) were calculated based on the following Equation (3.1):

$$X = \left(1 - \frac{\text{Pore area}}{\text{Total area of ROI}}\right) \times 100\% \quad (3.1)$$

Furthermore, the absolute porosities of the as-printed and as-sintered iron scaffolds were calculated, using the weighing method and Equations (3.2 and 3.3):

$$\varphi_p = \left(1 - \frac{m_p/\rho_{ink}}{V_{bulk}}\right) \times 100\% \quad (3.2)$$

$$\varphi_s = \left(1 - \frac{m_s/\rho_{iron}}{V_{bulk}}\right) \times 100\% \quad (3.3)$$

where φ_p and φ_s are, respectively, the absolute porosities of the as-printed and the as-sintered iron scaffolds [%], m is the mass of the as-printed or as-sintered iron scaffold [g], V_{bulk} is the bulk volume of the scaffold [cm³], ρ_{ink} is the density of the iron ink (i.e., 4.41 g/cm³), and ρ_{iron} is the theoretical density of pure iron (i.e., 7.874 g/cm³).

In addition, the interconnected porosity of the as-sintered iron scaffolds was assessed using the Archimedes' principle as described in the ASTM standard B963-13 [43]. The value was calculated using Equation (3.4):

$$\varphi_i = \left(\frac{\rho_e}{\rho_o} \times \frac{m_{ao} - m_a}{m_{ao} - m_{eo}}\right) \times 100\% \quad (3.4)$$

where φ_i is the interconnected porosity of the as-sintered iron scaffolds [%], ρ_e is the density of ethanol (i.e., 0.789 g/cm³), ρ_o is the density of oil (i.e., 0.919 g/cm³), m_{ao} is the mass of the oil-impregnated iron scaffold weighed in air [g], m_a is the mass of the iron scaffold weighed in air [g], and m_{eo} is the mass of the oil-impregnated iron scaffold weighed in ethanol [g].

3.2.3 Phase identification

The phase composition of the as-sintered iron scaffolds was determined using an X-ray diffractometer (XRD, D8 Advance, Bruker, USA). XRD in the Bragg-Brentano geometry was equipped with a graphite monochromator and a Vantec position-sensitive detector that was set to work at 45 kV and 35 mA. A step size of 0.020° with a counting time of 10 s per step using Co K α radiation was employed. The XRD pattern was evaluated using the Diffac Suite.EVA v5.0 software (Bruker, USA) and the International Centre for Diffraction Data PDF-4 database.

3.2.4 Static *in vitro* immersion tests

Static *in vitro* immersion tests (up to 28 days, triplicates) were performed in the revised simulated body fluid (r-SBF) [44] using a cell culture incubator, under the following conditions: 5% CO₂, in an ambient O₂ atmosphere, relative humidity = 95%, temperature = 37 °C \pm 0.5 °C. The solution volume-to-surface area ratio was 6.7 mL/cm² [45]. Before the tests, the samples were sterilized and the r-SBF

solution was filtered using a 0.22 μm filter (Merck Millipore, Germany). The pH values were monitored during the immersion period using a pH electrode (InLab Expert Pro-ISM, METTLER TOLEDO, Switzerland). The concentrations of soluble calcium, phosphate and iron ions in the r-SBF solution were quantified using an inductively coupled plasma optical emission spectroscope (ICP-OES, iCAP 6500 Duo, Thermo Scientific, USA) after 1, 2, 7, 14, and 28 days of *in vitro* biodegradation. To determine the mass loss, the *in vitro* corrosion products were removed by immersing the as-corroded iron scaffolds at the abovementioned time points in a 50 vol% HCl solution (with a specific gravity of 1.19, Sigma Aldrich, Germany) containing 3.5 g/L hexamethylenetetramine (Sigma Aldrich, Germany) for 10 min, followed by ultrasonic cleaning in isopropyl alcohol for 15 min [46]. Subsequently, the samples were dried overnight in a desiccator and weighed using a balance with an accuracy of 0.1 mg. The cycle was repeated and the mass loss was plotted against the cleaning cycle to obtain the most accurate value, according to the ASTM standard G1-03 [46]. From the mass loss values, the average corrosion rate was determined based on the ASTM standard G31-72 [47] using Equation (3.5):

$$CR_{\text{immersion}} [\text{mm/year}] = 8.76 \times 10^4 \times \frac{m}{A \times \rho \times t} \quad (3.5)$$

where m is the mass loss [g], A is the surface area of the scaffolds [cm^2] calculated based on the initial scaffold design value, ρ is the theoretical density of pure iron (i.e., 7.874 g/ cm^3), and t is the duration of *in vitro* immersion [h].

3.2.5 Characterization of *in vitro* biodegradation products

The phases of the *in vitro* biodegradation products of the scaffolds after 28 days of immersion were identified using XRD (D8 Advance, Bruker, USA). In addition, the morphologies of the *in vitro* biodegradation products on the periphery of the iron scaffolds after 7, 14, and 28 days of continuous immersion were observed using SEM and their compositions were analyzed with an X-ray energy dispersive spectroscope (EDS, JEOL JSM-IT100, Japan). In addition to the periphery, the scaffolds after 7, 14, and 28 days of continuous immersion were ground with SiC #2000, and the corrosion products in the center of the structure were characterized using SEM-EDS. Also, the fraction of the remaining base material (pure iron) after *in vitro* immersion at the selected time points was calculated using ImageJ (Equation 3.1).

3.2.6 Electrochemical measurements

To study the electrochemical corrosion behavior, iron scaffold specimens were carefully prepared by partial mounting them in thermoplastic acrylic resin and exposing them to r-SBF (pH=7.40, temperature = 37 ± 0.5 °C). The exposed surface area was calculated, based on the design value of the scaffold. Before the

experiments, the mounted specimens were ultrasonically cleaned in isopropyl alcohol and then dried thoroughly. A three-electrode electrochemical system was configured, in which a graphite rod, an Ag/AgCl electrode, and the iron specimen, respectively, acted as the counter electrode, the reference electrode, and the working electrode. All the tests were carried out in triplicate using a Bio-Logic SP-200 potentiostat (Bio-Logic Science Instruments, France).

Before the electrochemical tests, the setup was allowed to reach a stable open circuit potential (OCP) for 1 h. The linear polarization resistance (LPR) tests of the iron specimens at different time points up to 28 days were carried out from -25 to +25 mV *versus* OCP at a scan rate of 0.167 mV/s. Consecutively, the electrochemical impedance spectroscopy (EIS) tests of the iron specimens at different time points up to 28 days were conducted using a sine amplitude of 10 mV *versus* OCP at a frequency scan between 100 kHz to 10 mHz. Moreover, potentiodynamic polarization (PDP) tests were performed on the specimens after 1 day and 28 days of immersion, with polarization between -300 to +500 mV *versus* OCP at a scan rate of 0.5 mV/s. From the PDP results, the corrosion rates were calculated according to the ASTM standard G102-89 [48] and using Equation (3.6):

$$CR_{electrochemical} [\text{mm/y}] = 3.27 \times 10^{-3} \times EW \times \frac{i_{corr}}{\rho} \quad (3.6)$$

where EW is the equivalent weight of iron (valence 2), i_{corr} is the current density [$\mu\text{A}/\text{cm}^2$], and ρ is the theoretical density of pure iron [g/cm^3].

3.2.7 Uniaxial compression tests

An Instron universal testing machine (ElectroPuls E10000, Germany) with a 10 kN load cell was used to evaluate the compressive mechanical properties of the as-sintered iron scaffolds as well as the specimens retrieved after 1, 2, 7, 14 and 28 days of *in vitro* immersion. The tests were performed at a crosshead speed of 3 mm/min. The mechanical properties of the porous iron scaffolds, including the quasielastic gradient (referred as elastic modulus) and yield strength, were obtained following the ISO standard 13314 [49]. The slope of the first linear region in the stress-strain graph was defined as the elastic modulus. A parallel line to the initial linear elastic region, offset by 0.2% strain, was drawn and the stress value at the intersection with the stress-strain curve was determined as the yield strength. The tests were performed in triplicate. The average values with standard deviations are reported hereafter.

3.2.8 Cytocompatibility evaluation

Preculture of MC3T3-E1 cells and the preparation of iron extract media

Preosteoblasts MC3T3-E1 (Sigma Aldrich, Germany) were pre-cultured for 7 days in α -minimum essential medium (α -MEM, Thermo Fisher Scientific, USA)

without ascorbic acid but supplemented with 10% fetal bovine serum (FBS, Thermo Fisher Scientific, USA) and 1% penicillin/streptomycin (p/s, Thermo Fisher Scientific, USA). α -MEM without ascorbic acid was used to maintain the cells in the preosteoblastic state. The cells were incubated at 37 °C in a humidified atmosphere with 5% CO₂ and 2% O₂ (relative humidity = 95%). The culture medium was refreshed every 2 to 3 days.

The iron extract culture media were prepared by immersing the sterilized porous iron scaffolds (10.25 mm in height and 9.75 mm in diameter) in α -MEM (without ascorbic acid, but with 10% FBS, 1% p/s) for 72 h at 37 °C in a 5% CO₂ and 2% O₂ atmosphere with 95% relative humidity [50]. The specimen-to-medium ratio was 5 cm²/mL, in which the surface area of the scaffolds was calculated based on the design value. Thereafter, the supernatant was collected, filtered, and diluted into 75%, 50%, 25%, and 10% from the original concentration. Furthermore, the iron ion concentration in the original (100%) iron extract media was quantified using ICP-OES (iCAP 6500 Duo, Thermo Scientific, USA). All media were kept at 4 °C prior to cell tests.

Indirect cytotoxicity tests

To evaluate the indirect cytocompatibility of the iron scaffolds, the PrestoBlue assay (Thermo Fisher Scientific, USA) was performed. The MC3T3-E1 preosteoblasts (1×10^4 cells) were cultured in 200 μ L of 100%, 75%, 50%, 25% and 10% iron extract media using 48-well plates. The same number of cells was cultured in the original α -MEM (without ascorbic acid, but with 10% FBS, 1% p/s) as the negative control. After 1, 3, and 7 days of culture, the iron extract media were replaced with 200 μ L fresh pure α -MEM (without ascorbic acid, but with 10% FBS, 1% p/s) to prevent the interference of iron ions with the assay. Consecutively, 20 μ L of PrestoBlue reagents (Thermo Fisher Scientific, USA) were added, and the specimens were incubated at 37 °C for 1 h. Afterwards, the absorbance values were measured with a Victor X3 microplate reader (PerkinElmer, USA) at a wavelength of 530 - 590 nm. The tests were performed in triplicate. The average metabolic activity of the cells is reported as a percentage of the negative control, calculated using Equation (3.7):

$$\text{Metabolic activity [\%]} = \frac{\text{Absorbance (specimen)}}{\text{Absorbance (negative control)}} \times 100 \quad (3.7)$$

To observe the morphology of the preosteoblasts grown in the iron extract media, the cytoskeleton and nucleus of the cells were stained using rhodamine phalloidin and 4',6-diamidino-2-phenylindole (DAPI) dyes, respectively. The MC3T3-E1 preosteoblasts (1×10^4 cells) were cultured for 3 days on 48-well glass disks in 200 μ L of iron extract media. The same number of cells was cultured in the original α -MEM (without ascorbic acid, but with 10% FBS, 1% p/s) as the

negative control. After culture, the specimens were washed with PBS (Thermo Fisher Scientific, USA), fixed using 4% formaldehyde (Sigma Aldrich, Germany) for 15 min at room temperature, then washed with PBS, and permeabilized with 0.5% triton/PBS (Sigma Aldrich, Germany) at 4 °C for 5 min. Then, 1% bovine serum albumin/PBS (BSA, Sigma Aldrich, Germany) was added per well and followed by incubation for 5 min. Consecutively, 1:1000 rhodamine phalloidin (Thermo Fisher Scientific, USA) in 1% BSA/PBS was added per well, followed by 1 h incubation at 37 °C. Afterwards, the specimens were rinsed in 0.5% tween/PBS (Sigma Aldrich, Germany) and washed with PBS. Finally, the specimens were mounted on a glass slide with Prolong gold (Life Technologies, USA), containing the DAPI dye. Thereafter, the morphology of the cells cultured in different iron extracts was observed using a fluorescence microscope (ZOE cell imager, Bio-Rad, USA). From staining images, the number of cells and the cell spreading area were determined by counting the nucleus of the cells using ImageJ (NIH, USA).

Direct cytotoxicity tests

To evaluate the direct cytocompatibility of the iron scaffolds, the Trypan blue cell counting assay was performed. First, the porous iron scaffolds (10.25 mm in height and 9.75 mm in diameter) were pre-immersed in α -MEM (without ascorbic acid, but with 10% FBS, 1% p/s) for 5 min and placed in the 6-well plate. After that, the MC3T3-E1 preosteoblasts (1×10^6 cells per specimen) were pipetted into the porous iron scaffolds. Subsequently, 10 mL of α -MEM was added per well to immerse the scaffold. The same number of cells was cultured for all experimental groups. For every time point, the tests were performed in triplicate. After 1, 3, and 7 days of culture, the cells were trypsinized from the scaffolds and the well plates and then suspended. 10 μ L of each cell suspension was mixed with 10 μ L of trypan blue dye (Bio-Rad, USA) and subsequently pipetted into a dual-chamber cell counting slide. The number of living cells was counted using an automated cell counter (TC20, Bio-Rad, USA). The average number of living cells with standard deviations are reported.

In addition, to observe the distribution and morphology of MC3T3-E1 cells seeded on the porous iron scaffolds, a live/dead staining assay was performed, followed by SEM imaging. The MC3T3-E1 preosteoblasts (2×10^5 cells per specimen) were seeded on the iron scaffolds (2.05 mm in height and 9.75 mm in diameter) and cultured in 2 mL α -MEM (without ascorbic acid, but with 10% FBS, 1% p/s). After 3 days of culture, the specimens were washed with PBS and immersed in PBS containing 2 μ L/mL of calcein (Thermo Fisher Scientific, USA) and 1.5 μ L/mL of ethidium homodimer-1 (Thermo Fisher Scientific, USA) for 30 min in the dark at room temperature. Thereafter, the live and dead cells on the

iron scaffolds were observed using a fluorescence microscope (ZOE Fluorescent Cell Imager, Bio-Rad, USA). Furthermore, SEM imaging of cell morphologies on the iron scaffolds was performed. Briefly, after 3 days of culture, the specimens were washed in PBS, fixed with 4% formaldehyde (Sigma Aldrich, Germany) for 20 min, followed by dehydration stages in 30, 50, 70, and 100% ethanol for 10 min each, and they were further preserved using hexamethyldisilazane (Sigma Aldrich, Germany) for 30 min. The specimens were dried for 2 h prior to SEM imaging.

3.2.9 Statistical analysis

All values are expressed as mean \pm standard deviation. The statistical analysis of the PrestoBlue results was performed with two-way ANOVA followed by the Tukey *post hoc* test. For the direct cytocompatibility cell count results, statistical analysis was conducted with one-way ANOVA, followed by the Tukey *post hoc* test.

3.3 Results

3.3.1 Structural characteristics of the porous iron scaffolds

The porous iron scaffolds exhibited a free-standing characteristic, where the struts bridged above the underlying layers (Figure 3.2a). Sufficient powder loading in the ink (Figure 3.2b) and strong bond between powder particles and binder (Figure 3.2c) allowed the scaffolds with a high aspect ratio to be built and to stay intact without distortions or shrinkage after 3D printing. The as-printed specimens had an absolute porosity of $47 \pm 4\%$, with an average strut width of $420.3 \pm 5.5 \mu\text{m}$, and a strut spacing of $390.6 \pm 5.6 \mu\text{m}$ (Table 3.1).

Table 3.1. Structural characteristics of the extrusion-based 3D printed porous iron scaffolds.

Sample groups	Strut width (μm)	Strut spacing (μm)	Absolute porosity (%)	Interconnected porosity (%)
Design	410	400	50	-
As-printed iron	420 ± 6	391 ± 6	47 ± 4	-
As-sintered iron	411 ± 6	399 ± 6	67 ± 2	65 ± 1

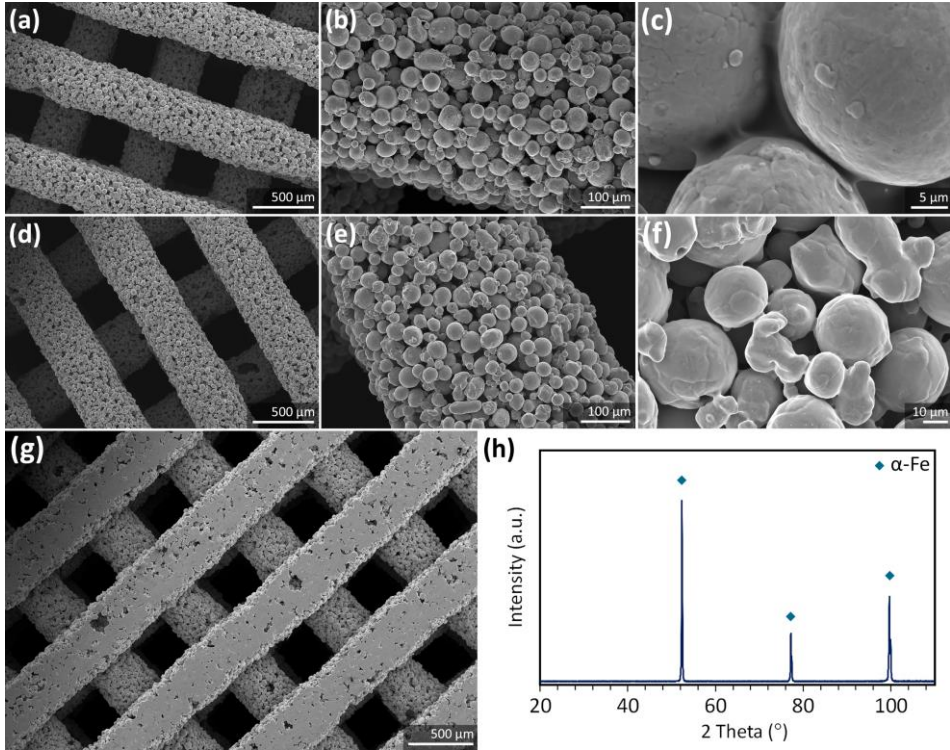


Figure 3.2. Morphology and phase composition of the porous iron scaffolds: SEM images of (a, b, c) the as-printed iron scaffolds and (d, e, f) the as-sintered iron scaffolds at different magnifications, (g) the cross section of the polished struts, and (h) the XRD pattern of the scaffolds after sintering.

After sintering (Figure 3.2d-e), the dimensions of the specimens were slightly reduced by $2.3 \pm 0.2\%$ (height) and $2.5 \pm 0.2\%$ (diameter). The strut width changed to $411.2 \pm 5.9 \mu\text{m}$, while the strut spacing became $398.9 \pm 5.7 \mu\text{m}$ (Table 3.1). At the periphery of the scaffolds, the fusion of iron particles with evident open pores between the necks of iron powder particles could be observed (Figure 3.2f). On the cross section, a partially sintered microstructure with pores ranging between 26 and 135 μm inside the struts was observed (Figure 3.2g). Despite the presence of micropores, the average solid fraction of the struts was high (*i.e.*, $89 \pm 4\%$). The absolute porosity of the as-sintered specimens was $67 \pm 2\%$ and the total interconnected porosity was $65 \pm 1\%$, corresponding to a pore interconnectivity of 96%. Based on the XRD analysis, the as-sintered iron scaffolds only contained the α -iron phase (Figure 3.2h) without any detectable binder residues.

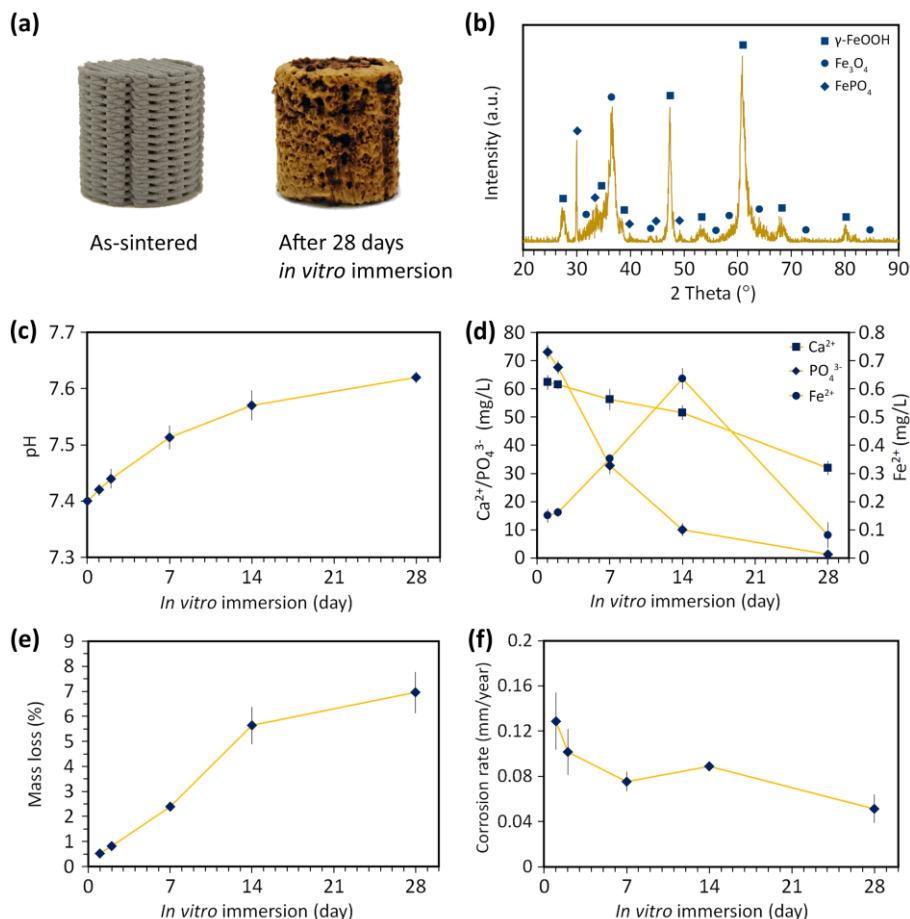


Figure 3.3. *In vitro* corrosion characteristics of the porous iron scaffolds: (a) visual observation of the scaffolds before and after 28 days of immersion, (b) XRD pattern of the corrosion products on the iron scaffolds at day 28, (c) pH values of the r-SBF solution, (d) the Ca , PO_4 , and Fe ion concentrations in the r-SBF throughout the immersion period, (e) the mass loss percentages, and (f) the corrosion rate of the scaffolds.

3.3.2 *In vitro* biodegradation behavior and the corrosion products

After 28 days of static *in vitro* immersion, a thick brown corrosion layer almost entirely covered the periphery of the specimens (Figure 3.3a). The corrosion products were mostly composed of iron oxide hydroxide (γ -FeOOH), magnetite (Fe_3O_4), and iron phosphate (FePO_4) (Figure 3.3b). The immersion tests performed with 5% CO_2 and 2% O_2 slightly increased the pH of the r-SBF solution to 7.62 at day 28 (Figure 3.3c).

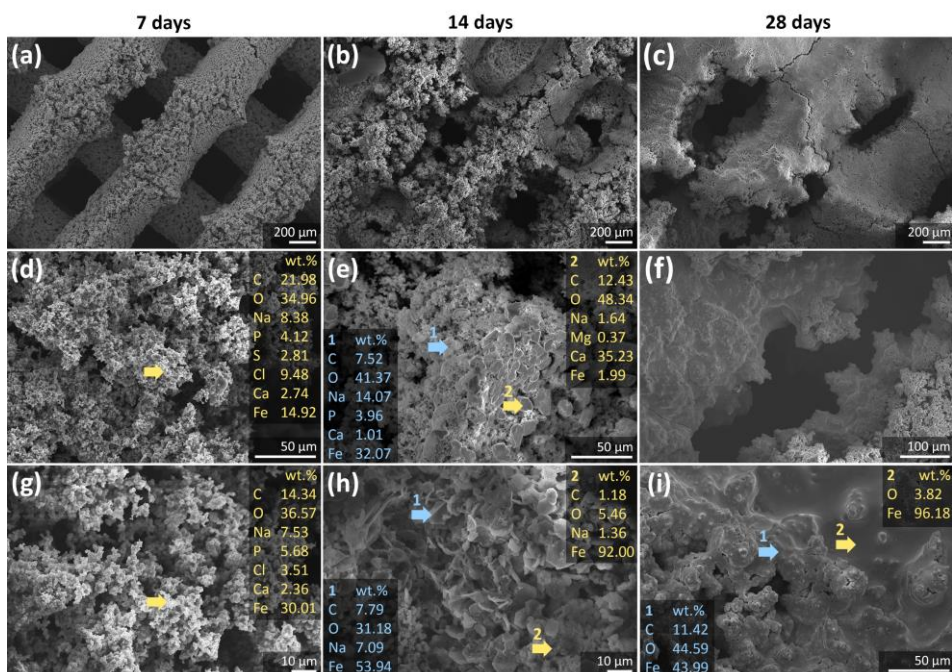


Figure 3.4. Morphology and chemical compositions of the *in vitro* corrosion products at the periphery of the porous iron scaffolds: SEM and EDS point analysis of the corrosion products after (a, d, g) 7 days, (b, e, h) 14 days, and (c, f, i) 28 days of immersion. The arrow and number indicate where the EDS point analysis was performed and the corresponding elemental composition, respectively.

Throughout the *in vitro* immersion tests, the release of iron ions to the r-SBF solution remained < 1 ppm (Figure 3.3d). The concentration of iron ions increased from 0.15 ppm to 0.64 ppm in the first 14 days of immersion and then decreased to 0.08 ppm (at day 28). On the other hand, the concentrations of calcium and phosphate ions in the r-SBF solution continuously decreased over time (Figure 3.3d). A much higher rate of reduction in the concentration of the phosphate ion in the solution was observed in the first 14 days of immersion (Figure 3.3d), while a slightly higher precipitation rate of calcium ions on the specimens was noticed between days 14 and 28. The mass of the iron scaffolds was reduced by $7 \pm 1\%$ after 28 days of immersion (Figure 3.3e). The average *in vitro* corrosion rate after 1 day of immersion was 0.28 ± 0.05 mg/cm²/day, but declined to 0.11 ± 0.01 mg/cm²/day after 28 days. According to the ASTM standard G31-72 [47], the average corrosion rates after 1 day and 28 days of immersion could be converted into 0.13 ± 0.03 and 0.05 ± 0.01 mm/y, respectively (Figure 3.3f).

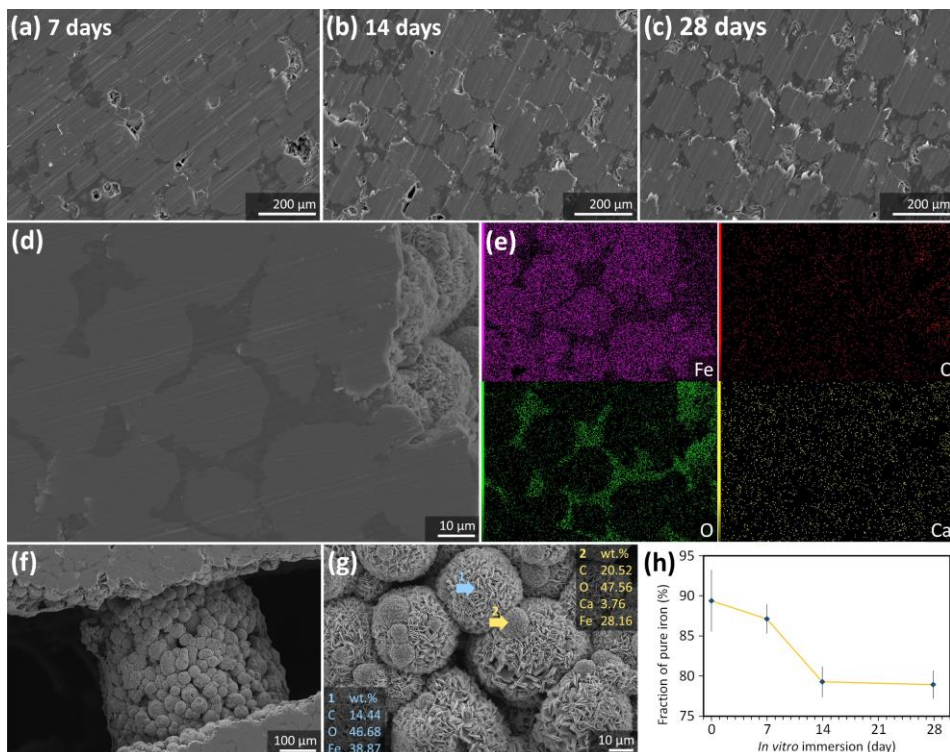


Figure 3.5. Morphology and chemical compositions of the *in vitro* corrosion products in the center of the porous iron scaffolds: the cross section of the scaffolds after (a) 7, (b) 14, and (c) 28 days of immersion, (d) a magnified view of the corrosion products at day 28 in the pore network and (e) the elemental mapping, (f) corrosion products on the struts after 28 days of immersion and (g) the enlarged view of the corrosion products with EDS point analysis, and (h) reductions in the pure iron fraction in the struts during the immersion period. The arrow and number indicate where the EDS point analysis was performed and the corresponding elemental composition, respectively.

After 7 days of immersion, loose corrosion products surrounded the struts of the scaffolds (Figure 3.4a). Fine granules of the corrosion products, which were rich in iron, oxygen, and carbon and contained sodium, calcium, phosphorus, and chlorine, were identified (Figure 3.4d, g). After 14 days of immersion, the thickness of the corrosion layer increased and almost filled the macropores of the iron scaffolds (Figure 3.4b). The morphologies of the corrosion products consisted of a mixture of fine and coarse granules (Figure 3.4e) and a flake-like structure (Figure 3.4h). The composition of the finer granules was similar to the one seen after 7 days of immersion (Figure 3.4e, EDS 1), whereas the coarser granules mainly contained calcium, oxygen, and carbon with trace amounts of iron, sodium, and magnesium (Figure 3.4e, EDS 2). In the flake-like corrosion products, iron and oxygen were dominant, but carbon and sodium existed too

(Figure 3.4h). After 28 days of immersion, the corrosion products developed into a more compact structure (Figure 3.4c, f). The dense corrosion layer was composed of iron, carbon, and oxygen (Figure 3.4i, EDS 1) or iron and oxygen (Figure 3.4i, EDS 2).

In addition to the periphery, the corrosion products were also formed in the interconnected pore network of the struts of the scaffolds (Figure 3.5a-c). The corrosion products in the micropores were predominantly composed of oxygen with traces of iron, calcium, and carbon (Figure 3.5d-e). Moreover, two other types of corrosion products were identified in the center of the scaffolds after 28 days of immersion (Figure 3.5f-g). One type, on the strut surface, had a flake-like morphology and contained iron, oxygen, and carbon (Figure 3.5g, EDS 1). The other type had a crystal-like spherical morphology and contained iron, oxygen, carbon, and calcium (Figure 3.5g, EDS 2). As the biodegradation progressed, the pure iron present in the scaffolds was gradually consumed. The pure iron fraction in the struts reduced from $89 \pm 4\%$ before the start of the immersion test to $87 \pm 2\%$, $79 \pm 2\%$, and $79 \pm 2\%$ after 7, 14, and 28 days of immersion, respectively (Figure 3.5h).

3.3.3 Electrochemical responses

According to the PDP curves (Figure S3.2a), the corrosion potential of the iron scaffolds shifted from -781 ± 22 mV after 1 day of immersion to -676 ± 17 mV after 28 days of immersion. At the same time points, the corrosion current densities decreased from 8.0 ± 0.3 $\mu\text{A}/\text{cm}^2$ to 3.5 ± 0.6 $\mu\text{A}/\text{cm}^2$ (Figure S3.2a). According to the ASTM standard G102-89 [48], the corrosion rate, based on the current densities, were calculated to be 0.09 and 0.04 mm/y after 1 day and 28 days of immersion, respectively. The results were quite close to the values obtained from the *in vitro* immersion tests in the cell culture incubator. Moreover, the polarization resistance of the iron scaffolds was 3.3 ± 0.6 $\text{k}\Omega\cdot\text{cm}^2$ after 1 day of immersion. It increased to 8.4 ± 1.4 $\text{k}\Omega\cdot\text{cm}^2$ at day 7 and reduced to 4.9 ± 0.7 $\text{k}\Omega\cdot\text{cm}^2$ at day 9 of immersion (Figure S3.2b). From day 9, the value continuously increased with an average rate of 0.35 $\text{k}\Omega\cdot\text{cm}^2$ per day until day 21, became 9.1 ± 2.1 $\text{k}\Omega\cdot\text{cm}^2$. At day 28 of immersion, the polarization resistance was 26.7 ± 6.5 $\text{k}\Omega\cdot\text{cm}^2$.

The Bode plots of the impedance against frequency (Figure 3.6a, S3.2c) generally showed increases in the impedance modulus for low (*e.g.*, 0.01 Hz) and medium (*e.g.*, 10 Hz) frequencies for the entire duration of the immersion tests. The Bode plots impedance at 0.01 Hz after 1 day and 28 days of immersion were 2.8 ± 0.6 $\text{k}\Omega\cdot\text{cm}^2$ and 33.1 ± 2.4 $\text{k}\Omega\cdot\text{cm}^2$, respectively. At these time points, the Bode impedance at 10 Hz were 0.3 ± 0.1 $\text{k}\Omega\cdot\text{cm}^2$ and 11.4 ± 1.4 $\text{k}\Omega\cdot\text{cm}^2$, respectively. In the Bode plot of phase angle against frequency (Figure 3.6b), the

phase angle values at high frequencies (*e.g.*, 10 kHz) decreased from -1.3° after 1 day to -53.9° after 28 days of immersion. In the case of low frequencies (*e.g.*, 0.1 Hz), however, the phase angle values moved towards more positive values, showing a shift in the peak of the plot from a higher frequency to a lower frequency throughout the immersion time (Figure 3.6b).

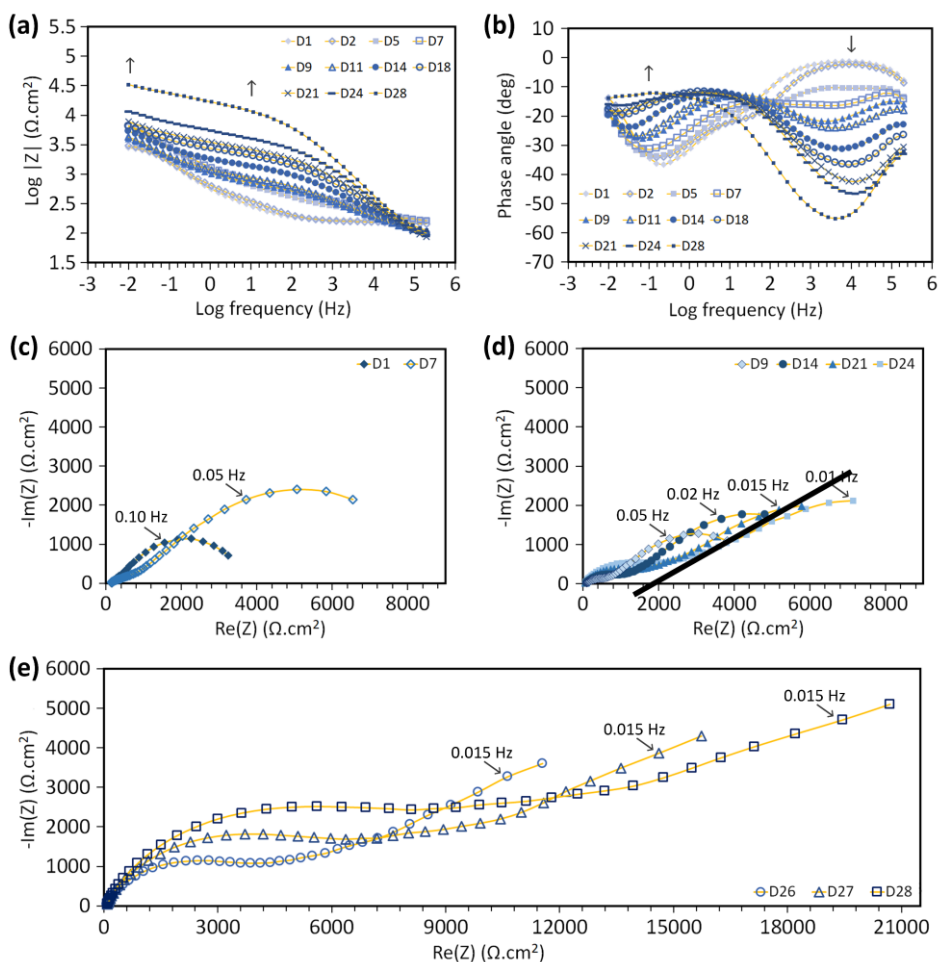


Figure 3.6. Electrochemical impedance spectroscopy of the porous iron scaffolds: the Bode plots of (a) impedance modulus and (b) phase angle against frequency for up to 28 days of immersion, Nyquist spectra (c) after 1 and 7 days, (d) 9, 14, 21, and 24 days, and (e) 26 to 28 days of immersion. The arrows in Bode plots indicate the change in the impedance and phase angle values with time for a specific frequency.

The Nyquist plots displayed three different types of spectra throughout the immersion test. The Nyquist plot after 1 day of immersion showed a single

capacitive arc (Figure 3.6c). After 7 days of immersion, the Nyquist plot showed a larger curve than that of the 1-day immersion plot (Figure 3.6c). From 9 until 24 days of immersion, the Nyquist plots exhibited a two-semicircle continuous arc that began with a smaller semicircle at a higher frequency and continued with an inclined slope forming a second larger curve at a lower frequency (Figure 3.6d). In addition to the increase in the diameter of the semicircle arc over time, the angle of the inclined slope decreased as corrosion progressed (Figure 3.6d). After 28 days of immersion, the semicircle at the high-frequency region was larger and extended with a moderately inclined straight line for the lower frequencies (Figure 3.6e).

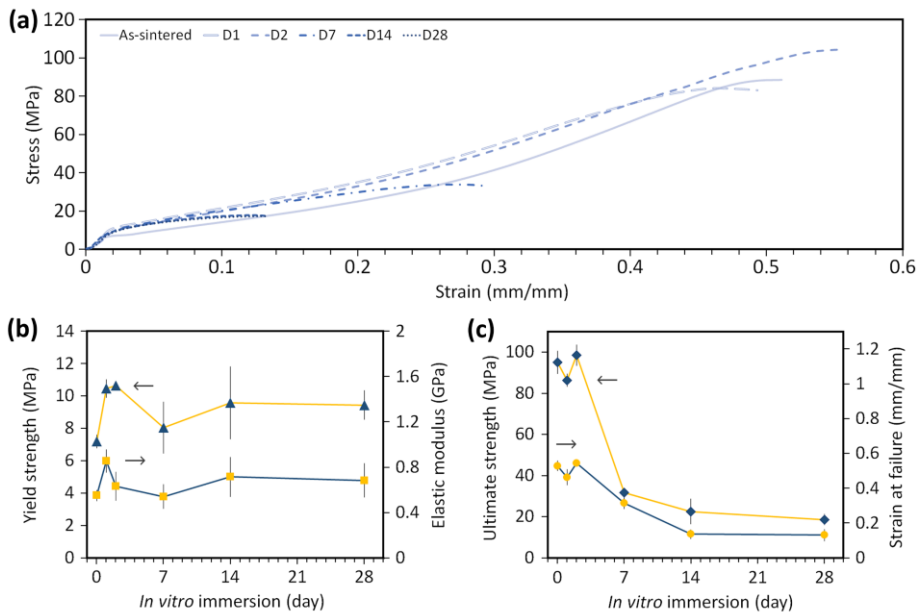


Figure 3.7. Mechanical properties of the porous iron scaffolds: (a) compressive stress-strain curves, (b) the yield strength and elastic modulus, and (c) the ultimate strength and strain at failure of the scaffolds before and after *in vitro* immersion for up to 28 days.

3.3.4 Mechanical properties

The uniaxial compressive stress-strain curves of the porous iron scaffolds (Figure 3.7a) began with a linear elastic region, followed by a trend resembling strain-hardening during the plastic deformation stage until specimen failure. The as-sintered iron scaffolds exhibited a yield strength of 7.2 ± 0.4 MPa and an elastic modulus of 0.6 ± 0.1 GPa. Over the *in vitro* immersion period of 28 days, the yield strength of the scaffolds increased to 10.6 ± 0.2 MPa after 2 days of

immersion and slightly reduced to 9.4 ± 0.9 MPa after 28 days of immersion (Figure 3.7b). Likewise, the elastic modulus increased to 0.6 ± 0.1 GPa after 2 days of immersion and stabilized at an average value of 0.7 ± 0.2 GPa after 28 days of immersion (Figure 3.7b). On the other hand, the ultimate strength remarkably dropped from 96 ± 6 MPa to 32 ± 2 MPa after 7 days of immersion. Then, it further decreased to 19 ± 7 MPa after 28 days of immersion (Figure 3.7c). Moreover, the iron scaffolds became less ductile after the immersion tests and a notable decline in strain at failure from $53 \pm 3\%$ to $31 \pm 3\%$ was observed after 7 days of immersion. The strain at failure further decreased to $13 \pm 3\%$ after 28 days of immersion (Figure 3.7c).

3.3.5 *In vitro* cytotoxicity against MC3T3-E1 preosteoblasts

The 100% iron extract medium contained 120.4 ± 3.7 ppm of iron ions. The exposure to the 100% iron extract medium resulted in instant cytotoxicity, with $25.6 \pm 4.8\%$ metabolic activity remaining after 24 h and almost no metabolically active cells after 7 days of culture (Figure 3.8a). After the iron extract was diluted to 75% of its original, a metabolic activity of $73.3 \pm 9.3\%$ was detected after 24 h culture. However, the trend of decreased activity with culture time (*i.e.*, $33.3 \pm 5.9\%$ after 7 days) remained unchanged. When the iron extract medium was further diluted to $\leq 50\%$, the growth of the preosteoblasts was only slightly inhibited, as indicated by the high metabolic activity ($> 80\%$) even after 7 days of culture (Figure 3.8a).

From the stained samples, the cell counts from 100%, 75%, and 50% iron extracts were 133 ± 16 (Figure 3.8c), 190 ± 63 (Figure 3.8d), and 753 ± 59 (Figure 3.8e), respectively. More cells were observed when they were cultured in a lower-concentration iron extract medium. Furthermore, the individual stress fibers and filopodia of each cell cultured in the 100% and 75% iron extract remained recognizable (Figure 3.8c-d). The preosteoblasts in the 75% iron extract exhibited a polygonal shape and were more outspread ($2580.5 \pm 247.5 \mu\text{m}^2$ per cell) than the cells grown in the 100% iron extract ($1736.4 \pm 209.9 \mu\text{m}^2$ per cell).

The direct seeding of the preosteoblasts on the porous iron scaffolds resulted in a reduction in the living cell count after 24 h of culture (*i.e.*, $2.8 \pm 0.3 (\times 10^5)$ cells) (Figure 3.8b). The viable cells continuously declined to $5.6 \pm 1.5 (\times 10^4)$ cells, after 3 days of culture ($p < 0.001$). Interestingly, at day 7 of culture, the viable cell count slightly increased to $6.9 \pm 2.0 (\times 10^4)$ cells (statistically not significant). Although it was challenging to quantify the live/dead staining results, a number of viable (green) preosteoblasts were detectable on the iron scaffolds (Figure 3.8f-h). More importantly, the stained preosteoblasts showed a homogenous distribution over the struts of the porous iron scaffolds (Figure 3.8f-h), indicating a good cell seeding efficiency in the direct assays. Furthermore, on the SEM

images, the surviving cells were identified with extended filopodia in the porous structure of the scaffolds (Figure 3.8i) as well as on the corrosion products (Figure 3.8j-k).

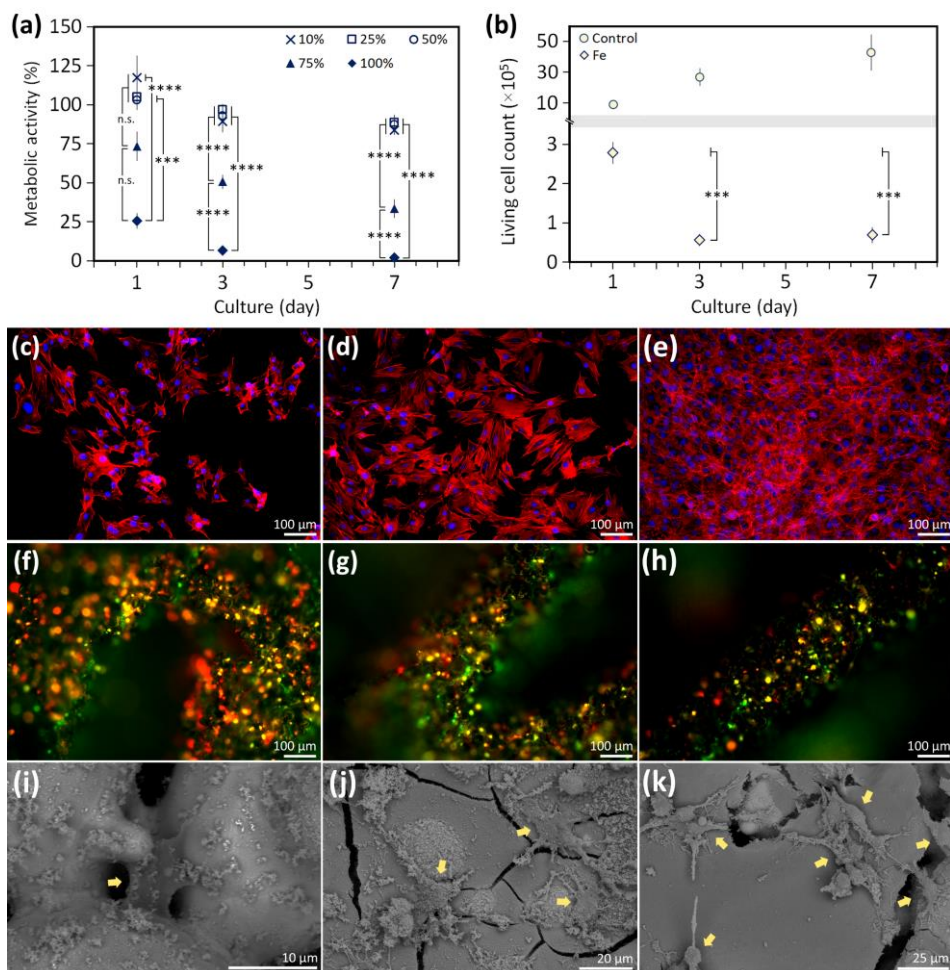


Figure 3.8. *In vitro* biological evaluation of the iron scaffolds towards preosteoblasts MC3T3-E1: (a) indirect metabolic activity of preosteoblasts cultured in iron extracts for 1, 3, and 7 days, (b) the number of living preosteoblasts after 1, 3, and 7 days of direct culture on the porous iron scaffolds, (c-e) rhodamine phalloidin (red) and DAPI (blue) stained preosteoblasts after 3 days of culture in (c) 100%, (d) 75%, and (e) 50% iron extracts, (f-h) calcein acetoxymethyl (green, indicating living cells) and ethidium homodimer-1 (red, indicating dead cells) stained preosteoblasts on the scaffolds, and (i-k) the morphology of the cells after 3 days of direct cell culture on the iron scaffolds. ***, $p < 0.001$; ****, $p < 0.0001$.

3.4 Discussion

In this study, an extrusion-based 3D printing process followed by debinding and sintering was developed to fabricate porous iron scaffolds with a lay-down pattern for bone substitution. Since the biodegradation rate of bulk iron is generally too low [9,10], a geometrically ordered porous design was employed to speed up the rate of biodegradation of the specimens while maintaining the other important properties of porous iron, including its structural integrity and bone-mimicking mechanical properties. Our results showed that the lay-down pattern design, indeed, enhanced the corrosion rate of the iron scaffolds, while the bone-mimicking mechanical properties were retained. As for the cytocompatibility, the results obtained here were comparable to those reported in the other studies of porous iron [26,34,35].

3.4.1 Extrusion-based 3D printing and post-processing

The developed fabrication process delivered porous pure iron scaffolds with a strut size and a strut spacing close to the design values (Table 3.1). The use of an optimized ink formulation and ink synthesis process was of great importance for achieving such promising results. The choice of hypromellose as the binder is because of its straightforward preparation, biocompatibility [51], and its suitable rheological properties for extrusion. The iron ink was prepared with 49 vol% powder loading to strike a balance between the printability (Figure S3.1a-c) and the self-holding characteristics of the struts. The optimized powder-to-binder ratio demonstrated shear-thinning flow behavior (Table S3.1) and ensured sustainable printing without clogging in the nozzle tip and enabled the fabrication of the porous iron scaffolds with a high aspect ratio.

Following the extrusion-based 3D printing, heat treatment of the porous iron scaffolds was performed as post-processing, which started with a debinding stage where the temperature was set at a point where thermal decomposition of hypromellose took place (Figure S3.1d). Afterwards, the heat treatment continued to a solid-state sintering stage at a higher temperature, where iron powder particles bonded together and formed necks. The parameters of the sintering process (*i.e.*, temperature and holding time) were chosen based on the obtained solid fractions of the struts of the scaffolds under various conditions (Figure S3.1e). The chosen sintering temperature (1200 °C) and time (6 h) resulted in the porous iron scaffolds with an $89 \pm 4\%$ solid fraction of the struts and an absolute porosity of $67 \pm 2\%$. It should be mentioned that a higher solid fraction can be achieved and will lead to a higher strength of the scaffolds as a result of enhanced densification [52]. However, in the case of the scaffolds intended for use as biodegradable implants, partial sintering may offer an advantage, because the scaffolds will have more exposed powder particle

boundary area in the struts. Under the present sintering condition, the porous iron scaffolds possessed a pore interconnectivity of 96% (Figure 3.2). It is well known that porous bone substitutes with interconnected macro- and micropores offer improved biofunctionality by favoring the adhesion, growth, and differentiation of cells during bone regeneration [53]. Due to a partial solid-state sintering process, the shrinkage of the iron scaffolds was small (*i.e.*, < 2.6%). Furthermore, under the chosen sintering condition, the iron scaffolds were only composed of the α -iron single phase (Figure 3.2h), confirming the absence of any carbon residues from the decomposed polymer that could have diffused into the base material.

3.4.2 *In vitro* corrosion characteristics and mechanisms

The static *in vitro* corrosion rate of porous iron scaffolds (0.11 ± 0.01 mg/cm²/day at day 28) (Figure 3.3f), is much higher than that of cast pure iron (*i.e.*, 0.04–0.06 mg/cm²/day) [54] and that of rapidly prototyped porous iron (*i.e.*, 0.04–0.08 mg/cm²/day) [26], and electrodeposited iron foam (*i.e.*, 0.023 mg/cm²/day) [55]. The higher corrosion rate of the scaffolds was attributed to the struts that contained sintered powder particle boundaries with a micropore network. The random microporous interconnectivity provides many intricate sites that are favorable for autocatalytic corrosion [56–58], thereby resulting in the enhanced dissolution of iron. Furthermore, corrosion occurred not only at the periphery (Figure 3.4) but also in the struts and the center of the scaffolds (Figure 3.5). The penetration of the r-SBF solution into the center of the scaffolds under static immersion tests can be attributed to the capillary action in the pore network [59], thereby enhancing the corrosion of the scaffold as a whole. Nevertheless, the static *in vitro* corrosion rate (0.05 ± 0.01 mm/y at day 28) is still lower than the pure iron with a refined grain structure, manufactured by electroforming (*i.e.*, 0.40 mm/y) [60], cross-rolling (*i.e.*, 0.11–0.14 mm/y) [61], and selective laser melting (*i.e.*, 0.085 mm/y) [62], and thus requires an improvement to achieve an expected biodegradation rate of an ideal bone substitute (*i.e.*, 0.2 to 0.5 mm/y) [63].

When iron is exposed to a corrosive fluid, the corrosion is governed by an anodic reaction, followed by the reduction of the dissolved oxygen and water into hydroxide ions. As the corrosion proceeds, the pH of the medium increases, and iron (II, III) hydroxides form *via* the reaction of iron and hydroxide ions. Since iron (III) hydroxide is less stable, it will transform into a more stable compound, *i.e.*, iron oxide hydroxide. Moreover, due to the hypoxia condition in the incubator, the iron (II) hydroxide undergoes an anaerobic *Schikorr* reaction to form magnetite. Also, the release of iron ions increase the surrounding pH level and promote the precipitation of phosphate and bicarbonate ions from the r-SBF

solution. The abovementioned corrosion reactions [62] explain the formation of iron oxide (hydroxide) and iron phosphate at the periphery (Figure 3.3b and 3.4), as well as the presence of iron, calcium, carbon, and oxygen in the center of the scaffolds (Figure 3.5) that were identified after 28 days of *in vitro* immersion.

Iron ions in the r-SBF were hardly detected by the ICP-OES analysis (Figure 3.3d), due to the participation of iron ions in the formation of iron-based corrosion products that are largely insoluble in a physiological condition [34]. The release trend of iron ions was upward in the first 14 days of immersion, corresponding to the elevation of the solution pH value to 7.57. During the same period, a faster reduction of phosphate ions in the r-SBF was observed, as compared to the reduction of calcium ions. Besides the reaction with iron ions, the early period of calcium and phosphate ion reduction could also be related to the precipitation of calcium phosphate-based corrosion products (Figure 3.4). Between days 14 and 28, a declining trend of iron ion release was noted. The slight increase in the pH level after 14 days of immersion may have accelerated the precipitation of iron phosphate and carbonate compounds, which explains the decreasing trends of iron ions and more consumption of calcium ions in the medium than in the first 14 days (Figure 3.3d). The precipitation of iron/calcium carbonate releases hydrogen ions, which balances the alkalinity of the solution. In addition, with the *in vitro* corrosion occurring in a 5% CO₂ environment, the pH of the r-SBF was also effectively maintained. The pH value slightly increased to 7.62 at the end of the immersion tests.

From the electrochemical perspective, the corrosion mechanism and kinetics of the porous iron scaffolds evolved during the immersion period (Figure 3.6). The Bode impedance modulus values at the low frequency (*i.e.*, 0.01 Hz) indicate the charge transfer resistance of the material during biodegradation and those at medium frequency (*i.e.*, 10 Hz) are related to the corrosion product formation [64,65]. The increasing trend of impedance modulus values at the low and medium frequencies (Figure S3.2c) suggests the continuous build-up of corrosion products on the iron scaffolds throughout the immersion tests [14,66]. In addition, the Bode plot of the phase angle values is indicative of the corrosion susceptibility of the material as well. A phase angle value at a high frequency (*e.g.*, at 10 kHz) close to 0°, which was observed in the specimen after 1 day of biodegradation (Figure 3.6b), indicates that the material is susceptible to corrosion [67,68]. On the contrary, the phase angle shifts to a more negative value when the material exhibits more corrosion resistance, as observed for the specimens subjected to 28 days of biodegradation [67,68].

Based on the Nyquist plot after 1 day of immersion (Figure 3.6c), a single arc was observed, implying the initial active corrosion of iron with a capacitive behavior [58]. The diameter of the capacitive arc indicates the corrosion rate of

the material. The greater the diameter size, the slower the corrosion rate [69]. As the corrosion test progressed to day 7, the diameter of the arc increased, showing that even at the initial stage, the corrosion products hindered the progress of the corrosion process. Thereafter, between days 7 and 9, the Nyquist spectra transformed into a two-semicircle pattern (Figure 3.6d). The pattern remained until 24 days of immersion. The two-semicircular arcs present in the Nyquist spectra have been reported as an indication of a corrosion mechanism that combines active and diffusive processes [70]. From the observations after 7 and 14 days of immersion, corrosion products accumulated at the periphery (Figure 3.4), in the center (Figure 3.5), and in the micropore network of the specimens. The active corrosion process most probably occurred on any available iron surface, while the diffusion action is expected to have taken place through the corrosion product layer that was still relatively loose and dispersed. As the corrosion advanced from day 9 to day 24 (Figure 3.6d), the diameter of the arcs grew larger along with a tendency towards a more diffusive corrosion mechanism, as suggested by an increase in the arc diameter and a decreased incline slope for the lower frequencies [71]. Approaching day 28, when nearly all of the corrosion products had been turned into a dense layer, the corrosion mechanism evolved into a solely diffusion-controlled mechanism (Figure 3.6e), which is hallmarked by a straight line in the Nyquist spectra in the low-frequency region [58].

From the *in vitro* immersion tests and the electrochemical analysis of the porous iron scaffolds, it is clear that the formation of the corrosion products hindered the direct dissolution of iron, hence reducing the corrosion rate over time. The evolution of the corrosion products from a loose layer to a densely structured layer during the *in vitro* immersion period is observed. This makes the long-term corrosion mechanism of porous iron scaffolds strongly dependent on the diffusion process [58]. An improvement in the corrosion rate of porous iron scaffolds can be achieved by performing dynamic *in vitro* immersion tests [35]. Although with the continuous liquid flow during *in vitro* immersion, substantial amounts of corrosion products may still adhere to the scaffolds after 28 days [35]. In an *in vivo* study on iron-based stents, a slower corrosion rate than the one estimated from the *in vitro* tests was found, due to the formation of insoluble iron-based corrosion products [72]. Therefore, the strategies to modify the corrosion products (*e.g.*, to make them less adhering) are of great interest for the further development of porous iron scaffolds as bone substitutes.

3.4.3 Bone-mimicking mechanical properties

For *ad interim* metallic bone scaffolds, the mechanical properties must be maintained for a certain period until the new bone tissue can take over the mechanical role of the implant and bear physiological loading. Therefore, the

control over the *in vivo* degradation rate of the material is of great importance to better estimate the rate of biodegradation and avoid a sudden loss of the structural integrity of the scaffold. The mechanical properties of the porous iron scaffolds made by extrusion-based 3D printing remained in the range of those of cancellous bone (*i.e.*, $E = 0.5\text{--}20$ GPa and $\sigma_y = 0.2\text{--}80$ MPa) despite 28 days of *in vitro* biodegradation (Figure 3.7) [73,74].

From the stress-strain curves, the as-sintered porous iron scaffolds (Figure 3.7a) exhibited the typical mechanical characteristics of a ductile material. Unlike most geometrically ordered 3D printed porous metallic scaffolds [75,76], the stress-strain curves of the iron scaffolds did not exhibit a plateau stage. The stress-strain curves of the iron scaffolds with a 0° to 90° lay-down pattern were found to be quite similar to those of the 3D printed scaffolds designed using the solid Schwartz *p*-unit cells, which also have 90° interconnections between their struts [37,77]. In addition to the pattern, the pore network in the struts of the scaffolds acted as the center of stress concentration. The distribution of a large number of pores in the struts can also contribute to the strain-hardening effect during plastic deformation [78], which is similar to the dispersion-strengthening effect of second-phase precipitation [79].

As an actively corroding material, the *in vitro* immersion influenced the yield strength and elastic modulus of the porous iron scaffolds (Figure 3.7b). The effects of corrosion on the mechanical properties could be explained by the formation of corrosion products (Figure 3.4 and 3.5) and a drop in the fraction of pure iron fraction in the makeup of the specimens (Figure 3.5h). The interfacial bonding between iron and its corrosion products might affect the mechanical properties too [80]. Since the elastic modulus and yield strength were measured over a small range of strains during initial deformation, where loading could still be transferred across iron powder particle necks and the interfaces between iron and the corrosion products, the formation of the corrosion products led to increases in the yield strength and elastic modulus after 2 days of immersion. Afterwards, the values fluctuated throughout the 28 days of immersion but remained higher than those of the initial scaffolds. The slight increase in the yield strength and elastic modulus could be explained by considering the corrosion products as a reinforcing phase in the porous iron matrix that provided a strengthening effect. The addition of iron oxide (*i.e.*, 2 and 5 wt%) has, indeed, been reported to improve the elastic mechanical properties of the iron-iron oxide composite [81]. The fluctuations in the yield strength and elastic modulus over the immersion time may be due to the evolution of the corrosion product morphology that influenced their interfacial bonding with the specimens. Another relevant factor could be the decreasing fraction of iron in the scaffolds as

corrosion progressed. The latter would significantly affect the ductility of the scaffolds (Figure 3.7c).

3.4.4 Cytocompatibility

Different levels of preosteoblast viability (Figure 3.8a) were observed, depending on the dilution level of the iron extract. According to the ISO 10993-5 [82], the 100% iron extract was severely toxic (level 4) with nearly no metabolically active cells. The 75% iron extract was categorized as moderately toxic (level 3) with more than 50% growth inhibition, while the iron extracts $\leq 50\%$ were slightly toxic (level 1) with more than 80% metabolic activity even after 7 days of culture. Moreover, the rhodamine-phalloidin and DAPI staining (Figure 3.8c-e) clearly showed the unfavorable effects of undiluted extracts on the growth of the preosteoblasts. The number of cells increased in the diluted extracts contributing to the higher metabolic activity detected. The cytotoxicity of iron is often related to the uncontrolled formation of ROS, including superoxide anions and hydroxyl radicals *via* the Fenton reactions [83]. Although a proper ROS level plays an important part in some biological events, such as the activation of signaling pathways and gene expression, excessive ROS may lead to oxidative stresses, which will harm the cells [83].

Of note, the iron extracts were prepared with an extraction ratio of 5 cm²/mL, which is higher than the most reported extraction ratios in the *in vitro* studies of iron-based materials (*e.g.*, 2.5 cm²/mL [26] and 1.25 cm²/mL [37,62,84]). In addition to the relatively high solution volume-to-surface area ratio, the 72 h iron extraction in the cell culture medium resulted in a higher iron ion concentration as compared to the extract from the r-SBF medium, which is most likely due to the presence of serum [85,86]. A higher extraction ratio combined with a high iron ion release of the scaffolds created in this study explains the immediate cytotoxicity of the 100% iron extract that was observed. A safe iron ion concentration for bone marrow stem cells has been reported to be < 75 mg/L [8], which is similar to the results obtained in our extraction-based assays with $\leq 50\%$ iron extracts and the other results obtained from indirect cell culture [26,37,62,84]. Most *in vivo* studies on iron-based materials for implant applications have found those biomaterials to be systemically biocompatible [9,87–89], while only a few studies have found some evidence of local inflammation post implantation [88,89]. In our indirect assays, the more cytocompatible iron extracts (*i.e.*, $\leq 50\%$) are more likely to correspond to the actual *in vivo* conditions, given the fact that the dynamic flow of body fluids will inevitably decrease the concentration of iron ions in the implant vicinity. Given the high baseline of iron loading in the blood (*i.e.*, 0.447 g/L), the release of iron

ions from an implant is too small to cause systemic toxicity [90]. Local tissue toxicity analysis is, therefore, more relevant for such porous iron.

The present direct cell seeding tests demonstrated a cytotoxic effect of the porous iron scaffolds with a 17-fold reduction of viable cells within the first 3 days of culture, and afterwards only growth inhibition. Reductions in cell viability were also observed in the direct culture of mouse bone marrow stem cells on 60 vol% porous Fe-30Mn scaffolds [25], human osteosarcoma cells on 40 vol% porous Fe-30Mn6Si1Pd scaffolds [23], 3T3 fibroblasts [26] as well as rabbit bone marrow stem cells [29] on porous iron scaffolds. Interestingly, despite significant reductions in the number of viable cells, the preosteoblasts were still found stretching in the pores (Figure 3.8i) and adhering to the corrosion products of the porous iron scaffolds (Figure 3.8j-k). The spreading morphology of the preosteoblasts may be due to the combined effect of the surface morphology and the presence of calcium- and phosphate-based corrosion products that are known to be osteoconductive [9]. Since *in vitro* cytocompatibility assessment cannot completely mimic the *in vivo* conditions, these preliminary results warrant *in vivo* studies on 3D printed porous iron scaffolds, particularly to study the local cyto- and histo-compatibility of the porous iron scaffolds.

3.5 Conclusion

In this study, the iron scaffolds with a lay-down pattern were successfully fabricated by using extrusion-based 3D printing and subsequent sintering, which allowed for comprehensive characterization of the material for application as a biodegradable bone substitute. The structure of the fabricated porous iron scaffolds was highly interconnected, owing to the presence of macropores from the pattern design and random micropores in the struts. After 28 days of static *in vitro* immersion, the mass of the porous iron reduced by 7%. The *in vitro* corrosion rate decreased from 0.28 down to 0.11 mg/cm²/day, with different corrosion mechanisms operating over the 28 days of static immersion. The yield strength and elastic modulus of the porous iron scaffolds slightly increased due to the formation of corrosion products in the struts during the 28 days of *in vitro* corrosion. These values remained within the range of the mechanical properties of cancellous bone. The direct culture of preosteoblasts on the iron scaffolds revealed cytotoxicity, due to the high concentration of iron ions, as explained by the results from the extraction-based assays. Further *in vitro* cytotoxicity experiments (*e.g.*, co-culture of multiple types of cells and *in vivo* studies) should be performed [37] under dynamic conditions. Taken together, our results showed that extrusion-based 3D printing could deliver porous iron scaffolds with enhanced biodegradability and bone-mimicking mechanical properties for potential application as bone substitutes. Introducing bioactive components in

the form of coatings [10] or inside the scaffold body to form composites [30,63] may be explored to further improve the biofunctionalities of such 3D printed porous iron scaffolds.

3.6 Supplementary material

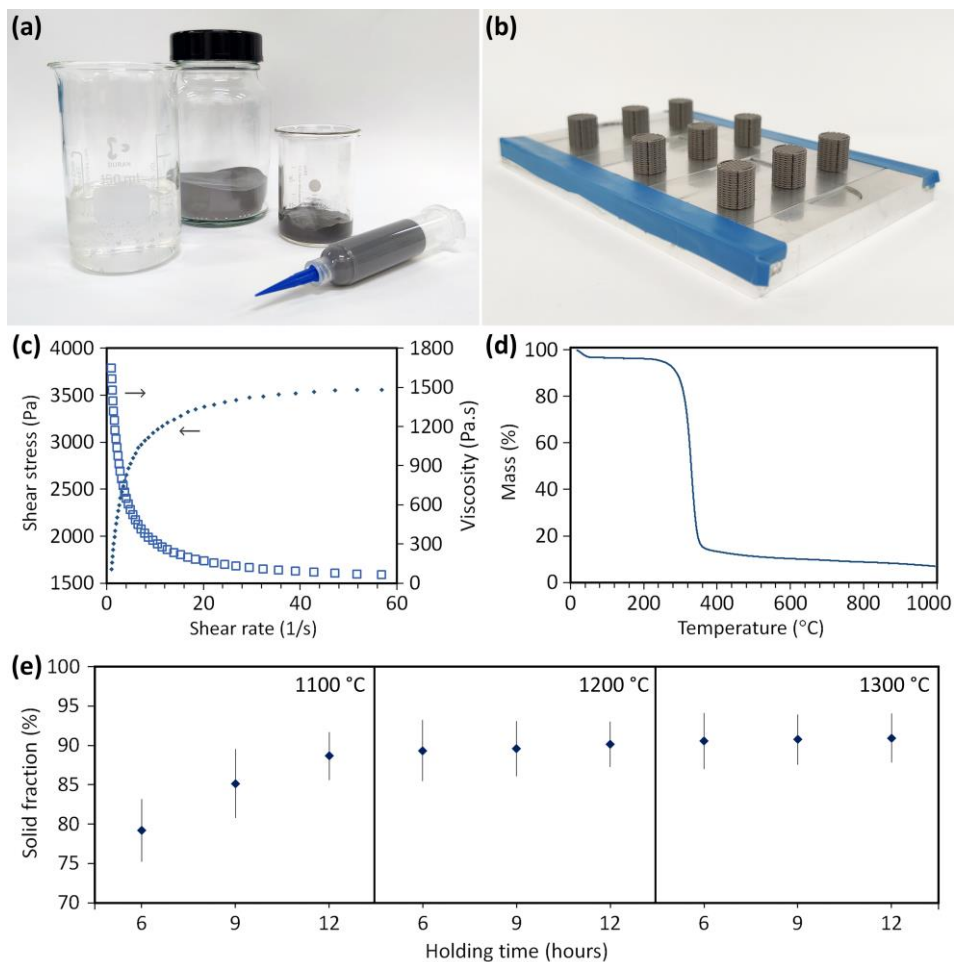


Figure S3.1. (a) Materials for ink preparation, from left to right *i.e.*, 5 wt% hypromellose aqueous solution, iron powder, ink mixture and 10 mL cartridge, (b) as-printed iron scaffolds on the build plate, (c) rheological behavior of the iron ink, (d) TGA graph of hypromellose, and (e) solid fractions of struts under different sintering conditions of temperature and time.

Table S3.1. Rheological parameters of the iron ink, of which τ_0 is the yield stress, n the flow behavior index, and K the consistency index of the fluid.

Fe ink	τ_0 (Pa)	n	K
49 vol%	1039 ± 46	0.205 ± 0.028	1143 ± 105

The yield stress τ_0 was determined by extrapolation of the stress curve to zero shear rate. The flow behavior index n and the consistency index of the fluid K were obtained by fitting the shear stress *versus* shear rate curve into the constitutive equation of the Herschel-Bulkley model (S1).

$$\tau = \tau_0 + K\dot{\gamma}^n \quad (\text{S1})$$

The ink viscosity was calculated using Equation (S2):

$$\eta = K\dot{\gamma}^{n-1} + \tau_0\dot{\gamma}^{-1} \quad (\text{S2})$$

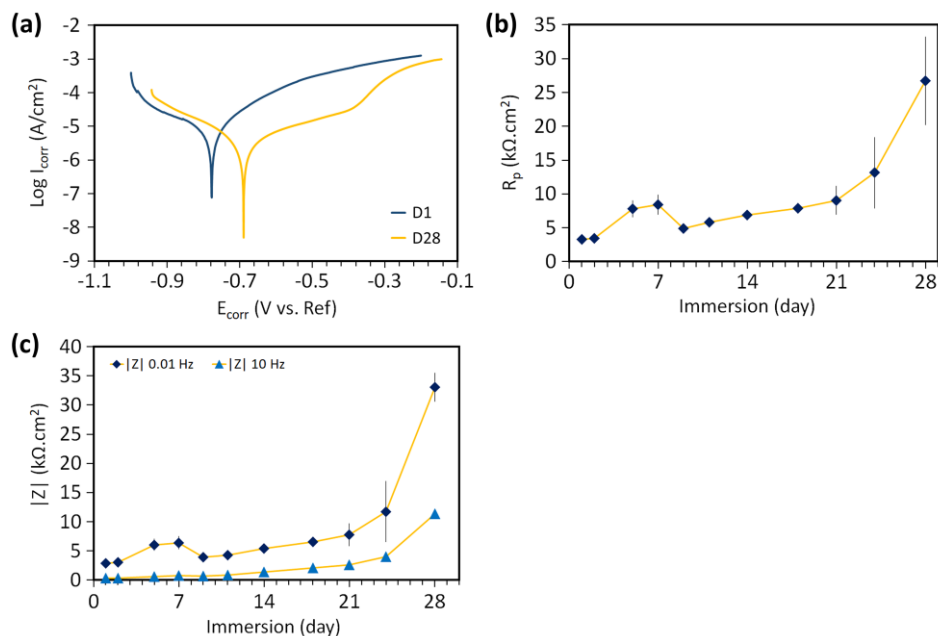


Figure S3.2. Electrochemical characteristics of the porous iron scaffolds: (a) potentio-dynamic polarization (PDP) curves after 1 day and 28 days of immersion in r-SBF, (b) linear polarization resistance (LPR) as a function of immersion time, and (c) relative impedance moduli at low (0.01 Hz) and medium (10 Hz) frequencies over immersion time.

Bibliography

- [1] R. Gorejová, L. Haverová, R. Oriňáková, A. Oriňák, M. Oriňák, Recent advancements in Fe-based biodegradable materials for bone repair, *J. Mater. Sci.* 54 (2019) 1913–1947. <https://doi.org/10.1007/s10853-018-3011-z>.
- [2] N. Abbaspour, R. Hurrell, R. Kelishadi, Review on iron and its importance for human health, *J. Res. Med. Sci.* 19 (2014) 164.
- [3] E. Balogh, G. Paragh, V. Jeney, Influence of iron on bone homeostasis, *Pharmaceuticals*. 11 (2018) 1–18. <https://doi.org/10.3390/ph11040107>.
- [4] F. Atashi, A. Modarressi, M.S. Pepper, The role of reactive oxygen species in mesenchymal stem cell adipogenic and osteogenic differentiation: A review, *Stem Cells Dev.* 24 (2015) 1150–1163. <https://doi.org/10.1089/scd.2014.0484>.
- [5] M. Parelman, B. Stoecker, A. Baker, D. Medeiros, Iron restriction negatively affects bone in female rats and mineralization of hFOB osteoblast cells, *Exp. Biol. Med.* 231 (2006) 378–386. <https://doi.org/10.1177/153537020623100403>.
- [6] J.G. Messer, P.T. Cooney, D.E. Kipp, Iron chelator deferoxamine alters iron-regulatory genes and proteins and suppresses osteoblast phenotype in fetal rat calvaria cells, *Bone*. 46 (2010) 1408–1415. <https://doi.org/10.1016/j.bone.2010.01.376>.
- [7] D. Praticò, M. Pasin, O.P. Barry, A. Ghiselli, G. Sabatino, L. Iuliano, G.A. Fitzgerald, F. Violi, Iron-dependent human platelet activation and hydroxyl radical formation: Involvement of protein kinase C, *Circulation*. 99 (1999) 3118–3124. <https://doi.org/10.1161/01.CIR.99.24.3118>.
- [8] E. Zhang, H. Chen, F. Shen, Biocorrosion properties and blood and cell compatibility of pure iron as a biodegradable biomaterial, *J. Mater. Sci. Mater. Med.* 21 (2010) 2151–2163. <https://doi.org/10.1007/s10856-010-4070-0>.
- [9] T. Kraus, F. Moszner, S. Fischerauer, M. Fiedler, E. Martinelli, J. Eichler, F. Witte, E. Willbold, M. Schinhammer, M. Meischel, P.J. Uggowitzer, J.F. Löffler, A. Weinberg, Biodegradable Fe-based alloys for use in osteosynthesis: Outcome of an *in vivo* study after 52 weeks, *Acta Biomater.* 10 (2014) 3346–3353. <https://doi.org/10.1016/j.actbio.2014.04.007>.
- [10] S. Ray, U. Thormann, M. Eichelroth, M. Budak, C. Biehl, M. Rupp, U. Sommer, T. El Khassawna, F.I. Alagboso, M. Kampschulte, M. Rohnke, A. Henß, K. Peppler, V. Linke, P. Quadbeck, A. Voigt, F. Stenger, D. Karl, R. Schnettler, C. Heiss, K.S. Lips, V. Alt, Strontium and bisphosphonate coated iron foam scaffolds for osteoporotic fracture defect healing, *Biomaterials*. 157 (2018) 1–16. <https://doi.org/10.1016/j.biomaterials.2017.11.049>.
- [11] M.H. Emily Walker, Magnesium, iron and zinc alloys, the trifecta of bioresorbable orthopaedic and vascular implantation - A review, *J. Biotechnol. Biomater.* 5 (2015) 1. <https://doi.org/10.4172/2155-952X.1000178>.
- [12] Y.P. Feng, A. Blanquer, J. Fornell, H. Zhang, P. Solsona, M.D. Baró, S. Suriñach, E. Ibáñez, E. García-Lecina, X. Wei, R. Li, L. Barrios, E. Pellicer, C. Nogués, J. Sort, Novel Fe-Mn-Si-Pd alloys: Insights into mechanical, magnetic, corrosion resistance and biocompatibility performances, *J. Mater. Chem. B*. 4 (2016) 6402–6412. <https://doi.org/10.1039/c6tb01951j>.
- [13] J. Hufenbach, H. Wendrock, F. Kochta, U. Kühn, A. Gebert, Novel biodegradable Fe-Mn-C-S alloy with superior mechanical and corrosion properties, *Mater. Lett.* 186 (2017) 330–333. <https://doi.org/10.1016/j.matlet.2016.10.037>.
- [14] J. Zhou, Y. Yang, M. Alonso Frank, R. Detsch, A.R. Boccaccini, S. Virtanen, Accelerated degradation behavior and cytocompatibility of pure iron treated with sandblasting, *ACS Appl. Mater. Interfaces*. 8 (2016) 26482–26492. <https://doi.org/10.1021/acsami.6b07068>.
- [15] A.H.M. Yusop, N.M. Daud, H. Nur, M.R.A. Kadir, H. Hermawan, Controlling the degradation kinetics of porous iron by poly(lactic-co-glycolic acid) infiltration for use as temporary medical implants, *Sci. Rep.* 5 (2015) 1–17. <https://doi.org/10.1038/srep11194>.
- [16] L. Haverová, R. Oriňáková, A. Oriňák, R. Gorejová, M. Baláž, P. Vanýsek, M. Kupková, M. Hrubovčáková, P. Mudroň, J. Radoňák, Z.O. Králová, A.M. Turoňová, An *in vitro* corrosion study of open cell iron structures with PEG coating for bone replacement applications,

- Metals (Basel). 8 (2018) 1–21. <https://doi.org/10.3390/met8070499>.
- [17] R. Gorejová, R. Oriňáková, Z.O. Králová, M. Baláž, M. Kupková, M. Hrubovčáková, L. Haverová, M. Džupon, A. Oriňák, F. Kal'avský, K. Koval', *In vitro* corrosion behavior of biodegradable iron foams with polymeric coating, *Materials* (Basel). 13 (2020) 184. <https://doi.org/10.3390/ma13010184>.
- [18] Y. Su, S. Champagne, A. Trenggono, R. Tolouei, D. Mantovani, H. Hermawan, Development and characterization of silver containing calcium phosphate coatings on pure iron foam intended for bone scaffold applications, *Mater. Des.* 148 (2018) 124–134. <https://doi.org/10.1016/j.matdes.2018.03.061>.
- [19] J. He, H. Ye, Y. Li, J. Fang, Q. Mei, X. Lu, F. Ren, Cancellous-bone-like porous iron scaffold coated with strontium incorporated octacalcium phosphate nanowhiskers for bone regeneration, *ACS Biomater. Sci. Eng.* 5 (2019) 509–518. <https://doi.org/10.1021/acsbiomaterials.8b01188>.
- [20] R. Alavi, A. Trenggono, S. Champagne, H. Hermawan, Investigation on mechanical behavior of biodegradable iron foams under different compression test conditions, *Metals* (Basel). 7 (2017) 202. <https://doi.org/10.3390/met7060202>.
- [21] J. Čapek, D. Vojtěch, Microstructural and mechanical characteristics of porous iron prepared by powder metallurgy, *Mater. Sci. Eng. C.* 43 (2014) 494–501. <https://doi.org/10.1016/j.msec.2014.06.046>.
- [22] J. Čapek, D. Vojtěch, A. Oborná, Microstructural and mechanical properties of biodegradable iron foam prepared by powder metallurgy, *Mater. Des.* 83 (2015) 468–482. <https://doi.org/10.1016/j.matdes.2015.06.022>.
- [23] Y.P. Feng, N. Gaztelumendi, J. Fornell, H.Y. Zhang, P. Solsona, M.D. Baró, S. Suriñach, E. Ibáñez, L. Barrios, E. Pellicer, C. Nogués, J. Sort, Mechanical properties, corrosion performance and cell viability studies on newly developed porous Fe-Mn-Si-Pd alloys, *J. Alloys Compd.* 724 (2017) 1046–1056. <https://doi.org/10.1016/j.jallcom.2017.07.112>.
- [24] M. Heiden, E. Nauman, L. Stanciu, Bioresorbable Fe–Mn and Fe–Mn–HA materials for orthopedic implantation: Enhancing degradation through porosity control, *Adv. Healthc. Mater.* 6 (2017) 1–12. <https://doi.org/10.1002/adhm.201700120>.
- [25] S.M. Huang, E.A. Nauman, L.A. Stanciu, Investigation of porosity on mechanical properties, degradation and in-vitro cytotoxicity limit of Fe₃₀Mn using space holder technique, *Mater. Sci. Eng. C.* 99 (2019) 1048–1057. <https://doi.org/10.1016/j.msec.2019.02.055>.
- [26] P. Sharma, K.G. Jain, P.M. Pandey, S. Mohanty, *In vitro* degradation behaviour, cytocompatibility and hemocompatibility of topologically ordered porous iron scaffold prepared using 3D printing and pressureless microwave sintering, *Mater. Sci. Eng. C.* 106 (2020) 110247. <https://doi.org/10.1016/j.msec.2019.110247>.
- [27] D.T. Chou, D. Wells, D. Hong, B. Lee, H. Kuhn, P.N. Kumta, Novel processing of iron-manganese alloy-based biomaterials by inkjet 3-D printing, *Acta Biomater.* 9 (2013) 8593–8603. <https://doi.org/10.1016/j.actbio.2013.04.016>.
- [28] D. Hong, D.T. Chou, O.I. Velikokhatnyi, A. Roy, B. Lee, I. Swink, I. Issaev, H.A. Kuhn, P.N. Kumta, Binder-jetting 3D printing and alloy development of new biodegradable Fe-Mn-Ca/Mg alloys, *Acta Biomater.* 45 (2016) 375–386. <https://doi.org/10.1016/j.actbio.2016.08.032>.
- [29] C. Yang, Z. Huan, X. Wang, C. Wu, J. Chang, 3D printed Fe scaffolds with HA nanocoating for bone regeneration, *ACS Biomater. Sci. Eng.* 4 (2018) 608–616. <https://doi.org/10.1021/acsbiomaterials.7b00885>.
- [30] H. Ma, T. Li, Z. Huan, M. Zhang, Z. Yang, J. Wang, J. Chang, C. Wu, 3D printing of high-strength bioscaffolds for the synergistic treatment of bone cancer, *NPG Asia Mater.* 10 (2018) 31–44. <https://doi.org/10.1038/s41427-018-0015-8>.
- [31] D.K. Mishra, P.M. Pandey, Experimental investigation into the fabrication of green body developed by micro-extrusion-based 3D printing process, *Polym. Compos.* 41 (2020) 1986–2002. <https://doi.org/10.1002/pc.25514>.
- [32] D.K. Mishra, P.M. Pandey, Effect of sintering parameters on the microstructure and compressive mechanical properties of porous Fe scaffold fabricated using 3D printing and

- pressure less microwave sintering, *Proc. Inst. Mech. Eng. Part C J. Mech. Eng. Sci.* 234 (2020) 4305–4320. <https://doi.org/10.1177/0954406220921416>.
- [33] D.K. Mishra, P.M. Pandey, Mechanical behaviour of 3D printed ordered pore topological iron scaffold, *Mater. Sci. Eng. A*. 783 (2020) 139293. <https://doi.org/10.1016/j.msea.2020.139293>.
- [34] Y. Li, H. Jahr, K. Lietaert, P. Pavanram, A. Yilmaz, L.I. Fockaert, M.A. Leeftang, B. Pouran, Y. Gonzalez-Garcia, H. Weinans, J.M.C. Mol, J. Zhou, A.A. Zadpoor, Additively manufactured biodegradable porous iron, *Acta Biomater.* 77 (2018) 380–393. <https://doi.org/10.1016/j.actbio.2018.07.011>.
- [35] Y. Li, H. Jahr, P. Pavanram, F.S.L. Bobbert, U. Puggi, X.Y. Zhang, B. Pouran, M.A. Leeftang, H. Weinans, J. Zhou, A.A. Zadpoor, Additively manufactured functionally graded biodegradable porous iron, *Acta Biomater.* 96 (2019) 646–661. <https://doi.org/10.1016/j.actbio.2019.07.013>.
- [36] C. Shuai, W. Yang, Y. Yang, H. Pan, C. He, F. Qi, D. Xie, H. Liang, Selective laser melted Fe-Mn bone scaffold: Microstructure, corrosion behavior and cell response, *Mater. Res. Express.* 7 (2019) 015404. <https://doi.org/10.1088/2053-1591/ab62f5>.
- [37] D. Carluccio, C. Xu, J. Venezuela, Y. Cao, D. Kent, M. Birmingham, A.G. Demir, B. Previtali, Q. Ye, M. Dargusch, Additively manufactured iron-manganese for biodegradable porous load-bearing bone scaffold applications, *Acta Biomater.* 103 (2020) 346–360. <https://doi.org/10.1016/j.actbio.2019.12.018>.
- [38] A.A. Zadpoor, J. Malda, Additive manufacturing of biomaterials, tissues, and organs, *Ann. Biomed. Eng.* 45 (2017) 1–11. <https://doi.org/10.1007/s10439-016-1719-y>.
- [39] Y. Qin, P. Wen, H. Guo, D. Xia, Y. Zheng, L. Jauer, R. Poprawe, M. Voshage, J.H. Schleifenbaum, Additive manufacturing of biodegradable metals: Current research status and future perspectives, *Acta Biomater.* 98 (2019) 3–22. <https://doi.org/10.1016/j.actbio.2019.04.046>.
- [40] N.E. Putra, M.J. Mirzaali, I. Apachitei, J. Zhou, A.A. Zadpoor, Multi-material additive manufacturing technologies for Ti-, Mg-, and Fe-based biomaterials for bone substitution, *Acta Biomater.* 109 (2020) 1–20. <https://doi.org/10.1016/j.actbio.2020.03.037>.
- [41] C. Shuai, G. Liu, Y. Yang, F. Qi, S. Peng, W. Yang, C. He, G. Wang, G. Qian, A strawberry-like Ag-decorated barium titanate enhances piezoelectric and antibacterial activities of polymer scaffold, *Nano Energy.* 74 (2020) 104825. <https://doi.org/10.1016/j.nanoen.2020.104825>.
- [42] Y. Yang, C. Lu, S. Peng, L. Shen, D. Wang, F. Qi, C. Shuai, Laser additive manufacturing of Mg-based composite with improved degradation behaviour, *Virtual Phys. Prototyp.* 15 (2020) 278–293. <https://doi.org/10.1080/17452759.2020.1748381>.
- [43] ASTM B963-17, Standard test methods for oil content, oil-impregnation efficiency, and surface-connected porosity of sintered powder metallurgy (PM) products using Archimedes' principle, ASTM International, 2017. <https://doi.org/10.1520/B0963-14>.
- [44] A. Oyane, H.M. Kim, T. Furuya, T. Kokubo, T. Miyazaki, T. Nakamura, Preparation and assessment of revised simulated body fluids, *J. Biomed. Mater. Res. - Part A*. 65 (2003) 188–195. <https://doi.org/10.1002/jbm.a.10482>.
- [45] L. Yang, E. Zhang, Biocorrosion behavior of magnesium alloy in different simulated fluids for biomedical application, *Mater. Sci. Eng. C*. 29 (2009) 1691–1696. <https://doi.org/10.1016/j.msec.2009.01.014>.
- [46] ASTM G1-03, Standard practice for preparing, cleaning, and evaluating corrosion test specimens, ASTM International. (2017). <https://doi.org/10.1520/G0001-03R17E01.2>.
- [47] ASTM G32-72, Standard practice for laboratory immersion corrosion testing of metals., ASTM International. (2004). <https://doi.org/10.1520/G0031-72R04.2>.
- [48] ASTM G102-89, Standard practice for calculation of corrosion rates and related information from electrochemical measurements, ASTM International, 2015. <https://doi.org/10.1520/G0102-89R15E01>.
- [49] ISO 13314, Mechanical testing of metals - Ductility testing - Compression test for porous and cellular metals, International Organization for Standardization, 2011. <https://doi.org/ISO 13314:2011>.

- [50] ISO 10993-12, Sample preparation and reference materials, International Organization for Standardization, 2012. [https://doi.org/10.1016/S0080-8784\(08\)60069-1](https://doi.org/10.1016/S0080-8784(08)60069-1).
- [51] C.L. Li, L.G. Martini, J.L. Ford, M. Roberts, The use of hypromellose in oral drug delivery, *J. Pharm. Pharmacol.* 57 (2005) 533–546. <https://doi.org/10.1211/0022357055957>.
- [52] I. Rishmawi, M. Salarian, M. Vlasea, Tailoring green and sintered density of pure iron parts using binder jetting additive manufacturing, *Addit. Manuf.* 24 (2018) 508–520. <https://doi.org/10.1016/j.addma.2018.10.015>.
- [53] J.M. Seok, T. Rajangam, J.E. Jeong, S. Cheong, S.M. Joo, S.J. Oh, H. Shin, S.H. Kim, S.A. Park, Fabrication of 3D plotted scaffold with microporous strands for bone tissue engineering, *J. Mater. Chem. B* 8 (2020) 951–960. <https://doi.org/10.1039/c9tb02360g>.
- [54] T. Huang, J. Cheng, Y.F. Zheng, *In vitro* degradation and biocompatibility of Fe-Pd and Fe-Pt composites fabricated by spark plasma sintering, *Mater. Sci. Eng. C* 35 (2014) 43–53. <https://doi.org/10.1016/j.msec.2013.10.023>.
- [55] J. He, F.L. He, D.W. Li, Y.L. Liu, D.C. Yin, A novel porous Fe/Fe-W alloy scaffold with a double-layer structured skeleton: Preparation, *in vitro* degradability and biocompatibility, *Colloids Surfaces B Biointerfaces* 142 (2016) 325–333. <https://doi.org/10.1016/j.colsurfb.2016.03.002>.
- [56] F. Xie, X. He, S. Cao, M. Mei, X. Qu, Influence of pore characteristics on microstructure, mechanical properties and corrosion resistance of selective laser sintered porous Ti-Mo alloys for biomedical applications, *Electrochim. Acta* 105 (2013) 121–129. <https://doi.org/10.1016/j.electacta.2013.04.105>.
- [57] E. Aghion, Y. Perez, Effects of porosity on corrosion resistance of Mg alloy foam produced by powder metallurgy technology, *Mater. Charact.* 96 (2014) 78–83. <https://doi.org/10.1016/j.matchar.2014.07.012>.
- [58] P. Sharma, P.M. Pandey, Corrosion behaviour of the porous iron scaffold in simulated body fluid for biodegradable implant application, *Mater. Sci. Eng. C* 99 (2019) 838–852. <https://doi.org/10.1016/j.msec.2019.01.114>.
- [59] D.S. Oh, Y.J. Kim, M.H. Hong, M.H. Han, K. Kim, Effect of capillary action on bone regeneration in micro-channeled ceramic scaffolds, *Ceram. Int.* 40 (2014) 9583–9589. <https://doi.org/10.1016/j.ceramint.2014.02.033>.
- [60] M. Moravej, A. Purnama, M. Fiset, J. Couet, D. Mantovani, Electroformed pure iron as a new biomaterial for degradable stents: *In vitro* degradation and preliminary cell viability studies, *Acta Biomater.* 6 (2010) 1843–1851. <https://doi.org/10.1016/j.actbio.2010.01.008>.
- [61] C.S. Obayi, R. Tolouei, C. Paternoster, S. Turgeon, B.A. Okorie, D.O. Obikwelu, G. Cassar, J. Buhagiar, D. Mantovani, Influence of cross-rolling on the micro-texture and biodegradation of pure iron as biodegradable material for medical implants, *Acta Biomater.* 17 (2015) 68–77. <https://doi.org/10.1016/j.actbio.2015.01.024>.
- [62] C. Shuai, S. Li, G. Wang, Y. Yang, S. Peng, C. Gao, Strong corrosion induced by carbon nanotubes to accelerate Fe biodegradation, *Mater. Sci. Eng. C* 104 (2019) 109935. <https://doi.org/10.1016/j.msec.2019.109935>.
- [63] C. Gao, M. Yao, S. Li, P. Feng, S. Peng, C. Shuai, Highly biodegradable and bioactive Fe-Pd-bredigite biocomposites prepared by selective laser melting, *J. Adv. Res.* 20 (2019) 91–104. <https://doi.org/10.1016/j.jare.2019.06.001>.
- [64] C. Valero, A. Igual, Electrochemical aspects in biomedical alloy characterization: Electrochemical impedance spectroscopy, in: *Biomedical Engineering, Trends in Materials Science*, 2011: pp. 283–306. <https://doi.org/10.5772/13039>.
- [65] J. Tedim, M.L. Zheludkevich, A.C. Bastos, A.N. Salak, A.D. Lisenkov, M.G.S. Ferreira, Influence of preparation conditions of layered double hydroxide conversion films on corrosion protection, *Electrochim. Acta* 117 (2014) 164–171. <https://doi.org/10.1016/j.electacta.2013.11.111>.
- [66] A. Xu, F. Zhang, F. Jin, R. Zhang, B. Luo, T. Zhang, The evaluation of coating performance by analyzing the intersection of Bode plots, *Int. J. Electrochem. Sci.* 9 (2014) 5125.
- [67] M. Mahdavian, M.M. Attar, Another approach in analysis of paint coatings with EIS measurement: Phase angle at high frequencies, *Corros. Sci.* 48 (2006) 4152–4157. <https://doi.org/10.1016/j.corsci.2006.03.012>.

- [68] Y. Zuo, R. Pang, W. Li, J.P. Xiong, Y.M. Tang, The evaluation of coating performance by the variations of phase angles in middle and high frequency domains of EIS, *Corros. Sci.* 50 (2008) 3322–3328. <https://doi.org/10.1016/j.corsci.2008.08.049>.
- [69] X. Liu, S. Chen, H. Ma, G. Liu, L. Shen, Protection of iron corrosion by stearic acid and stearic imidazoline self-assembled monolayers, *Appl. Surf. Sci.* 253 (2006) 814–820. <https://doi.org/10.1016/j.apsusc.2006.01.038>.
- [70] D. You, N. Pebere, F. Dabosi, An investigation of the corrosion of pure iron by electrochemical techniques and in situ observations, *Corros. Sci.* 34 (1993) 5–15. [https://doi.org/10.1016/0010-938X\(93\)90254-E](https://doi.org/10.1016/0010-938X(93)90254-E).
- [71] B.A. Mei, O. Munteshari, J. Lau, B. Dunn, L. Pilon, Physical interpretations of Nyquist plots for EDLC electrodes and devices, *J. Phys. Chem. C* 122 (2018) 194–206. <https://doi.org/10.1021/acs.jpcc.7b10582>.
- [72] A. Drynda, T. Hassel, F.W. Bach, M. Peuster, *In vitro* and *in vivo* corrosion properties of new iron-manganese alloys designed for cardiovascular applications, *J. Biomed. Mater. Res. - Part B Appl. Biomater.* 103 (2015) 649–660. <https://doi.org/10.1002/jbm.b.33234>.
- [73] T.M. Keaveny, W.C. Hayes, Mechanical properties of cortical and trabecular bone, *Bone* 7 (1993) 285–344.
- [74] T.M. Keaveny, E.F. Morgan, G.L. Niebur, O.C. Yeh, Biomechanics of trabecular bone, *Annu. Rev. Biomed. Eng.* 3 (2001) 307–333.
- [75] S.M. Ahmadi, S.A. Yavari, R. Wauthle, B. Pouran, J. Schrooten, H. Weinans, A.A. Zadpoor, Additively manufactured open-cell porous biomaterials made from six different space-filling unit cells: The mechanical and morphological properties, *Materials (Basel)* 8 (2015) 1871–1896. <https://doi.org/10.3390/ma8041871>.
- [76] F.S.L. Bobbert, K. Lietaert, A.A. Eftekhari, B. Pouran, S.M. Ahmadi, H. Weinans, A.A. Zadpoor, Additively manufactured metallic porous biomaterials based on minimal surfaces: A unique combination of topological, mechanical, and mass transport properties, *Acta Biomater.* 53 (2017) 572–584. <https://doi.org/10.1016/j.actbio.2017.02.024>.
- [77] N. Soro, H. Attar, X. Wu, M.S. Dargusch, Investigation of the structure and mechanical properties of additively manufactured Ti-6Al-4V biomedical scaffolds designed with a Schwartz primitive unit-cell, *Mater. Sci. Eng. A* 745 (2019) 195–202. <https://doi.org/10.1016/j.msea.2018.12.104>.
- [78] Y.N. Podrezov, L.G. Shtyka, D.G. Verbylo, Strain hardening of porous iron under uniaxial compression, *Powder Metall. Met. Ceram.* 39 (2000) 92–96. <https://doi.org/10.1007/BF02677449>.
- [79] G. Cui, X. Wei, E.A. Olevsky, R.M. German, J. Chen, The manufacturing of high porosity iron with an ultra-fine microstructure via free pressureless spark plasma sintering, *Materials (Basel)* 9 (2016) 1–9. <https://doi.org/10.3390/ma9060495>.
- [80] S.Y. Fu, X.Q. Feng, B. Lauke, Y.W. Mai, Effects of particle size, particle/matrix interface adhesion and particle loading on mechanical properties of particulate-polymer composites, *Compos. Part B Eng.* 39 (2008) 933–961. <https://doi.org/10.1016/j.compositesb.2008.01.002>.
- [81] J. Cheng, T. Huang, Y.F. Zheng, Microstructure, mechanical property, biodegradation behavior, and biocompatibility of biodegradable Fe-Fe₂O₃ composites, *J. Biomed. Mater. Res. - Part A* 102 (2014) 2277–2287. <https://doi.org/10.1002/jbm.a.34882>.
- [82] ISO 10993-5, Tests for *in vitro* cytotoxicity, International Organization for Standardization, 2009. <https://doi.org/10.1021/es0620181>.
- [83] Y.F. He, Y. Ma, C. Gao, G.Y. Zhao, L.L. Zhang, G.F. Li, Y.Z. Pan, K. Li, Y.J. Xu, Iron overload inhibits osteoblast biological activity through oxidative stress, *Biol. Trace Elem. Res.* 152 (2013) 292–296. <https://doi.org/10.1007/s12011-013-9605-z>.
- [84] M.S. Dargusch, A. Dehghan-Manshadi, M. Shahbazi, J. Venezuela, X. Tran, J. Song, N. Liu, C. Xu, Q. Ye, C. Wen, Exploring the role of manganese on the microstructure, mechanical properties, biodegradability, and biocompatibility of porous iron-based scaffolds, *ACS Biomater. Sci. Eng.* 5 (2019) 1686–1702. <https://doi.org/10.1021/acsbiomaterials.8b01497>.
- [85] V. Wagener, A.S. Faltz, M.S. Killian, P. Schmuki, S. Virtanen, Protein interactions with corroding metal surfaces: Comparison of Mg and Fe, *Faraday Discuss.* 180 (2015) 347–

360. <https://doi.org/10.1039/c4fd00253a>.
- [86] R. Oriňaková, R. Gorejová, Z.O. Králová, A. Oriňak, I. Shepa, J. Hovancová, A. Kovalčíková, Z.L. Bujňáková, N. Király, M. Kaňuchová, M. Baláž, M. Strečková, M. Kupková, M. Hrubovčáková, F. Kaľavský, M. Oriňak, Influence of albumin interaction on corrosion resistance of sintered iron biomaterials with polyethyleneimine coating, *Appl. Surf. Sci.* 509 (2020) 145379. <https://doi.org/10.1016/j.apsusc.2020.145379>.
- [87] M. Fântânariu, L.C. Trincă, C. Solcan, A. Trofin, Ș. Strungaru, E.V. Șindilar, G. Plăvan, S. Stanciu, A new Fe-Mn-Si alloplastic biomaterial as bone grafting material: *In vivo* study, *Appl. Surf. Sci.* 352 (2015) 129–139. <https://doi.org/10.1016/j.apsusc.2015.04.197>.
- [88] Q. Feng, D. Zhang, C. Xin, X. Liu, W. Lin, W. Zhang, S. Chen, K. Sun, Characterization and *in vivo* evaluation of a bio-corrodible nitrided iron stent, *J. Mater. Sci. Mater. Med.* 24 (2013) 713–724. <https://doi.org/10.1007/s10856-012-4823-z>.
- [89] M. Traverson, M. Heiden, L.A. Stanciu, E.A. Nauman, Y. Jones-Hall, G.J. Breur, *In vivo* evaluation of biodegradability and biocompatibility of Fe₃₀Mn alloy, *Vet. Comp. Orthop. Traumatol.* 31 (2018) 10–16. <https://doi.org/10.3415/VCOT-17-06-0080>.
- [90] E. Scarcello, D. Lison, Are Fe-based stenting materials biocompatible? A critical review of *in vitro* and *in vivo* studies, *J. Funct. Biomater.* 11 (2020) 2. <https://doi.org/10.3390/jfb11010002>.

Poly(2-ethyl-2-oxazoline) coating on biodegradable porous Fe

Additively manufacturing of porous iron offers a unique opportunity to increase its biodegradation rate by taking advantage of arbitrarily complex porous structures. Nevertheless, achieving the required biodegradation profile remains challenging due to the natural passivation of iron that decreases the biodegradation rate. Moreover, the biocompatibility of iron is reported to be limited. Here, we address both challenges by applying poly(2-ethyl-2-oxazoline) coating to extrusion-based 3D printed porous iron. We characterized the specimens by performing *in vitro* biodegradation, electrochemical measurements, time-dependent mechanical tests, and *in vitro* cytocompatibility assays. The coated porous iron exhibited a biodegradation rate that was 2.6× higher than that of non-coated counterpart and maintained the bone-mimicking mechanical properties throughout *in vitro* biodegradation. Despite the formation of dense biodegradation products, the coating ensured relatively stable biodegradation (*i.e.*, 17% reduction in the degradation rate between days 14 and 28) as compared to that of non-coated specimens (*i.e.*, 43% drop). Furthermore, the coating could be identified even after biodegradation, demonstrating the longevity of the coating. Finally, the coated specimens significantly increased the viability and supported the attachment and growth of preosteoblasts. Our results demonstrate the great potential of poly(2-ethyl-2-oxazoline) coating for addressing the multiple challenges associated with the clinical adoption of porous iron.

4.1 Introduction

Over the past decade, iron-based scaffolds have been developed as a new class of biodegradable materials to fulfil the requirements of temporary orthopedic implants [1]. The development of iron-based biomaterials, however, remains challenging due to their too low rates of biodegradation [2]. The biodegradation process of iron results in the formation of corrosion products (*e.g.*, iron hydroxides and iron phosphate) that hinder oxygen transport to iron in the subsurface [3], thereby slowing down the continued corrosion of iron. The other major challenge in the use of iron-based biomaterials is their limited cytocompatibility [4]. While several studies have tried to address the abovementioned challenges [5,6], they remain unresolved. Alloying iron with lower standard electrode potential elements is one of the most widely used strategies [6–8]. Alternatively, adding alloying elements to iron can generate new phases that induce local galvanic corrosion and, thus, speed up its corrosion [6,8]. However, such alloying elements can be even more cytotoxic than iron.

The recent advances in additive manufacturing (AM) techniques, such as selective laser melting (SLM) [9–11] and extrusion-based 3D printing [12], have enabled the fabrication of iron-based biomaterials with arbitrarily complex hierarchical geometries and fully interconnected pores. A highly porous structure has much large surface area than its solid counterpart, favoring accelerated biodegradation of iron. However, this approach may become less effective over time for iron, as dense passive biodegradation products gradually form.

Biofunctionalization with polymer or bioceramic coatings is another strategy to both alter the biodegradation behavior of iron and provide osteogenic properties [13,14]. While the addition of bioceramics induces osteogenic properties, these coatings tend to reduce the biodegradation rate of iron due to their stable nature [15–18]. Polymer coatings (*e.g.*, based on polylactic acid (PLA) [19–21], poly(lactic-co-glycolic acid (PLGA) [22], polyethylene glycol (PEG) [23], and polyethyleneimine (PEI) [24]) enhance the biodegradation of iron too [20–24]. Moreover, these coatings have been shown to be cytocompatible for various cell types [25–27].

Gradual hydrolyzation of biodegradable polymer coatings (*i.e.*, PLA and PLGA) creates an acidic environment [23] that accelerates the dissolution of biodegradation products, thereby exposing more bare iron surface to biodegradation [20–22]. Although PEG is often regarded as a non-biodegradable polymer, it is known to be sensitive to oxidative degradation due to its polyether backbone [28]. Indeed, the coating layer should not biodegrade too quickly in order to make sure it can foster continuous transport of metallic ions out of the

bulk material, while preventing the strong adhesion of degradation products that would otherwise inhibit further corrosion of iron.

Recently, poly(2-alkyl/aryl-2-oxazoline)-based polymers (PAOx) have received much attention as PEG alternatives in biomedical applications [29,30]. Unlike PEG, PAOx possess a tertiary amide backbone, which makes the polymer highly stable under biologically relevant conditions [31,32]. Moreover, PAOx are highly versatile, offering a broad range of end-group and side-chain functionalization possibilities attainable through copolymerization [29]. Poly(2-ethyl-2-oxazoline) (PEtOx) is the most investigated PAOx derivative, due to its similar hydrophilicity to PEG and balanced amphiphilicity [30]. PEtOx has demonstrated great potential for application in tissue regeneration and as the basis of a wide variety of drug delivery systems [33–35]. However, it has never been applied for the bio-functionalization of AM porous iron.

We have recently demonstrated how extrusion-based 3D printing can deliver hierarchical porous iron with much enlarged surface area (to improve their biodegradability) and bone-mimicking mechanical properties [12]. Here, we combined this fabrication method with PEtOx coatings to develop multifunctional porous iron scaffolds, which were then thoroughly characterized by performing *in vitro* biodegradation experiments, electrochemical measurements, time-dependent measurements of mechanical properties, and *in vitro* cytocompatibility assays.

4.2 Materials and methods

4.2.1 3D printing of porous iron scaffolds

Porous iron scaffolds with a diameter of $\varnothing = 10$ mm and a height of $h = 10.5$ mm were manufactured using extrusion-based 3D printing (Figure 4.1), followed by debinding and sintering, as described in Chapter 3, section 3.2.1. These scaffolds will hereafter be referred to as non-coated iron.

4.2.2 Synthesis and characterization of poly(2-ethyl-2-oxazoline)

We added 2.02 mol of distilled 2-ethyl-2-oxazoline (203.6 mL, Polymer Chemistry Innovations, Arizona, USA), 300.7 mL ethyl acetate (purity 99.9%, extra dry, Fisher Scientific), and 20.19 mmol of distilled methyl p-toluenesulfonate (3.055 mL, purity 98%, Sigma Aldrich) to a 1-L Schott bottle that was equipped with a magnetic stirrer and was sealed in a glovebox under an inert and dry atmosphere. The polymerization mixture was heated for 21 h at 60 °C in an oil bath, followed by a cool-down step to reach the room temperature. The polymer was terminated in the glovebox with 22.21 mmol, 9.34 mL tetramethylammonium hydroxide solution (25 wt% in methanol) [36]. The

reaction was filtered and subsequently concentrated in *vacuo*. The residue was dissolved in deionized water and was purified by dialysis in water, followed by freeze-drying to yield (114 g, 57%) a white solid. The molar mass (M_n) values of the PEtOx polymer were characterized using size-exclusion chromatography (SEC, Agilent 1260-series high-performance liquid chromatography system, USA) and was calculated against the linear PEtOx standards (Avroxa, Belgium). The dispersity (\mathcal{D}) values were calculated against the linear PMMA standard (Polymer Standard Service). In addition, ^1H nuclear magnetic resonance (NMR) analysis was conducted using a Bruker Avance 400 spectrometer (400 MHz, USA) to confirm the composition of the PEtOx polymer (Figure S4.2).

4.2.3 Surface biofunctionalization

The PEtOx-OH terminated polymer (purity >95%, $M_{n, \text{theoretical}} = 9.9$ kDa, $M_{n, \text{SEC}} = 9.7$ kDa (PEtOx standard calibration), and $\mathcal{D} = 1.10$, Figure S4.3) was dissolved in 96% ethanol with a concentration of 10% w/v. The iron scaffolds were immersed into the PEtOx-OH solution. A vacuum pressure of 7 kPa was applied for 15 min to infiltrate the polymer into the open pores of the scaffolds. After that, the scaffolds were dried overnight. These scaffolds will hereafter be referred to as PEtOx-coated iron (Figure 4.1).

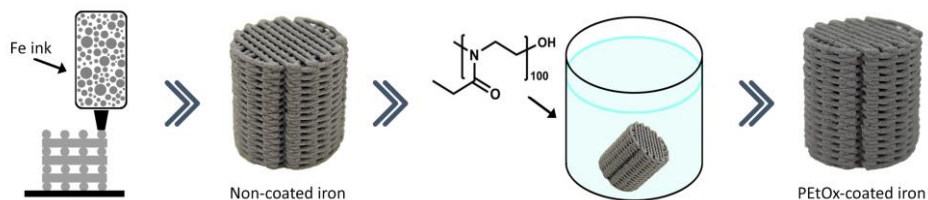


Figure 4.1. Illustrations of extrusion-based 3D printing, non-coated iron scaffolds, the process of coating the porous iron scaffolds in a PEtOx-OH solution, and a PEtOx-coated iron specimen.

4.2.4 Characterization of the surface-biofunctionalized scaffolds

The morphologies of the non-coated iron and PEtOx-coated iron were examined using a scanning electron microscope (SEM, JEOL JSM-IT100, Japan), and both the strut sizes and strut spacings were measured. The chemical composition of the coating was analyzed using X-ray energy dispersive spectroscopy (EDS, JEOL JSM-IT100, Japan). The cross section of the PEtOx-coated iron was imaged using the same SEM and the coating thickness was measured. The regions of interest on the cross sections of the struts were determined and the pore area was selected using ImageJ (NIH, USA). The solid fraction of the struts was calculated with Equation (3.1).

In addition, the chemistry of the PEtOx-OH polymer and that of the PEtOx-coated iron specimen were determined using a Fourier-transform infrared spectroscope (FTIR, Nicolet iS50 FT-IR, Thermo Scientific, USA) equipped with built-in attenuated total reflection (ATR) and a liquid nitrogen-cooled mercury-cadmium-telluride detector. The phase composition of the PEtOx-coated iron specimen was identified using an X-ray diffractometer (XRD, Bruker D8 Advance diffractometer in the Bragg-Brentano geometry). The XRD was equipped with a graphite monochromator and a Lynxeye position-sensitive detector and operated using Cu K α radiation at 45 kV and 40 mA and with a step size of 0.030° and a counting time of 2 s per step. The X-ray datasets were analyzed using the Diffrac Suite.EVA v5.2 software (Bruker, USA).

4.2.5 Characterization of the porosity of the scaffolds

The non-coated iron and PEtOx-coated iron scaffolds were weighed to determine the increase in mass due to coating. A dry weighing method was used to obtain the absolute porosity values, as described in Chapter 3, with Equations (3.2) and (3.3). In addition, based on the ASTM standard B963-13 [37] and as described in Chapter 3, Equation (3.4), the interconnected porosity values of the non-coated iron and PEtOx-coated iron scaffolds were determined. The density of the PEtOx-coated iron scaffold ($\rho_{PEtOx-Fe}$) was 6.41 g/cm³.

4.2.6 Immersion tests and biodegradation product characterization

The immersion tests for PEtOx-coated iron scaffolds were performed in the revised simulated body fluid (r-SBF, static environment) whose ion concentrations are the same with those of the total human blood plasma [38]. The immersion continued uninterrupted for 2, 7, 14, and 28 days (in triplicate) under the conditions in detail in Chapter 3, section 3.2.4. There was 6.7 mL of the medium for every 1 cm² of the scaffold surface area [39]. The non-coated iron were included as the control group. The pH values of the fluid were measured both close to the specimens and far from them using a pH electrode (InLab Expert Pro-ISM, METTLER TOLEDO, Switzerland). In addition, the concentrations of soluble iron, calcium, and phosphate ions were measured using an inductively coupled plasma optical emission spectroscope ICP-OES (iCAP 6500 Duo, Thermo Scientific, USA).

At selected time points (*i.e.*, 7, 14, and 28 d), the morphologies of the biodegradation products on the periphery of the PEtOx-coated iron were observed using SEM (JEOL JSM-IT100, Japan), and the main elemental compositions of the biodegradation products were determined using EDS (JEOL JSM-IT100, Japan). The phase compositions of the biodegradation products of the PEtOx-coated iron after 28 days of immersion were determined using XRD (D8 Advance, Bruker, USA).

To examine the remaining PEOx coating layer after 28 days of immersion, the biodegraded scaffolds were gently shaken during retrieval from the immersion medium to remove loosely attached peripheral biodegradation products. The surface of the scaffolds beneath the peripheral degradation products was investigated using SEM and EDS. In addition, the biodegraded scaffolds were cut through a transverse plane at the center of the scaffold, the cross section was polished, and the biodegradation products formed inside the struts (*i.e.*, in the micropores between sintered Fe powder particles) were examined. The remaining solid fraction in the PEOx-coated iron struts after 28 days of immersion was calculated using ImageJ (NIH, USA) and Equation (3.1).

Furthermore, the mass losses of the non-coated iron and PEOx-coated iron scaffolds were calculated after the dissolution of the biodegradation products of the scaffolds, as described in Chapter 3, section 3.2.4, following the ASTM standard G1-03 [40]. From the mass loss values, the average corrosion rate was calculated, based on the ASTM standard G31-72 [41] with Equation (3.5).

4.2.7 Electrochemical measurements

The electrochemical responses of the PEOx-coated iron scaffolds during biodegradation were measured in r-SBF for up to 28 days (temperature = 37 ± 0.5 °C and pH = 7.40) using a three-electrode setup consisting of an Ag/AgCl electrode (the reference), a graphite rod (the counter electrode), and the test specimen (the working electrode) that was connected to a Bio-Logic SP-200 potentiostat (Bio-Logic Science Instruments, France).

The PEOx-coated iron specimens (in triplicate, for every time point) were prepared for open circuit potential (OCP), linear polarization resistance (LPR) and electrochemical impedance spectroscopy (EIS) measurements with parameters as described in detail in Chapter 3, section 3.2.6. The resulting Nyquist and Bode curves were plotted and analyzed. The Nyquist impedance data points at low frequencies (*i.e.*, at 0.2 to 0.05 Hz) were linearly extrapolated and the angles between the line and x-axis were determined.

4.2.8 Mechanical tests

Uniaxial compressive mechanical properties of the PEOx-coated iron scaffolds and the specimens retrieved at multiple time points (*i.e.*, after 7, 14, and 28 days of immersion, in triplicate for every time point) were determined using a mechanical testing machine (100 kN load cell, Zwick Z100, Germany), following the ISO standard 13314:2011 [42]. The elastic modulus and yield strength were determined as described in Chapter 3, section 3.2.7.

4.2.9 Cytocompatibility evaluation

Preculture of cells and preparation of iron extracts

Mouse preosteoblasts (MC3T3-E1, Sigma Aldrich, Germany) were precultured for 7 days in a cell culture incubator with the following conditions as described in Chapter 3, section 3.2.8. The cell culture medium consisting of the α -minimum essential medium (α -MEM, Thermo Fisher Scientific, USA) without ascorbic acid but supplemented with 10% fetal bovine serum (FBS, Thermo Fisher Scientific, USA) and 1% penicillin/streptomycin (p/s, Thermo Fisher Scientific, USA) was used. The same cell culture medium was used in the preparation of iron extracts and for the cell culture assays.

Extracts were obtained from the PEO-coated iron scaffolds (sizes: $\varnothing = 9.75$ mm and $h = 10.25$ mm) after 72 h of incubation [43] in the cell culture medium with conditions, as described in Chapter 3, section 3.2.8. The extracts were diluted to 75%, 50%, or 25%. The concentration of iron ions in the 100% extract was measured using ICP-OES (iCAP 6500 Duo, Thermo Scientific, USA).

Indirect test: PrestoBlue assay

Preosteoblasts MC3T3-E1 (1×10^4 cells, in 48-well plates, triplicate) were cultured in 200 μ L of the PEO-coated iron extract with various degrees of dilution for 1, 3, and 7 days. The PrestoBlue assay (as described in Chapter 3, section 3.2.8) was utilized to evaluate the metabolic activity of the cells that was calculated with Equation (3.7).

Direct assays: Viable cell count and live/dead staining

Preosteoblasts MC3T3-E1 (5×10^4 cells) were seeded onto the PEO-coated iron (sizes: $\varnothing = 9.75$ mm and $h = 1.3$ mm) and were cultured in 6-well plates with 8 mL of the cell culture medium (triplicate) for 1, 4, 7, 14, and 28 days. The Trypan blue reagent (Bio-Rad, USA) and cell counting methods (as described in Chapter 3, section 3.2.8) were utilized to determine the number of viable cells after cell culture. After 4, 7, and 14 days of culture, the preosteoblasts were stained using calcein and ethidium homodimer-1 (Thermo Fisher Scientific, USA). Furthermore, the morphology of the preosteoblasts present on the scaffolds was examined with SEM after 14 days of culture.

4.2.10 Statistical analysis

The statistical analysis was carried out using two-way ANOVA and Tukey multiple comparison *post hoc* test for PrestoBlue and Trypan blue assays in the cell culture experiments (**** = $p < 0.0001$, *** = $p < 0.001$, ** = $p < 0.01$, and * = $p < 0.05$, n.s. = not significant).

Table 4.1. Characteristics of the extrusion-based 3D printed porous iron and PEtOx-coated iron scaffolds.

Sample group	Strut width (μm)	Strut spacing (μm)	Absolute porosity (%)	Interconnected porosity (%)
Design	410	400	50	-
Non-coated iron	411 ± 6	399 ± 6	69 ± 1	67 ± 2
PEtOx-coated iron	412 ± 4	398 ± 5	62 ± 1	61 ± 1

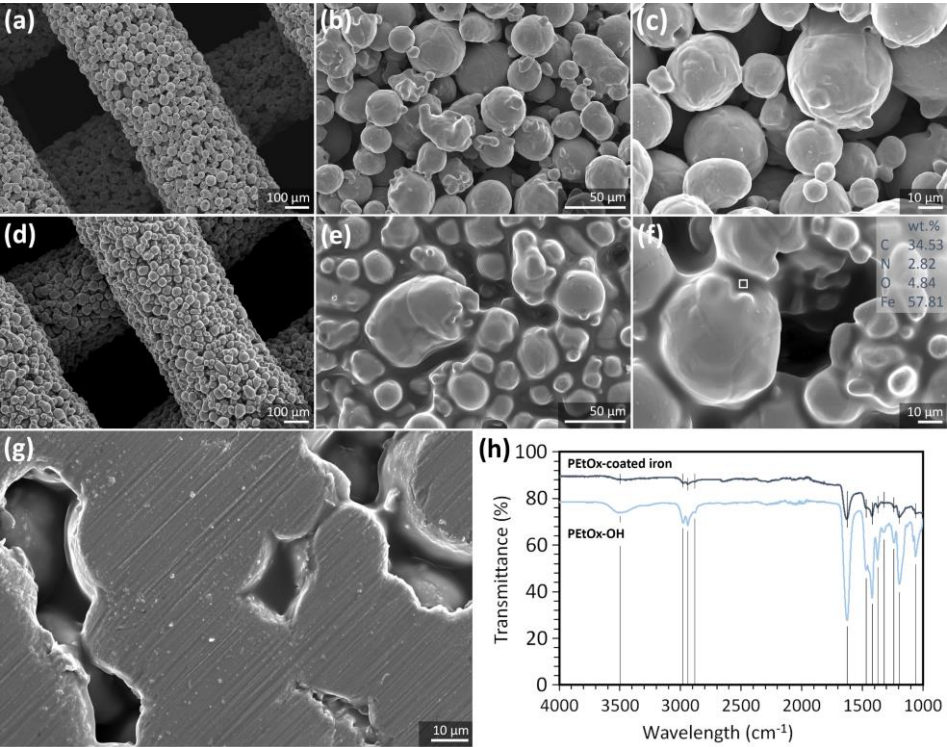


Figure 4.2. The morphologies of (a, b, c) non-coated iron and (d, e, f) PEtOx-coated iron at different magnifications, (g) the cross section of the PEtOx-coated iron scaffold struts, and (h) the FTIR graph of the PETox-OH polymer and PETox-coated porous iron specimens.

4.3 Results

4.3.1 Morphological and chemical characterization of the scaffolds

The extrusion-based 3D printed porous iron scaffolds demonstrated a 0° and 90° lay-down pattern, essentially replicating the design (Figure 4.2a-c). Their dimensions were 9.75 ± 0.03 mm in diameter and 10.24 ± 0.02 mm in height. Their actual strut size was 411 ± 6 μm with an actual strut spacing of 399 ± 6 μm and an actual interconnected porosity of $67 \pm 2\%$ (Table 4.1). After PEOx coating, the porous structure and the strut geometry of the scaffolds remained almost unchanged (Figure 4.2d). A relatively uniform layer of PEOx coating covered the surface of partially sintered iron powder particles (Figure 4.2e), and contained Fe, C, O, and N (Figure 4.2f). The coating was very thin with a thickness of 2.0 ± 0.5 μm (Figure 4.2g). The dimensions of the coated scaffolds hardly changed, with a diameter of 9.75 ± 0.02 mm and a height of 10.25 ± 0.01 mm, but the coating moderately altered the strut width and strut spacing to 413 ± 4 μm and 397 ± 5 μm , respectively.

In addition, the PEOx-coated iron scaffolds had a lower interconnected porosity, (*i.e.*, $61 \pm 1\%$) (Table 4.1) and an increased solid fraction (*i.e.*, $94 \pm 4\%$) than the non-coated iron. The XRD analysis of the PEOx-coated iron scaffold revealed the presence of the α -iron phase, confirming that the coating process did not induce oxidation and did not affect the purity of the base material (Figure S4.1). The FTIR spectrum of the PEOx-coated iron scaffolds showed various transmittance bands that were similar to those of the PEOx-OH polymer, but with lower intensities (Figure 4.2h). The FTIR valleys at 1061 cm^{-1} , 1194 cm^{-1} , and 1238 cm^{-1} indicated the presence of C-C stretching, while the bands at 1322 cm^{-1} , 1374 cm^{-1} , and 1470 cm^{-1} indicated the presence of C-H bending [44]. The FTIR bands at 1419 cm^{-1} and 1625 cm^{-1} were respectively attributed to CH_3 bending and C=O (amide) stretching [45]. On the PEOx-coated iron scaffolds, the C=O (amide) valley was shifted to 1628 cm^{-1} . Moreover, the transmittance bands at 2874 cm^{-1} , 2939 cm^{-1} and 2977 cm^{-1} suggested the existence of CH_2 stretching [44,46]. The OH bonding at 3488 cm^{-1} on the PEOx-OH polymer was attributed to the hydroxyl terminated feature of the polymer. On the other hand, the OH group appeared to be diminished on the PEOx-coated iron scaffold.

4.3.2 *In vitro* biodegradation characteristics

Yellow-brownish biodegradation products appeared on the periphery of the PEOx-coated iron scaffolds after 28 days of static *in vitro* immersion (Figure 4.3a). At the 2nd day of immersion, the PEOx-coated iron scaffolds exhibited a biodegradation rate of 0.32 ± 0.01 mm/y. At the 14th day of immersion, the biodegradation rate dropped to 0.16 ± 0.04 mm/y. Then, the rate

of biodegradation continued to decline until it reached 0.13 ± 0.02 mm/y at the 28th day of immersion (Figure 4.3b). On the other hand, the biodegradation rate of the non-coated iron specimens were 0.11 ± 0.03 mm/y at the 2nd day of immersion, which declined to 0.09 ± 0.02 mm/y at the 14th day of immersion and further dropped to 0.05 ± 0.03 mm/y at day 28 (Figure 4.3b).

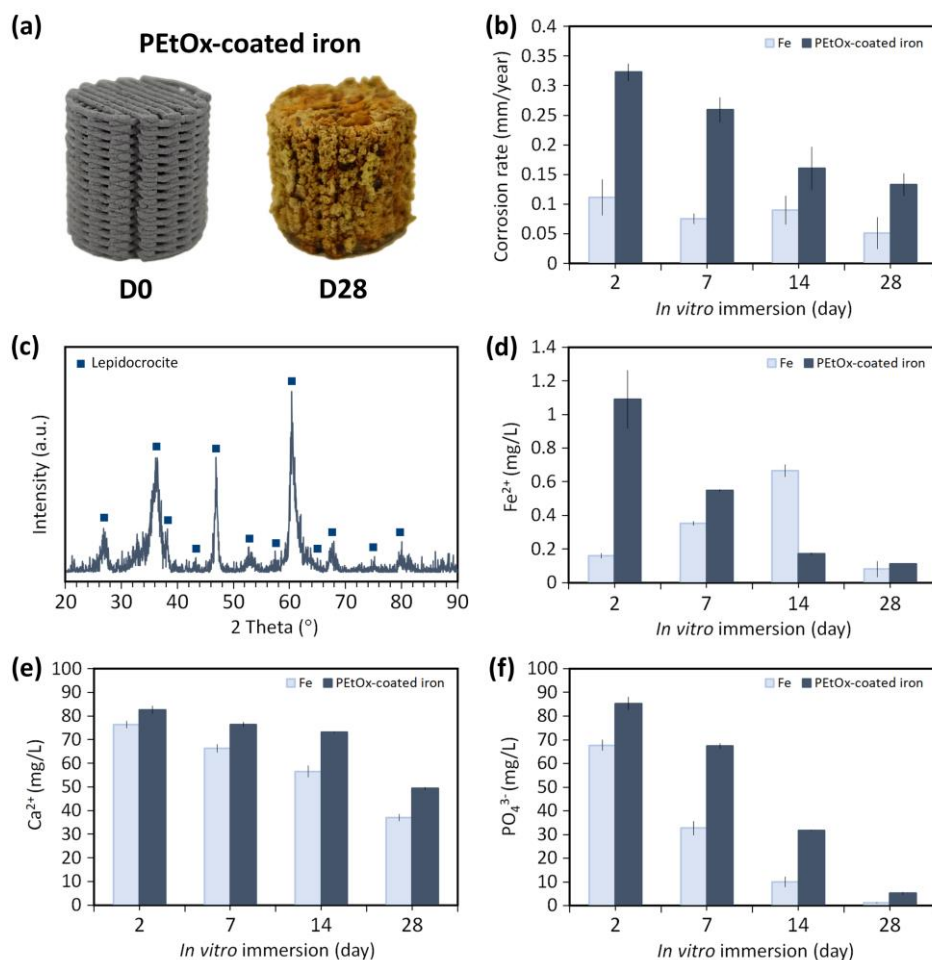


Figure 4.3. The *in vitro* biodegradation of the PETOx-coated iron scaffolds: (a) visualization of the specimens before and after 28 days of biodegradation, (b) corrosion rate, (c) the phase compositions of biodegradation products on day 28, and the time-dependent concentrations of (d) iron, (e) calcium, and (f) phosphate ions in the r-SBF solution during the *in vitro* biodegradation experiments.

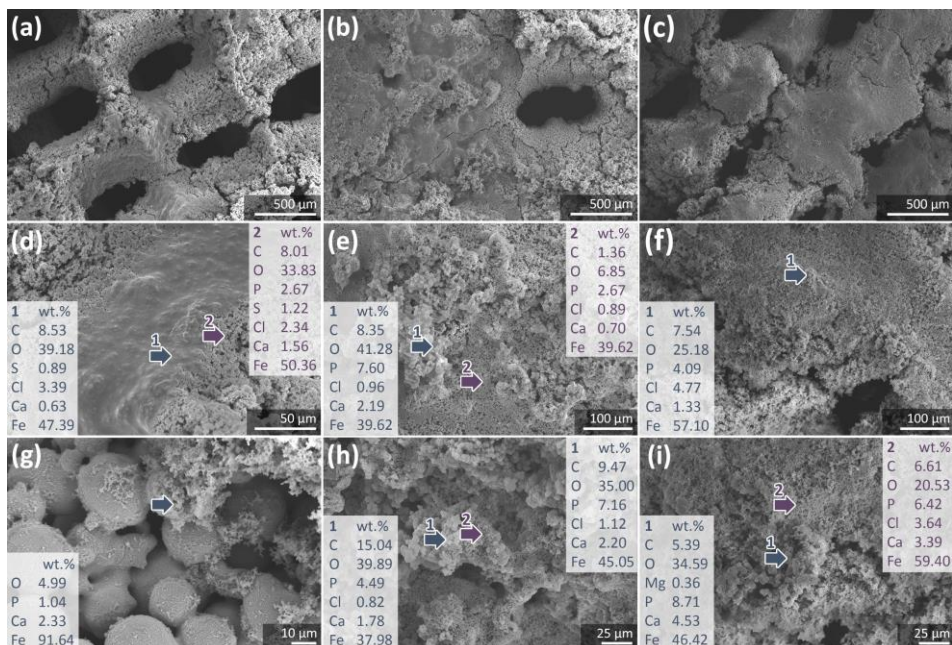


Figure 4.4. The morphologies and chemical compositions of the biodegradation products on the periphery of the PEO-coated iron scaffolds after (a, d, g) 2, (b, e, h) 14, and (c, f, i) 28 days *in vitro* biodegradation. The arrow and number indicate the location of the EDS measurements.

Throughout the *in vitro* biodegradation experiments, the pH values in the vicinity of the PEO-coated iron and the pH values distant from the scaffolds remained around 7.68 to 7.70, slightly higher than the values measured for the non-coated iron specimens (*i.e.*, 7.63). As the biodegradation experiments progressed, iron ions were continuously released to r-SBF (Figure 4.3d). The iron ion concentration from the PEO-coated iron scaffolds was the highest on the 2nd day of immersion (*i.e.*, 2.26 ± 0.30 mg/L), while the iron ions released from the non-coated scaffolds gradually increased until the 14th day of immersion (*i.e.*, 0.67 ± 0.04 mg/L). Subsequently, the iron ion concentrations decreased until day 28 when they reached 0.11 ± 0.01 mg/L and 0.08 ± 0.05 mg/L for the PEO-coated iron and non-coated specimens, respectively. Meanwhile, the calcium and phosphate ions present in the immersion medium continuously decreased with time (Figure 4.3e-f). The decrease in phosphate ion concentration was more pronounced in the case of the non-coated specimens than the PEO-coated iron scaffolds. In the case of the PEO-coated iron specimens, the measured concentrations of phosphate ions were 85.3 ± 2.7 mg/L on day 2, 67.4 ± 1.1 mg/L on day 7, 31.7 ± 0.1 mg/L on day 14, and 5.2 ± 0.6 mg/L on day 28, while the phosphate ion concentrations associated with the non-coated specimens were

67.66 ± 2.3 mg/L on day 2, 32.74 ± 3.0 mg/L on day 7, 10.02 ± 2.2 mg/L on day 14, and 1.2 ± 0.3 mg/L on day 28.

4.3.3 Characteristics of the biodegradation products

After 28 days of *in vitro* immersion, the biodegradation products of the PEtOx-coated iron scaffolds at the periphery were identified as lepidocrocite (Figure 4.3c) and a $78 \pm 6\%$ solid fraction of the PEtOx-coated iron specimens was retained. In addition, Fe and O appeared to be the main elements in the biodegradation products, along with C, Ca, P, Cl, S, and Mg (Figure 4.4). The biodegradation product layer after 7 days of immersion was less compact than the layer formed at the later time points of immersion (*i.e.*, days 14 and 28, Figure 4.4a-c). At the 7th day of immersion (Figure 4.4a), the biodegradation products formed on the PEtOx-coated iron specimens were dense and granulated with two distinct chemical compositions: one containing C, O, S, Cl, Ca, P, and Fe ((Figure 4.4d) and the other being composed of Fe, Ca, P, and O (Figure 4.4g). The detection of the latter suggested the formation of iron/calcium phosphate compounds. On days 14 and 28, the biodegradation products appeared to be denser (Figure 4.4b-c). At a higher magnification, the morphology of the biodegradation products formed on the PEtOx-coated iron scaffolds appeared to be granulated with a variety of very fine porous features (Figure 4.4e-f). On days 14 and 28, the chemical compositions of the biodegradation products (*i.e.*, C, O, Cl, Ca, P and Fe) were similar to those on day 7 with somewhat increased concentrations of calcium and phosphorus (Figure 4.4h-i).

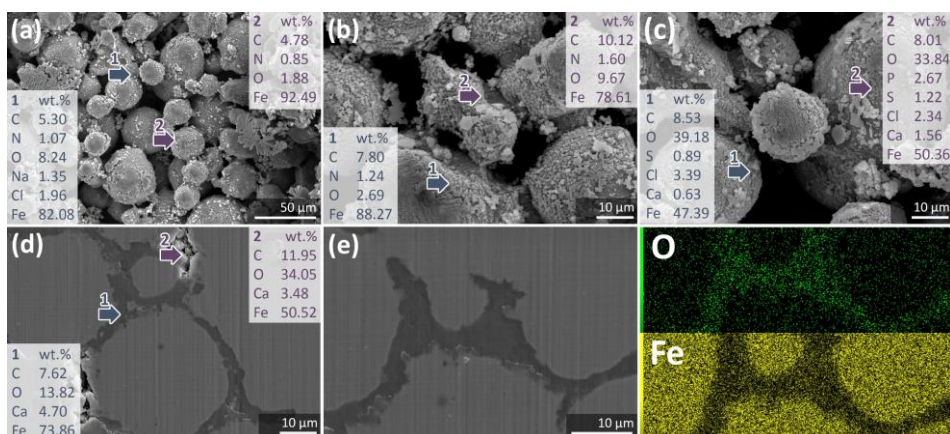


Figure 4.5. The morphologies and chemical compositions of the biodegradation products of the PEtOx-coated iron scaffolds on day 28: (a, b, c) beneath the dense layer on the periphery imaged at different magnifications, (d, e) cross section at the center, and (f) the EDS mapping on the cross section. The arrows and numbers indicate the locations of the EDS measurements.

Underneath the peripheral layer of the biodegradation products (Figure 4.5a-c), the interconnected porous struts of the PEO-coated iron scaffolds were still clearly discernible. The surface of the interconnected iron particles was also covered by the biodegradation products. EDS analysis on the biodegradation products revealed the presence of N together with C, O, Na, Cl, and Fe (Figure 4.5a). The N content (in terms of mass percentage) was lower than its initial value (Figure 4.2f). Interestingly, at different spots, N was found along with C, O, and Fe (Figure 4.5b), corresponding to the same chemical composition as found in the initial PEO coating (Figure 4.2f). Other spots on the periphery of the specimens exhibited biodegradation products with similar chemical compositions (Figure 4.5c). At the center of the PEO-coated iron scaffolds, solid biodegradation products (containing Fe, Ca, C, and O) were observed in the interconnected micro-pores of the struts, suggesting the formation of iron/calcium carbonate compounds (Figure 4.5d). However, only Fe and O were detected in the EDS map (Figure 4.5e).

4.3.4 Electrochemical measurements

Over the 28 days of *in vitro* biodegradation, the OCP value of the PEO-coated iron scaffolds only changed insignificantly (Figure 4.6a). The average OCP value on the 2nd day of immersion was -674 ± 6 mV, which essentially stabilized at -670 ± 21 mV, -671 ± 28 mV, and -677 ± 38 mV, respectively, on days 7, 14, and 28. To the contrary, the average OCP value of the non-coated iron specimens increased significantly throughout the immersion period (Figure 4.6a). The OCP values were -696 ± 5 mV on day 2, -677 ± 5 mV on day 7, -673 ± 1 mV on day 14, and -600 ± 65 mV on day 28. From the LPR tests of the PEO-coated iron specimens (Figure 4.6b), the average polarization resistance (R_p) value on the 2nd day of immersion was 5.0 ± 0.7 k Ω .cm². Then, the R_p values increased to 5.7 ± 1.1 k Ω .cm², 6.6 ± 1.2 k Ω .cm², and 9.2 ± 3.2 k Ω .cm² on days 7, 14, and 28, respectively. For the non-coated iron specimens (Figure 4.6b), the R_p values substantially increased from 3.3 ± 0.8 k Ω .cm² on day 2 to 29.9 ± 4.8 k Ω .cm² on day 28.

The impedance Nyquist plots of the PEO-coated iron scaffolds (EIS measurements) showed two distinct types of electrochemical responses: while a single semicircle can be observed on day 2 (Figure 4.6c), an extra time constant (semicircle arc) was observed from day 7 to day 28 (Figure 4.6d-e). The linear extrapolation line in the impedance Nyquist in the low frequency region (*i.e.*, 0.2 to 0.05 Hz) exhibited angles of 43.4° , 42.7° , 41.7° , 44.8° , and 41.9° to the x-axis after 2, 7, 14, 21, and 28 d of immersion, respectively (Figure 4.6c-e). The impedance magnitudes agreed with the R_p values. At a frequency of 0.01 Hz, the impedance Bode values of the PEO-coated iron specimens were 3.6 ± 0.3 k Ω .cm², 4.2 ± 0.6 k Ω .cm², 5.8 ± 0.9 k Ω .cm², and 7.9 ± 3.3 k Ω .cm², after 2, 7, 14,

and 28 days of immersion, respectively (Figure 4.6f). In the low frequency region (*e.g.*, 0.1 Hz), the Bode phase angle shifted towards a more positive value, from $-38 \pm 2^\circ$ on day 2 to $-22 \pm 1^\circ$ and $-15 \pm 5^\circ$, on days 14 and 28, respectively (Figure 4.6g). In the higher frequency region (*e.g.*, at 10 kHz), however, the phase angle moved towards a more negative value from $-1.1 \pm 0.4^\circ$ on day 2 to $-17 \pm 3^\circ$ and $-34 \pm 10^\circ$ on days 14 and 28, respectively.

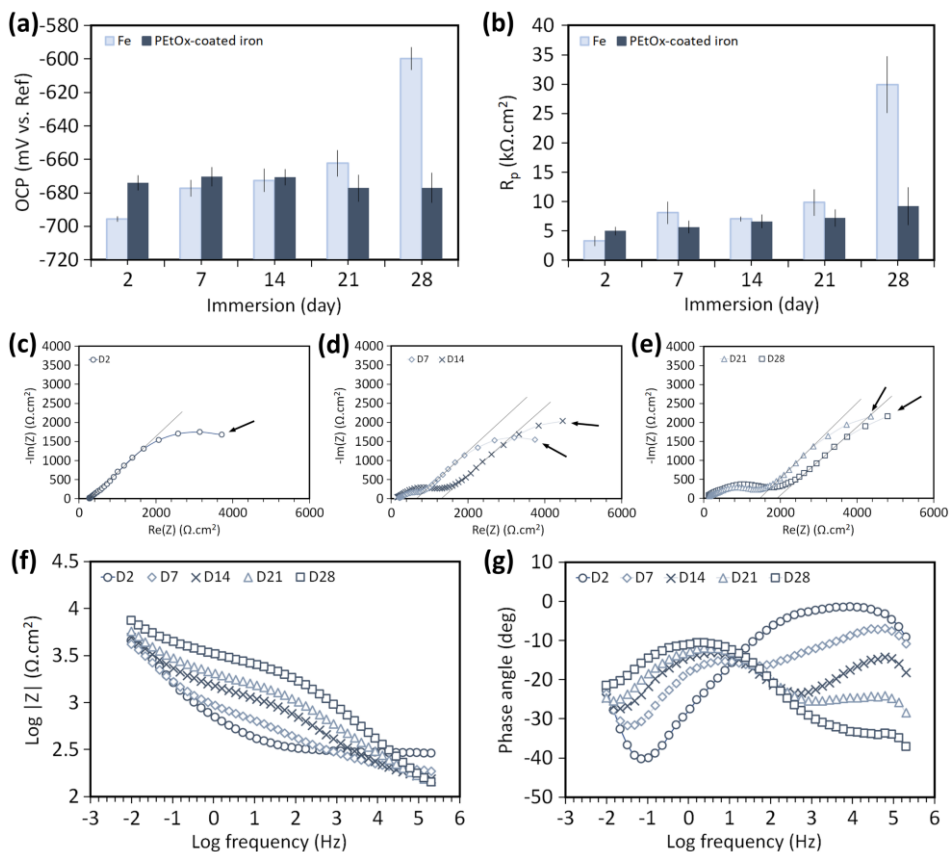


Figure 4.6. The electrochemical measurements of the PETox-coated iron scaffolds during the biodegradation experiments: the evolution of the (a) OCP and (b) R_p values with time. (c, d, e) The Nyquist impedance curves at different time points. (f, g) The Bode impedance plot and phase angle values at different time points. The arrows indicate a specific frequency of 0.01 Hz. The lines indicate the linear extrapolation of Nyquist impedance at 0.2 to 0.05 Hz.

4.3.5 Mechanical properties

The PETox-coated iron scaffolds exhibited smooth stress-strain curves under uniaxial compression even after *in vitro* biodegradation for 28 d. The

stress-strain curves initiated with a linear elastic region, followed by a region with a less steep rate of stress increase resembling the plastic deformation region (Figure 4.7a). The PEO-coated iron scaffolds were less ductile after biodegradation with the strain-to-failure dropping from $0.44 \pm 0.07\%$ to $0.35 \pm 0.05\%$ after 28 days of immersion. In addition, the PEO-coated iron specimens had a yield strength and an elastic modulus of 6.2 ± 0.8 MPa and 0.5 ± 0.09 GPa, respectively. On days 7 and 28, the yield strengths were 4.9 ± 1.4 MPa and 5.3 ± 1.0 MPa (Figure 4.7b). At the same time points, the elastic moduli were 0.41 ± 0.08 GPa and 0.41 ± 0.06 GPa (Figure 4.7b).

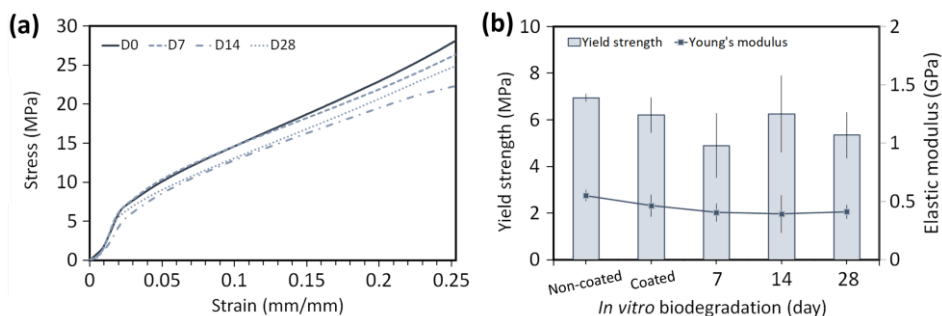


Figure 4.7. The mechanical properties of the PEO-coated iron specimens: (a) stress-strain curves. Changes in the (b) yield strength and elastic modulus with biodegradation time.

4.3.6 *In vitro* cytocompatibility

The MC3T3-E1 preosteoblasts cultured in 100% extracts associated with the PEO-coated specimens, containing 105.4 ± 5.7 mg/L iron ion, exhibited a very low metabolic activity (*i.e.*, $13 \pm 1\%$ to $23 \pm 3\%$) throughout the cell culture period of 7 days (Figure 4.8a). The metabolic activity of the preosteoblasts improved to $43 \pm 7\%$ when cultured in 75% extract for 24 h. However, the value dropped to $25 \pm 3\%$ after 7 days of cell culture. At the 50% and 25% extracts, the metabolic activities of the cells were above 80% at all cell culture time points (Figure 4.8a).

In addition, the direct culture of preosteoblasts on the PEO-coated iron scaffolds showed a significant increase in the number of cells after 7 days of culture ($p < 0.01$), which was maintained over the remaining culture period (Figure 4.8b). The numbers of viable preosteoblasts counted on the PEO-coated iron scaffolds were higher at all the time points than those on the non-coated iron scaffolds (*i.e.*, $p < 0.01$ at day 4 and $p < 0.0001$ at the 7th, 14th, and 28th day, Figure 4.8b). In agreement with the cell counting assay, the live/dead staining revealed more viable (green-stained) cells adhered on the PEO-coated iron than the non-coated scaffolds at all the time points. The number of nonviable (red-stained)

cells on the non-coated iron increased from the 4th day to the 14th day of cell culture (Figure 4.8c-e). However, the preosteoblasts remained viable (green-stained) on the PEOx-coated iron scaffolds throughout the 14 days of cell culture period (Figure 4.8g-i). On the non-coated specimens, the morphology of the preosteoblasts was rounded and the cells were covered by particulate biodegradation products after 14 days of cell culture (Figure 4.8f). On the contrary, the cells were spread and developed extended filopodia on the PEOx-coated iron surface (Figure 4.8j).

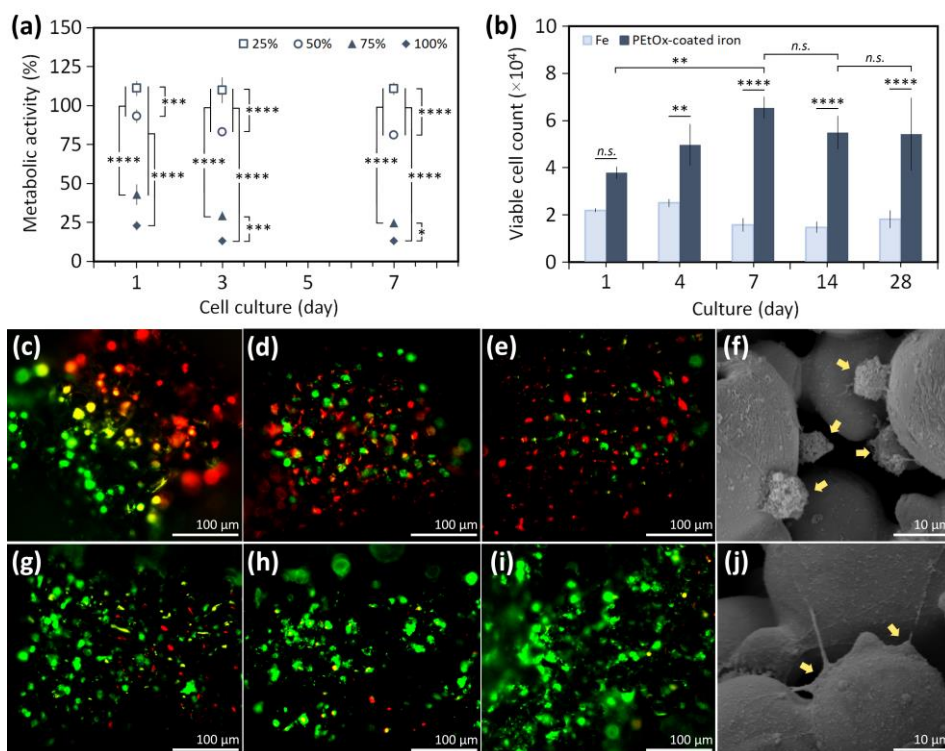


Figure 4.8. The cytocompatibility of the PEOx-coated iron scaffolds tested using MC3T3-E1 preosteoblasts: (a) the metabolic activity of the cells cultured with the extracts retrieved at different time points, (b) the viable cell counts over 28 days of culture. The live/dead staining of (c, d, e) the non-coated iron and (g, h, i) PEOx-coated iron specimens after 4, 7, and 14 days of culture, and the typical morphology of the cells cultured in (f) the non-coated iron and (j) PEOx-coated iron scaffolds (after 14 days of culture). **** = $p < 0.0001$, *** = $p < 0.001$, ** = $p < 0.01$, * = $p < 0.05$ and *n.s.* = *not significant*

4.4 Discussion

The PEOx coating applied to extrusion-based 3D printed iron scaffolds hold great promise, given that they have the potential to improve various properties of

iron-based scaffolds, thereby enabling them to function as biodegradable bone substitutes. The favorable properties of PEtOx-coated porous iron include (i) an enhanced *in vitro* biodegradation rate (*i.e.*, 0.13 mm/y) that is 2.6 times higher than its non-coated counterpart, (ii) bone-mimicking mechanical properties [47] with a yield strength of 5.3 – 6.2 MPa and an elastic modulus of 0.41 – 0.46 GPa maintained even after 28 days of biodegradation, and (iii) enhanced cell viability and cell adhesion due to the presence of the PEtOx coating.

4.4.1 PEtOx coating on extrusion-based 3D printed porous iron

The biomaterial developed here can be further improved using the other approaches available in the literature, such as alloying the base material prior to coating, fine-tuning the polymer concentration, and the application of other types of PAOx polymers. We immersed the 3D printed scaffolds in the polymeric solution, aided by a moderate vacuum. Similar to the dip coating technique, this is a reliable and straightforward method to create a thin and uniform layer on a material with a complex porous structure [48–50]. The use of vacuum was intended to ensure a thorough distribution of the polymer solution inside the open pores of the scaffolds. Vacuum has also been shown to improve the interfacial bonding of polymer and iron [22]. Aided by the negative pressure, the PEtOx polymer formed a relatively homogenous thin coating layer on the struts of the scaffolds (Figure 4.2d). A relatively dense coating layer was observed on the necking of the iron powder particles (Figure 4.2e-f). This can be attributed to the concave shape of the necking region that acts like a reservoir, holding extra polymer solution during the coating process. Importantly, the PEtOx layer on the surface of the porous iron scaffolds only marginally reduced the total porosity and preserved the high pore interconnectivity of the scaffolds (Table 4.1).

The PEtOx-OH polymer has several functional groups, including ethyl -CH₂-CH₃, carbonyl C=O (tertiary amide) and a terminal hydroxyl group (OH) (Figure 4.1). The small thickness of the coating meant that the overall intensities of the functional groups were decreased when measured on porous specimens. The valleys in the FTIR graph were, nevertheless, clearly visible, save for the diminished hydroxyl group, confirming the presence of the polymer on the iron surfaces (Figure 4.2h). The flattened hydroxyl valleys in the FTIR graph of the coated scaffold suggested that this moiety participated in the polymer interaction with the iron surface. Besides that, a slight shift and decreased signal of the C=O amide stretch band also implied that these amide groups took part in the interfacial bonding of the polymer to the iron surface [51]. From the FTIR peaks, some of the C=O amide and other functional groups (*e.g.*, -CH₂-CH₃) were present on the PEtOx-coated iron scaffold surface. It is believed that these groups are responsible for the properties of the coating material. For example, the C=O

functional group is known for its hydrophilic behavior while the ethyl $-\text{CH}_2-\text{CH}_3$ functional group behaves more hydrophobically.

4.4.2 Biodegradation behavior

In general, scaffolds with a higher porosity (or larger surface area) are expected to degrade faster. That said, the surface of an implanted porous iron-based biomaterial will most likely be covered by the degradation products, passivating the material to some degree. Altering the surface chemistry of iron could be an effective approach to minimizing the adhesion of the corrosion products and facilitating continued biodegradation. Surface modification involving polymers has been reported in several studies and positive effects on the biodegradation behavior of iron-based biomaterials have been demonstrated [13,14].

The *in vitro* biodegradability of the PEOx-coated iron (*i.e.*, 0.13 mm/y at day 28) was found to be similar to that of cross-rolled pure iron [52], but higher than SLM porous iron with 59% porosity [53]. The PEOx coating increased the *in vitro* biodegradation rate by 2.6 times relative to the non-coated scaffolds. The improvement is comparable to that of other porous irons with polymer coatings [22,23]. For example, porous iron coated with PLGA has been reported to exhibit a biodegradation rate (day 28) that is 2.3 times higher than that of bare porous iron [22]. In addition, the biodegradation rate of a porous iron foam with a 5-15 wt% PEG coating has been found to be 1.4-2.3 times higher than that of a corresponding bare iron foam (day 28) [23].

As a result of biodegradation, iron ions were released, which then interacted with the other ionic compounds present in the r-SBF medium and participated in the formation of the biodegradation products. The macro-scale morphology of the biodegradation products of the PEOx-coated iron (Figure 4.4c) appeared to be similar to that of the dense products observed on the surface of the non-coated iron. At the micro-scale, however, the morphology of the degradation products formed on the surface of the PEOx-coated iron scaffolds was clearly porous (Figure 4.4g-i), which is distinctly different from the products formed on the surface of the non-coated iron (as reported in our previous publication [12]). Such a porous morphology is believed to influence the biodegradation rate. From day 14 to 28, the *in vitro* biodegradation rate of the PEOx-coated iron reduced only by 17%. During the same period, the biodegradability of the non-coated specimens decreased by 43%.

In addition to controlling the scaffold degradation rate, the PEOx coating altered the chemistry of the iron-based biodegradation products too. The main phase of the PEOx-coated iron biodegradation products was lepidocrocite. Such a phase has been observed on the biodegraded functionally graded porous iron

[53] as well, resulting from the chemical reactions described in [54]. Interestingly, no iron phosphate or iron oxide products were formed on the coated scaffolds, unlike the biodegradation products on the non-coated specimens (as reported elsewhere [12]). The Fe-based degradation products containing phosphate have been reported to prevent corrosion from occurring further [55]. In addition, based on the EDS analysis, the biodegradation products of the PEtOx-coated iron at 14 and 28 days of *in vitro* immersion in r-SBF contained a larger variety of elements than those present on the non-coated iron (as reported elsewhere [12]). The absence of phosphate-based degradation products and the enriched elements in the chemical compositions of the biodegradation products are likely the reasons for the reduced passivation of the PEtOx-coated iron. Moreover, Ca and P precipitates were present at all time points (Figure 4.4), which was not the case for the non-coated specimens. The precipitation of Ca/P elements correlated with the decreases in the concentrations of Ca^{2+} and PO_4^{3-} in the r-SBF (Figure 4.3e-f). While Ca ions may be present both in Ca/P precipitates and in other compounds (*e.g.*, calcium carbonates), we may still assume that all Ca is used for the formation of the Ca/P precipitates. This simplifying assumption allows us to determine the Ca/P ratio. On day 7, the Ca/P ratio varied between 0.58 and 2.24. On days 14 and 28, the range of the determined Ca/P ratios narrowed to 0.26-0.40 and 0.32-0.53, respectively. Although the Ca/P ratios found do not correspond to the stoichiometry of hydroxyapatite (*i.e.*, $\text{Ca/P} = 1.67$), low Ca/P ratios (*e.g.*, 0.5) are reported to be beneficial for osteoblast viability, collagen synthesis, and alkaline phosphatase activity [56].

The biodegradation of polymers is known to create an acidic environment. For example, 7-day biodegradation of iron coated with PLGA resulted in a reduced pH value of 6.87 [22]. However, such a phenomenon was not observed in our study. The stable pH values around 7.70 during the biodegradation tests were in line with the expected stability of the polymer. From these, we can infer that the hydrolysis of the PEtOx polymer did not occur at all or at least to an extent that would affect the local and bulk pH. PAOx have been reported to be non-biodegradable [32] and to exhibit high stability in water [57], while being susceptible to oxidative degradation in the presence of hydrogen peroxide and transition metal ions that act as catalysts [58]. To the best of our knowledge, however, the degradation of PEtOx due to the presence of iron ions in a physiologically relevant environment has not been reported before. It is only known that the degradation of PEtOx is much slower in a $\text{Fe}/\text{H}_2\text{O}_2$ environment than in a $\text{Cu}/\text{H}_2\text{O}_2$ environment [59]. Interestingly, the chemical characteristics of PEtOx (*i.e.*, the N element present in the PEtOx backbone) could still be detected at several spots beneath the peripheral biodegradation products on the

PEtOx-coated iron scaffolds after 28 days of biodegradation (Figure 4.5). This finding is consistent with the observation that the pH remained relatively stable throughout the immersion period. In addition, we examined the surface characteristics and chemical composition of the PEtOx thin film after 7 days of immersion in the r-SBF medium (Figure S4.4, Table S4.1). After exposure, the wt% value of the N element in the film was similar to the value prior to immersion. It confirmed the non-biodegradability of the polymer and indicated that the PEtOx polymer did not elute to the r-SBF medium. Moreover, the surface of the polymer film contained the Na, Cl, and K elements after immersion, clearly showing that diffusion of ionic compounds occurred in the polymer matrix. The absence of Ca/P-based compounds implied that the precipitation only occurred due to the biodegradation of iron. However, no clear interface between PEtOx and iron was observed on the cross section, likely because the thin polymer layer is not strong enough to survive the cutting and polishing processes of the biodegraded specimens. Even if the coating loses its integrity during the biodegradation process, its remnants may still assist the biodegradation of iron.

The electrochemical measurements of the PEtOx-coated iron demonstrated a relatively stable OCP trend over the 28 days of immersion (Figure 4.6a), which was in contrast to the OCP trend of the non-coated iron. Over the immersion period, the R_p values obtained from LPR measurements of the PEtOx-coated iron scaffolds marginally increased but remained much lower than those of the non-coated pure iron (Figure 4.6b). These electrochemical characteristics indicate that the stable PEtOx coating allows the corrosion of the porous iron to proceed further. Unlike other types of coatings, *e.g.*, those made of bioceramics [15–17], the effect of the PEtOx coating on the porous morphology of the biodegradation products (Figure 4.4g-i) led to the reduced R_p values, thus enabling the sustained biodegradability of iron over time. The Nyquist plots of the coated iron specimens exhibited a single semicircle initially and then an extra time constant arc pattern at later times of exposure (Figure 4.6c-e). As comparison, the Bode and Nyquist impedance of the non-coated iron specimens have been reported elsewhere [12]. Initially, the Nyquist semicircle arc of the PEtOx-coated iron (at day 2) had a much larger diameter than that of the non-coated iron. The larger Nyquist arc diameter indicates a higher polarization resistance value, which can be due to the presence of the PEtOx coating. This evidence is supported by the higher R_p value of the PEtOx-coated iron scaffolds during the first 2 days of immersion (Figure 4.6a-b). The occurrence of an extra time constant in the Nyquist plot indicates active and diffusive biodegradation mechanisms occurring simultaneously with time [60]. The Nyquist impedance in the low frequency region (at 0.2 to 0.05 Hz) demonstrated a Warburg diffusion characteristics [61,62], indicated by the angle of the extrapolation line very close to 45° at all time points (Figure 4.6c-e). The

Warburg characteristic strongly suggests the biodegradation mechanism of the PEOx-coated iron occurred by ion diffusion through the coating layer [62]. At the later time points, the Warburg effect was maintained due to the porous morphology of the biodegradation products of the coated scaffolds. Moreover, The Nyquist arcs of the PEOx-coated iron scaffolds (from day 7 to day 28) had a similar diameter to the Nyquist arc of the non-coated iron on day 14, but were much smaller than the Nyquist arc of the non-coated iron on day 28. The Bode impedance modulus values of the PEOx-coated iron scaffolds at 0.01 Hz displayed a similar trend to that of the R_p values, which were much lower, as compared to the values reported for the non-coated iron after 28 days of immersion. Altogether, the SEM and EDS analyses of the degradation products, the longevity of the coating layer, and the electrochemical responses indicate that the PEOx coating promoted the biodegradation of iron largely *via* a diffusion mechanism through the polymer layer. The morphology and chemistry of the iron-based biodegradation products were altered due to the coating, thus inhibiting the biodegradation process to a lesser extent than the corresponding bare specimens. The exact mechanism operating during immersion in r-SBF still needs to be studied.

4.4.3 Mechanical properties

The strength and stiffness of biodegradable implants tend to reduce as the biodegradation progresses. The PEOx-coated iron possessed bone-mimicking mechanical properties that fall into the range of the mechanical properties of cancellous bone ($E = 0.02\text{--}2.0$ GPa and $\sigma_y = 0.1\text{--}30$ MPa [47]). These properties were maintained even after 28 days of *in vitro* biodegradation (Figure 4.7). The PEOx coating layer did not significantly influence the yield strength and elastic modulus of the as-sintered specimens (Figure 4.7b). During mechanical testing, the mechanical load was transferred across the iron scaffold as well as the interface between the iron and PEOx coating layer. The PEOx polymer itself and the modified geometrical parameter (*i.e.*, the increased strut thickness and decreased porosity, Table 4.1) did not have any remarkable strengthening effect, which was ascribed to the small thickness of the coating layer and the amorphous and brittle nature of PEOx [46].

As the biodegradation process progressed, the solid fraction of the scaffolds decreased, reducing the overall mechanical properties of the scaffolds. By day 28, the yield strength and elastic modulus of the PEOx-coated iron scaffolds had decreased by 13.8% and 11.3%, respectively (Figure 4.7b-c). In comparison, the mechanical integrity of biodegraded iron foams coated with PEG is reported to have been deteriorated after 6 weeks of *in vitro* biodegradation, although the biodegradation rate (*i.e.*, 0.04 to 0.06 mm/y) was lower than that of our PEOx-

coated iron scaffolds [63]. In the current study, however, the PEOx-coated iron scaffolds maintained their structural integrity and a ductility > 30% even after 28 days of *in vitro* biodegradation, suggesting that the coating did not adversely affect the biodegradation mechanism (*e.g.*, no severe localized corrosion attack). Such a ductile behavior is expected to improve the resistance of the specimens against fatigue failure [64].

4.4.4 Cytocompatibility

The cytocompatibility of biodegradable metals strongly depends on the concentrations of the released metallic ions and the precipitated biodegradation products. The preosteoblasts cultured in the PEOx-coated iron extracts (prepared from 72 h incubation) exhibited a very low metabolic activity (Figure 4.8a). It has been reported that 53.2 to 88.5 mg/L of iron ion concentrations inhibit the preosteoblasts growth by 50% [65]. The iron ion concentration of the 100% PEOx-coated iron extract was much higher than these values. The cytocompatibility level was, therefore, rank 4 (the lowest according to ISO 10993-5 [66]). A high iron ion concentration induces the formation of more reactive oxygen species, which causes oxidative stress on cells and tissue [67]. When the extracts were diluted to 50% or a lower concentration, the preosteoblasts became metabolically active (80% or higher), indicating a very mild cytotoxic response (rank 1) [66].

In the direct cell culture assays, the PEOx coating significantly enhanced the viability and growth of the cells, as revealed by the live/dead assay, SEM imaging of cell morphology and the cell counts at various culture times (Figure 4.8b-j). These findings indicate that the coating supported the early response of preosteoblast cells with possible positive effects on the late cellular functions. When a polymer-coated iron scaffold is introduced to a protein-containing medium, the adsorption of proteins on the scaffold surface may occur, as observed in the case of PEI-coated iron in an albumin-containing medium [68]. Protein adsorption on surfaces creates a conditioned provisional layer favorable for cell attachment and has been reported to stimulate osteoblast adhesion [69,70]. At the same time, the released iron ions may interact with the proteins in the medium [71,72], preventing the precipitation of iron-based degradation products and thereby maintaining a supportive interface for both cell response and biodegradation rate. Our short-term cytocompatibility results are similar to those available in the literature on polymer-coated iron scaffolds, including preosteoblasts MC3T3-E1 cultured on PLA-coated iron [19], human skin fibroblasts cultured on PLGA-coated iron [22], human dermal fibroblasts cultured on PEG-coated iron [73], and bone marrow stromal cells cultured on collagen-coated Fe₃O₄ [74]. To the best knowledge of the authors, *in vivo* study

on the PEtOx polymer intended specifically for bone tissue regeneration has not yet been reported. Various POx-based polymers have however been studied *in vivo* with promising results [30], *e.g.*, for intraocular [75] or macromolecular antioxidant therapy [76] applications. The *in vitro* biological experiments performed in this research should be first extended further to assess the osteogenic potential of the coated scaffolds by investigating cell differentiation, extracellular matrix formation and mineralization, followed by additional assays to better understand the long-term performance of the developed biomaterials and then *in vivo* studies. Moreover, the addition of bioactive elements to iron-based biomaterials [77–79] is another suggested avenue for further research. Such additions could yield further improvements in the long-term biocompatibility of such biomaterials and may be used with or without biofunctional coatings.

4.5 Conclusion

We developed extrusion-based 3D printed porous iron scaffolds biofunctionalized with PEtOx polymer coatings and demonstrated their superior performance including an enhanced rate of biodegradation, bone-mimicking mechanical properties, and significantly enhanced cell viability. These properties underscore the potential of the developed biomaterials for application as bone substitutes. In summary, the PEtOx coating promoted the biodegradation of iron largely *via* a diffusion mechanism through the polymer layer. The coating also altered the morphology and chemistry of the iron-based biodegradation products, *i.e.*, making them porous, and prevented phosphate-based products from forming. The *in vitro* biodegradation rate of the PEtOx-coated iron scaffolds increased by 2.6 times, as compared to their non-coated counterparts, while improving cell viability and growth simultaneously. In addition, the PEtOx-coated iron maintained its bone-mimicking mechanical properties throughout the 28 days of the *in vitro* biodegradation experiments. Additional (*in vivo*) experiments are required for further evaluation of the developed biomaterials prior to clinical adoption.

4.6 Supplementary material

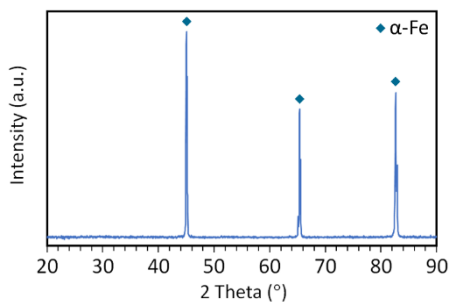


Figure S4.1. XRD pattern of the PEtOx-coated iron scaffolds.

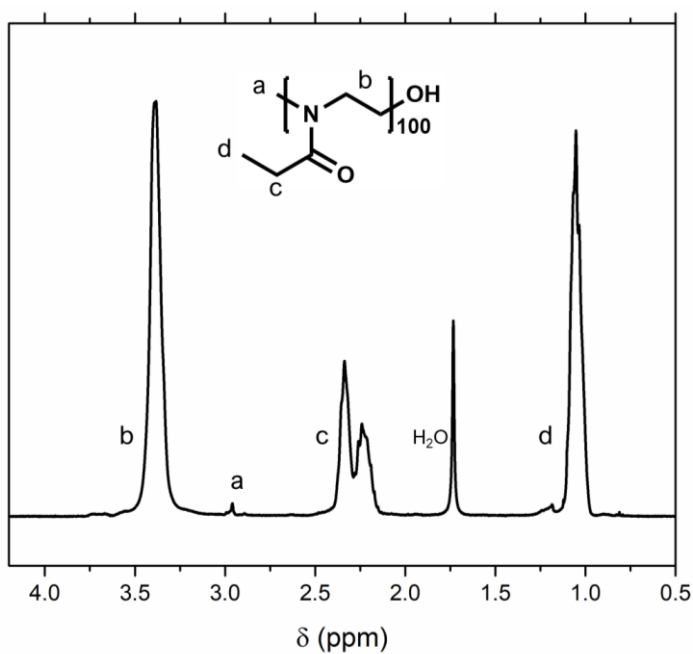


Figure S4.2. ¹H-NMR graph of CH₃-PEtOx100-OH in CDCl₃.

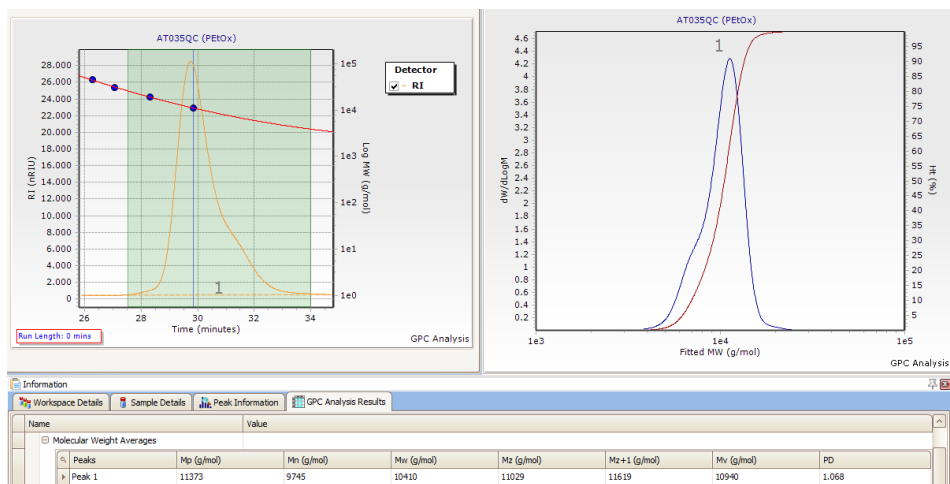


Figure S4.3. Size exclusion chromatogram (SEC, left) and the molar mass distribution calculated against poly(2-ethyl-2-oxazoline) standards: $M_w = 10,410$; $M_n = 9,745$; $\bar{D} = 1.068$ (right).

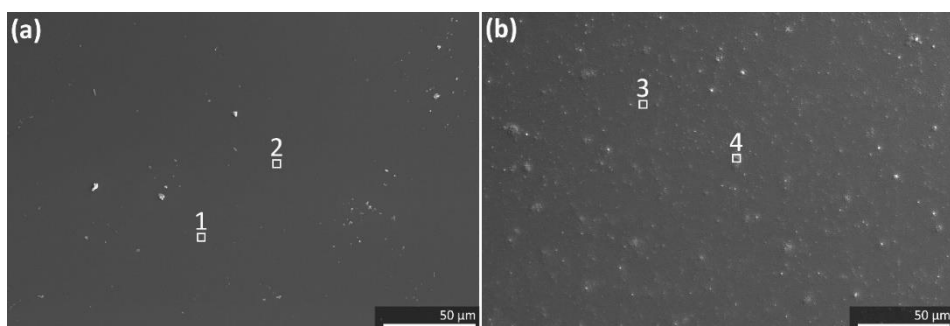


Figure S4.4. Surface morphologies of the PETox thin film (a) before and (b) after exposure to r-SBF for 7 days. The square mark with number indicates the location of EDS analysis, whose results are reported in Table S1.

Table S4.1. Chemical compositions of the PETox thin film after exposure to r-SBF for 7 days, determined by EDS analysis.

EDS point	C	N	O	Na	Cl	K
1	63.93	3.53	32.53	-	-	-
2	65.09	3.67	31.24			
3	58.40	3.66	24.03	6.08	1.25	6.58
4	59.23	3.87	22.46	6.18	1.51	6.75

Bibliography

- [1] R. Gorejová, L. Haverová, R. Oriňáková, A. Oriňák, M. Oriňák, Recent advancements in Fe-based biodegradable materials for bone repair, *J. Mater. Sci.* 54 (2019) 1913–1947. <https://doi.org/10.1007/s10853-018-3011-z>.
- [2] J. He, F.L. He, D.W. Li, Y.L. Liu, Y.Y. Liu, Y.J. Ye, D.C. Yin, Advances in Fe-based biodegradable metallic materials, *RSC Adv.* 6 (2016) 112819–112838. <https://doi.org/10.1039/C6RA20594A>.
- [3] T. Kraus, F. Moszner, S. Fischerauer, M. Fiedler, E. Martinelli, J. Eichler, F. Witte, E. Willbold, M. Schinhammer, M. Meischel, P.J. Uggowitzer, J.F. Löffler, A. Weinberg, Biodegradable Fe-based alloys for use in osteosynthesis: Outcome of an *in vivo* study after 52 weeks, *Acta Biomater.* 10 (2014) 3346–3353. <https://doi.org/10.1016/j.actbio.2014.04.007>.
- [4] E. Zhang, H. Chen, F. Shen, Biocorrosion properties and blood and cell compatibility of pure iron as a biodegradable biomaterial, *J. Mater. Sci. Mater. Med.* 21 (2010) 2151–2163. <https://doi.org/10.1007/s10856-010-4070-0>.
- [5] D. Xia, F. Yang, Y. Zheng, Y. Liu, Y. Zhou, Research status of biodegradable metals designed for oral and maxillofacial applications: A review, *Bioact. Mater.* 6 (2021) 4186–4208. <https://doi.org/10.1016/j.bioactmat.2021.01.011>.
- [6] Y.F. Zheng, X.N. Gu, F. Witte, Biodegradable metals, *Mater. Sci. Eng. R Reports.* 77 (2014) 1–34. <https://doi.org/10.1016/j.mser.2014.01.001>.
- [7] M. Schinhammer, A.C. Hänzli, J.F. Löffler, P.J. Uggowitzer, Design strategy for biodegradable Fe-based alloys for medical applications, *Acta Biomater.* 6 (2010) 1705–1713. <https://doi.org/10.1016/j.actbio.2009.07.039>.
- [8] K. Munir, A. Biesiekierski, C. Wen, Y. Li, Biodegradable alloys, in *Structural Biomaterials - Properties, Characteristics and Selection*, Woodhead Publishing Series in Biomaterials (2021) 189–228. <https://doi.org/10.1016/b978-0-12-818831-6.00001-x>.
- [9] Y. Li, H. Jahr, K. Lietaert, P. Pavanram, A. Yilmaz, L.I. Fockaert, M.A. Leeftang, B. Pouran, Y. Gonzalez-Garcia, H. Weinans, J.M.C. Mol, J. Zhou, A.A. Zadpoor, Additively manufactured biodegradable porous iron, *Acta Biomater.* 77 (2018) 380–393. <https://doi.org/10.1016/j.actbio.2018.07.011>.
- [10] D. Carluccio, C. Xu, J. Venezuela, Y. Cao, D. Kent, M. Bermingham, A.G. Demir, B. Previtali, Q. Ye, M. Dargusch, Additively manufactured iron-manganese for biodegradable porous load-bearing bone scaffold applications, *Acta Biomater.* 103 (2020) 346–360. <https://doi.org/10.1016/j.actbio.2019.12.018>.
- [11] C. Shuai, W. Yang, Y. Yang, H. Pan, C. He, F. Qi, D. Xie, H. Liang, Selective laser melted Fe-Mn bone scaffold: Microstructure, corrosion behavior and cell response, *Mater. Res. Express.* 7 (2019) 015404. <https://doi.org/10.1088/2053-1591/ab62f5>.
- [12] N.E. Putra, M.A. Leeftang, M. Minneboo, P. Taheri, L.E. Fratila-Apachitei, J.M.C. Mol, J. Zhou, A.A. Zadpoor, Extrusion-based 3D printed biodegradable porous iron, *Acta Biomater.* 121 (2021) 741–756. <https://doi.org/10.1016/j.actbio.2020.11.022>.
- [13] R. Oriňáková, R. Gorejová, Z. Orságová Králová, A. Oriňák, Surface modifications of biodegradable metallic foams for medical applications, *Coatings.* 10 (2020) 819. <https://doi.org/10.3390/coatings10090819>.
- [14] A.H. Yusop, A. Al Sakka, H. Nur, Modifications on porous absorbable Fe-based scaffolds for bone applications : A review from corrosion and biocompatibility viewpoints, *J. Biomed. Mater. Res. Part B Appl. Biomater.* (2021) 1–27. <https://doi.org/10.1002/jbm.b.34893>.
- [15] H. Chen, E. Zhang, K. Yang, Microstructure, corrosion properties and bio-compatibility of calcium zinc phosphate coating on pure iron for biomedical application, *Mater. Sci. Eng. C.* 34 (2014) 201–206. <https://doi.org/10.1016/j.msec.2013.09.010>.
- [16] N. Mohd Daud, N.B. Sing, A.H. Yusop, F.A. Abdul Majid, H. Hermawan, Degradation and invitro cell-material interaction studies on hydroxyapatite-coated biodegradable porous iron for hard tissue scaffolds, *J. Orthop. Transl.* 2 (2014) 177–184. <https://doi.org/10.1016/j.jot.2014.07.001>.

- [17] A. Adhilakshmi, K. Ravichandran, T.S.N. Sankara Narayanan, Protecting electrochemical degradation of pure iron using zinc phosphate coating for biodegradable implant applications, *New J. Chem.* 42 (2018) 18458–18468. <https://doi.org/10.1039/c8nj02986e>.
- [18] Y. Su, S. Champagne, A. Trenggono, R. Tolouei, D. Mantovani, H. Hermawan, Development and characterization of silver containing calcium phosphate coatings on pure iron foam intended for bone scaffold applications, *Mater. Des.* 148 (2018) 124–134. <https://doi.org/10.1016/j.matdes.2018.03.061>.
- [19] M. Hrubovčáková, M. Kupková, M. Džupon, M. Giretová, L. Medvecký, R. Džunda, Biodegradable polylactic acid and polylactic acid/hydroxyapatite coated iron foams for bone replacement materials, *Int. J. Electrochem. Sci.* 12 (2017) 11122–11136. <https://doi.org/10.20964/2017.12.53>.
- [20] Y. Qi, H. Qi, Y. He, W. Lin, P. Li, L. Qin, Y. Hu, L. Chen, Q. Liu, H. Sun, Q. Liu, G. Zhang, S. Cui, J. Hu, L. Yu, D. Zhang, J. Ding, Strategy of metal-polymer composite stent to accelerate biodegradation of iron-based biomaterials, *ACS Appl. Mater. Interfaces.* 10 (2018) 182–192. <https://doi.org/10.1021/acsami.7b15206>.
- [21] X. Li, W. Zhang, W. Lin, H. Qiu, Y. Qi, X. Ma, H. Qi, Y. He, H. Zhang, J. Qian, G. Zhang, R. Gao, D. Zhang, J. Ding, Long-term efficacy of biodegradable metal-polymer composite stents after the first and the second implantations into porcine coronary arteries, *ACS Appl. Mater. Interfaces.* 12 (2020) 15703–15715. <https://doi.org/10.1021/acsami.0c00971>.
- [22] A.H.M. Yusop, N.M. Daud, H. Nur, M.R.A. Kadir, H. Hermawan, Controlling the degradation kinetics of porous iron by poly(lactic-co-glycolic acid) infiltration for use as temporary medical implants, *Sci. Rep.* 5 (2015) 1–17. <https://doi.org/10.1038/srep11194>.
- [23] L. Haverová, R. Oriňáková, A. Oriňák, R. Gorejová, M. Baláž, P. Vanýsek, M. Kupková, M. Hrubovčáková, P. Mudroň, J. Radoňák, Z.O. Králová, A.M. Turoňová, An *in vitro* corrosion study of open cell iron structures with PEG coating for bone replacement applications, *Metals (Basel).* 8 (2018) 1–21. <https://doi.org/10.3390/met8070499>.
- [24] R. Gorejová, R. Oriňáková, Z. Orságová Králová, M. Baláž, M. Kupková, M. Hrubovčáková, L. Haverová, M. Džupon, A. Oriňák, F. Kaľavský, K. Koval', *In vitro* corrosion behavior of biodegradable iron foams with polymeric coating, *Materials (Basel).* 13 (2020) 1–17. <https://doi.org/10.3390/ma13010184>.
- [25] J.Z. Wang, M.L. You, Z.Q. Ding, W. Bin Ye, A review of emerging bone tissue engineering via PEG conjugated biodegradable amphiphilic copolymers, *Mater. Sci. Eng. C.* 97 (2019) 1021–1035. <https://doi.org/10.1016/j.msec.2019.01.057>.
- [26] S. Jin, X. Xia, J. Huang, C. Yuan, Y. Zuo, Y. Li, J. Li, Recent advances in PLGA-based biomaterials for bone tissue regeneration, *Acta Biomater.* 127 (2021) 56–79. <https://doi.org/10.1016/j.actbio.2021.03.067>.
- [27] R. Baptista, M. Guedes, Morphological and mechanical characterization of 3D printed PLA scaffolds with controlled porosity for trabecular bone tissue replacement, *Mater. Sci. Eng. C.* 118 (2021) 111528. <https://doi.org/10.1016/j.msec.2020.111528>.
- [28] C.W. McGary Jr, Degradation of poly(ethylene oxide), *J. Polym. Sci.* 46 (1960) 51–57.
- [29] V.R. De La Rosa, Poly(2-oxazoline)s as materials for biomedical applications, *J. Mater. Sci. Mater. Med.* 25 (2014) 1211–1225. <https://doi.org/10.1007/s10856-013-5034-y>.
- [30] T. Lorson, M.M. Lübtow, E. Wegener, M.S. Haider, S. Borova, D. Nahm, R. Jordan, M. Sokolski-Papkov, A. V. Kabanov, R. Luxenhofer, Poly(2-oxazoline)s based biomaterials: A comprehensive and critical update, *Biomaterials.* 178 (2018) 204–280. <https://doi.org/10.1016/j.biomaterials.2018.05.022>.
- [31] H.P.C. Van Kuringen, J. Lenoir, E. Adriaens, J. Bender, B.G. De Geest, R. Hoogenboom, Partial hydrolysis of Poly(2-ethyl-2-oxazoline) and potential implications for biomedical applications?, *Macromol. Biosci.* 12 (2012) 1114–1123. <https://doi.org/10.1002/mabi.201200080>.
- [32] B. Pidhatika, M. Rodenstein, Y. Chen, E. Rakhmatullina, A. Mühlebach, C. Acikgöz, M. Textor, R. Konradi, Comparative stability studies of Poly(2-methyl-2-oxazoline) and Poly(ethylene glycol) brush coatings, *Biointerphases.* 7 (2012) 1–4. <https://doi.org/10.1007/s13758-011-0001-y>.
- [33] T.R. Dargaville, B.G. Hollier, A. Shokoohmand, R. Hoogenboom, Poly(2-oxazoline)

- hydrogels as next generation three-dimensional cell supports, *Cell Adhes. Migr.* 8 (2014) 88–93. <https://doi.org/10.4161/cam.28205>.
- [34] O. Sedlacek, R. Hoogenboom, Drug delivery systems based on poly(2-oxazoline)s and poly(2-oxazine)s, *Adv. Ther.* 3 (2020) 1900168. <https://doi.org/10.1002/adtp.201900168>.
- [35] Y. You, K. Kobayashi, B. Colak, P. Luo, E. Cozens, L. Fields, K. Suzuki, J. Gautrot, Engineered cell-degradable poly(2-alkyl-2-oxazoline) hydrogel for epicardial placement of mesenchymal stem cells for myocardial repair, *Biomaterials*. 269 (2021) 120356. <https://doi.org/10.1016/j.biomaterials.2020.120356>.
- [36] V.R. De La Rosa, S. Tempelaar, P. Dubois, R. Hoogenboom, L. Mespouille, Poly(2-ethyl-2-oxazoline)-block-polycarbonate block copolymers: From improved end-group control in poly(2-oxazoline)s to chain extension with aliphatic polycarbonate through a fully metal-free ring-opening polymerisation process, *Polym. Chem.* 7 (2016) 1559–1568. <https://doi.org/10.1039/c5py01913c>.
- [37] ASTM B963-17, Standard test methods for oil content, oil-impregnation efficiency, and surface-connected porosity of sintered powder metallurgy (PM) products using Archimedes' principle, ASTM International, 2017. <https://doi.org/10.1520/B0963-14>.
- [38] A. Oyane, H.M. Kim, T. Furuya, T. Kokubo, T. Miyazaki, T. Nakamura, Preparation and assessment of revised simulated body fluids, *J. Biomed. Mater. Res. - Part A*. 65 (2003) 188–195. <https://doi.org/10.1002/jbm.a.10482>.
- [39] L. Yang, E. Zhang, Biocorrosion behavior of magnesium alloy in different simulated fluids for biomedical application, *Mater. Sci. Eng. C*. 29 (2009) 1691–1696. <https://doi.org/10.1016/j.msec.2009.01.014>.
- [40] ASTM G1-03, Standard practice for preparing, cleaning, and evaluating corrosion test specimens, ASTM International, (2017). <https://doi.org/10.1520/G0001-03R17E01.2>.
- [41] ASTM G31-72, Standard practice for laboratory immersion corrosion testing for metals, ASTM International, 2004. <https://doi.org/10.1520/G0031-72R04>.
- [42] ISO 13314, Mechanical testing of metals - Ductility testing - Compression test for porous and cellular metals, International Organization for Standardization, 2011. <https://doi.org/ISO 13314:2011>.
- [43] ISO 10993-12, Sample preparation and reference materials, International Organization for Standardization, 2012. [https://doi.org/10.1016/S0080-8784\(08\)60069-1](https://doi.org/10.1016/S0080-8784(08)60069-1).
- [44] A. Colombo, F. Gherardi, S. Goidanich, J.K. Delaney, E.R. De La Rie, M.C. Ubaldi, L. Toniolo, R. Simonutti, Highly transparent poly(2-ethyl-2-oxazoline)-TiO₂ nanocomposite coatings for the conservation of matte painted artworks, *RSC Adv.* 5 (2015) 84879–84888. <https://doi.org/10.1039/c5ra10895k>.
- [45] E.D.H. Mansfield, K. Sillence, P. Hole, A.C. Williams, V. V. Khutoryanskiy, POZylation: a new approach to enhance nanoparticle diffusion through mucosal barriers, *Nanoscale*. 7 (2015) 13671–13679. <https://doi.org/10.1039/c5nr03178h>.
- [46] G.K. Abilova, D.B. Kaldybekov, E.K. Ozhmukhametova, A.Z. Saimova, D.S. Kazybayeva, G.S. Irmukhametova, V. V. Khutoryanskiy, Chitosan/poly(2-ethyl-2-oxazoline) films for ocular drug delivery: Formulation, miscibility, *in vitro* and *in vivo* studies, *Eur. Polym. J.* 116 (2019) 311–320. <https://doi.org/10.1016/j.eurpolymj.2019.04.016>.
- [47] E.F. Morgan, G.U. Unnikrisnan, A.I. Hussein, Bone mechanical properties in healthy and diseased states, *Annu. Rev. Biomed. Eng.* 20 (2018) 119–43. <https://doi.org/10.1146/annurev-bioeng-062117-121139>.
- [48] K. Gulati, S. Ramakrishnan, M.S. Aw, G.J. Atkins, D.M. Findlay, D. Losic, Biocompatible polymer coating of titania nanotube arrays for improved drug elution and osteoblast adhesion, *Acta Biomater.* 8 (2012) 449–456. <https://doi.org/10.1016/j.actbio.2011.09.004>.
- [49] I.A. Neacșu, A.I. Nicoară, O.R. Vasile, B.Ș. Vasile, Inorganic micro- and nanostructured implants for tissue engineering, *Nanobiomaterials Hard Tissue Eng. Appl. Nanobiomaterials*. (2016) 271–295. <https://doi.org/10.1016/B978-0-323-42862-0.00009-2>.
- [50] S. Julmi, A.K. Krüger, A.C. Waselau, A. Meyer-Lindenberg, P. Wriggers, C. Klose, H.J. Maier, Processing and coating of open-pored absorbable magnesium-based bone implants, *Mater. Sci. Eng. C*. 98 (2019) 1073–1086. <https://doi.org/10.1016/j.msec.2018.12.125>.

- [51] P. Taheri, J. Wielant, T. Hauffman, J.R. Flores, F. Hannour, J.H.W. De Wit, J.M.C. Mol, H. Terryn, A comparison of the interfacial bonding properties of carboxylic acid functional groups on zinc and iron substrates, *Electrochim. Acta.* 56 (2011) 1904–1911. <https://doi.org/10.1016/j.electacta.2010.10.079>.
- [52] C.S. Obayi, R. Tolouei, C. Paternoster, S. Turgeon, B.A. Okorie, D.O. Obikwelu, G. Cassar, J. Buhagiar, D. Mantovani, Influence of cross-rolling on the micro-texture and biodegradation of pure iron as biodegradable material for medical implants, *Acta Biomater.* 17 (2015) 68–77. <https://doi.org/10.1016/j.actbio.2015.01.024>.
- [53] Y. Li, H. Jahr, P. Pavanram, F.S.L. Bobbert, U. Puggi, X.Y. Zhang, B. Pouran, M.A. Leeftang, H. Weinans, J. Zhou, A.A. Zadpoor, Additively manufactured functionally graded biodegradable porous iron, *Acta Biomater.* 96 (2019) 646–661. <https://doi.org/10.1016/j.actbio.2019.07.013>.
- [54] N.E. Putra, M.A. Leeftang, P. Taheri, L.E. Fratila-Apachitei, J.M.C. Mol, J. Zhou, A.A. Zadpoor, Extrusion-based 3D printing of *ex situ*-alloyed highly biodegradable MRI-friendly porous iron-manganese scaffolds, *Acta Biomater.* 134 (2021) 774–790. <https://doi.org/10.1016/j.actbio.2021.07.042>.
- [55] A. Drynda, T. Hassel, F.W. Bach, M. Peuster, *In vitro* and *in vivo* corrosion properties of new iron-manganese alloys designed for cardiovascular applications, *J. Biomed. Mater. Res. - Part B Appl. Biomater.* 103 (2015) 649–660. <https://doi.org/10.1002/jbm.b.33234>.
- [56] H. Liu, H. Yazici, C. Ergun, T.J. Webster, H. Bermek, An *in vitro* evaluation of the Ca / P ratio for the cytocompatibility of nano-to-micron particulate calcium phosphates for bone regeneration, *Acta Biomater.* 4 (2008) 1472–1479. <https://doi.org/10.1016/j.actbio.2008.02.025>.
- [57] T.X. Viegas, M.D. Bentley, J.M. Harris, Z. Fang, K. Yoon, B. Dizman, R. Weimer, A. Mero, G. Pasut, F.M. Veronese, Polyoxazoline: Chemistry, properties, and applications in drug delivery, *Bioconjug. Chem.* 22 (2011) 976–986. <https://doi.org/10.1021/bc200049d>.
- [58] J. Ulbricht, R. Jordan, R. Luxenhofer, On the biodegradability of polyethylene glycol, polypeptides and poly(2-oxazoline)s, *Biomaterials.* 35 (2014) 4848–4861. <https://doi.org/10.1016/j.biomaterials.2014.02.029>.
- [59] J. Ulbricht, Insights into polymer biodegradation: Investigations on oxidative, hydrolytic and enzymatic pathways, Doctoral Thesis, Universität Würzburg, 2018.
- [60] D. You, N. Pebere, F. Dabosi, An investigation of the corrosion of pure iron by electrochemical techniques and in situ observations, *Corros. Sci.* 34 (1993) 5–15. [https://doi.org/10.1016/0010-938X\(93\)90254-E](https://doi.org/10.1016/0010-938X(93)90254-E).
- [61] T. Chen, H. Huang, H. Ma, D. Kong, Effects of surface morphology of nanostructured PbO₂ thin films on their electrochemical properties, *Electrochim. Acta.* 88 (2013) 79–85. <https://doi.org/10.1016/j.electacta.2012.10.009>.
- [62] S. Skale, V. Doleček, M. Slemnik, Electrochemical impedance studies of corrosion protected surfaces covered by epoxy polyamide coating systems, *Prog. Org. Coatings.* 62 (2008) 387–392. <https://doi.org/10.1016/j.porgcoat.2008.02.003>.
- [63] R. Oriňáková, R. Gorejová, Z. Orságová Kráľová, L. Haverová, A. Oriňák, I. Maskal'ová, M. Kupková, M. Džupon, M. Baláž, M. Hrubovčáková, T. Sopčák, A. Zubrik, M. Oriňák, Evaluation of mechanical properties and hemocompatibility of open cell iron foams with polyethylene glycol coating, *Appl. Surf. Sci.* 505 (2020) 144634. <https://doi.org/10.1016/j.apsusc.2019.144634>.
- [64] A. Sharma, M.C. Oh, B. Ahn, Recent advances in very high cycle fatigue behavior of metals and alloys—a review, *Metals (Basel).* 10 (2020) 1–23. <https://doi.org/10.3390/met10091200>.
- [65] A. Yamamoto, R. Honma, M. Sumita, Cytotoxicity evaluation of 43 metal salts using murine fibroblasts and osteoblastic cells, *J. Biomed. Mater. Res.* 39 (1998) 331–40. [https://doi.org/10.1002/\(SICI\)1097-4636\(199802\)39:2<331::AID-JBM22>3.0.CO;2-E](https://doi.org/10.1002/(SICI)1097-4636(199802)39:2<331::AID-JBM22>3.0.CO;2-E).
- [66] ISO 10993-5, Tests for *in vitro* cytotoxicity, International Organization for Standardization, 2009. <https://doi.org/10.1021/es0620181>.
- [67] Y.F. He, Y. Ma, C. Gao, G.Y. Zhao, L.L. Zhang, G.F. Li, Y.Z. Pan, K. Li, Y.J. Xu, Iron overload inhibits osteoblast biological activity through oxidative stress, *Biol. Trace Elem.*

- Res. 152 (2013) 292–296. <https://doi.org/10.1007/s12011-013-9605-z>.
- [68] R. Oriňáková, R. Gorejová, Z.O. Králová, A. Oriňák, I. Shepa, J. Hovancová, A. Kovalčíková, Z.L. Bujňáková, N. Király, M. Kaňuchová, M. Baláž, M. Strečková, M. Kupková, M. Hrubovčáková, F. Kaľavský, M. Oriňák, Influence of albumin interaction on corrosion resistance of sintered iron biomaterials with polyethyleneimine coating, *Appl. Surf. Sci.* 509 (2020) 145379. <https://doi.org/10.1016/j.apsusc.2020.145379>.
- [69] J. Wei, T. Igarashi, N. Okumori, T. Igarashi, T. Maetani, B. Liu, M. Yoshinari, Influence of surface wettability on competitive protein adsorption and initial attachment of osteoblasts, *Biomed. Mater.* 4 (2009) 045002. <https://doi.org/10.1088/1748-6041/4/4/045002>.
- [70] E.A. Dos Santos, M. Farina, G.A. Soares, K. Anselme, Surface energy of hydroxyapatite and β -tricalcium phosphate ceramics driving serum protein adsorption and osteoblast adhesion, *J. Mater. Sci. Mater. Med.* 19 (2008) 2307–2316. <https://doi.org/10.1007/s10856-007-3347-4>.
- [71] V. Wagener, A.S. Faltz, M.S. Killian, P. Schmuki, S. Virtanen, Protein interactions with corroding metal surfaces: Comparison of Mg and Fe, *Faraday Discuss.* 180 (2015) 347–360. <https://doi.org/10.1039/c4fd00253a>.
- [72] R. Eid, N.T.T. Arab, M.T. Greenwood, Iron mediated toxicity and programmed cell death: A review and a re-examination of existing paradigms, *Biochim. Biophys. Acta - Mol. Cell Res.* 1864 (2017) 399–430. <https://doi.org/10.1016/j.bbamcr.2016.12.002>.
- [73] R. Oriňáková, R. Gorejová, J. Macko, A. Oriňák, M. Kupková, M. Hrubovčáková, J. Ševc, R.M. Smith, Evaluation of *in vitro* biocompatibility of open cell iron structures with PEG coating, *Appl. Surf. Sci.* 475 (2019) 515–518. <https://doi.org/10.1016/j.apsusc.2019.01.010>.
- [74] S. Huang, A. Ulloa, E. Nauman, L. Stanciu, Collagen coating effects on Fe–Mn bioresorbable alloys, *J. Orthop. Res.* 38 (2020) 523–535. <https://doi.org/10.1002/jor.24492>.
- [75] F. Pluronic, Y. Hwang, P. Chiang, W. Hong, C. Chiao, I. Chu, Study *in vivo* intraocular biocompatibility of in situ gelation hydrogels: Poly(2-ethyl oxazoline)-block-Poly(e-caprolactone)-block-Poly(2-ethyl oxazoline) copolymer, *Matrigel and Pluronic F127, PLoS One.* 8 (2013) 1–9. <https://doi.org/10.1371/journal.pone.0067495>.
- [76] J. Tong, X. Yi, R. Luxenhofer, W.A. Banks, R. Jordan, M.C. Zimmerman, A. V. Kabanov, Conjugates of superoxide dismutase 1 with amphiphilic poly(2-oxazoline) block copolymers for enhanced brain delivery: Synthesis, characterization and evaluation *in vitro* and *in vivo*, *Mol. Pharm.* 10 (2013) 360–377. <https://doi.org/10.1021/mp300496x>.
- [77] H. Ma, T. Li, Z. Huan, M. Zhang, Z. Yang, J. Wang, J. Chang, C. Wu, 3D printing of high-strength bioscaffolds for the synergistic treatment of bone cancer, *NPG Asia Mater.* 10 (2018) 31–44. <https://doi.org/10.1038/s41427-018-0015-8>.
- [78] C. Shuai, Y. Li, Y. Yang, S. Peng, W. Yang, F. Qi, S. Xiong, H. Liang, L. Shen, Bioceramic enhances the degradation and bioactivity of iron bone implant, *Mater. Res. Express.* 6 (2019) 115401. <https://doi.org/10.1088/2053-1591/ab45b9>.
- [79] C. Gao, M. Yao, S. Li, P. Feng, S. Peng, C. Shuai, Highly biodegradable and bioactive Fe–Pd-bredigite biocomposites prepared by selective laser melting, *J. Adv. Res.* 20 (2019) 91–104. <https://doi.org/10.1016/j.jare.2019.06.001>.

***Ex situ*-alloy highly biodegradable MRI-friendly porous Fe-Mn**

Additively manufactured biodegradable porous iron has been only very recently demonstrated. Two major limitations of such a biomaterial are very low biodegradability and incompatibility with magnetic resonance imaging (MRI). Here, we present a novel biomaterial that resolves both of those limitations. We used extrusion-based 3D printing to fabricate *ex situ*-alloyed biodegradable iron-manganese scaffolds that are non-ferromagnetic and exhibit enhanced rates of biodegradation. We developed ink formulations containing iron and 25, 30, or 35 wt% manganese powders, and debinding and sintering process to achieve Fe-Mn scaffolds with 69% porosity. The Fe₂₅Mn scaffolds had the ϵ -martensite and γ -austenite phases, while the Fe₃₀Mn and Fe₃₅Mn scaffolds had only the γ -austenite phase. All iron-manganese alloys exhibited weakly paramagnetic behavior, confirming their potential to be used as MRI-friendly bone substitutes. The *in vitro* biodegradation rates of the scaffolds were very much enhanced (i.e., 4.0 to 4.6 times higher than that of porous iron), with the Fe₃₅Mn alloy exhibiting the highest rate of biodegradation (i.e., 0.23 mm/y). While the elastic moduli and yield strengths of the scaffolds decreased over 28 days of *in vitro* biodegradation, those values remained in the range of cancellous bone. The culture of preosteoblasts on the porous iron-manganese scaffolds revealed that cells could develop filopodia on the scaffolds, but their viability was reduced by the effect of biodegradation. Altogether, this research marks a major breakthrough and demonstrates the great prospects of multi-material extrusion-based 3D printing to further address the remaining issues of porous iron-based materials.

5.1 Introduction

Iron is one of the promising biodegradable metals. Unlike magnesium, it has excellent processability [1,2] and its rate of biodegradation is slow enough to provide continued mechanical support while the bone regeneration process progresses. However, the *in vivo* biodegradability of iron is so low that it may elicit immunogenic responses similar to bio-inert materials [3]. In addition, iron is ferromagnetic by nature, which complicates the imaging procedure for the patients who are exposed to a strong magnetic field, typically in magnetic resonance imaging (MRI) [4]. To address both fundamental issues of iron, alloying of iron with manganese has been proposed [5]. The addition of 28 wt% or more manganese to iron promotes austenicity, making the alloy anti-ferromagnetic and, thus, MRI-friendly [6]. Furthermore, manganese has a lower standard electrode potential than iron (*i.e.*, -1.18 V versus -0.44 V). Because iron and manganese form solid solution, the standard electrode potential of the alloy tends to decrease with increasing manganese content, thus allowing for faster biodegradation [7]. As for the biocompatibility, despite naturally occurring in the human body, iron and manganese at high doses can be toxic [8,9]. Considering all these factors is of great importance in the design of iron-manganese alloys intended for bone substitution.

For bone substitution, the geometrical design of Fe-Mn alloy scaffolds needs to imitate the hierarchical structure of native bone as well as its mechanical properties. A rationally designed and precisely manufactured porous structure is one of the key geometrical features [10,11]. The porosity, pore shape, and pore sizes will not only influence the mechanical properties, but also determine (to a large extent) the biodegradation kinetics and biofunctionality of the resulting biomaterial [12–16]. In realizing complex geometrical designs, iron-manganese alloys have been fabricated with a variety of techniques, such as casting [17–19], powder metallurgy [20–22], space holder method [12–14,23], and sponge impregnation [24]. However, these techniques are restricted to achieving non-conforming porous structures without precisely controlled pore characteristics and limited pore interconnectivity. Recent advances in 3D printing technologies have removed the restrictions and presented an unprecedented opportunity to fabricate geometrically ordered bone-substituting materials of almost any structural design [16,25].

In recent years, porous iron-manganese alloy structures have been 3D printed with binder jetting [26,27] and selective laser melting [28–30]. As compared to those techniques, extrusion-based 3D printing followed by debinding and sintering offers a more robust and versatile approach to the *ex situ* alloying of Fe and Mn and the fabrication of porous multi-material scaffolds that

are otherwise highly demanding for the other 3D printing techniques [31–33]. To date, no study on extrusion-based 3D printed porous iron-manganese scaffolds has appeared in the literature. Here, we report, for the first time, the successful fabrication of *ex situ*-alloyed porous iron with 25, 30, or 35 wt% manganese using extrusion-based 3D printing. We also performed comprehensive characterization of the porous materials, including *in vitro* biodegradation behavior, electrochemical responses, and biodegradation-dependent mechanical properties, as well as *in vitro* cytocompatibility assessment using the MC3T3-E1 cell line.

5.2 Materials and methods

5.2.1 Powder mixture and ink preparation

Iron powder (99.88 wt% purity; spherical morphology; particle size distribution: $D_{10} = 25.85 \mu\text{m}$, $D_{50} = 39.93 \mu\text{m}$ and $D_{90} = 53.73 \mu\text{m}$, Figure 5.1a) and manganese powder (99.86 wt% purity; irregular morphology; particle size distribution: $D_{10} = 7.69 \mu\text{m}$, $D_{50} = 20.89 \mu\text{m}$ and $D_{90} = 41.58 \mu\text{m}$, Figure 5.1b) were used as the starting materials for the preparation of iron-manganese-containing inks. Both powders were purchased from Material Technology Innovations Co. Ltd., China. Iron-manganese powder mixtures (with 25, 30, and 35 wt% manganese, hereafter denoted as Fe₂₅Mn, Fe₃₀Mn, and Fe₃₅Mn, respectively) were prepared using a roller mixer (CAT Zipperer GmbH, Germany) at 80 rpm for 18 h. As for the binder preparation, hydroxypropyl methylcellulose (hypromellose) powder ($M_w \sim 86 \text{ kDa}$, Sigma Aldrich, Germany) was dissolved in a water-ethanol solution with a 5 wt% concentration [34]. The addition of ethanol to the solvent was intended to minimize the reactivity of the binder with the manganese powder. Then, the mixed iron-manganese powders were blended with the hypromellose binder to prepare 3D printable iron-manganese-containing inks at a mass ratio of 7:1 [34]. The mixed powder mass ratios in the inks corresponded to the volume ratios of 49.6% for Fe₂₅Mn, 49.7% for Fe₃₀Mn, and 49.8% for Fe₃₅Mn. The ink density was calculated from the volume fractions of the iron-manganese powder and the binder and their theoretical densities. In addition, the rheological behaviors of the inks were studied using an MCR302 rheometer (Anton Paar GmbH, Germany).

5.2.2 Extrusion-based 3D printing, debinding and sintering

Porous iron-manganese scaffolds (10 mm in diameter and 10.5 mm in height) were designed as a lay-down pattern and 3D printed following the characteristics described in Chapter 3, section 3.2.1 (Figure 5.1c). The iron-manganese-containing inks were extruded at a printing speed of 3.5 mm/s and

under pressures of 280 kPa, 290 kPa, and 300 kPa for the Fe₂₅Mn, Fe₃₀Mn, and Fe₃₅Mn inks, respectively.

The as-printed iron-manganese scaffolds were placed inside a tube furnace (STF16/180, Carbolite Gero Ltd., UK) under highly pure argon flow (purity = 99.9999%; inlet pressure = 1 bar). Debinding and sintering were respectively performed at 350 °C for 3 h and at 1200 °C for 6 h, followed by natural cooling in the furnace. The as-sintered porous iron-manganese scaffolds were ultrasonically cleaned in isopropyl alcohol for 15 min prior to subsequent investigations. The exact compositions of the porous iron-manganese alloys after sintering were determined by using an inductively coupled plasma optical emission spectroscopy (ICP-OES, iCAP 6500 Duo, Thermo Scientific, USA).

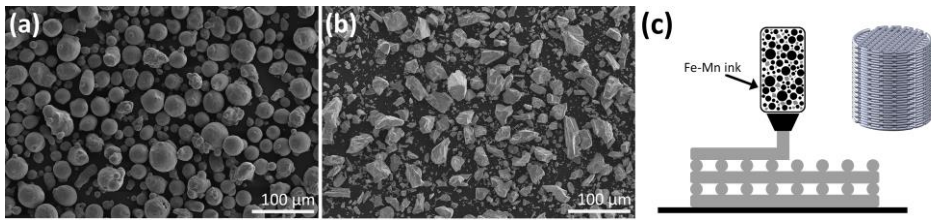


Figure 5.1. Morphologies of (a) iron and (b) manganese powders, and (c) a schematic illustration of extrusion-based 3D printing and the design of porous iron-manganese scaffolds in a lay-down pattern of 0° and 90°.

5.2.3 Macro- and microstructural characterization

The dimensions of the porous iron-manganese alloy scaffolds were measured to determine the dimensional changes occurring during sintering. The porous structures of the iron-manganese alloy scaffolds were observed using a scanning electron microscope (SEM, JEOL JSM-IT100, Japan) and their morphological characteristics (*i.e.*, strut width and strut spacing) were determined. The absolute porosities were calculated based on the dry weighing method, as described in Chapter 3, with Equations (3.2) and (3.3), where the ρ_{ink} is the density of the iron-manganese-containing ink (*i.e.*, 4.36 g/cm³ for Fe₂₅Mn, 4.35 g/cm³ for Fe₃₀Mn, and 4.34 g/cm³ for Fe₃₅Mn), and ρ_{Fe-Mn} is the theoretical density of the iron-manganese alloy (*i.e.*, 7.70 g/cm³ for Fe₂₅Mn, 7.66 g/cm³ for Fe₃₀Mn, and 7.63 g/cm³ for Fe₃₅Mn). The interconnected porosity of the iron-manganese alloy scaffolds was determined using the Archimedes' principle and according to the ASTM standard B963-13 [35] and as described in Chapter 3, Equation (3.4).

In addition, the cross sections of the as-sintered porous iron-manganese alloy struts were observed using the SEM and the elemental compositions were

mapped using X-ray energy dispersive spectroscopy (EDS, JEOL JSM-IT100, Japan). The regions of interest on the cross sections of struts were defined and the pore area was selected using ImageJ (NIH, USA). The solid fraction of strut was calculated with Equation (3.1).

5.2.4 Phase identification

The phases in the porous iron-manganese alloys were identified using an X-ray diffractometer (XRD, D8 Advance, Bruker, USA) with the parameters described in Chapter 4, section 4.2.4. The resulting XRD patterns were analyzed with the Diffrac Suite.EVA v5.2 software.

5.2.5 *In vitro* immersion and biodegradation product characterization

In vitro immersion tests of the porous iron-manganese specimens were performed using a revised simulated body fluid (r-SBF) [36] for 1, 2, 7, 14 and 28 d (in triplicate for every time point) under the conditions, as described in Chapter 3, section 3.2.4. A 6.7 mL medium per 1 cm² scaffold surface area was used [37]. The pH values of the medium were recorded using a pH electrode (InLab Expert Pro-ISM, METTLER TOLEDO, Switzerland). To determine the mass loss, the *in vitro* biodegradation products on the porous iron-manganese alloy specimens were dissolved according to the ASTM standard G1-03 [38], as described in Chapter 3, section 3.2.4. The remaining iron-manganese material was weighed and the average corrosion rate was determined according to the ASTM standard G31-72 [39], with Equation (3.5).

Following uninterrupted immersion until the selected time points (*i.e.*, 1, 2, 7, 14, and 28 d), the morphological characteristics of the biodegradation products on the periphery and in the center of the porous iron-manganese alloys were observed using SEM (JEOL JSM-IT100, Japan) and the chemical elements in the biodegradation product compounds were identified using EDS (JEOL JSM-IT100, Japan). The solid fraction of the remaining iron-manganese material after uninterrupted immersion for 28 d was calculated using ImageJ (NIH, USA) and Equation (3.1). The phases of the biodegradation products after 28 d immersion were analyzed using XRD (D8 Advance, Bruker, USA). Furthermore, the soluble iron, manganese, calcium, and phosphate ion concentrations in r-SBF were measured using ICP-OES (iCAP 6500 Duo, Thermo Scientific, USA).

5.2.6 Magnetic susceptibility evaluation

Porous iron-manganese specimens (with an average mass of 39.7 ± 4 mg, in triplicate, before and after *in vitro* immersion for 28 d) were exposed to an applied magnetic field of 2 T at room temperature in a vibrating sample magnetometer chamber (VSM 7307, Lake Shore, USA). Porous Ti-6Al-4V samples were added to the tests as the control group. The magnetic hysteresis

loops obtained were analyzed to determine the saturation magnetization, remanence magnetization, and magnetic susceptibility values.

5.2.7 Electrochemical measurements

The electrochemical responses of the porous iron-manganese alloys were investigated using a three-electrode setup connected to a Bio-Logic SP-200 potentiostat (Bio-Logic Science Instruments, France). The electrochemical system consisted of a Ag/AgCl electrode as the reference electrode, a graphite rod as the counter electrode, and the iron-manganese alloy specimen as the working electrode. The specimens were prepared through partial embedding in a thermoplastic acrylic resin, followed by ultrasonic cleaning in isopropyl alcohol and thorough drying. Subsequently, the specimens were immersed in the r-SBF medium (temperature = 37 ± 0.5 °C; pH = 7.40). The exposed surface area of the specimens was calculated, based on the initial design value of the scaffold. The electrochemical measurements of open circuit potential (OCP), linear polarization resistance (LPR) and electrochemical impedance spectroscopy (EIS) were conducted, following the parameters as described in detail in Chapter 3, section 3.2.6.

5.2.8 Uniaxial compression tests

The compressive mechanical properties of the porous iron-manganese specimens, including the specimens retracted at the selected time points of the *in vitro* immersion test, were evaluated using a mechanical testing machine (Zwick Z100, Germany) with a 100 kN load cell. The tests were displacement-controlled and were performed according to the ISO standard 13314:2011 [40]. The elastic modulus and yield strength were determined as described in Chapter 3, section 3.2.7. The plastic deformation curves up to a strain of 0.1 mm/mm were fitted to Equation (5.1) to quantify the initial strain-hardening exponent value of the porous iron-manganese specimens.

$$\sigma = K\varepsilon^n \quad (5.1)$$

where σ is stress [MPa], K is the strength coefficient, ε is strain [mm/mm], and n is the strain-hardening exponent.

5.2.9 Cytocompatibility evaluation

Cell culture and preparation of iron-manganese alloy extracts

Mouse preosteoblast cells (MC3T3-E1, Sigma Aldrich, Germany) were pre-cultured for 7 d in a cell incubator following the conditions, as described in Chapter 3, section 3.2.8. The cell culture medium was made of α -minimum essential medium (α -MEM,) without ascorbic acid, but supplemented with 10%

fetal bovine serum (FBS) and 1% penicillin/streptomycin (p/s). All the cell culture medium components were purchased from Thermo Fisher Scientific, USA.

Extracts were obtained after 72 h incubation of sterilized porous iron-manganese specimens (10.15 mm in diameter and 10.55 mm in height) in the cell culture medium [41], as described in Chapter 3, section 3.2.8. The concentrations of iron and manganese ions in the 100% extract were measured using ICP-OES (iCAP 6500 Duo, Thermo Scientific, USA).

Indirect assays: PrestoBlue and F-actin/nucleus staining

The preosteoblasts (1×10^4 cells) were cultured with 200 μ L iron-manganese alloy extracts in 48-well plates (in triplicate) for 1, 3, and 7 d. The metabolic activity of preosteoblasts cultured in the iron-manganese alloy extracts was evaluated using the PrestoBlue assay (Thermo Fisher Scientific, USA) as described in Chapter 3, section 3.2.8, and Equation (3.7). The F-actin and nucleus of the preosteoblasts, after being exposed to the iron-manganese alloy extracts for 3 d, were stained using rhodamine phalloidin (Thermo Fisher Scientific, USA) and 4',6-diamidino-2-phenylindole (DAPI, Life Technologies, USA), following the procedure described in Chapter 3, section 3.2.8. The morphology of the F-actins and nuclei was observed using a fluorescence microscope (ZOE cell imager, Bio-Rad, USA).

Direct assays: Viable cell count and live/dead staining

The MC3T3-E1 preosteoblasts (5×10^4 cells per sample) were seeded into the porous iron-manganese specimens (1.3 mm in height and 10.15 mm in diameter) and were cultured for 1, 4, 7, 14, and 28 d in 6-well plates containing 8 mL of the cell culture medium. Porous pure iron specimens were included as the control group. After cell culture, the viable preosteoblasts were counted using the Trypan blue assay (Bio-Rad, USA) with an automated cell counter (TC20, Bio-Rad, USA), as described in Chapter 3, section 3.2.8. The morphology of the preosteoblasts after 4 d of culture with the porous iron-manganese specimens was observed using calcein and ethidium homodimer-1 staining (Thermo Fisher Scientific, USA) and SEM imaging. In addition, the porous iron-manganese specimens immersed in the cell culture medium (in the incubator) for 7 and 28 d were investigated to observe the strut morphology and identify the biodegradation products that could have affected the cytocompatibility.

5.2.10 Statistical analysis

The statistical analysis of the PrestoBlue and viable cell count results was performed with two-way ANOVA, followed by a Tukey multiple comparison *post hoc* test (**** = $p < 0.0001$, *** = $p < 0.001$, ** = $p < 0.01$, and * = $p < 0.05$, *n.s.* = not significant).

5.3 Results

5.3.1 Characteristics of the porous iron-manganese alloys

The extrusion-based 3D printed porous iron-manganese scaffolds, *i.e.*, Fe₃₅Mn (Figure 5.2), Fe₃₀Mn (Figure S5.1), and Fe₂₅Mn (Figure S5.2) exhibited very similar geometric characteristics to the original scaffold design of the 0° and 90° pattern (Figure 5.2a). The optimum mixed powder loading and the shear-thinning behavior of the iron-manganese-containing ink (Figure S5.3) allowed a smooth 3D printing process to create the scaffolds with a high aspect ratio and free-standing feature. Furthermore, iron and manganese particles from the elemental powders were homogeneously distributed in the struts (Figure 5.2a-c).

After sintering, the porous iron-manganese alloy scaffolds (Figure 5.2d, S5.1-5.2) slightly expanded in size (*i.e.*, a 0.3 to 0.5% increase in diameter and a 1.4 to 1.6% increase in height). On the periphery, spherical powder particles fused and were occasionally bridged by irregularly shaped powder particles (Figure 5.2e-f, S5.1, S5.2). The specific configuration of powder particle bonding resulted in micro-porosity inside the struts, with solid fractions equal to $67 \pm 2\%$, $64 \pm 3\%$, and $63 \pm 2\%$ for the Fe₂₅Mn, Fe₃₀Mn, and Fe₃₅Mn scaffolds, respectively. From the cross sectional EDS analysis, manganese completely diffused into the iron matrix (Figure 5.2g, S5.1, S5.2), confirming the occurrence of alloying during the sintering process and the successful synthesis of the materials.

Table 5.1. Structural characteristics of the extrusion-based 3D printed porous iron-manganese scaffolds.

Sample groups		Strut width (μm)	Strut spacing (μm)	Absolute porosity (%)	Interconnected porosity (%)
Fe ₂₅ Mn	As-printed	410 ± 6	400 ± 6	43 ± 5	-
	As-sintered	411 ± 6	398 ± 6	69 ± 2	67 ± 1
Fe ₃₀ Mn	As-printed	409 ± 5	401 ± 5	44 ± 4	-
	As-sintered	412 ± 7	398 ± 7	69 ± 2	67 ± 1
Fe ₃₅ Mn	As-printed	409 ± 5	402 ± 6	43 ± 2	-
	As-sintered	412 ± 6	398 ± 5	69 ± 1	68 ± 1

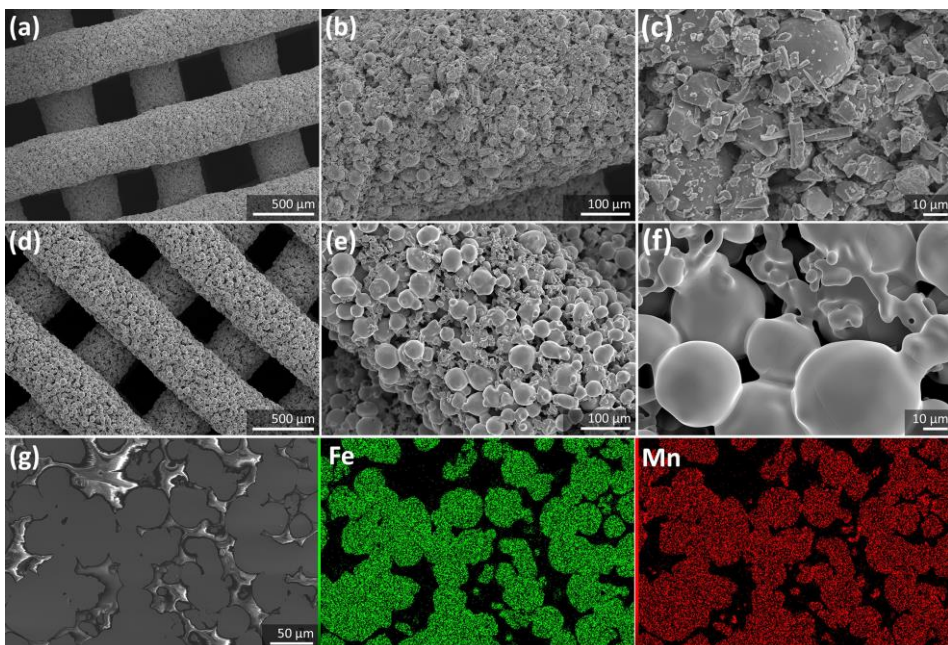


Figure 5.2. Morphologies of porous Fe₃₅Mn: (a, b, c) in the as-printed condition and (d, e, f) in the as-sintered condition at different magnifications, and (g) EDS mapping on the cross section of porous iron-manganese struts.

Table 5.2. Chemical compositions of the as-sintered porous iron-manganese alloys.

As-sintered sample	Fe (wt%)	Mn (wt%)	Impurities
Fe ₂₅ Mn	74.94 ± 0.14	24.87 ± 0.16	0.19 ± 0.02
Fe ₃₀ Mn	70.05 ± 0.05	29.72 ± 0.02	0.23 ± 0.03
Fe ₃₅ Mn	65.31 ± 0.11	34.51 ± 0.07	0.18 ± 0.06

The as-sintered iron-manganese alloys had an average absolute porosity of 69% and a pore interconnectivity up to 98.6%. The detailed structural characteristics of the as-printed and as-sintered porous iron-manganese scaffolds are presented in Table 5.1. As a result of the complete diffusion of manganese into iron (Figure 5.2g), the porous Fe₂₅Mn alloy had the dual ϵ -martensite and γ -austenite phases, whereas the porous Fe₃₀Mn and Fe₃₅Mn alloys had only the γ -austenite phase (Figure 5.3a). In addition, a very small amount (< 2 wt%) of manganese oxide was detected in the scaffolds, which was actually present in the initial manganese powder before ink preparation. The chemical compositions of

the as-sintered porous iron-manganese alloys slightly deviated from the design values (Table 5.2).

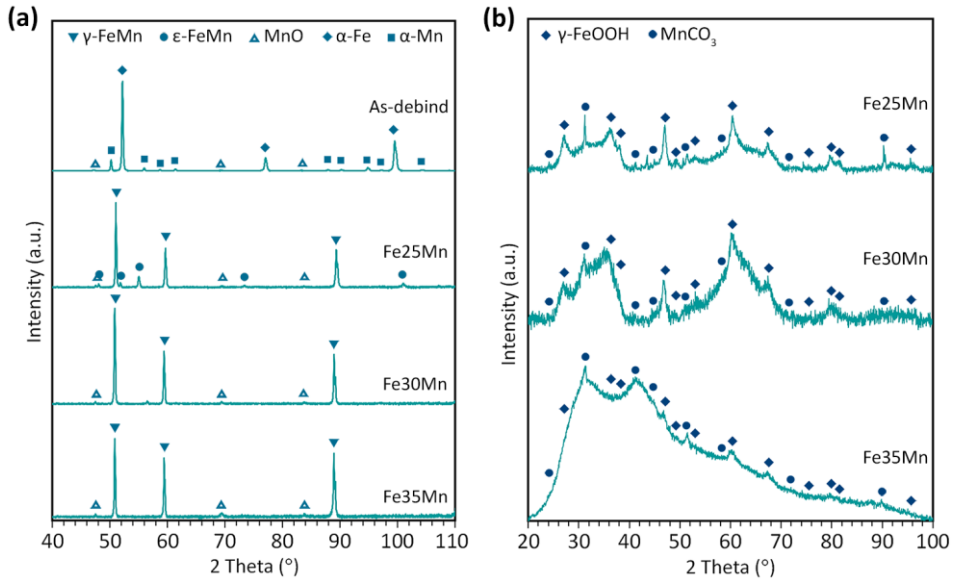


Figure 5.3. Phase compositions of (a) the porous iron-manganese scaffolds in the as-debinded and as-sintered conditions and (b) after 28 d of *in vitro* biodegradation.

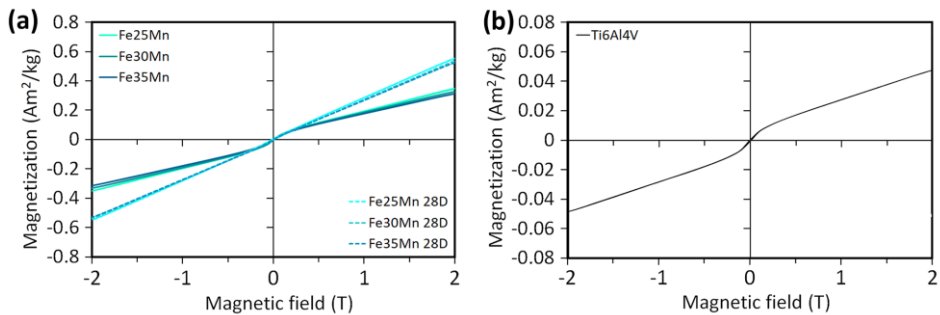


Figure 5.4. Magnetization curves of (a) the porous iron-manganese alloys (as-built and after 28 d of *in vitro* biodegradation) and (b) porous Ti-6Al-4V.

5.3.2 Magnetic properties

In the applied magnetic field of 2 T, all the porous iron-manganese alloys exhibited very low saturation magnetization values (*i.e.*, $0.35 \text{ Am}^2/\text{kg}$ for Fe25Mn, $0.32 \text{ Am}^2/\text{kg}$ for Fe30Mn, and Fe35Mn), which were quite close to the magnetization value of Ti-6Al-4V (Figure 5.4). After 28 d of immersion in r-SBF,

the magnetization increased up to $0.58 \text{ Am}^2/\text{kg}$, but the values were still at a relatively low level. The slight increase in magnetization could be due to the ferrimagnetic behavior of the residual biodegradation products (*e.g.*, iron or manganese oxides) that remained on the struts even after the ultrasonic cleaning step. Furthermore, the magnetic susceptibility of all the porous iron-manganese alloys did not significantly change ($\chi = 3.0\text{--}4.4 \times 10^{-3}$) even after 28 d of immersion.

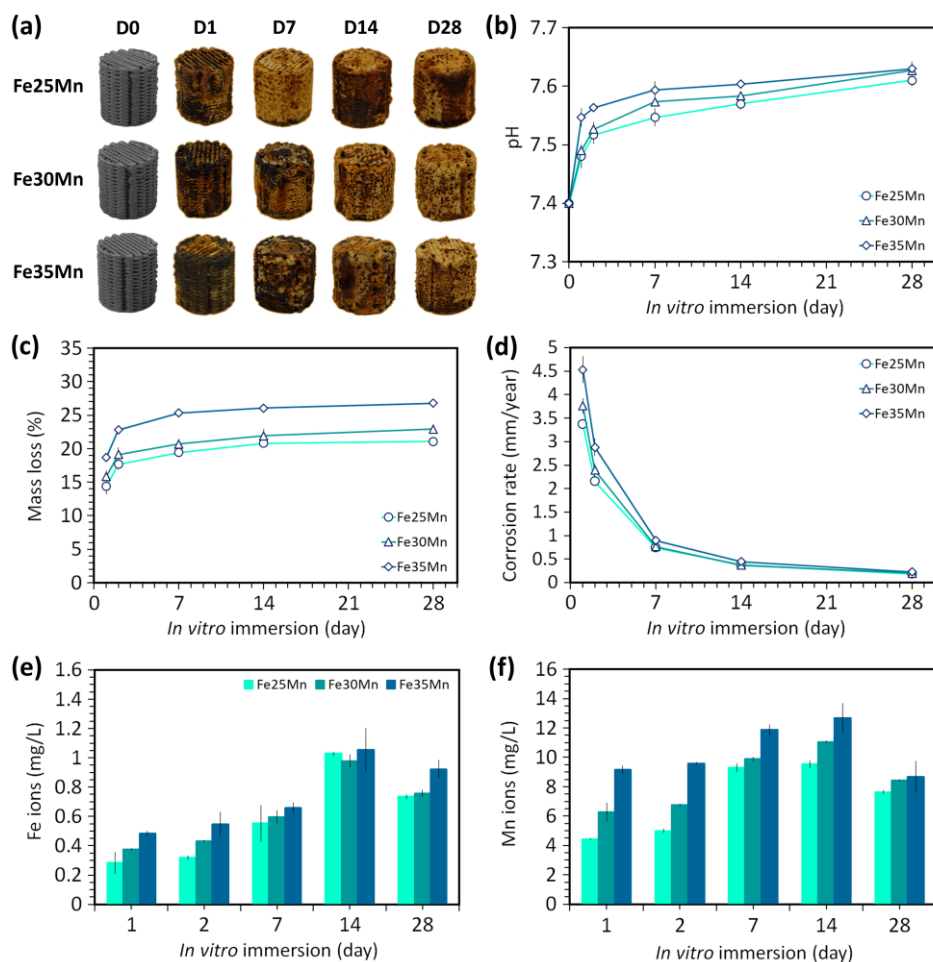


Figure 5.5. *In vitro* biodegradation characteristics of the porous iron-manganese alloys: (a) visual inspection of the scaffolds at different time points of biodegradation, (b) variations of pH values of the immersion medium with time, (c) mass losses with time, (d) corrosion rates with time, and the concentrations of (e) iron and (f) manganese ions released during biodegradation.

5.3.3 *In vitro* biodegradation performance

During the static *in vitro* immersion tests, yellow-brownish corrosion products were deposited on the porous iron-manganese alloy strut surfaces (Figure 5.5a). The immersion tests in a cell incubator provided a precisely controlled 5% CO₂ atmosphere. The pH level of the r-SBF medium was maintained between 7.61–7.63 throughout the 28 d of the immersion test (Figure 5.5b). The average mass loss due to biodegradation was larger for the alloy with a higher manganese content (Figure 5.5c). At the beginning of the immersion test, (*i.e.*, after 1 d), the *in vitro* biodegradation rates of the porous iron-manganese specimens were 3.37 ± 0.19 mm/y, 3.76 ± 0.16 mm/y, and 4.53 ± 0.28 mm/y for Fe₂₅Mn, Fe₃₀Mn, and Fe₃₅Mn, respectively (Figure 5.5d). After 28 d of immersion, however, the biodegradation rates decreased to 0.18 mm/y, 0.20 mm/y, and 0.23 mm/y (± 0.01), respectively (Figure 5.5d).

During *in vitro* biodegradation, iron and manganese ions were gradually released to the r-SBF medium (Figure 5.5e-f). The ion release reached a peak after 14 d of immersion, and then decreased. The iron ion concentrations were relatively low from the all scaffold groups (*i.e.*, approximately 1 ppm at 14 d) (Figure 5.5e). Meanwhile, the manganese ion concentrations reached 9.5–12.7 ppm at the same time point (Figure 5.5f). The amount of manganese ion release from the alloy with a higher manganese content was larger. As the biodegradation continued to day 28, the base material (*i.e.*, the iron-manganese alloy) was progressively consumed, accompanied by the decreases in the solid fraction to $42 \pm 8\%$ (Fe₂₅Mn), $39 \pm 3\%$ (Fe₃₀Mn), and $31 \pm 9\%$ (Fe₃₅Mn).

5.3.4 Characteristics of the biodegradation products

A dense layer of biodegradation products was formed on the struts after 24 h of immersion (Figure 5.6a). The biodegradation products grew with time and almost filled the macropores of the scaffolds at day 28 (Figure 5.6b-d). Similar observations were made for the porous Fe₃₀Mn (Figure S5.4) and Fe₂₅Mn (Figure S5.5) scaffolds. In addition, the peripheral biodegradation products were identified to be iron oxyhydroxide (γ -FeOOH) and rhodochrosite (MnCO₃) (Figure 5.3b). Correspondingly, the major elements present in the peripheral biodegradation products were found to be iron, manganese, oxygen, and carbon (Figure 5.6e-j).

After 24 h immersion, the biodegradation products at the periphery of the porous Fe₃₅Mn scaffolds transformed from a mixture of iron- and manganese-based compounds (Figure 5.6e, h) to those with a higher concentration of manganese at day 7 (Figure 5.6f, i), and finally changed to iron-based compounds at day 28 (Figure 5.6g, j). During the 28 d of immersion, the biodegradation products at the periphery of the Fe₃₀Mn scaffold specimens (Figure S5.4)

evolved in a similar manner to those on the porous Fe₃₅Mn scaffold specimens. However, the biodegradation products on the periphery of the Fe₂₅Mn scaffold specimens were predominantly made of iron-based compounds after 24 h of immersion. Afterwards, the compounds transformed to manganese-based compounds after 7 d and back to iron-based compounds after 28 d (Figure S5.5). At the center of the scaffolds with pore networks, the 28 d biodegradation products were predominantly carbon- and oxygen-based compounds (Figure 5.6k, S5.4, S5.5).

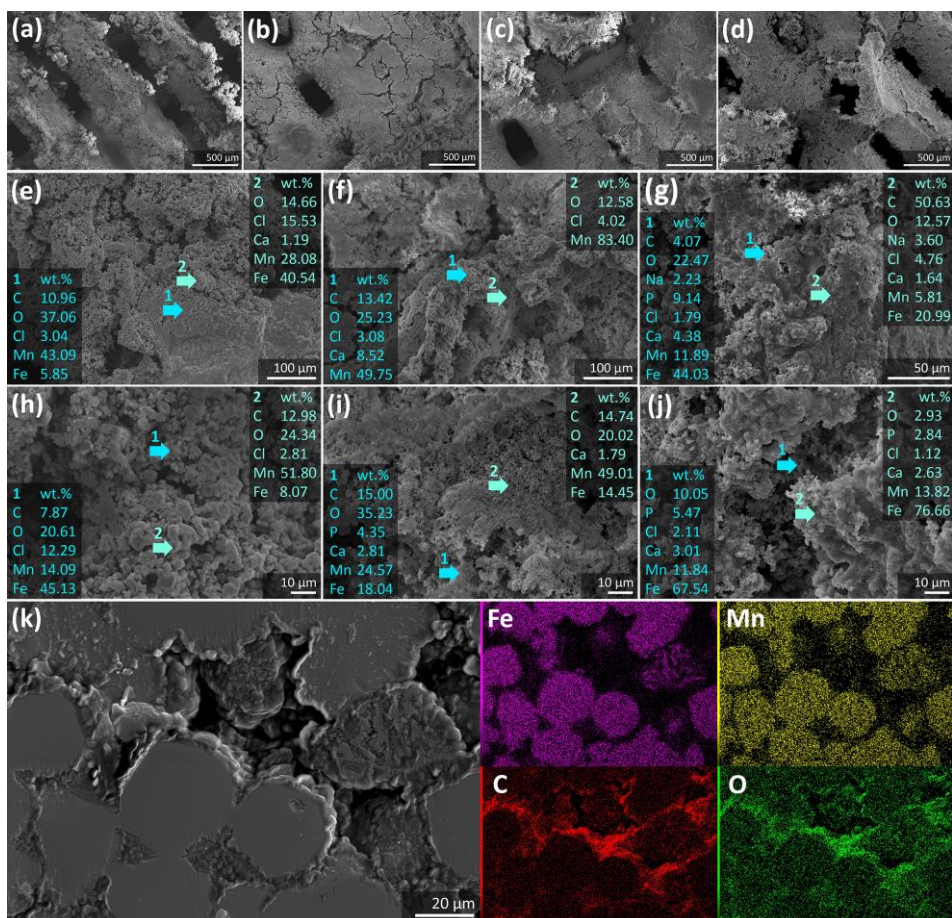


Figure 5.6. Morphologies and chemical compositions of the *in vitro* biodegradation products on porous Fe₃₅Mn struts: on the periphery after (a, e, h) 24 h, (b, f, i) 7 d, (c) 14 d, and (d, g, j) 28 d of biodegradation, and (k) at the center of the scaffolds after 28 d of biodegradation. The arrow and number indicate the location of EDS analysis.

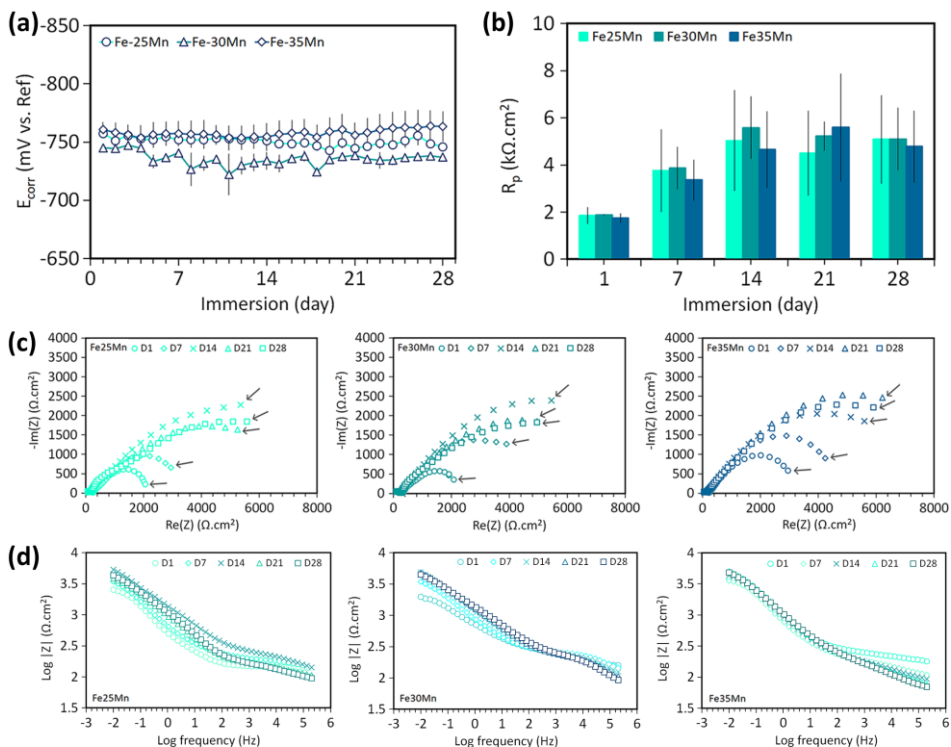


Figure 5.7. Electrochemical responses of the porous iron-manganese alloys during 28 d of biodegradation: (a) OCP and (b) polarization resistance values from the LPR measurements; (c) impedance Nyquist and (d) Bode plots at different time points.

5.3.5 Electrochemical measurements

The OCP values of the porous iron-manganese alloys were stable during the 28 d of biodegradation (Figure 5.7a). After 24 h of immersion, the OCP values were -757 ± 2 mV, -745 ± 3 mV, and -761 ± 6 mV for Fe25Mn, Fe30Mn, and Fe35Mn, respectively. After 28 d of immersion, the OCP values only changed marginally to -746 ± 4 mV, -745 ± 3 mV, and -737 ± 3 mV, respectively. On the other hand, the OCP values of porous iron increased from -706 ± 2 mV after 24 h of immersion to -608 ± 49 mV after 28 d of immersion. From the LPR measurements, the average polarization resistance values of the porous iron-manganese alloys showed an increasing trend during the initial 14 d of immersion and remained relatively stable afterwards (Figure 5.7b). Meanwhile, the average polarization resistance values of porous iron increased with immersion time. After 24 h, the average polarization resistance values were 1.9 ± 0.3 $\text{k}\Omega\cdot\text{cm}^2$, 1.9 ± 0.2 $\text{k}\Omega\cdot\text{cm}^2$, 3.5 ± 0.6 $\text{k}\Omega\cdot\text{cm}^2$ for Fe25Mn, Fe30Mn, and Fe35Mn, respectively.

After 28 d of immersion, the average polarization resistance values increased to $3.3 \pm 0.6 \text{ k}\Omega\cdot\text{cm}^2$, $5.1 \pm 1.3 \text{ k}\Omega\cdot\text{cm}^2$, and $4.8 \pm 1.5 \text{ k}\Omega\cdot\text{cm}^2$, respectively. For the porous iron scaffolds, the average polarization resistance value significantly increased from $3.2 \pm 0.8 \text{ k}\Omega\cdot\text{cm}^2$ after 24 h of immersion to $23.4 \pm 4.4 \text{ k}\Omega\cdot\text{cm}^2$ after 28 d of immersion (Figure 5.7b).

The impedance Nyquist plots of the porous iron-manganese alloys displayed semicircles that grew larger with increasing immersion time up to 14 d and slightly fluctuated towards 28 d of immersion (Figure 5.7c). At the low frequency (*i.e.*, 0.01 Hz), the Bode impedance magnitude values of the porous iron manganese alloys had a similar trend as the polarization resistance (Figure 5.7d). After 24 h, the impedance magnitude values at 0.01 Hz were $2.5 \pm 0.9 \text{ k}\Omega\cdot\text{cm}^2$, $2.0 \pm 0.2 \text{ k}\Omega\cdot\text{cm}^2$, $3.9 \pm 0.7 \text{ k}\Omega\cdot\text{cm}^2$ for Fe₂₅Mn, Fe₃₀Mn, and Fe₃₅Mn, respectively. After 28 d of immersion, the values increased to $4.3 \pm 1.5 \text{ k}\Omega\cdot\text{cm}^2$, $4.5 \pm 1.1 \text{ k}\Omega\cdot\text{cm}^2$, and $4.8 \pm 1.4 \text{ k}\Omega\cdot\text{cm}^2$, respectively.

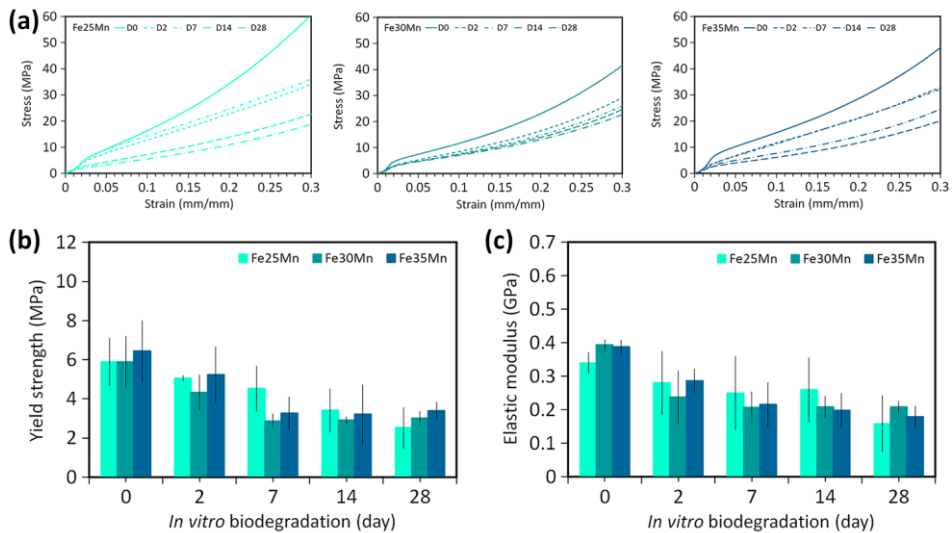


Figure 5.8. Compressive mechanical properties of the porous iron-manganese alloys: (a) the stress-strain curves, (b) the yield strength and (c) elastic modulus values during 28 d of biodegradation.

5.3.6 Mechanical properties

Under uniaxial compression, all the porous iron-manganese specimens exhibited smooth stress-strain curves that started with a linear elastic region, followed by a plastic deformation region that corresponded to the typical strain-hardening behavior (**Figure 5.8a**). Among all the as-sintered iron-manganese alloys, the porous Fe₂₅Mn alloy exhibited the highest strain-hardening rate with

a strain-hardening exponent value of 0.80 (Figure 5.8a). Meanwhile, the porous Fe₃₀Mn and Fe₃₅Mn specimens demonstrated strain-hardening exponent values of 0.74 and 0.66, respectively. Prior to the *in vitro* immersion tests, the porous iron-manganese specimens (Fe₂₅Mn, Fe₃₀Mn, and Fe₃₅Mn) possessed yield strengths of 5.9 ± 1.2 MPa, 5.9 ± 1.3 MPa, and 6.4 ± 1.6 MPa, respectively. The elastic modulus values were 0.34 ± 0.03 GPa, 0.39 ± 0.02 GPa, 0.39 ± 0.02 GPa, respectively.

As a result of biodegradation, the yield strengths (Figure 5.8b) and elastic moduli (Figure 5.8c) of all the scaffold groups gradually decreased over time. After 28 d, the yield strengths were 3.0 ± 1.0 MPa, 3.0 ± 0.3 MPa, and 3.4 ± 0.4 MPa for Fe₂₅Mn, Fe₃₀Mn, and Fe₃₅Mn, respectively. At the same time, the elastic modulus values decreased to 0.16 ± 0.08 GPa, 0.21 ± 0.02 GPa, and 0.18 ± 0.03 GPa, respectively. Furthermore, the strain-hardening exponent declined up to 0.57 after 28 d of biodegradation.

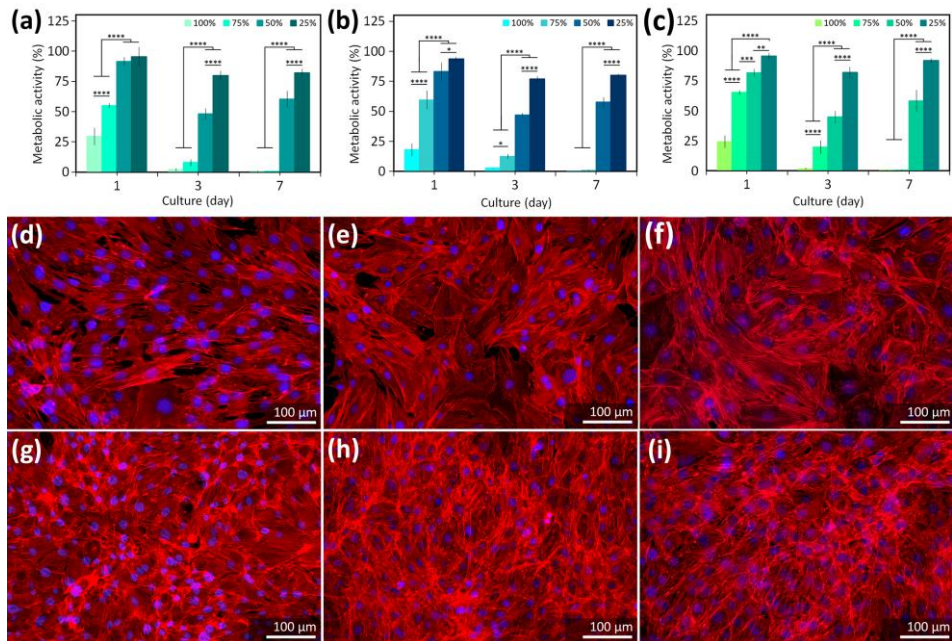


Figure 5.9. Indirect cytocompatibility of the various porous iron-manganese alloys for MC3T3-E1 preosteoblasts: (a, b, c) the metabolic activity of preosteoblasts after 1, 3, and 7 d of culture; rhodamine phalloidin (red) and DAPI (blue) fluorescence staining of preosteoblasts after 3 d of culture in (d, e, f) the 75% and (g, h, i) the 50% extracts of Fe₂₅Mn, Fe₃₀Mn and Fe₃₅Mn, respectively. **** = $p < 0.0001$, *** = $p < 0.001$, ** = $p < 0.01$, and * = $p < 0.05$.

5.3.7 *In vitro* cytotoxicity against preosteoblasts

The extracts of the porous iron-manganese specimens contained iron and manganese ions with concentrations of 60.2 ± 1.1 mg/mL and 52.4 ± 0.9 mg/mL for Fe₂₅Mn, 62.2 ± 1.1 mg/mL and 46.7 ± 0.5 mg/mL for Fe₃₀Mn, and 62.8 ± 1.7 mg/mL and 37.5 ± 0.8 mg/mL for Fe₃₅Mn, respectively. The indirect cell tests (*i.e.*, the PrestoBlue assay) (Figure 5.9a-c) revealed immediate cytotoxicity for all the 100% iron-manganese extracts with less than 30% metabolic activity of preosteoblasts after 24 h of cell culture and almost no metabolic activity after 7 d of cell culture. Similar cytotoxic effects were observed for all the 75% iron-manganese alloy extracts after 3 d of the culture and onwards. For the 50% iron-manganese alloy extracts, the metabolic activity of the cells reduced during the initial 3 d of cell culture and recovered after 7 d of cell culture. However, the values were still around 60%. Nonetheless, the preosteoblasts could proliferate and spread nicely, forming a confluent cell layer after 3 d of cell culture in the 75% extracts (Figure 5.9d-f) and 50% extracts (Figure 5.9g-i). The 25% iron-manganese extracts behaved the best with a more than 85% metabolic activity of preosteoblasts at all the time points.

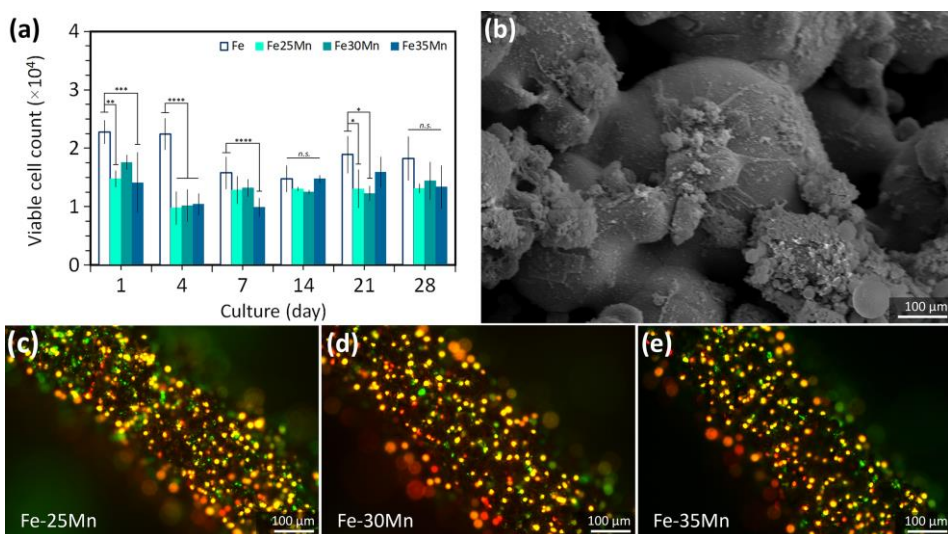


Figure 5.10. Direct cytocompatibility of the porous iron-manganese alloys: (a) the number of viable MC3T3-E1 preosteoblasts after up to 28 d of culture; (b) the morphology of preosteoblasts after 4 d of culture on the porous iron-manganese specimens; (c, d, e) calcein acetoxyethyl (green, showing viable cells) and ethidium homodimer-1 (red, showing damaged cells) fluorescence staining of preosteoblasts after 4 d of culture on porous Fe₂₅Mn, Fe₃₀Mn, and Fe₃₅Mn, respectively. **** = $p < 0.0001$, *** = $p < 0.001$, ** = $p < 0.01$, * = $p < 0.05$, and *n.s.* = not significant.

The direct culture of the preosteoblasts on the porous iron-manganese alloys resulted in a decreased number of viable cells after 24 h of culture relative to the pure iron scaffolds (*i.e.*, $1.4\text{--}1.8 \times 10^4$ cells) (Figure 5.10a). The number of preosteoblasts depleted after 7 d of culture to $0.9\text{--}1.3 \times 10^5$ cells and fluctuated during the subsequent cell culture period (*i.e.*, $1.3\text{--}1.5 \times 10^4$ cells and $1.3\text{--}1.4 \times 10^4$ cells after 14 and 28 d, respectively). The preosteoblasts attached to the surfaces developed many filopodia, although the cellular body was rather round-shaped (Figure 5.10b). Furthermore, a few green fluorescence-stained (viable) preosteoblasts were observed on all the porous iron-manganese specimens (Figure 5.10c-e). Nonetheless, the fluorescent staining showed uniformly seeded cells on the struts, indicating the high seeding efficiency of the assays.

5.4 Discussion

The extrusion-based 3D printed porous iron-manganese scaffolds developed in this research exhibited a highly encouraging potential to meet most of the requirements for iron-based bone substitution, including (i) weak paramagnetic properties with a very low magnetic susceptibility, meaning that the synthesized materials successfully tackled the fundamental issue of the MRI-incompatibility of pure iron, and (ii) significantly enhanced *in vitro* biodegradability (*i.e.*, $0.20\text{--}0.23$ mm/y) due to the addition of 30–35 wt% manganese to iron. The achieved values fall into the range of the suitable biodegradation rates for ideal bone substitutes (*i.e.*, $0.2\text{--}0.5$ mm/y) [42]. Furthermore, the porous alloys possessed sufficient mechanical properties even after a 28 d biodegradation period (*i.e.*, $E = 0.16\text{--}0.21$ GPa and $\sigma_y = 3.0\text{--}3.4$ MPa), and these values stayed within the range of the cancellous bone [43]. These results can be considered major breakthroughs in the development of porous iron-based biodegradable implants, motivating the follow-up research to address the important issue of cytocompatibility.

5.4.1 Extrusion-based 3D printing of the porous iron-manganese scaffolds

In the present research, extrusion-based 3D printing was successfully applied for the multi-material additive manufacturing of *ex situ*-alloyed porous iron-manganese scaffolds. The key to a successful fabrication process lies in a proper iron-manganese-containing ink formulation that should be stable and possess the required rheological properties for extrusion-based 3D printing. The hypromellose binder in the ink provides the ink with shear-thinning properties (Figure S5.3), which is particularly important for stable flow of the ink during the 3D printing process. The mixed iron-manganese powder loadings of 49.55 vol% (Fe₂₅Mn), 49.66 vol% (Fe₃₀Mn), and 49.78 vol% (Fe₃₅Mn) resulted in printable iron-manganese inks with the ability to retain the strut shape upon extrusion. The

ink formulations and 3D printing process parameters delivered the porous iron-manganese scaffolds with structural characteristics that were close to the original design (Figure 5.2a-c).

The 3D printed porous iron-manganese scaffolds were subjected to debinding to remove the binder in the inks at the temperature where the binder decomposed [34]. Considering more compact morphologies of the as-printed iron-manganese alloy struts, the debinding time was extended to 3 h from 1 h that was previously used for pure iron [34], to allow thorough binder removal and prevent any interactions between the binder residual and iron-manganese powder mixture. Thereafter, the porous iron-manganese scaffolds were sintered to facilitate the diffusion of manganese into iron and simultaneously get the powder particles bonded (Figure 5.2d-g). At high temperatures, manganese tends to be volatile [44]. As the temperature increases for the sintering stage, manganese sublimates and the vapor flows into the micropores of the struts, settling on the surface of the iron powder particles. Then, manganese diffuses into iron powder particles, leading to the expansion of the original iron particles, and the creation of a solid solution. As a consequence of this process, the as-sintered porous iron-manganese scaffolds expanded by 1.6%, which was also encountered in other fabrication routes involving sintering [21].

Iron-manganese alloys with more than 23 wt% manganese have a minor amount of the ϵ -martensite phase, together with the γ -austenite phase [45]. When higher than 28 wt% manganese is added to iron, only the γ -austenite single phase is present [45]. In the present research, the ϵ -martensite and γ -austenite dual phases were detected in the porous Fe₂₅Mn alloy and only the γ -austenite single phase was found in the porous Fe₃₀Mn and Fe₃₅Mn alloys (Figure 5.3a), which is in agreement with the literature. The presence of these phases instead of the α -ferrite phase is of crucial importance, as they provide anti-ferromagnetic behavior [46,47], which is required for iron-based biomaterials to be MRI-friendly.

Furthermore, the as-sintered porous iron-manganese alloys possessed a relatively low solid fraction of 63–67%, which may be a result of the diffusion of 25–35 wt% manganese into iron, leaving open pore spaces within the struts [22]. All the iron-manganese alloy scaffolds had an absolute porosity of 69% and up to 98.6% of pores were interconnected (Table 5.1). For bone substitution applications, open pores are advantageous for both biodegradability and biological properties. Well-channeled pore networks offer large surface area between powder particles, hence encouraging biodegradation and stimulating bone cell adhesion and ingrowth [48,49].

Table 5.3. Magnetic properties of the extrusion-based 3D-printed porous iron-manganese alloys in comparison with those found in the literature.

Sample groups	Magnetic susceptibility		Saturation magnetization at 2 T (Am ² /kg)	Remanence magnetization (Am ² /kg)	Ref.
	χ $\times 10^{-3}$	χ_g $\times 10^{-6}$ (m ³ /kg)			
Fe	5100 ± 47	640 ± 6	190.4 ± 0.1	0.0656 ± 0.0008	
Fe ₂₅ Mn	Do	3.5 ± 0.2	0.44 ± 0.03	0.349 ± 0.003	
	D28	4.4 ± 1.1	0.57 ± 0.14	0.58 ± 0.02	
Fe ₃₀ Mn	Do	3.4 ± 0.3	0.44 ± 0.04	0.32 ± 0.01	This study
	D28	3.0 ± 0.1	0.39 ± 0.02	0.54 ± 0.04	
Fe ₃₅ Mn	Do	3.3 ± 0.1	0.42 ± 0.02	0.316 ± 0.003	
	D28	3.1 ± 0.2	0.40 ± 0.03	0.53 ± 0.02	
Ti6Al4V	0.35 ± 0.04	0.08 ± 0.01	0.045 ± 0.001	0.0022 ± 0.0002	
Fe ₂₅ Mn	-	0.19	0.08*	0.011	
Fe ₃₀ Mn	-	0.19	0.08*	0.005	[50]
Fe ₃₅ Mn	-	0.18	0.07*	0.003	
Fe ₃₀ Mn ₆ Si ₁ Pd	-	-	0.4	-	[19]
Porous Fe ₃₀ Mn ₆ Si ₁ Pd	-	-	13.5	-	[13]
Fe ₃₅ Mn	-	-	0.5**	-	[22]

*at 0.5 T magnetic field; ** at 5 T.

5.4.2 Magnetic behavior

The ϵ -martensite and γ -austenite phases in the iron-manganese alloys are known for their anti-ferromagnetic properties [50]. In the present research, the magnetization of the porous iron-manganese alloys was measured in a high

magnetic field of 2 T, which is the typical intensity used in clinical MRI machines [51]. The magnetization saturation values of the porous iron-manganese alloys were three orders of magnitude lower than that of pure iron (Table 5.3), even after 28 d of biodegradation with the formation of degradation products that were ferrimagnetic. The magnetic properties of the porous iron-manganese alloys in comparison with the values found in the literature are listed in Table 5.3.

Even when the applied magnetic field is removed, the remanent magnetization of pure iron was still relatively high (*i.e.*, 0.0656), compared to that of the iron-manganese alloys (*i.e.*, < 0.0007) or Ti-6Al-4V (*i.e.*, 0.0022). The magnetic susceptibility values (χ) of the porous iron-manganese alloys (*i.e.*, $3.0\text{--}4.4 \times 10^{-3}$) were three orders of magnitude lower than that of pure iron (*i.e.*, 5.1). However, the values were still one order of magnitude higher than that of Ti-6Al-4V (*i.e.*, 0.3×10^{-3}). A material whose magnetic susceptibility value falls into the range of $10^{-5} < |\chi - \chi_{\text{water}}| < 10^{-2}$ (with $\chi_{\text{water}} = -9.05 \times 10^{-6}$) belongs to the first kind of magnetic field compatible materials [52]. The magnetic properties of such a material do not interfere significantly with the magnetic field of MRI machines, but may produce MRI artefacts [52]. Based on this theoretical analysis, the porous iron-manganese alloys developed in the present research can be categorized as the magnetic field compatibility of the first kind, which is in the same category as Ti-6Al-4V.

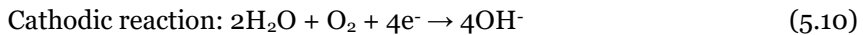
For most weakly paramagnetic medical devices (*e.g.*, titanium-based implants), MRI artefacts are inevitably observed, although the material is considered to be MRI-safe [53]. During MRI, a sharp transition in the magnetic susceptibility occurs between the paramagnetic material and the human tissue (*e.g.*, soft tissue = -9.05×10^{-6} and cortical bone = -8.86×10^{-6} [52]), which affects the readout [54]. It has recently been reported that a reduction in the volume of MRI artefacts can be achieved by introducing a porous geometry into the material [55–57], which is relevant to the bone substitution application. In general, our results have shown the prospects of iron-manganese scaffolds as weakly paramagnetic iron-based bone substitutes. In the near future, the detailed tests of the porous iron-manganese alloys, including the evaluation of the magnetically induced torque and displacement force, and radiofrequency-induced heating [51], will be performed to better understand the paramagnetic behavior of these biomaterials.

5.4.3 Biodegradation *in vitro*

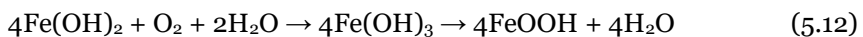
The *in vitro* biodegradation rates of the porous iron-manganese alloys at 28 d (*i.e.*, 0.18, 0.20, and 0.23 mm/y for Fe₂₅Mn, Fe₃₀Mn, and Fe₃₅Mn, respectively) are in the range of the values reported for Fe-Mn alloys in the literature (Table 5.4). Assuming a stable biodegradation rate beyond the 28 d of

the immersion tests, the porous Fe₃₀Mn and Fe₃₅Mn alloys degraded at the rates that are within the range of the ideal biodegradation rates suggested for bone substitutes (*i.e.*, 0.2–0.5 mm/y) [42]. The values were about 4.0 to 4.6 times higher than that of porous pure iron, fabricated by using the same 3D printing technique [34]. An addition of manganese to iron is known to improve the rate of biodegradation significantly by lowering the standard electrode potential [7,22]. In addition, the manganese-rich regions in the struts (Figure 5.2g) may promote local micro-galvanic corrosion. Besides the porous struts with original powder particle boundaries, the diffusion of manganese into iron powder particles created more open micropores, as compared to the pure iron counterpart [34], which would significantly increase the available surface area in the struts for the initiation of biodegradation.

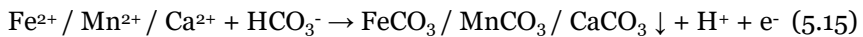
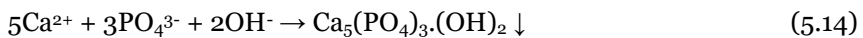
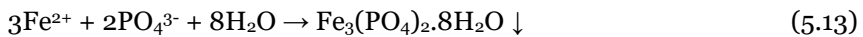
The biodegradation reactions can be described in a simplified way as:



As the biodegradation progresses (Equations 5.8-5.9), the local solution becomes alkaline due to the OH⁻ products of the cathodic reaction (Equation 5.10). The alkalinity of the solution with raised local pH will induce the precipitation of Fe- and Mn-based biodegradation products. For example, Fe²⁺ can be hydrolyzed to form Fe(OH)₂ (Equation 5.11). Then, Fe(OH)₂ can be further oxidized to form Fe(OH)₃ (Equation 5.12). Since Fe(OH)₃ is less stable, it will transform into a more stable compound (*e.g.*, FeOOH, Equation 5.12):



Besides FeOOH, the precipitated biodegradation products may contain calcium-based, phosphate-based, or carbonate-based compounds as well through the following reactions (Equations 13–15):



From these potential precipitation reactions, only γ-FeOOH and MnCO₃ were detected (Figure 5.3b). The calcium and phosphorus precipitates of low concentrations were identified only at the periphery, mostly during the late periods of the biodegradation tests (Figure 5.6f-g).

As a whole, the biodegradation products formed on the struts on the periphery as well as at the center of the scaffold (Figure 5.6), thereby passivating

the base material and decreasing the biodegradation rate during the subsequent immersion period (Figure 5.5d). The gradual densification of the morphology of the corrosion products (Figure 5.6) slows down the corrosion process too. During biodegradation, the variations of iron and manganese ion release with time could be attributed to their participation in the corrosion products (Figure 5.5e, f). Manganese ions were released ~10 times more than iron ions throughout the 28 d biodegradation, which is in agreement with the data reported in other studies [58,59]. The faster release of manganese ions is closely related to the medium composition and atmospheric condition. It has been reported that bicarbonate ions (HCO_3^-) promote faster manganese ion release [59]. In addition, biodegradation, occurring under a 5% CO_2 atmosphere, helps in maintaining the availability of HCO_3^- in the r-SBF medium [60]. These interactions not only induce manganese ion release but also cause the formation of carbonate compounds (*i.e.*, MnCO_3 , Equation 15).

As for the iron-based biodegradation products, the formation of $\gamma\text{-FeOOH}$ was identified (Figure 5.3b). Unlike the porous pure iron [34], iron phosphate biodegradation product did not form during the biodegradation of the porous iron-manganese alloys, as observed by other researchers [22,50]. In addition, calcium phosphate precipitation did not seem to have happened to a great extent. The concentrations of calcium and phosphorus elements detected at the periphery were relatively low (Figure 5.6i-j). In the center of the scaffolds (Figure S5.6), only very small amounts of calcium were detected in the Fe₃₀Mn and Fe₃₅Mn scaffolds along with iron, manganese, carbon and oxygen. Although the local solution could be alkalized by the cathodic response during the early period of the immersion tests (Equation 10), the pH value would be balanced by the hydrogen ions released during the hydrolysis of ferrous ions (Equation 11) and the precipitation of MnCO_3 compounds (Equation 15). A recent study showed that the local pH value of porous iron-manganese remained between 7.1 to 7.3 after 24 h immersion in Hank's balanced salt solution [61,62]. In this case, the formation of stable calcium phosphate might have been impeded, since the precipitation was more favorable at a higher pH value [63]. Moreover, the absence of calcium phosphate compounds might be possible due to the swift release of iron or manganese ions and the formation of iron-manganese products during biocorrosion [13].

Overall, the biodegradation products of the porous iron-manganese alloys, both at the periphery and at the center of the scaffolds, appeared to be more chemically diverse (Figure 5.6) than those of porous pure iron [34]. After 28 d of immersion, a variety of elements, including calcium, phosphorus, sodium, carbon, oxygen, and even traces of chlorine, were present in the peripheral degradation products of the porous iron-manganese alloys (Figure 5.6g, j). At the

center, carbon was detected to be participating in the oxide-containing degradation products (Figure 5.6k).

Table 5.4. *In vitro* biodegradation rates obtained from the immersion tests of the extrusion-based 3D-printed porous iron-manganese alloys in comparison with those found in the literature.

Material and fabrication method		Porosity (%)	Immersion condition	Time point	Corrosion rate (mm/y)	Ref.
Fe25Mn	Extrusion-based 3D printing and sintering	69	Static, 37 °C, 5% CO ₂ , r-SBF	28 d	0.18-0.23	This study
Fe30Mn						
Fe35Mn						
Fe35Mn	Space holder	27.3 ± 0.6	Static, 37 °C, SBF	14 d	0.5	[12]
		40.0 ± 3.9				
		48.2 ± 0.3				
Fe35Mn	Binder jetting	39.3 ± 1.5	Static, 37 °C, Hank's balanced salt solution	28 d	0.03	[27]
Fe30Mn	Space holder	43	Static - 37 °C, 5% CO ₂ , DMEM	30 d	0.79	[14]
Fe20Mn	Powder metallurgy and sintering	13.9	Quasi static - 37 °C, 5% CO ₂ , Hank's balanced salt solution	30 d	0.116 ± 0.009	[22]
Fe30Mn		20.6			0.141 ± 0.012	
Fe35Mn		21.3			0.306 ± 0.022	
Fe30Mn	Space holder	32.5 ± 3	Static, 37 °C, 5% CO ₂ , αMEM	30 d	0.389 ± 0.05	[23]
Fe25Mn	Selective laser melting	66.72 ± 2.4	Static, 37 °C, SBF	30 d	0.23 ± 0.05	[28]
Fe35Mn	Selective laser melting	42.6 ± 0.2	Quasi static, 37 °C, SBF	30 d	0.42 ± 0.03	[29]
Fe30Mn	Sponge impregnation and sintering	84.6 ± 2.9	Static - 37 °C, SBF	14 d	0.81	[24]

The electrochemical responses of the porous iron-manganese alloys indicated stable OCP values throughout the immersion period, as compared to porous iron scaffolds (Figure 5.7a). In addition, the polarization resistance values of the porous iron-manganese alloys are much lower, compared to the polarization resistance exhibited by porous iron (Figure 5.7b). Such trends of OCP and polarization resistance imply that iron-manganese biodegradation products are less passivating, compared to those for pure iron. This means that the porous iron-manganese alloys can maintain the same level of propensity to biodegrade over the immersion time. Moreover, both Nyquist (Figure 5.7c) and Bode impedance plots (Figure 5.7d) demonstrated the same trend as the LPR results. The Nyquist plots of porous iron-manganese remain in a semicircle shape throughout the immersion time (Figure 5.7c), unlike the impedance plots of porous iron scaffolds reported in our previous publication [34]. Altogether, the EDS analysis (Figure 5.6) and electrochemical results (Figure 5.7) demonstrated that the biodegradation products, particularly those involving the participation of manganese, influenced the corrosion resistance of the iron-based passivating layer. Although a more detailed study would be required, this finding is in agreement with the hypothesis suggested by other researchers on iron-manganese alloys containing more than 20 wt% manganese [22,64,65].

Furthermore, the volume losses of the porous iron-manganese alloys found in the immersion tests were 21.1–26.8% (calculated from the mass loss values) after 28 d. Although the corrosion rates of the porous iron-manganese alloys are in the range of the values reported in the literature (Table 5.4), the recent *in vivo* research on a porous Fe₃₀Mn biomaterial (with 38–47% porosity) has reported 10.1–20.9% volume loss after 48 weeks of implantation [30]. The biodegradation of iron-based biomaterials has been reported to be slower *in vivo* than *in vitro* [66]. This is because the biodegradation of iron-manganese is strongly dependent on the dissolved O₂ availability (Equation 10). The *in vitro* immersion tests in the current research were performed in an ambient O₂ atmosphere (*i.e.*, 21%), which was very different from the low concentration of dissolved O₂ near bone marrow region (*e.g.*, < 4.2%) [67]. Therefore, future *in vitro* biodegradation tests of iron-based materials should be performed in a controlled O₂ environment. More *in vivo* studies on the porous iron-manganese alloys need to be carried out to determine to what extent the *in vitro* biodegradation results can be translated to the actual conditions.

5.4.4 Mechanical behavior

Biodegradation decreases the mechanical properties of bone substitutes over time. The rate of bone regeneration and the rate of decrease in the mechanical properties of the implant should, therefore, be balanced with each other to ensure

that the mechanical support continues to be available at all times. The porous iron-manganese biomaterials presented here exhibited bone-mimicking mechanical properties in the range of cancellous bone ($E = 0.02\text{--}2.0$ GPa and $\sigma_y = 0.1\text{--}30$ MPa [43]) even after 28 d of *in vitro* biodegradation. The influence of the manganese content on the mechanical properties of our porous biomaterials was limited, which is in contrast with the observations made for bulk iron-manganese alloys that show decreases in the yield strength as the manganese content increases [50]. This could be explained, considering the strong dependence of the mechanical properties of the porous materials on the bonding between the sintered powder particles and the distribution of the random open micropores present in the struts. In addition, the γ -austenite phase in the porous iron-manganese could retain the ductility of the materials even after biodegradation (Figure 5.8a), which is an important mechanical property for bone substitutes to be able to endure cyclic loading.

Due to the decreases in the solid fraction of the iron-manganese scaffolds after 28 d of biodegradation, the yield strengths and elastic moduli of the porous iron-manganese alloys declined by 47.2–57.1% and 47.1–53.9%, respectively (Figure 5.8b, c). Degradation of the mechanical properties has also been reported in other studies after *in vitro* biodegradation [29,68]. In *in vivo* studies, however, reductions in elastic modulus (by as much as 42.3%) and yield strength (by 23.3%) have been reported only after 48 weeks [30]. Although the retrieved specimens may still contain newly matured bone tissue in the pores of the scaffolds, which may contribute to its mechanical properties, the higher mechanical properties that are observed *in vivo* are most likely due to the slower biodegradation of the materials *in vivo*, as previously discussed.

5.4.5 Cytocompatibility

The biocompatibility of an iron-manganese alloy is closely related to the concentration of iron and manganese ions released into the cell culture medium. To evaluate the indirect cytotoxicity of the porous iron-manganese alloys, the iron-manganese extracts were prepared under an extreme condition (*i.e.*, 72 h extraction in the physiological conditions [69]). The metabolic activity of preosteoblasts (Figure 5.9a–c) improved with the dilution ratio of the extract. The original 100% iron-manganese extracts showed instantaneous metabolic inhibition for preosteoblasts and cell lysis with no viable cells left for actin and nucleus staining. For this reason, all the 100% iron-manganese extracts would be categorized as cytotoxic grade 4, according to ISO 10993-5 [69]. Likewise, the 75% iron-manganese extracts demonstrated an immediate metabolic activity reduction, however, nice spreading and a healthy morphology of the cells were still present (Figure 5.9d–f). Therefore, the 75% extracts fall into the (moderately)

cytotoxic grade 3 category. After 2× dilution (50%), the iron-manganese extracts were categorized as mildly toxic (grade 2), where less than 50% metabolic inhibition was observable, although the growth of preosteoblasts did not appear to be hindered (Figure 5.9g-i). At 4× dilution (25%), the iron-manganese alloy extracts exhibited a non-cytotoxic response (grade 1) with > 80% preosteoblast metabolic activity.

The inhibitory concentrations (IC_{50}) of iron and manganese ions towards preosteoblasts have been reported to be 53.2–88.5 mg/L and 4.8 mg/L, respectively [8]. In the 100% iron-manganese extracts, the iron ion release was 60.2–62.8 mg/L, which is in the range of the IC_{50} value. At the same time, the manganese ion release, which varied between 37.5–52.4 mg/L, is significantly higher than the IC_{50} value, which is why the extracts at higher concentrations were cytotoxic. The systemic toxicity due to iron ions is usually rare, because most iron ions are not free-flowing, but chaperoned by proteins (*e.g.*, transferrin [70]). However, extensive exposure of free iron ions can induce oxidative stresses [71]. In the case of manganese, bone is one of the tissues with a significant manganese reserve [72]. This could explain the observation that despite the high concentration of manganese ions even after 4× dilution, the preosteoblast metabolic activity remained undisturbed. Nevertheless, a too high manganese ion concentration in bone is strongly related to neurotoxicity [72].

The present direct cultures involved a high ratio of cell culture medium volume to the sample surface area, which may better mimic the actual human body conditions, considering the possibility that more medium could help reduce the local accumulation of metal ions. Our results, however, demonstrated the cytotoxicity during the initial period of cell culture, *i.e.*, during 4 d, and cell growth inhibition up to 28 d (Figure 5.10a). The cytotoxic results were similar to those obtained in several *in vitro* studies [13,23], but at the same time contradicted those of other studies [24,28–30]. To understand the direct cell culture results better, we examined the biodegradation of the porous iron-manganese alloys in the cell culture medium. Unlike in the r-SBF medium (Figure 5.6), hardly any biodegradation products were deposited even after 7 d and 28 d of immersion in the cell culture medium. This occurred due to the presence of serum in the cell culture medium [73,74], where metal ions were bonded by proteins [70,72], thus preventing the deposition of the biodegradation products. The struts of the scaffolds remained porous, being almost identical to those in the as-sintered structures (Figure S5.7). Undeniably, such a porous surface morphology allowed for rapid biodegradation (=more metal ion release), therefore inducing cytotoxicity. In earlier *in vivo* studies, iron-based biomaterials have been found to be systemically biocompatible [3,75–77], which is in agreement with our indirect cell culture results with a higher dilution ratio of the

extract. Even so, other researchers have also found the evidence of *in vivo* local inflammation, caused by iron-based biomaterials [76,77]. Despite the existing *in vitro* cytotoxicity, the preosteoblasts extended filopodia (Figure 5.10b) that may be due to the porous morphology of the struts and deposited calcium and phosphorus compounds as the biodegradation products (Figure S5.7). Considering the much enhanced *in vitro* biodegradation rates of the porous iron-manganese alloys as compared to the biodegradation rate of pure iron, the obtained cytotoxicity results are not a surprise. Introducing a bioactive ceramic material into the iron-based scaffolds [78–80] will be explored to improve the biocompatibility of the porous iron-based materials in order to meet all the requirements for ideal bone substitution.

5.5 Conclusion

We fabricated porous *ex situ*-alloyed iron-manganese scaffolds using extrusion-based 3D printing from elemental powders for the first time and characterized the *in vitro* properties of these materials for their intended use as bone substitutes. The scaffolds presented hierarchical interconnected pore networks with accurately controlled macropores and randomly distributed micropores. The addition of manganese to iron transformed the latter into a weakly paramagnetic material, which means these biomaterials can be classified as the first kind MRI-friendly biomaterials. The *in vitro* biodegradation rates of the porous iron-manganese alloys developed here are within the range of 0.18–0.23 mm/y after 28 d, as desired for ideal bone substitution. The mechanical properties of the porous iron-manganese scaffolds decreased over the *in vitro* biodegradation period of 28 d, but the strengths and elastic moduli remained in the range of the mechanical properties of the cancellous bone. The indirect cultures of preosteoblasts evidenced various levels of cytocompatibility of the porous iron-manganese alloys, depending on the dilution ratio of the extract. In the direct cultures, the cells showed their ability to attach to the scaffolds by developing numerous filopodia, but their viability was reduced by the presence of manganese and its associated effects on the scaffolds biodegradation. In conclusion, extrusion-based 3D printing is a viable multi-material additive manufacturing technique and, in combination with sintering, could deliver MRI-friendly porous iron-manganese biomaterials with significantly enhanced biodegradability and bone-mimicking mechanical properties as desired for bone substitutes.

5.6 Supplementary material

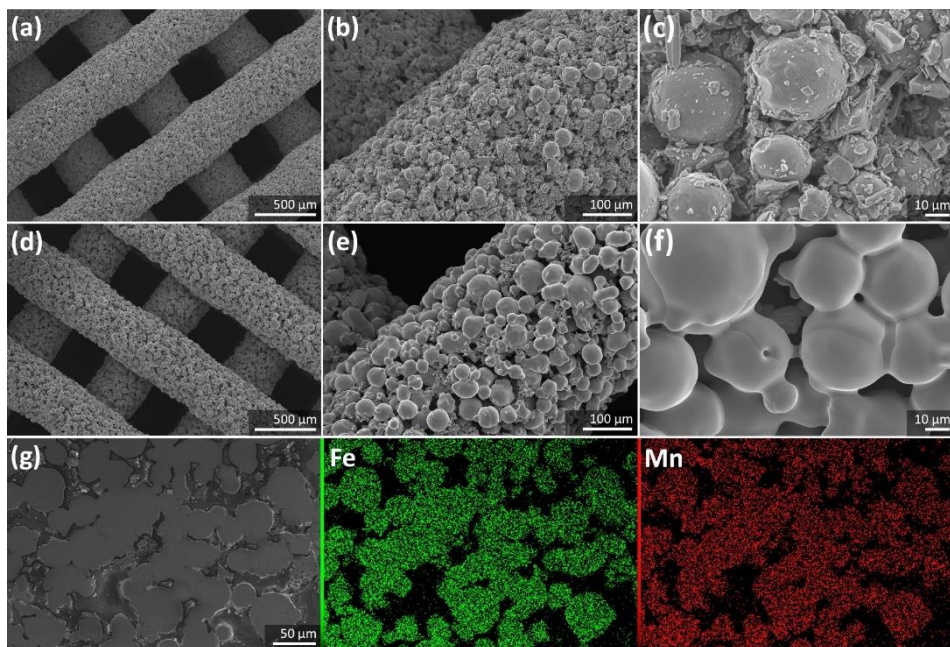


Figure S5.1. Morphologies of porous Fe₃₀Mn: (a, b, c) in the as-printed condition and (d, e, f) in the as-sintered condition at different magnifications, and (g) chemical composition mapping on the cross section of porous iron-manganese struts.

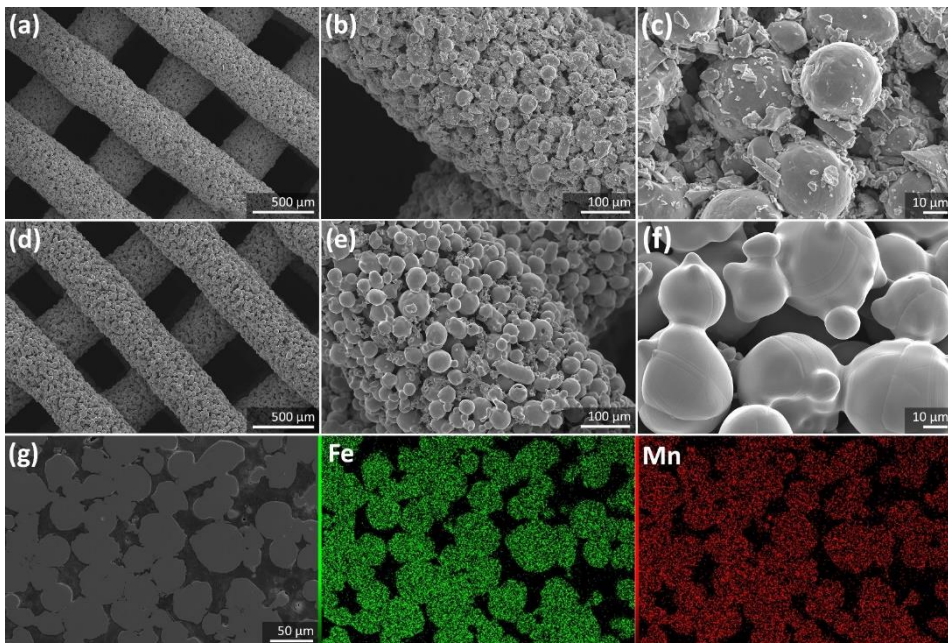


Figure S5.2. Morphologies of porous Fe₂₅Mn: (a, b, c) in the as-printed condition and (d, e, f) in the as-sintered condition at different magnifications, and (g) chemical composition mapping on the cross section of porous iron-manganese struts.

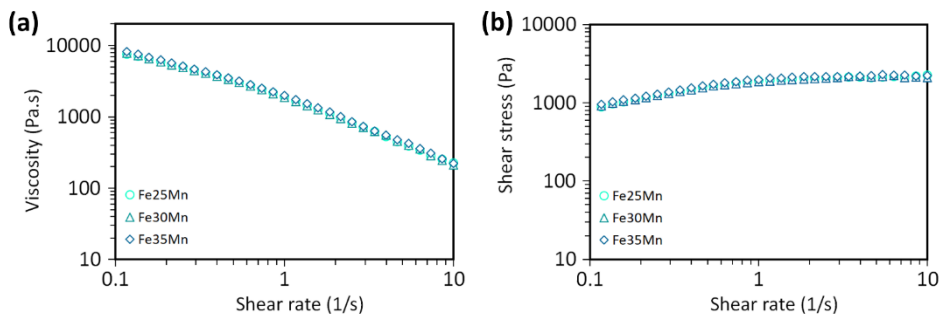


Figure S5.3. Rheology curves of the iron-manganese-containing inks: (a) the viscosity values and (b) the shear stress values as a function of shear rate.

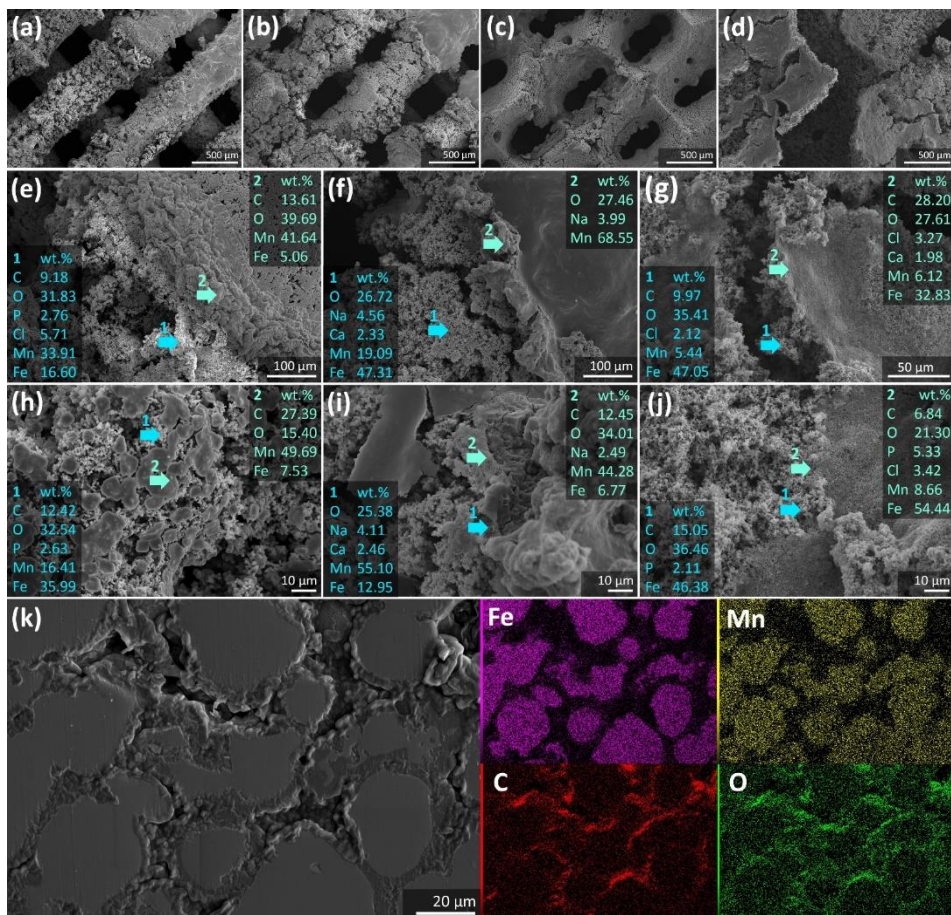


Figure S5.4. Morphologies and chemical compositions of the *in vitro* biodegradation products on porous Fe₃₀Mn: at the periphery after (a, e, h) 24 h, (b, f, i) 7 d, (c) 14 d, and (d, g, j) 28 d of biodegradation, and (k) in the center of the scaffolds after 28 d of biodegradation. The arrow and number indicate the location of the EDS analysis.

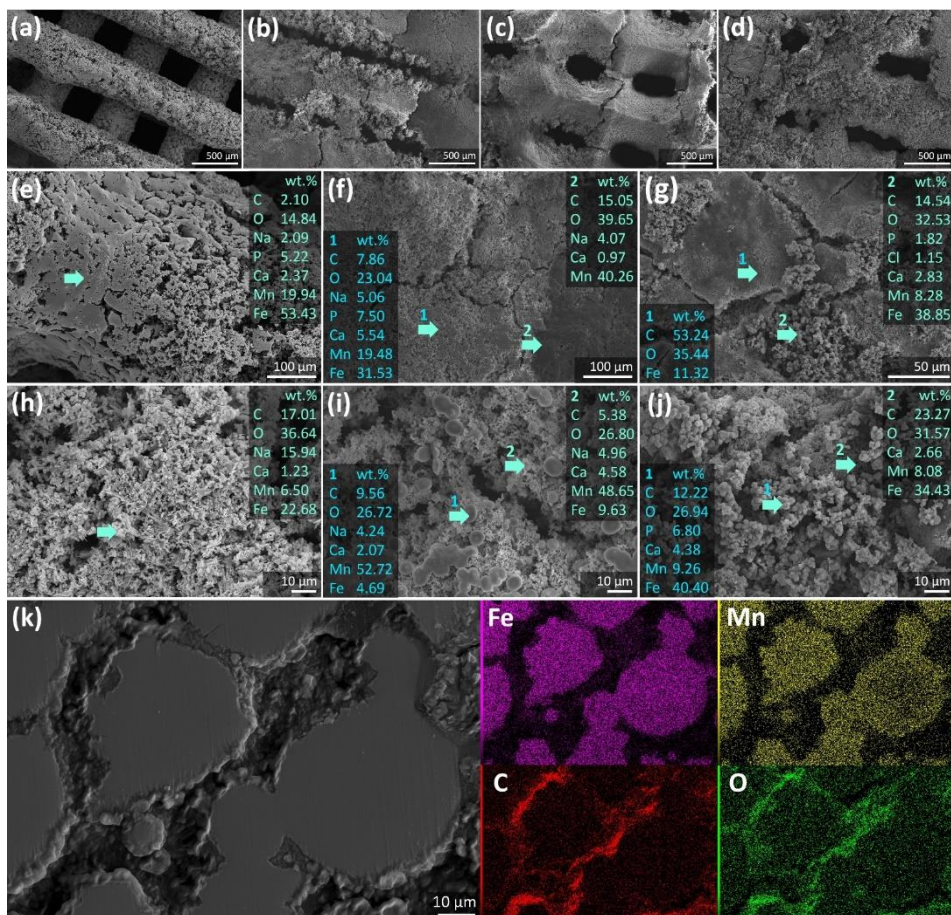


Figure S5.5. Morphologies and chemical compositions of the *in vitro* biodegradation products on porous Fe₂₅Mn: at the periphery after (a, e, h) 24 h, (b, f, i) 7 d, (c) 14 d, and (d, g, j) 28 d of biodegradation, and (k) in the center of the scaffolds after 28 d of biodegradation. The arrow and number indicate the location of the EDS analysis.

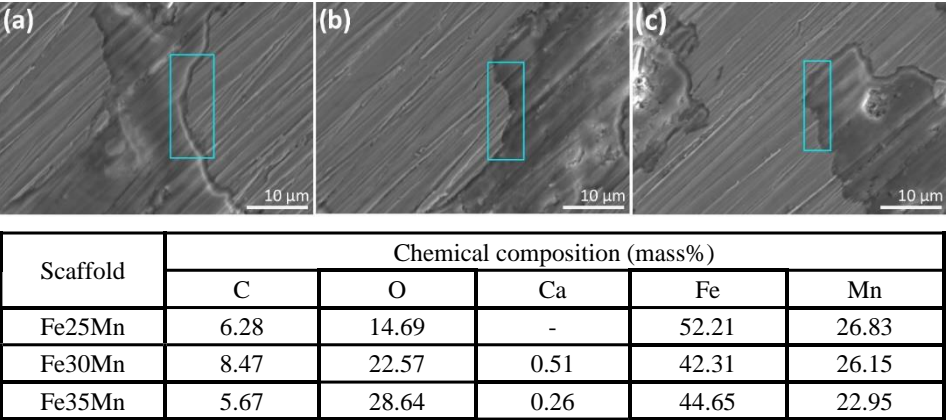


Figure S5.6. Morphologies and chemical compositions of the *in vitro* biodegradation products on the cross section of the porous (a) Fe₂₅Mn, (b) Fe₃₀Mn, and (c) Fe₃₅Mn after 28 d of biodegradation, at high magnification. The selected region indicate the location of the EDS analysis.

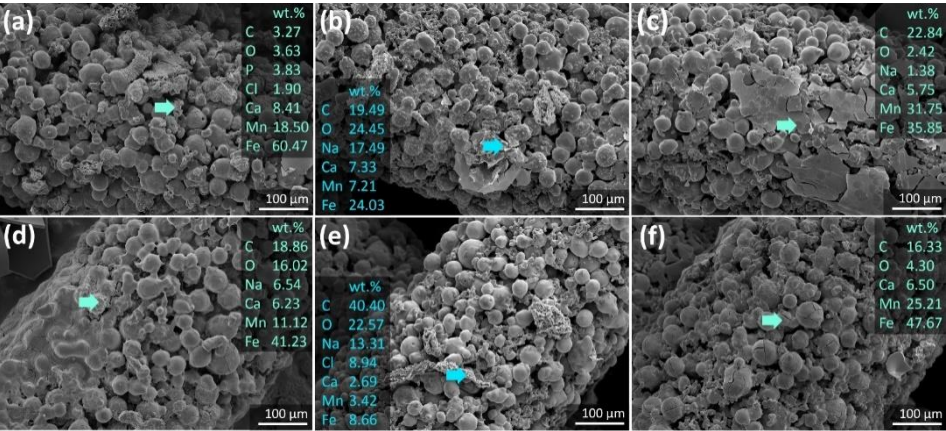


Figure S5.7. *In vitro* biodegradation products and the strut morphologies of porous (a, d) Fe₂₅Mn, (b, e) Fe₃₀Mn, and (c, f) Fe₃₅Mn after (a, b, c) 7 d and (d, e, f) 28 d immersion in the cell culture medium.

Bibliography

- [1] J. He, F.L. He, D.W. Li, Y.L. Liu, Y.Y. Liu, Y.J. Ye, D.C. Yin, Advances in Fe-based biodegradable metallic materials, *RSC Adv.* 6 (2016) 112819–112838. <https://doi.org/10.1039/C6RA20594A>.
- [2] R. Gorejová, L. Haverová, R. Oriňáková, A. Oriňák, M. Oriňák, Recent advancements in Fe-based biodegradable materials for bone repair, *J. Mater. Sci.* 54 (2019) 1913–1947. <https://doi.org/10.1007/s10853-018-3011-z>.
- [3] T. Kraus, F. Moszner, S. Fischerauer, M. Fiedler, E. Martinelli, J. Eichler, F. Witte, E. Willbold, M. Schinhammer, M. Meischel, P.J. Uggowitzer, J.F. Löffler, A. Weinberg, Biodegradable Fe-based alloys for use in osteosynthesis: Outcome of an *in vivo* study after 52 weeks, *Acta Biomater.* 10 (2014) 3346–3353. <https://doi.org/10.1016/j.actbio.2014.04.007>.
- [4] L. Filli, R. Luechinger, T. Frauenfelder, S. Beck, R. Guggenberger, N. Farshad-Amacker, G. Andreisek, Metal-induced artifacts in computed tomography and magnetic resonance imaging: comparison of a biodegradable magnesium alloy versus titanium and stainless steel controls, *Skeletal Radiol.* 44 (2015) 849–856. <https://doi.org/10.1007/s00256-014-2057-5>.
- [5] H. Hermawan, H. Alamdari, D. Mantovani, D. Dubé, Iron-manganese: New class of metallic degradable biomaterials prepared by powder metallurgy, *Powder Metall.* 51 (2008) 38–45. <https://doi.org/10.1179/174329008X284868>.
- [6] Y. Ishikawa, Y. Endoh, Antiferromagnetism of γ -FeMn alloys, *J. Appl. Phys.* 39 (1968) 1318–1319. <https://doi.org/10.1063/1.1656274>.
- [7] M. Schinhammer, A.C. Hânzi, J.F. Löffler, P.J. Uggowitzer, Design strategy for biodegradable Fe-based alloys for medical applications, *Acta Biomater.* 6 (2010) 1705–1713. <https://doi.org/10.1016/j.actbio.2009.07.039>.
- [8] A. Yamamoto, R. Honma, M. Sumita, Cytotoxicity evaluation of 43 metal salts using murine fibroblasts and osteoblastic cells, *J. Biomed. Mater. Res.* 39 (1998) 331–40. [https://doi.org/10.1002/\(SICI\)1097-4636\(199802\)39:2<331::AID-JBM22>3.0.CO;2-E](https://doi.org/10.1002/(SICI)1097-4636(199802)39:2<331::AID-JBM22>3.0.CO;2-E).
- [9] E. Zhang, H. Chen, F. Shen, Biocorrosion properties and blood and cell compatibility of pure iron as a biodegradable biomaterial, *J. Mater. Sci. Mater. Med.* 21 (2010) 2151–2163. <https://doi.org/10.1007/s10856-010-4070-0>.
- [10] A.A. Zadpoor, Meta-biomaterials, *Biomater. Sci.* 8 (2020) 18–38. <https://doi.org/10.1039/c9bm01247h>.
- [11] S.M. Ahmadi, R. Kumar, E. V. Borisov, R. Petrov, S. Leeftang, Y. Li, N. Tümer, R. Huizenga, C. Ayas, A.A. Zadpoor, V.A. Popovich, From microstructural design to surface engineering: A tailored approach for improving fatigue life of additively manufactured meta-biomaterials, *Acta Biomater.* 83 (2019) 153–166. <https://doi.org/10.1016/j.actbio.2018.10.043>.
- [12] Q. Zhang, P. Cao, Degradable porous Fe-35wt.% Mn produced via powder sintering from NH_4HCO_3 porogen, *Mater. Chem. Phys.* 163 (2015) 394–401. <https://doi.org/10.1016/j.matchemphys.2015.07.056>.
- [13] Y.P. Feng, N. Gaztelumendi, J. Fornell, H.Y. Zhang, P. Solsona, M.D. Baró, S. Suriñach, E. Ibáñez, L. Barrios, E. Pellicer, C. Nogués, J. Sort, Mechanical properties, corrosion performance and cell viability studies on newly developed porous Fe-Mn-Si-Pd alloys, *J. Alloys Compd.* 724 (2017) 1046–1056. <https://doi.org/10.1016/j.jallcom.2017.07.112>.
- [14] M. Heiden, E. Nauman, L. Stanciu, Bioresorbable Fe–Mn and Fe–Mn–HA materials for orthopedic implantation: Enhancing degradation through porosity control, *Adv. Healthc. Mater.* 6 (2017) 1–12. <https://doi.org/10.1002/adhm.201700120>.
- [15] Y. Yin, Q. Huang, L. Liang, X. Hu, T. Liu, Y. Weng, T. Long, Y. Liu, Q. Li, S. Zhou, H. Wu, *In vitro* degradation behavior and cytocompatibility of ZK30/bioactive glass composites fabricated by selective laser melting for biomedical applications, *J. Alloys Compd.* 785 (2019) 38–45. <https://doi.org/10.1016/j.jallcom.2019.01.165>.
- [16] Y. Li, H. Jahr, J. Zhou, A.A. Zadpoor, Additively manufactured biodegradable porous metals, *Acta Biomater.* 115 (2020) 29–50. <https://doi.org/10.1016/j.actbio.2020.08.018>.
- [17] B. Liu, Y.F. Zheng, L. Ruan, *In vitro* investigation of Fe₃₀Mn₆Si shape memory alloy as potential biodegradable metallic material, *Mater. Lett.* 65 (2011) 540–543. <https://doi.org/10.1016/j.matlet.2010.10.068>.
- [18] M. Schinhammer, P. Steiger, F. Moszner, J.F. Löffler, P.J. Uggowitzer, Degradation

- performance of biodegradable FeMnC(Pd) alloys, *Mater. Sci. Eng. C* 33 (2013) 1882–1893. <https://doi.org/10.1016/j.msec.2012.10.013>.
- [19] Y.P. Feng, A. Blanquer, J. Fornell, H. Zhang, P. Solsona, M.D. Baró, S. Suriñach, E. Ibáñez, E. García-Lecina, X. Wei, R. Li, L. Barrios, E. Pellicer, C. Nogués, J. Sort, Novel Fe-Mn-Si-Pd alloys: Insights into mechanical, magnetic, corrosion resistance and biocompatibility performances, *J. Mater. Chem. B* 4 (2016) 6402–6412. <https://doi.org/10.1039/c6tb01951j>.
- [20] H. Hermawan, D. Dubé, D. Mantovani, Development of degradable Fe-35Mn alloy for biomedical application, *Adv. Mater. Res.* 15 (2007) 107–112. <https://doi.org/10.4028/www.scientific.net/amr.15-17.107>.
- [21] M. Kupková, M. Hrubovčáková, M. Kupka, R. Orínáková, A.M. Turonová, Sintering behaviour, graded microstructure and corrosion performance of sintered Fe-Mn biomaterials, *Int. J. Electrochem. Sci.* 10 (2015) 9256–9268.
- [22] M.S. Dargusch, A. Dehghan-Manshadi, M. Shahbazi, J. Venezuela, X. Tran, J. Song, N. Liu, C. Xu, Q. Ye, C. Wen, Exploring the role of manganese on the microstructure, mechanical properties, biodegradability, and biocompatibility of porous iron-based scaffolds, *ACS Biomater. Sci. Eng.* 5 (2019) 1686–1702. <https://doi.org/10.1021/acsbiomaterials.8b01497>.
- [23] S.M. Huang, E.A. Nauman, L.A. Stanciu, Investigation of porosity on mechanical properties, degradation and *in-vitro* cytotoxicity limit of Fe₃₀Mn using space holder technique, *Mater. Sci. Eng. C* 99 (2019) 1048–1057. <https://doi.org/10.1016/j.msec.2019.02.055>.
- [24] P. Liu, D. Zhang, Y. Dai, J. Lin, Y. Li, C. Wen, Microstructure, mechanical properties, degradation behavior, and biocompatibility of porous Fe-Mn alloys fabricated by sponge impregnation and sintering techniques, *Acta Biomater.* 114 (2020) 485–496. <https://doi.org/10.1016/j.actbio.2020.07.048>.
- [25] A.A. Zadpoor, Additively manufactured porous metallic biomaterials, *J. Mater. Chem. B* 7 (2019) 4088–4117. <https://doi.org/10.1039/c9tb00420c>.
- [26] D.T. Chou, D. Wells, D. Hong, B. Lee, H. Kuhn, P.N. Kumta, Novel processing of iron-manganese alloy-based biomaterials by inkjet 3-D printing, *Acta Biomater.* 9 (2013) 8593–8603. <https://doi.org/10.1016/j.actbio.2013.04.016>.
- [27] D. Hong, D.T. Chou, O.I. Velikokhatnyi, A. Roy, B. Lee, I. Swink, I. Issaev, H.A. Kuhn, P.N. Kumta, Binder-jetting 3D printing and alloy development of new biodegradable Fe-Mn-Ca/Mg alloys, *Acta Biomater.* 45 (2016) 375–386. <https://doi.org/10.1016/j.actbio.2016.08.032>.
- [28] C. Shuai, W. Yang, Y. Yang, H. Pan, C. He, F. Qi, D. Xie, H. Liang, Selective laser melted Fe-Mn bone scaffold: Microstructure, corrosion behavior and cell response, *Mater. Res. Express* 7 (2019) 015404. <https://doi.org/10.1088/2053-1591/ab62f5>.
- [29] D. Carluccio, C. Xu, J. Venezuela, Y. Cao, D. Kent, M. Birmingham, A.G. Demir, B. Previtali, Q. Ye, M. Dargusch, Additively manufactured iron-manganese for biodegradable porous load-bearing bone scaffold applications, *Acta Biomater.* 103 (2020) 346–360. <https://doi.org/10.1016/j.actbio.2019.12.018>.
- [30] Y. Nie, G. Chen, H. Peng, S. Tang, Z. Zhou, F. Pei, B. Shen, *In vitro* and 48 weeks *in vivo* performances of 3D printed porous Fe-30Mn biodegradable scaffolds, *Acta Biomater.* 121 (2021) 724–740. <https://doi.org/10.1016/j.actbio.2020.12.028>.
- [31] A.L. Rutz, K.E. Hyland, A.E. Jakus, W.R. Burghardt, R.N. Shah, A multimaterial bioink method for 3D printing tunable, cell-compatible hydrogels, *Adv. Mater.* 27 (2015) 1607–1614. <https://doi.org/10.1002/adma.201405076>.
- [32] A.E. Jakus, S.L. Taylor, N.R. Geisendorfer, D.C. Dunand, R.N. Shah, Metallic architectures from 3D-printed powder-based liquid inks, *Adv. Funct. Mater.* 25 (2015) 6985–6995. <https://doi.org/10.1002/adfm.201503921>.
- [33] N.E. Putra, M.J. Mirzaali, I. Apachitei, J. Zhou, A.A. Zadpoor, Multi-material additive manufacturing technologies for Ti-, Mg-, and Fe-based biomaterials for bone substitution, *Acta Biomater.* 109 (2020) 1–20. <https://doi.org/10.1016/j.actbio.2020.03.037>.
- [34] N.E. Putra, M.A. Leeftang, M. Minneboo, P. Taheri, L.E. Fratila-Apachitei, J.M.C. Mol, J. Zhou, A.A. Zadpoor, Extrusion-based 3D printed biodegradable porous iron, *Acta Biomater.* 121 (2021) 741–756. <https://doi.org/10.1016/j.actbio.2020.11.022>.
- [35] ASTM B963-17, Standard test methods for oil content, oil-impregnation efficiency, and surface-connected porosity of sintered powder metallurgy (PM) products using Archimedes' principle, ASTM International, 2017. <https://doi.org/10.1520/B0963-14>.
- [36] A. Oyane, H.M. Kim, T. Furuya, T. Kokubo, T. Miyazaki, T. Nakamura, Preparation and

- assessment of revised simulated body fluids, *J. Biomed. Mater. Res. - Part A*. 65 (2003) 188–195. <https://doi.org/10.1002/jbm.a.10482>.
- [37] L. Yang, E. Zhang, Biocorrosion behavior of magnesium alloy in different simulated fluids for biomedical application, *Mater. Sci. Eng. C*. 29 (2009) 1691–1696. <https://doi.org/10.1016/j.msec.2009.01.014>.
- [38] ASTM G1-03, Standard practice for preparing, cleaning, and evaluating corrosion test specimens, ASTM International, (2017). <https://doi.org/10.1520/G0001-03R17E01.2>.
- [39] ASTM G32-72, Standard practice for laboratory immersion corrosion testing of metals., ASTM International, (2004). <https://doi.org/10.1520/G0031-72R04.2>.
- [40] ISO 13314, Mechanical testing of metals - Ductility testing - Compression test for porous and cellular metals, International Organization for Standardization, 2011. <https://doi.org/ISO 13314:2011>.
- [41] ISO 10993-12, Sample preparation and reference materials, International Organization for Standardization, 2012. [https://doi.org/10.1016/S0080-8784\(08\)60069-1](https://doi.org/10.1016/S0080-8784(08)60069-1).
- [42] C. Shuai, S. Li, S. Peng, P. Feng, Y. Lai, C. Gao, Biodegradable metallic bone implants, *Mater. Chem. Front.* 3 (2019) 544–62. <https://doi.org/10.1039/c8qm00507a>.
- [43] E.F. Morgan, G.U. Unnikrisnan, A.I. Hussein, Bone mechanical properties in healthy and diseased states, *Annu. Rev. Biomed. Eng.* 20 (2018) 119–43. <https://doi.org/10.1146/annurev-bioeng-062117-121139>.
- [44] A. Salak, M. Selecká, R. Bureš, Manganese in ferrous powder metallurgy, *Powder Metall. Prog.* 1 (2001) 41–58.
- [45] J. Martínez, S.M. Cotes, A.F. Cabrera, J. Desimoni, A. Fernández Guillermet, On the relative fraction of ϵ martensite in γ -Fe-Mn alloys, *Mater. Sci. Eng. A*. 408 (2005) 26–32. <https://doi.org/10.1016/j.msea.2005.06.019>.
- [46] A. Rabinkin, On magnetic contributions to $\gamma \rightarrow \epsilon$ phase transformations in Fe-Mn alloys, *Calphad*. 3 (1979) 77–84. [https://doi.org/10.1016/0364-5916\(79\)90008-7](https://doi.org/10.1016/0364-5916(79)90008-7).
- [47] M. Acet, T. Schneider, B. Gehrmann, E. Wassermann, The magnetic aspects of the γ - α and γ - ϵ martensitic transformations in Fe-Mn alloys, *J. Phys. IV*. 5 (1995) C8–379. <https://doi.org/10.1051/jp4>.
- [48] Z. Wang, C. Wang, C. Li, Y. Qin, L. Zhong, B. Chen, Z. Li, H. Liu, F. Chang, J. Wang, Analysis of factors influencing bone ingrowth into three-dimensional printed porous metal scaffolds: A review, *J. Alloys Compd.* 717 (2017) 271–285. <https://doi.org/10.1016/j.jallcom.2017.05.079>.
- [49] R. Wu, Y. Li, M. Shen, X. Yang, L. Zhang, X. Ke, G. Yang, C. Gao, Z. Gou, S. Xu, Bone tissue regeneration: The role of finely tuned pore architecture of bioactive scaffolds before clinical translation, *Bioact. Mater.* 6 (2021) 1242–1254. <https://doi.org/10.1016/j.bioactmat.2020.11.003>.
- [50] H. Hermawan, D. Dubé, D. Mantovani, Degradable metallic biomaterials: Design and development of Fe-Mn alloys for stents, *J. Biomed. Mater. Res. - Part A*. 93 (2010) 1–11. <https://doi.org/10.1002/jbm.a.32224>.
- [51] D. Bian, L. Qin, W. Lin, D. Shen, H. Qi, X. Shi, G. Zhang, H. Liu, H. Yang, J. Wang, D. Zhang, Y. Zheng, Magnetic resonance (MR) safety and compatibility of a novel iron bioresorbable scaffold, *Bioact. Mater.* 5 (2020) 260–274. <https://doi.org/10.1016/j.bioactmat.2020.02.011>.
- [52] J.F. Schenck, The role of magnetic susceptibility in magnetic resonance imaging: MRI magnetic compatibility of the first and second kinds, *Med. Phys.* 23 (1996) 815–850. <https://doi.org/10.1118/1.597854>.
- [53] K.M. Koch, B.A. Hargreaves, K.B. Pauly, W. Chen, G.E. Gold, K.F. King, Magnetic resonance imaging near metal implants, *J. Magn. Reson. Imaging*. 32 (2010) 773–87. <https://doi.org/10.1002/jmri.22313>.
- [54] P.M. Jungmann, C.A. Agten, C.W. Pfirrmann, R. Sutter, Advances in MRI around metal, *J. Magn. Reson. Imaging*. 46 (2017) 972–991. <https://doi.org/10.1002/jmri.25708>.
- [55] F.G. Shellock, Metallic neurosurgical implants: Evaluation of magnetic field interactions, heating, and artifacts at 1.5-Tesla, *J. Magn. Reson. Imaging*. 14 (2001) 295–299. <https://doi.org/10.1002/jmri.1185>.
- [56] F.G. Shellock, S. Valencerina, Septal repair implants: Evaluation of magnetic resonance imaging safety at 3 T, *Magn. Reson. Imaging*. 23 (2005) 1021–1025. <https://doi.org/10.1016/j.mri.2005.10.010>.
- [57] L.N. Carter, O. Addison, N. Naji, P. Seres, A.H. Wilman, D.E.T. Shepherd, L. Grover, S. Cox, Reducing MRI susceptibility artefacts in implants using additively manufactured

- porous Ti-6Al-4V structures, *Acta Biomater.* 107 (2020) 338–348. <https://doi.org/10.1016/j.actbio.2020.02.038>.
- [58] M. Schinhammer, I. Gerber, A.C. Hânzi, P.J. Uggowitzer, On the cytocompatibility of biodegradable Fe-based alloys, *Mater. Sci. Eng. C* 33 (2013) 782–789. <https://doi.org/10.1016/j.msec.2012.11.002>.
- [59] E. Mouzou, C. Paternoster, R. Tolouei, A. Purnama, P. Chevallier, D. Dubé, F. Prima, D. Mantovani, *In vitro* degradation behavior of Fe-20Mn-1.2C alloy in three different pseudo-physiological solutions, *Mater. Sci. Eng. C* 61 (2016) 564–573. <https://doi.org/10.1016/j.msec.2015.12.092>.
- [60] E. Mouzou, C. Paternoster, R. Tolouei, P. Chevallier, C.A. Biffi, A. Tuissi, D. Mantovani, CO₂-rich atmosphere strongly affects the degradation of Fe-21Mn-1C for biodegradable metallic implants, *Mater. Lett.* 181 (2016) 362–366. <https://doi.org/10.1016/j.matlet.2016.06.017>.
- [61] C. Tonna, C. Wang, D. Mei, S. V. Lamaka, M.L. Zheludkevich, J. Buhagiar, Biodegradation behaviour of Fe-based alloys in Hanks' Balanced Salt Solutions: Part I. material characterisation and corrosion testing, *Bioact. Mater.* 7 (2022) 426–440. <https://doi.org/10.1016/j.bioactmat.2021.05.048>.
- [62] C. Wang, C. Tonna, D. Mei, J. Buhagiar, M.L. Zheludkevich, S. V. Lamaka, Biodegradation behaviour of Fe-based alloys in Hanks' Balanced Salt Solutions: Part II. The evolution of local pH and dissolved oxygen concentration at metal interface, *Bioact. Mater.* 7 (2022) 412–425. <https://doi.org/10.1016/j.bioactmat.2021.05.014>.
- [63] X. Lu, Y. Leng, Theoretical analysis of calcium phosphate precipitation in simulated body fluid, *Biomaterials* 26 (2005) 1097–1108. <https://doi.org/10.1016/j.biomaterials.2004.05.034>.
- [64] Y.S. Zhang, X.M. Zhu, S.H. Zhong, Effect of alloying elements on the electrochemical polarization behavior and passive film of Fe-Mn base alloys in various aqueous solutions, *Corros. Sci.* 46 (2004) 853–876. <https://doi.org/10.1016/j.corsci.2003.09.002>.
- [65] M. Heiden, E. Walker, E. Nauman, L. Stanciu, Evolution of novel bioresorbable iron-manganese implant surfaces and their degradation behaviors *in vitro*, *J. Biomed. Mater. Res. - Part A* 103 (2015) 185–193. <https://doi.org/10.1002/jbm.a.35155>.
- [66] J. Venezuela, M.S. Dargusch, Addressing the slow corrosion rate of biodegradable Fe-Mn: Current approaches and future trends, *Curr. Opin. Solid State Mater. Sci.* 24 (2020) 100822. <https://doi.org/10.1016/j.cossms.2020.100822>.
- [67] J.A. Spencer, F. Ferraro, E. Roussakis, A. Klein, J. Wu, J.M. Runnels, W. Zaher, L.J. Mortensen, C. Alt, R. Turcotte, R. Yusuf, D. Côté, S.A. Vinogradov, D.T. Scadden, C.P. Lin, Direct measurement of local oxygen concentration in the bone marrow of live animals, *Nature* 508 (2014) 269–273. <https://doi.org/10.1038/nature13034>.
- [68] P. Sotoudeh Bagha, M. Khakbiz, N. Safaie, S. Sheibani, S. Ebrahimi-Barough, Effect of high energy ball milling on the properties of biodegradable nanostructured Fe-35 wt.%Mn alloy, *J. Alloys Compd.* 768 (2018) 166–175. <https://doi.org/10.1016/j.jallcom.2018.07.261>.
- [69] ISO 10993-5, Tests for *in vitro* cytotoxicity, International Organization for Standardization, 2009. <https://doi.org/10.1021/es0620181>.
- [70] R. Eid, N.T.T. Arab, M.T. Greenwood, Iron mediated toxicity and programmed cell death: A review and a re-examination of existing paradigms, *Biochim. Biophys. Acta - Mol. Cell Res.* 1864 (2017) 399–430. <https://doi.org/10.1016/j.bbamcr.2016.12.002>.
- [71] Y.F. He, Y. Ma, C. Gao, G.Y. Zhao, L.L. Zhang, G.F. Li, Y.Z. Pan, K. Li, Y.J. Xu, Iron overload inhibits osteoblast biological activity through oxidative stress, *Biol. Trace Elem. Res.* 152 (2013) 292–296. <https://doi.org/10.1007/s12011-013-9605-z>.
- [72] P. Chen, J. Bornhorst, M. Aschner, Manganese metabolism in humans, *Front. Biosci. - Landmark* 23 (2018) 1655–1679. <https://doi.org/10.2741/4665>.
- [73] V. Wagoner, A.S. Faltz, M.S. Killian, P. Schmuki, S. Virtanen, Protein interactions with corroding metal surfaces: Comparison of Mg and Fe, *Faraday Discuss.* 180 (2015) 347–360. <https://doi.org/10.1039/c4fd00253a>.
- [74] R. Oriňaková, R. Gorejová, Z.O. Králová, A. Oriňák, I. Shepa, J. Hovancová, A. Kovalčíková, Z.L. Bujňáková, N. Király, M. Kaňuchová, M. Baláž, M. Strečková, M. Kupková, M. Hrubovčáková, F. Kaľavský, M. Oriňák, Influence of albumin interaction on corrosion resistance of sintered iron biomaterials with polyethyleneimine coating, *Appl. Surf. Sci.* 509 (2020) 145379. <https://doi.org/10.1016/j.apsusc.2020.145379>.
- [75] M. Fântânariu, L.C. Trincă, C. Solcan, A. Trofin, Ș. Strungaru, E.V. Șindilar, G. Plăvan, S. Stanciu, A new Fe-Mn-Si alloplastic biomaterial as bone grafting material: *In vivo* study,

- Appl. Surf. Sci. 352 (2015) 129–139. <https://doi.org/10.1016/j.apsusc.2015.04.197>.
- [76] Q. Feng, D. Zhang, C. Xin, X. Liu, W. Lin, W. Zhang, S. Chen, K. Sun, Characterization and *in vivo* evaluation of a bio-corrodible nitrided iron stent, *J. Mater. Sci. Mater. Med.* 24 (2013) 713–724. <https://doi.org/10.1007/s10856-012-4823-z>.
- [77] M. Traverson, M. Heiden, L.A. Stanciu, E.A. Nauman, Y. Jones-Hall, G.J. Breur, *In vivo* evaluation of biodegradability and biocompatibility of Fe₃₀Mn alloy, *Vet. Comp. Orthop. Traumatol.* 31 (2018) 10–16. <https://doi.org/10.3415/VCOT-17-06-0080>.
- [78] H. Ma, T. Li, Z. Huan, M. Zhang, Z. Yang, J. Wang, J. Chang, C. Wu, 3D printing of high-strength bioscaffolds for the synergistic treatment of bone cancer, *NPG Asia Mater.* 10 (2018) 31–44. <https://doi.org/10.1038/s41427-018-0015-8>.
- [79] C. Shuai, Y. Li, Y. Yang, S. Peng, W. Yang, F. Qi, S. Xiong, H. Liang, L. Shen, Bioceramic enhances the degradation and bioactivity of iron bone implant, *Mater. Res. Express.* 6 (2019) 115401. <https://doi.org/10.1088/2053-1591/ab45b9>.
- [80] C. Gao, M. Yao, S. Li, P. Feng, S. Peng, C. Shuai, Highly biodegradable and bioactive Fe-Pd-bredigite biocomposites prepared by selective laser melting, *J. Adv. Res.* 20 (2019) 91–104. <https://doi.org/10.1016/j.jare.2019.06.001>.

***Ex situ*-composite bioactive and biodegradable porous Fe-Akermanite**

While additively manufactured porous iron and Fe-based materials has been successful in addressing the challenge of low rate of biodegradation, the insufficient bioactivity of these biomaterials hinder their progress towards clinical application. Here, we used extrusion-based 3D printing for additive manufacturing of iron-matrix composites containing silicate-based bioceramic particles (akermanite), thereby addressing both of the challenges in biodegradation and limited bioactivity. We developed inks that carried iron and 5, 10, 15, or 20 vol% of akermanite powder mixtures for the 3D printing process and optimized the debinding and sintering steps to produce geometrically-ordered iron-akermanite composites with an open porosity of 69–71%. The composite scaffolds preserved the designed geometry and the original α -Fe and akermanite phases. The *in vitro* biodegradation rates of the composites were improved as much as 2.6 times the biodegradation rate of geometrically identical pure iron. The yield strengths and elastic moduli of the scaffolds remained within the range of the mechanical properties of the cancellous bone, even after 28 days of biodegradation. The composite scaffolds (10–20 vol% akermanite) demonstrated improved MC3T3-E1 cell adhesion and higher levels of cell proliferation. The cellular secretion of collagen type-1 and the alkaline phosphatase activity on the composite scaffolds (10–20 vol% akermanite) were, respectively, higher than and comparable to Ti6Al4V in osteogenic medium. Taken together, these results clearly show the potential of 3D printed porous iron-akermanite composites for further development as promising bone substitutes.

Putra, N.E., Borg, K.G.N., Diaz-Payno, P.J., Leeftang, M.A., Klimopoulou, M., Taheri, P., Mol, J.M.C., Fratila-Apachitei, L.E., Huan, Z., Chang, J., Zhou, J., and Zadpoor, A.A., 2022. Additive manufacturing of bioactive and biodegradable porous iron-akermanite composites for bone regeneration. *Acta Biomaterialia*, 148, pp.355-373.

6.1 Introduction

Biodegradable iron-based biomaterials have been developed for several years to assist with the regeneration of critical size bone defects [1–4]. Numerous techniques have been used to enhance the biodegradation rate of Fe *in vitro*. For example, Fe has been alloyed with Ag [5,6], Mn [7–11], Mn-Ag [12–14] or Pd [15,16] to multiply microstructural phases with different values of nobility, hence triggering enhanced local corrosion through micro-galvanic interactions between the different phases. The recent advances in additive manufacturing techniques have enabled the fabrication of porous iron with exact geometrical designs to increase their biodegradation rate while maintaining their mechanical integrity over time [17–19]. While these two strategies (*i.e.*, alloying and making Fe structurally porous) address one of the abovementioned challenges regarding the use of iron as a bone-substituting biomaterial, they are incapable of providing iron with favorable bioactive properties that are required to stimulate bone regeneration. In fact, accelerated biodegradation of Fe can even negatively influence its biocompatibility because too much Fe²⁺ release can inhibit the *in vitro* metabolic activity of preosteoblasts [18,19]. Moreover, the addition of other alloying elements is unlikely to make the materials more biocompatible [20].

Here, we propose additively manufactured porous iron composites incorporating bioactive-degradable bioceramic particles to address both challenges simultaneously. For such composites, the relatively fast degradation of the bioceramic phase in Fe-matrix composites is expected at the beginning of the biodegradation period, increasing the initial biodegradation rate of the composite materials. Simultaneously, the dissolution of the bioceramic phase is expected to induce surface mineralization on the composite material, stimulating the adhesion, proliferation, and differentiation of osteoprogenitor cells [21]. With time, the dissolved bioceramic phase exposes additional surfaces inside the iron matrix for further biodegradation. To date, the Fe-based biocomposites have been developed with the reinforcement of hydroxyapatite (HA) [22–24], tricalcium phosphate (TCP) [25–27], calcium silicate (CaSiO₃) [28,29], magnesium silicide (Mg₂Si) [30–32], or bredigite (Ca₇Mg(SiO₄)₄) [33,34] using various fabrication methods. In general, the performance of several Fe-based biocomposites has been well acknowledged in improving both biodegradation and bioactivity of iron. Nevertheless, further research is still required to determine the appropriate choice of the bioceramic material and the optimum composition to provide the most effective biofunctionality for Fe-based biomaterials. Extrusion-based 3D printing has only been utilized for the fabrication of Fe-CaSiO₃ composite scaffolds [29].

In this study, we used akermanite ($\text{Ca}_2\text{Mg}(\text{Si}_2\text{O}_7)$) as the second structural component in the porous iron matrix to form composites that have not yet appeared in the literature. Recent developments in bioceramics for bone tissue engineering have shown Mg- and/or Si-based bioceramics to be promising alternatives to well-known Ca- and P-based bioceramics (*e.g.*, HA and TCP) [35,36]. For example, Mg has been found to stimulate the proliferation and osteogenic differentiation of osteoblasts [37]. In addition, Mg scaffolds have been shown to restore bone tissue *in vivo* successfully [38]. Likewise, Si can promote the synthesis of collagen type-1 and the calcification of the bony tissue [39,40]. Akermanite contains both Mg- and Si and *in vivo* studies have demonstrated that it can offer better osteogenic and angiogenic capabilities than TCP [41–43]. In addition, akermanite has been shown to significantly reduce the inflammatory responses of macrophages *in vivo* [44], allowing for better osseointegration.

Extrusion-based 3D printing of scaffolds for bone regeneration has been recently utilized for its merits in multi-material fabrication through alloying or compositing porous multi-functional Fe-based materials [11,29]. In this study, we used extrusion-based 3D printing technique for fabricating porous Fe-matrix composites with 5, 10, 15, and 20 vol% akermanite. We also comprehensively characterized the porous composites *in vitro* biodegradation behavior, the electrochemical response, the mechanical properties varying along with *in vitro* biodegradation, and the *in vitro* biological responses of preosteoblasts to these new biomaterials.

6.2 Materials and methods

6.2.1 Iron powder and synthesis of akermanite powder

Iron powder (purity = 99.88 wt%; spherical morphology; particle size < 63 μm , Figure 6.1a) was supplied by Material Technology Innovations Co. Ltd., China. Akermanite powder ($\text{Ca}_2\text{MgSi}_2\text{O}_7$; Mg wt% = 8.92; an irregular morphology; particle size < 45 μm , Figure 6.1b) was synthesized by using the sol-gel process with the use of tetraethyl orthosilicate [$(\text{C}_2\text{H}_5\text{O})_4\text{Si}$, TEOS], magnesium nitrate hexahydrate [$\text{Mg}(\text{NO}_3)_2 \cdot 6\text{H}_2\text{O}$], and calcium nitrate tetrahydrate [$\text{Ca}(\text{NO}_3)_2 \cdot 4\text{H}_2\text{O}$] as the raw materials [45], followed by a calcination step at 1300 °C for 3 h.

6.2.2 Iron-akermanite ink preparation and characterization

The iron and akermanite powder mixtures (with 5, 10, 15, and 20 vol% of akermanite, hereafter designated as Fe-5Ak, Fe-10Ak, Fe-15Ak, and Fe-20Ak, respectively) were prepared using a roller mixer (CAT Zipperer GmbH, Germany) at 80 rpm for 2 h. Then, the powder mixtures were blended with a water-based binder (made of a 5 wt% aqueous solution of hydroxypropyl methylcellulose with

$M_w \sim 86$ kDa, from Sigma Aldrich, Germany [19]) to create iron-akermanite inks with a powder volume ratio of 47.45%. The rheological characteristics of the inks were observed using an MCR302 rheometer (Anton Paar GmbH, Germany) and the results are presented in the supplementary material. In addition, to understand the dissolution characteristics of akermanite in the ink during 3D printing, the akermanite powder was mixed with demineralized water (with mass values equal to those in the Fe-5Ak and Fe-20Ak inks) for 2 h. Then, the supernatant was filtered through a 0.22 μm filter (Merck Millipore, Germany). The dissolved ions in the supernatant were quantified using an inductively coupled plasma optical emission spectroscope (ICP-OES, iCAP 6500 Duo, Thermo Scientific, USA).

6.2.3 Extrusion-based 3D printing, debinding and sintering

Porous iron-akermanite scaffolds (with $\phi = 10$ mm and $h = 10.5$ mm) were built through the extrusion of iron-akermanite inks using a 3D BioScaffolder 3.2 printer (GeSiM Bioinstruments and Microfluidics, Germany). The scaffolds were designed with characteristics described in Chapter 3, section 3.2.1 (Figure 6.1c). The extrusion-based 3D printing was performed at a printing speed of 5 mm/s under the printing pressures of 175 kPa, 205 kPa, 235 kPa, and 250 kPa, respectively, for the Fe-5Ak, Fe-10Ak, Fe-15Ak, and Fe-20Ak inks. After 3D printing, the green-body scaffolds were heat-treated, following the procedure described in Chapter 3, section 3.2.1.

6.2.4 Characterization of porosity, microstructure and phase composition

The dimensional changes imparted during the sintering process were determined by measuring the diameter and height of the iron-akermanite composite scaffolds before and after sintering. The morphology of the composite scaffolds was observed using a scanning electron microscope (SEM, JEOL JSM-IT100, Japan). Moreover, the strut size and strut spacing were measured. The chemical composition of the struts was mapped using X-ray energy dispersive spectroscopy (EDS) (JEOL JSM-IT100, Japan). The phases present in the iron-akermanite composites were identified using an X-ray diffractometer (XRD, D8 Advance, Bruker, USA) following the parameters described in Chapter 4, section 4.2.4. The obtained XRD patterns were analyzed with the DiffraC Suite.EVA v5.2 software. On the cross section of the composite scaffolds, the diffusion of iron into akermanite across the interfaces was inspected through EDS line analysis (JEOL JSM-IT100, Japan). The absolute porosities of the composite scaffolds were determined by dry weighing method as described in Chapter 3 with Equation (3.2) and (3.3). The interconnected porosities were measured using oil impregnation, based on the ASTM standard B963-13 [46], and calculated using Equation (3.4). The theoretical density of the iron-akermanite composite ($\rho_{\text{Fe-Ak}}$)

were 7.62 g/cm³ for Fe-5Ak, 7.38 g/cm³ for Fe-10Ak, 7.15 g/cm³ for Fe-15Ak, and 6.84 g/cm³ for Fe-20Ak.

6.2.5 Biodegradation experiments

Immersion tests

The iron-akermanite composite scaffolds were immersed in a revised simulated body fluid (r-SBF) [47] with 6.7 mL of r-SBF per 1 cm² scaffold surface area [48] for 1, 4, 7, 14, and 28 d ($n = 3$, for each time point), under the conditions as described in Chapter 3, section 3.2.4. The pH values of the r-SBF medium were monitored using a pH electrode (InLab Expert Pro-ISM, METTLER TOLEDO, Switzerland) during the *in vitro* immersion tests at selected time points.

Characterization of the biodegradation products

The concentrations of soluble Fe²⁺, Ca²⁺, Mg²⁺, Si⁺, and PO₄³⁻ ions in r-SBF were measured at various time points using ICP-OES (iCAP 6500 Duo, Thermo Scientific, USA). Following immersion until the preselected time points, the specimens were retrieved and the morphologies and chemical compositions of the biodegradation products on the periphery and at the center of the scaffolds were examined using SEM and EDS (JEOL JSM-IT100, Japan). The phases present in the biodegradation products after immersion for 4 d and 28 d were identified using XRD (D8 Advance, Bruker, USA). The biodegradation rates of the iron-akermanite composite scaffolds at different time points were determined using mass loss measurements, based on the ASTM standard G1-03 [49], as described in Chapter 3, section 3.2.4. The remaining composite material was weighed and the average biodegradation rate was calculated, following the ASTM standard G31-72 [50], with Equation (3.5).

Electrochemical measurements

The electrochemical response of the iron-akermanite composite scaffolds during biodegradation in the r-SBF medium at 37 ± 0.5 °C and with an initial pH of 7.40 was recorded using a Bio-Logic SP-200 potentiostat (Bio-Logic Science Instruments, France). A three-electrode setup included an Ag/AgCl electrode (reference electrode), a graphite bar (counter electrode), and the composite specimen partially embedded in an acrylic resin (working electrode). The exposed surface area of the composite specimen was calculated, based on the initial design value of the scaffold. The electrochemical measurements of open circuit potential (OCP), linear polarization resistance (LPR) and electrochemical impedance spectroscopy (EIS) were performed, following the parameters described in Chapter 3, section 3.2.6.

6.2.6 Mechanical tests

Compression tests were performed using a universal material testing machine (Zwick Z100, Germany, with a 100 kN load cell) to evaluate the mechanical properties of the as-sintered and as-biodegraded iron-akermanite composite scaffolds ($n = 3$). The compression tests were carried out at a crosshead speed of 3 mm/min, following the ISO standard 13314:2011 [51]. From the stress-strain curve, the quasi elastic gradient (referred as Young's modulus) and the compressive 0.2% offset stress (referred as yield strength) were determined, as described in Chapter 3, section 3.2.7.

6.2.7 Cytocompatibility evaluation

Preculture of preosteoblasts and cell culture medium

Murine MC3T3-E1 preosteoblasts (Sigma Aldrich, Germany) were precultured for 7 d in a cell culture incubator, following the conditions described in Chapter 3, section 3.2.8. The cell culture medium contained the α -minimum essential medium (α -MEM, Thermo Fisher Scientific, USA) without ascorbic acid and was supplemented with 10% fetal bovine serum (FBS, Thermo Fisher Scientific, USA) and 1% penicillin/streptomycin (p/s, Thermo Fisher Scientific, USA). The same cell culture medium was used for all other cell culture assays, unless otherwise stated.

Preparation of iron-akermanite extracts and PrestoBlue assay

Extracts were obtained after 72 h of incubation of the sterile composite scaffolds ($\phi = 9.7$ mm and $h = 10.3$ mm; $n = 3$) in the cell culture medium as described in Chapter 3, section 3.2.8. The extracts were filtered using a 0.22 μ m pore size filter (Merck Millipore, Germany) and were diluted to 75%, 50%, and 25% of their original concentrations.

The preosteoblasts (1×10^4 cells) were cultured in a 48-well plate containing 200 μ L iron-akermanite extracts for 1, 3, and 7 d ($n = 3$ for every extract concentration). The same preosteoblasts were cultured in the cell culture medium as the negative control. PrestoBlue assay (Thermo Fisher Scientific, USA) was utilized to evaluate the metabolic activity of the cells, following the procedure described in Chapter 3, section 3.2.8, and calculated with Equation (3.7).

Trypan blue assay and live-dead staining

The preosteoblasts (5×10^4 cells per specimen) were seeded and cultured on the iron-akermanite composite specimens ($\phi = 9.7$ mm and $h = 1.3$ mm) in 6-well plates with 8 mL of cell culture medium for 1, 4, 7, 14, and 28 d ($n = 3$ for every time point). Porous Ti6Al4V scaffolds were used as the reference material (positive control). The Trypan blue assay (Bio-Rad, USA), followed by cell

counting steps using an automated cell counter (TC20, Bio-Rad, USA), was used to calculate the number of the preosteoblasts present at the selected cell culture time points. In addition, the distribution and the viability of preosteoblasts was evaluated using calcein (green = live) and ethidium homodimer-1 (red = dead) staining (Thermo Fisher Scientific, USA) after 7, 14, and 28 d of cell culture. Procedures were described in Chapter 3, section 3.2.8.

Morphology of preosteoblasts on the composite scaffolds

The morphology of the preosteoblasts after 7, 14, and 28 d of cell culture on the composite scaffolds (*i.e.*, Fe-10Ak, Fe-15Ak, and Fe-20Ak) was observed using SEM (JEOL JSM-IT100, Japan). Additionally, the strut morphology and associated biodegradation products formed on the composite scaffolds (immersed in the cell culture medium for 14 and 28 d without cells) were examined using SEM and EDS.

Collagen type-1 staining

After cell culture for 7, 14, and 28 d, the composite scaffolds (*i.e.*, Fe-10Ak, Fe-15Ak, and Fe-20Ak) were washed with phosphate buffer saline (PBS) and were fixed with 4% formaldehyde (Sigma Aldrich, Germany) for 15 min. Then, the specimens were washed with PBS and permeabilized using 0.5% Triton/PBS (Sigma Aldrich, Germany). Consecutively, the scaffolds were incubated with anti-collagen type-1 primary antibody (1:100 per specimen, Thermo Fisher Scientific, USA) in 1% bovine serum albumin (BSA)/PBS, followed by washing with 0.5% Tween/PBS (Sigma Aldrich, Germany). The second incubation step was performed using Alexa Fluor 488 conjugated secondary antibody (1:200, Thermo Fischer Scientific, USA) in 1% BSA/PBS, followed by washing with 0.5% Tween/PBS (Sigma Aldrich, Germany). Subsequently, the specimens were washed with PBS. Thereafter, the specimens were imaged using a fluorescence microscope (ZOE cell imager, Bio-Rad, USA).

Alkaline phosphatase (ALP) activity

The ALP activities of the preosteoblasts were determined after 14 and 28 d of culture on the composite scaffolds (*i.e.*, Fe-10Ak, Fe-15Ak, and Fe-20Ak) using a fluorometric ALP assay kit (ab83371, Abcam, Thermo Fisher Scientific, USA). Porous monolithic iron and Ti-6Al-4V specimens were included as the negative and positive control groups, respectively. The positive control groups were cultured in the cell culture medium with additional osteogenic reagents (*i.e.*, ascorbic acid 1:1000 and β -glycerophosphate 1:500). The ALP measurements were conducted, following the steps described in the manufacturer's protocol. The ALP activities were reported in terms of fold-change against the negative control.

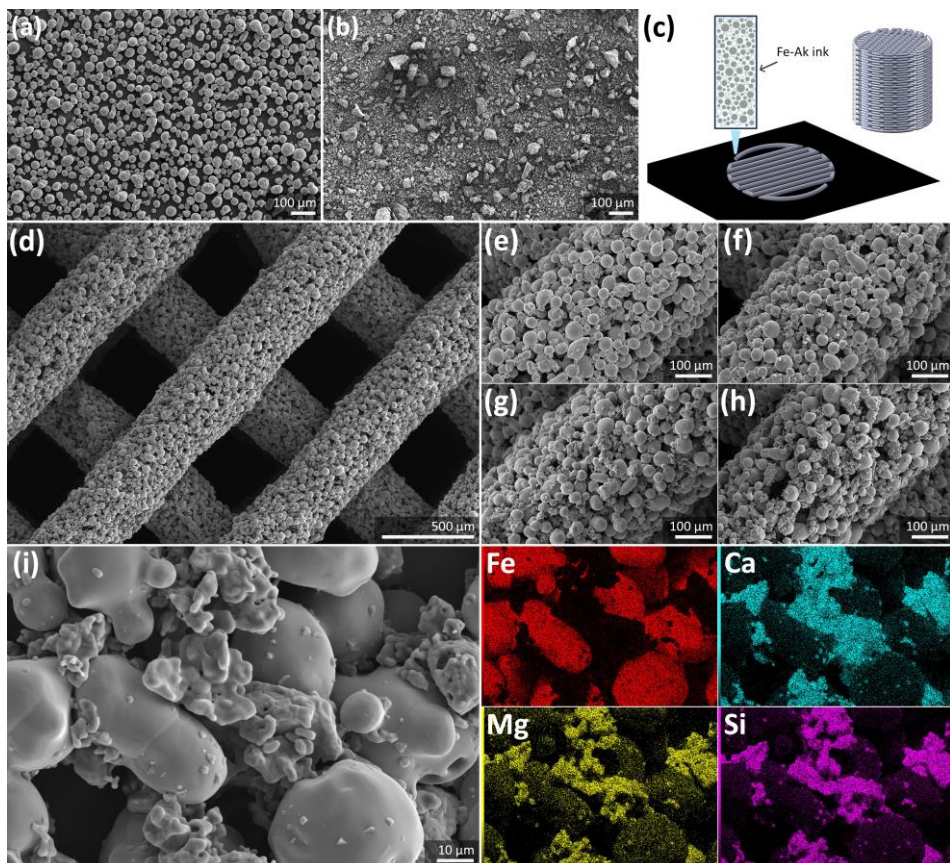


Figure 6.1. The morphologies of the starting powder materials: (a) iron and (b) akermanite. (c) The extrusion-based 3D printing and the design of porous iron-akermanite scaffolds with a 0° and 90° laydown pattern. (d) The morphology of the porous iron-akermanite composite scaffolds and the strut morphologies of the (e) Fe-5Ak, (f) Fe-10Ak, (g) Fe-15Ak, and (h) Fe-20Ak composites at a higher magnification. (i) EDS elemental mapping on the periphery of the porous iron-akermanite struts.

6.2.8 Statistical analysis

The statistical analysis of the cell counting results was performed with two-way ANOVA, followed by a Tukey multiple comparison *post hoc* test (**** = $p < 0.0001$, *** = $p < 0.001$, ** = $p < 0.01$, and * = $p < 0.05$, n.s. = not significant).

6.3 Results

6.3.1 Characteristics of the porous iron-akermanite composite scaffolds

The porous iron-akermanite scaffolds fabricated through extrusion-based 3D printing (Figure S6.1) closely followed the geometrical 0° and 90° lay-down pattern design even after the debinding and sintering steps (Figure 6.1d, Table

6.1). Successful extrusion-based 3D printing of iron-akermanite-containing inks strongly relies on adequate powder loading in the ink and its shear-thinning behavior (Figure S6.2). Due to sintering, the diameter and height of the composite scaffolds reduced by 2.7-3.4% and 1.9-2.1%, respectively. The struts of the composite scaffolds, nevertheless, continued to feature a random micro-porous structure (Figure 6.1d). The volume fraction of akermanite clearly increased, given the more irregularly shaped powder particles dispersed across the struts (Figure 6.1e-h). In addition to the sintered iron and akermanite powder particles, smaller akermanite particles adhering to the surfaces of iron particles were observed (Figure 6.1i). EDS mapping analysis detected Ca, Mg, and Si covering the surface of iron powder particles (Figure 6.1i).

The iron-akermanite composite scaffolds had interconnected porosities of $70 \pm 1\%$, $69 \pm 3\%$, $69 \pm 1\%$, and $71 \pm 1\%$ for the Fe-5Ak, Fe-10Ak, Fe-15Ak, and Fe-20Ak groups, respectively. The increasing akermanite volume in the iron matrix did not significantly influence the porosity of the specimens (Figure 6.2a). The XRD patterns displayed the α -Fe phase and $\text{Ca}_2\text{Mg}(\text{Si}_2\text{O}_7)$ phase in the porous iron-akermanite scaffolds with no additional crystalline compounds (Figure 6.2c). The intensity of the akermanite phase was relatively higher in the scaffold with a higher akermanite volume fraction. On the cross section of the struts, the iron and akermanite powder particles were observed to have undergone thorough co-sintering (Figure 6.2b). It was clear that the base material (gray color) belonged to iron and the dispersed particles (dark gray color) were akermanite. At a higher magnification, the interface between iron and akermanite revealed on the cross section of the Fe-20Ak specimens (Figure 6.2d) did not show any additional compounds formed and was free from any noticeable defects. Elemental diffusion from the iron phase to the akermanite phase occurred up to a depth of approximately $1.7 \mu\text{m}$ (Figure 6.2d).

Table 6.1. Structural characteristics of the extrusion-based 3D printed porous iron-akermanite scaffolds.

Sample group	Strut width (μm)	Strut spacing (μm)
Fe-5Ak	407 ± 8	402 ± 7
Fe-10Ak	408 ± 7	403 ± 9
Fe-15Ak	407 ± 7	403 ± 8
Fe-20Ak	408 ± 6	401 ± 6

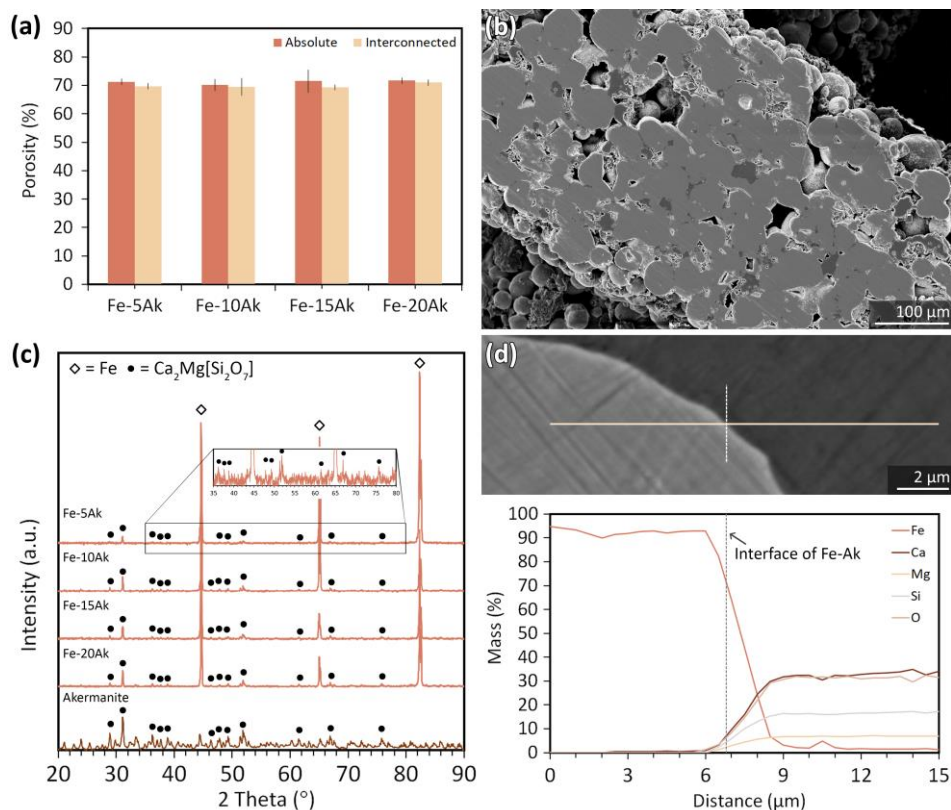


Figure 6.2. (a) The porosities of the iron-akermanite composite scaffolds, (b) the cross section of the struts, (c) the phase composition of akermanite powder and the composite scaffolds and (d) the EDS line analysis across the interfaces of iron and akermanite.

6.3.2 *In vitro* biodegradation behavior

After 1 d of *in vitro* immersion, the iron-akermanite composite scaffolds were covered by a layer of dark brown biodegradation products. The biodegradation products grew thicker into a yellow-brownish color during further immersion for up to 28 d (Figure 6.3a). The global pH value of the r-SBF medium maintained between 7.62 and 7.65 throughout the biodegradation period. The mass of the composite scaffolds decreased due to biodegradation. The mass loss percentage increased during the first 4 d of immersion, followed by a reduction to 7 d of immersion and the increases corresponding to 14 d and 28 d of immersion (Figure 6.3b). A larger mass loss was observed in the composite scaffold with a higher akermanite volume fraction. At day 14 of biodegradation, the degradation rates of the porous iron-akermanite scaffolds were 0.14 ± 0.01 mm/y, 0.16 ± 0.02 mm/y, 0.20 ± 0.01 , and 0.24 ± 0.02 mm/y for Fe-5Ak, Fe-

10Ak, Fe-15Ak, and Fe-20Ak, respectively. At the end of the immersion tests (*i.e.*, day 28), the *in vitro* biodegradation rates of the porous iron-akermanite scaffolds were 0.08 ± 0.01 mm/y, 0.09 ± 0.01 mm/y, 0.11 ± 0.02 mm/y, and 0.13 ± 0.01 mm/y for Fe-5Ak, Fe-10Ak, Fe-15Ak, and Fe-20Ak, respectively (Figure 6.3c). For comparison, the porous monolithic iron showed the degradation rates of 0.09 ± 0.02 mm/y at day 14 and 0.05 ± 0.02 mm/y at day 28 [19].

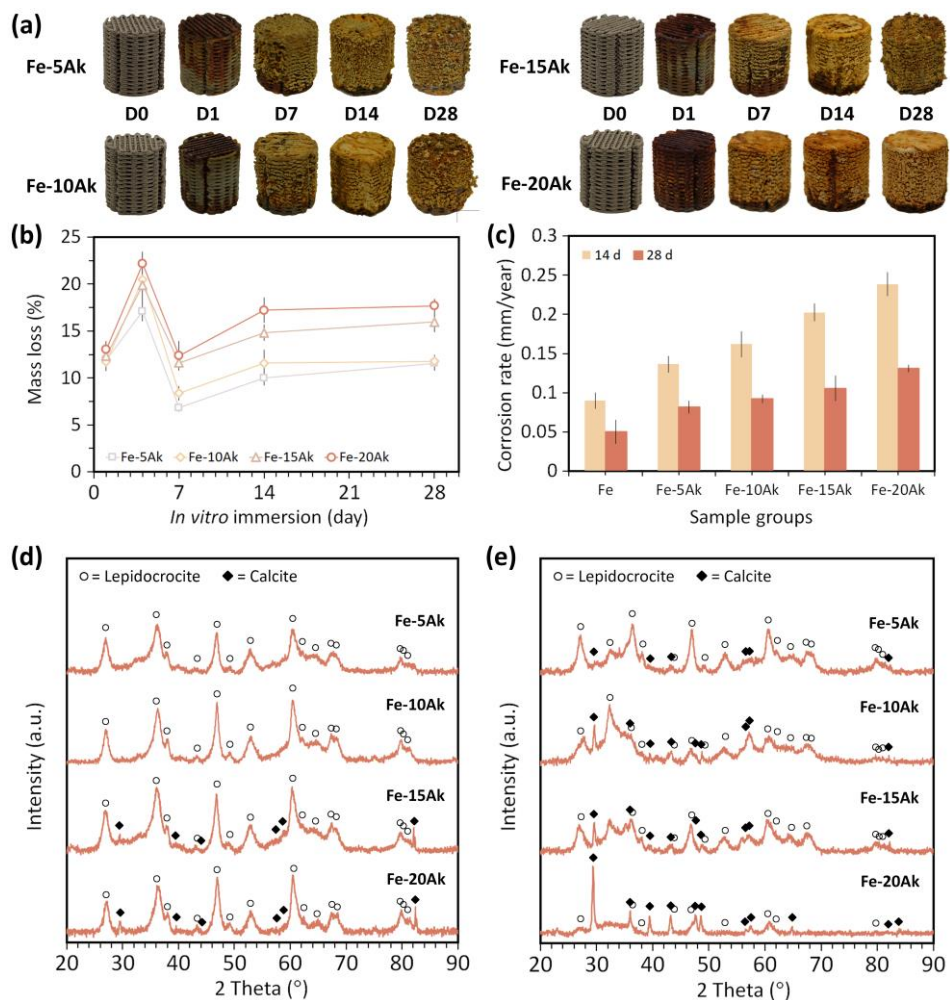


Figure 6.3. The *in vitro* biodegradation characteristics of the porous iron-akermanite composites: (a) the visual inspection of the porous iron-akermanite composite scaffolds before and after biodegradation at various time points, (b) mass loss vs. immersion time, and (c) corrosion rates on days 14 and 28 of immersion, and the phase compositions of the biodegradation products on days (d) 4 and (e) 28 of immersion.

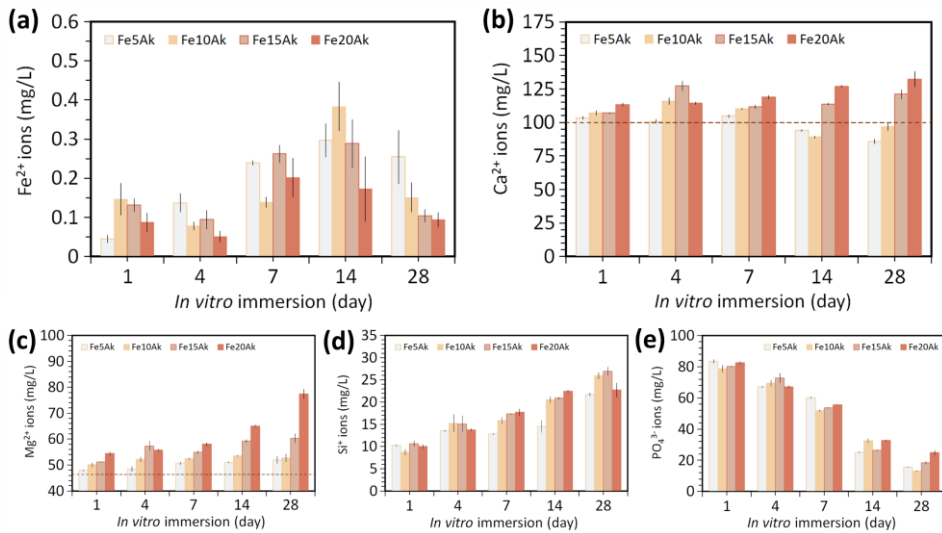


Figure 6.4. The variations of the concentrations of the (a) Fe^{2+} , (b) Ca^{2+} , (c) Mg^{2+} , (d) Si^{4+} , and (e) PO_4^{3-} ions in the biodegradation medium over time. The dash line indicates the initial ion concentration values in the r-SBF medium.

During biodegradation, Fe^{2+} , Ca^{2+} , Mg^{2+} , and Si^{4+} were steadily released to the r-SBF medium (Figure 6.4). The Fe^{2+} concentrations reached their peaks at day 14 (*i.e.*, 0.17 to 0.30 mg/L) and the ion release decreased towards the end of the immersion period (Figure 6.4a). In the case of the Fe-15Ak and Fe-20Ak specimens, the Ca^{2+} concentrations detected in the solution were higher at all time points, as compared to the initial Ca^{2+} concentration in the r-SBF medium (*i.e.*, 121.1 to 132.4 mg/L at day 28, Figure 6.4b). On the other hand, the Ca^{2+} concentrations in the solution corresponding to the Fe-5Ak and Fe-10Ak specimens remained largely unchanged in the first 7 d of immersion, but slightly reduced towards the end of immersion (*i.e.*, 85.8 to 96.6 mg/L at day 28, Figure 6.4b). At the same period of immersion, the Mg^{2+} and Si^{4+} concentrations steadily increased (*i.e.*, 52.0 to 77.4 mg/L and 21.7 to 26.9 mg/L, respectively, Figure 6.4c-d). As for the PO_4^{3-} ions in the r-SBF medium, the concentrations continually declined throughout the 28 d of immersion (Figure 6.4e).

6.3.3 Characteristics of the biodegradation products

The main phase in the peripheral degradation products of the porous iron-akermanite composites after 4 d and 28 d of immersion was lepidocrocite ($\gamma\text{-FeOOH}$) (Figure 6.3d-e). The calcite (CaCO_3) phase was detected on the Fe-15Ak and Fe-20Ak scaffolds after 4 d of immersion (Figure 6.3d) and its intensity increased towards 28 d of immersion (Figure 6.3e). By contrast, the CaCO_3 phase was observed on the Fe-5Ak and Fe-10Ak scaffolds only after 28 d of immersion

(Figure 6.3e). From the SEM micrographs, the struts of the composite scaffolds were fully enveloped by the degradation products as early as day 4 of the immersion tests (Figure 6.5a-c). The biodegradation products transformed into a denser structure throughout the immersion period (Figure 6.5, S6.4-6.6).

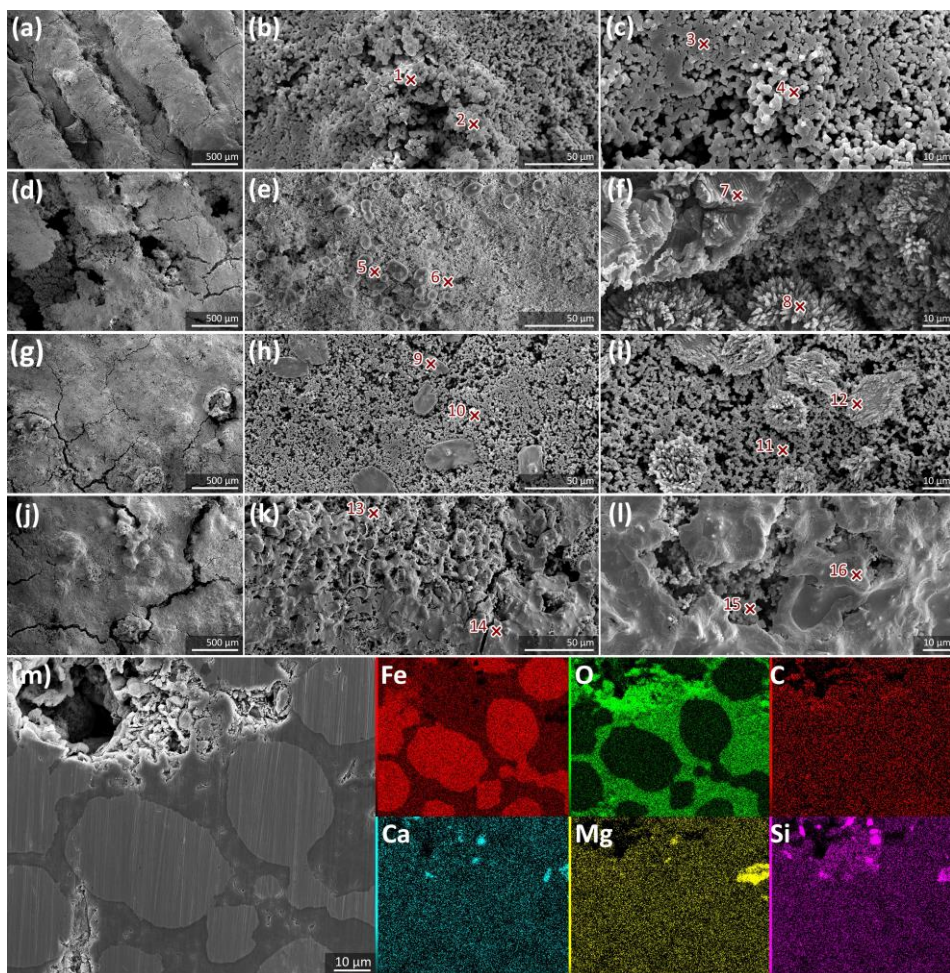


Figure 6.5. The morphologies of the *in vitro* biodegradation products formed on the porous Fe-20Ak scaffolds: on the periphery after (a, b, c) 4 d, (d, e, f) 7 d, (g, h, i) 14 d, and (j, k, l) 28 d of biodegradation, and (m) at the center of the scaffolds after 28 d of biodegradation. The cross marks with numbers indicate the locations of the EDS analyses whose results are presented in Table 6.2.

Table 6.2. Chemical compositions of the *in vitro* biodegradation products (wt%) on the periphery of the porous Fe-20Ak scaffolds, determined by EDS analysis.

Fe-20Ak	EDS point	C	O	Na	Mg	Si	Cl	P	Ca	Fe
4 d	1	36.35	19.94	-	0.46	0.36	-	-	0.94	41.95
	2	25.53	16.13	-	-	1.20	0.13	-	1.07	55.94
	3	24.25	9.41	-	-	-	-	-	-	68.70
	4	32.30	30.03	-	-	0.57	-	-	1.57	35.53
7 d	5	26.59	13.02	-	-	-	-	-	16.51	43.88
	6	25.11	19.03	-	0.59	0.16	-	4.02	7.52	43.56
	7	29.18	20.95	4.48	-	0.05	-	-	10.80	34.53
	8	18.41	33.73	-	-	0.19	-	-	25.32	22.35
14 D	9	30.68	23.24	0.07	1.15	-	-	-	19.77	25.09
	10	10.94	8.31	-	-	-	-	-	2.17	78.58
	11	4.46	1.58	-	0.66	-	-	-	18.27	75.02
	12	29.56	10.55	-	2.05	-	-	-	28.31	29.54
28 d	13	19.57	11.69	0.71	0.75	-	-	-	3.61	63.67
	14	31.88	7.78	0.31	0.54	-	-	-	26.51	32.98
	15	5.28	4.25	-	0.26	-	-	-	12.98	77.24
	16	20.20	14.30	-	1.18	-	-	-	46.69	17.82

The morphology of the peripheral biodegradation products was discernible in two major forms (Figure 6.5): a fine, particulate porous structure and coral-like precipitates decorating the surfaces. The coral-like degradation products were rich in Ca, while the porous particulate surfaces contained more Fe (Table 6.2). These elements corresponded to the phase compositions identified by XRD. On the Fe-20Ak composite scaffolds, the coral-like precipitates expanded over the biodegradation time, covering the particulate corrosion products (Figure 6.5). Similar observations were noted for the Fe-15Ak (Figure S6.4, Table S6.1), Fe-10Ak (Figure S6.5, Table S6.2) and Fe-5Ak (Figure S6.6, Table S6.3) composites.

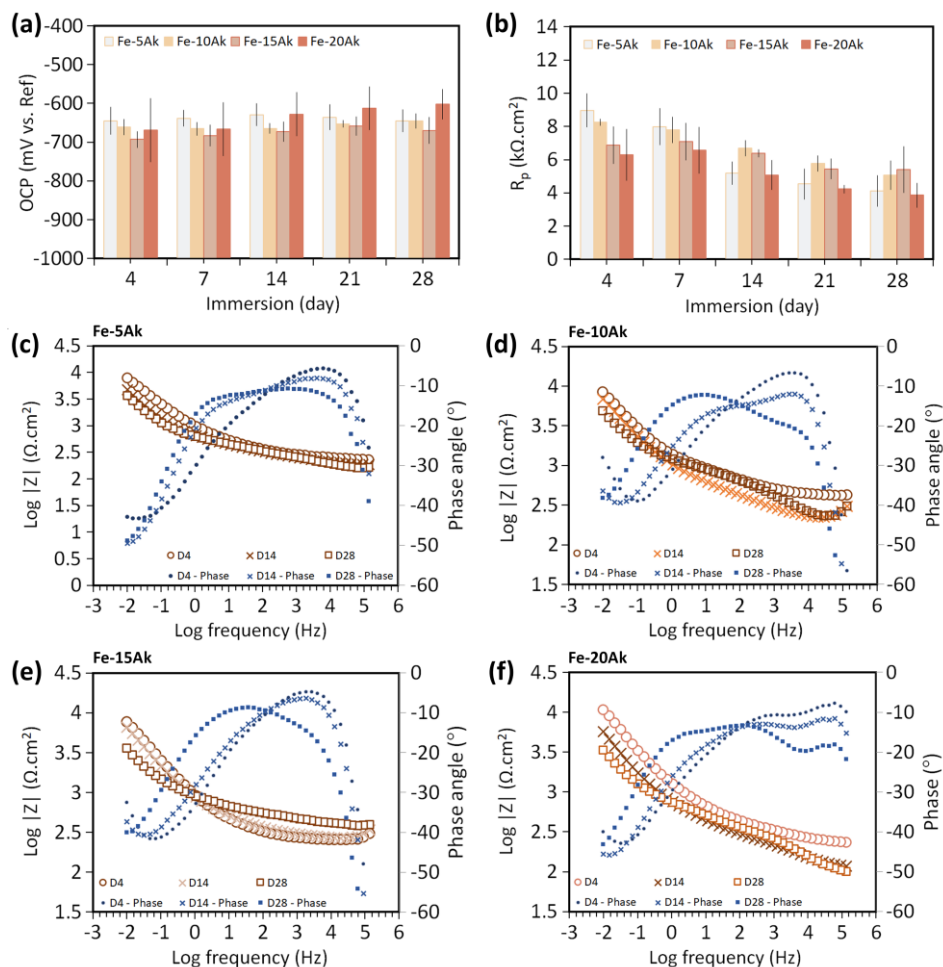


Figure 6.6. The electrochemical measurements of the porous iron-akermanite composite scaffolds during 28 d of biodegradation: (a) OCP and (b) the R_p values from the LPR tests; Bode plot of (c) Fe-5Ak, (d) Fe-10Ak, (e) Fe-15k, and (f) Fe-20Ak composites, indicating the impedance modulus values at different frequencies at some selected time points after biodegradation.

In addition to the Fe- and Ca-based products, magnesium was detected at lower concentrations in the peripheral degradation products (Table 6.2, S6.1-6.3). Silicon was only present on the Fe-20Ak composite scaffolds at the early immersion time points (*i.e.*, 4 d and 7 d) (Table 6.2). Furthermore, the degradation products at the center of the scaffolds appeared to be compact. Moreover, Fe, C and O, Ca, Mg and Si remnants were found in the Fe-20Ak (Figure 6.5m) and Fe-15Ak (Figure S6.4m) composite scaffolds. However, only

Fe, C, O and Ca elements were observed in the cross sectional biodegradation products of the Fe-10Ak (Figure S6.5m) and Fe-5Ak (Figure S6.6m) composites.

6.3.4 Electrochemical measurements

The iron-akermanite composite specimens (*i.e.*, Fe-5Ak, Fe-10Ak, Fe-15Ak and Fe-20Ak) showed relatively stable OCP values during the biodegradation experiments (Figure 6.6a). At the beginning of the biodegradation experiments (*i.e.*, after 4 d), the OCP values were -645 ± 36 mV, -661 ± 21 mV, -693 ± 21 mV, and -669 ± 82 mV, respectively. At the 28th day of biodegradation, the average OCP values had only marginally increased to -645 ± 29 mV, -645 ± 19 mV, -670 ± 34 mV, and -602 ± 39 mV, respectively. The average polarization resistance (R_p) values of the porous iron-akermanite composites (*i.e.*, Fe-5Ak, Fe-10Ak, Fe-15Ak and Fe-20Ak) obtained from the LPR tests exhibited a generally decreasing trend as the biodegradation progressed (Figure 6.6b). At day 4, the average R_p values were 9.0 ± 1.1 k Ω .cm², 8.3 ± 0.8 k Ω .cm², 6.9 ± 1.1 k Ω .cm², and 6.3 ± 1.6 k Ω .cm², respectively. After 28 d of biodegradation, the R_p values decreased to 4.1 ± 0.8 k Ω .cm², 5.1 ± 1.1 k Ω .cm², 5.4 ± 1.4 k Ω .cm², and 3.9 ± 0.7 k Ω .cm², respectively.

The impedance modulus values of the porous iron-akermanite composites at low frequencies, indicative of the charge transfer and hence resistance of the corroding system, followed a decreasing trend with time similar to the R_p results (Bode plots - Figure 6.6c-f). At a low frequency (*i.e.*, 0.01 Hz) and after 4 d of immersion, the impedance modulus values were 7.9 ± 1.8 k Ω .cm², 9.3 ± 0.9 k Ω .cm², 7.6 ± 1.8 k Ω .cm², and 10.7 ± 2.3 k Ω .cm², respectively, for Fe-5Ak, Fe-10Ak, Fe-15Ak, and Fe-20Ak. After 28 d of immersion, however, the impedance magnitude reduced to 3.7 ± 0.6 k Ω .cm², 4.8 ± 1.3 k Ω .cm², 5.1 ± 0.6 k Ω .cm², and 3.3 ± 0.6 k Ω .cm², respectively.

The impedance magnitudes at a higher frequency (*e.g.*, 100 Hz) relate to the evolution (*e.g.*, partial dissolution or growth) of the corrosion product formation over time [52–54]. After 4 d of immersion, the impedance modulus values at 100 Hz were 0.4 ± 0.1 k Ω .cm², 0.5 ± 0.2 k Ω .cm², 0.3 ± 0.1 k Ω .cm², and 0.43 ± 0.03 k Ω .cm², respectively for Fe-5Ak, Fe-10Ak, Fe-15Ak, and Fe-20Ak. At the same frequency, the impedance modulus values after 28 d of immersion became 0.3 ± 0.1 k Ω .cm², 0.6 ± 0.3 k Ω .cm², 0.6 ± 0.1 k Ω .cm², and 0.35 ± 0.01 k Ω .cm², respectively. The peak start of the Bode plot phase angle at low-to-mid frequencies showed a trend to shift from a higher frequency to a lower frequency as a function of time of exposure (Figure 6.6c-f). At a mid-frequency range (*i.e.*, 100 Hz), the phase angle values after 4 and 28 d of immersion for all composite scaffolds were relatively unchanged.

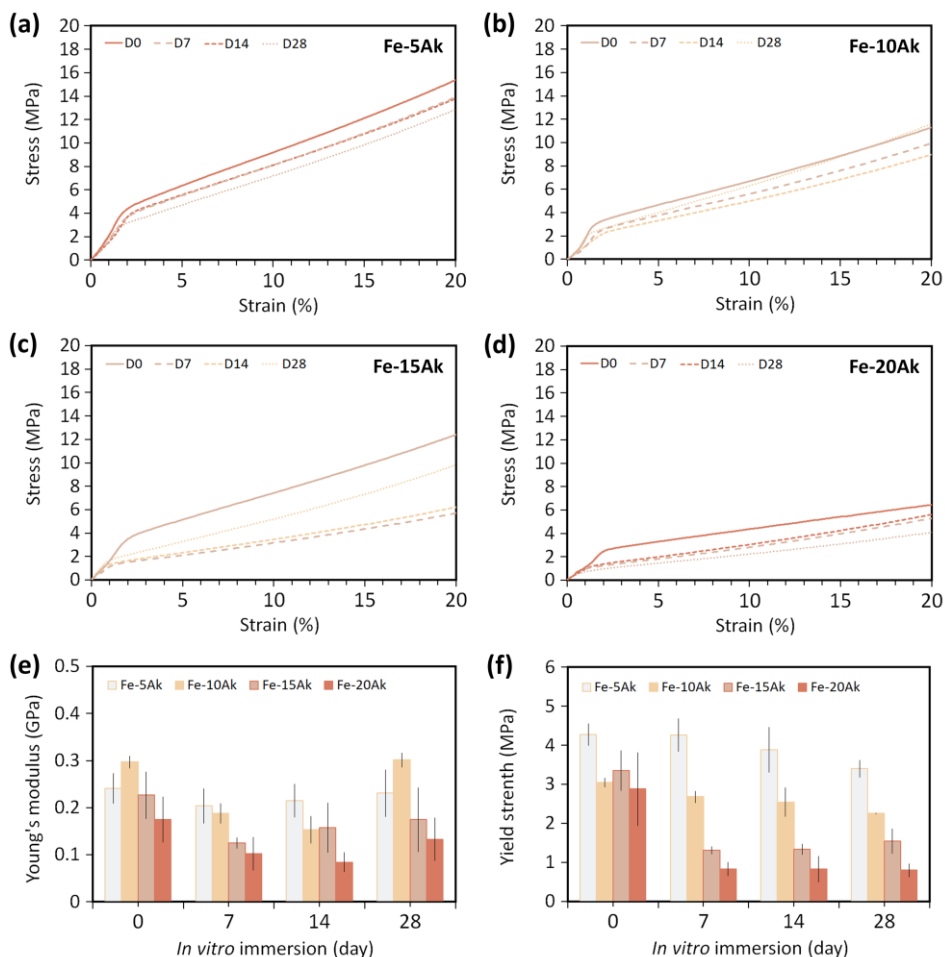


Figure 6.7. The compressive mechanical properties of the porous iron-akermanite composites: the stress-strain curves of (a) Fe-5Ak, (b) Fe-10Ak, (c) Fe-15Ak, and (d) Fe-20Ak scaffolds; (e) changes in Young's modulus and (f) yield strength during 28 d of biodegradation.

6.3.5 Mechanical properties

All the iron-akermanite composite scaffolds exhibited smooth stress-strain curves under uniaxial compression, starting with a linear elastic region and followed by a plastic deformation region that exhibited the hallmarks of strain hardening (Figure 6.7a). The composite scaffolds (*i.e.*, Fe-5Ak, Fe-10Ak, Fe-15Ak and Fe-20Ak) had Young's moduli of 0.24 ± 0.03 GPa, 0.30 ± 0.01 GPa, 0.23 ± 0.05 GPa, and 0.17 ± 0.05 GPa, respectively. The yield strengths were 4.3 ± 0.3 MPa, 3.0 ± 0.1 MPa, 3.4 ± 0.5 MPa, and 2.9 ± 0.9 MPa, respectively. After 7 d of biodegradation, the Young's moduli of the scaffolds reduced to 0.20 ± 0.04

GPa, 0.19 ± 0.02 GPa, 0.12 ± 0.01 GPa and 0.10 ± 0.04 GPa, respectively (Figure 6.7b). After 28 days of biodegradation, the Young's moduli improved from those measured at day 7 (*i.e.*, 0.23 ± 0.05 GPa, 0.30 ± 0.02 GPa, 0.17 ± 0.07 GPa and 0.13 ± 0.05 GPa, respectively), while being still lower than the initial values (Figure 6.7b). The yield strengths of the specimens (*i.e.*, Fe-5Ak, Fe-10Ak, Fe-15Ak and Fe-20Ak) reduced to 3.4 ± 0.2 MPa, 2.25 ± 0.02 MPa, 1.5 ± 0.3 MPa, and 0.8 ± 0.2 MPa (Figure 6.7c), respectively, after 28 d of biodegradation.

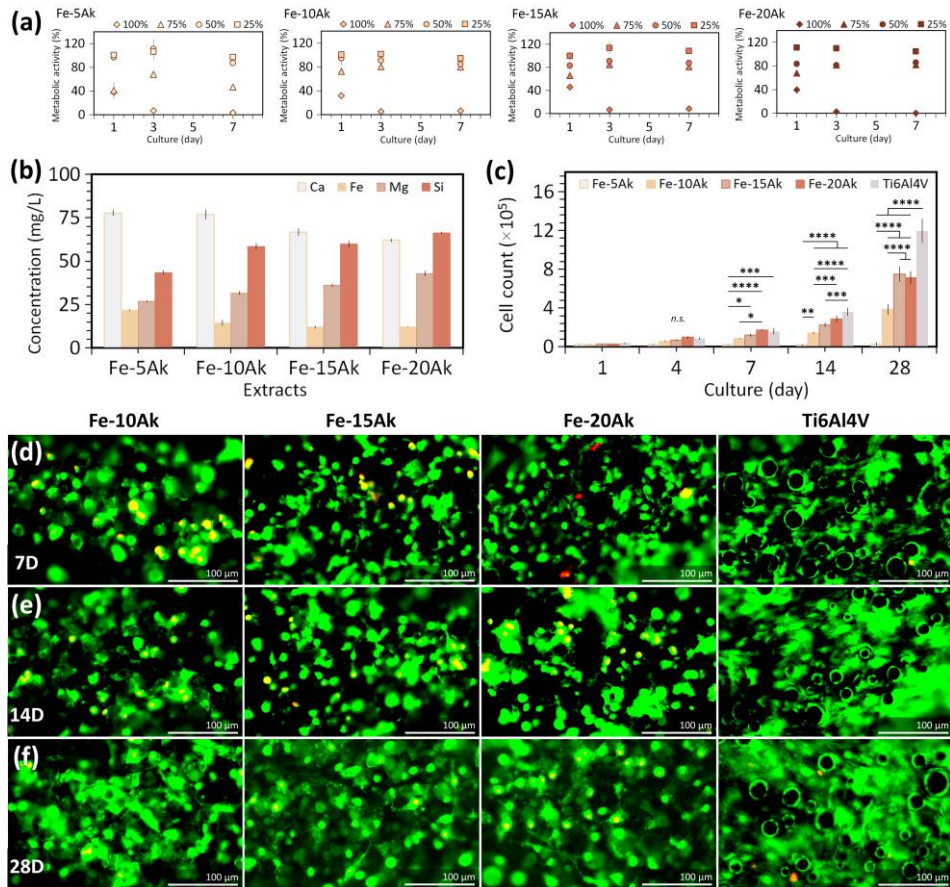


Figure 6.8. The compatibility of the porous iron-akermanite composites with the MC3T3-E1 preosteoblasts: (a) the metabolic activity of the preosteoblasts after culture with the extracts of the porous iron-akermanite composites, (b) The concentrations of the Ca, Fe, Mg, and Si ions in the iron-akermanite extracts, (c) the number of the cell counts over the 28 d of culture, and the live dead staining of the preosteoblasts on the porous Fe-10Ak, Fe-15Ak, and Fe-20Ak and Ti-6Al-4V scaffolds after (d) 7 d, (e) 14 d, and (f) 28 d of culture. **** = $p < 0.0001$, *** = $p < 0.001$, ** = $p < 0.01$, and * = $p < 0.05$.

6.3.6 Metabolic activity of cells

For the 50% and 25% extracts, the preosteoblasts were highly metabolically active (*i.e.*, > 80%) for all the iron-akermanite specimens (Figure 6.8a). When the extract concentration increased to 75%, the cells maintained their high levels of metabolic activity (*i.e.*, > 80%) for the Fe-10Ak, Fe-15Ak, and Fe-20Ak groups. These extracts were categorized as grade 1 (or non-cytotoxic) according to ISO 10993-5 [55]. However, the metabolic activity of preosteoblasts dropped to <50% when cultured in the 75% extracts of the Fe-5Ak composite (grade 2 or moderately reactive [55]). The inhibition of cell metabolic activity was only observed on all iron-akermanite extracts without any dilution (grade 4 or severely reactive [55]).

In the extracts of iron-akermanite, Ca^{2+} was the major component, followed by Si^{+} and Mg^{2+} , while the Fe^{2+} concentration was the lowest (Figure 6.8b). The Ca^{2+} concentration was 78 ± 2 mg/L, 77 ± 3 mg/L, 67 ± 2 mg/L, and 62 ± 1 mg/L for the Fe-5Ak, Fe-10Ak, Fe-15Ak, and Fe-20Ak extracts, respectively. The Ca^{2+} concentration decreased as the volume fraction of the akermanite increased in the specimens. Likewise, the Fe^{2+} concentration values (*i.e.*, 21.7 ± 0.4 mg/L, 15 ± 2 mg/L, 12 ± 1 mg/L, and 12.2 ± 0.2 mg/L, respectively) were lower in the extracts of the specimens with higher akermanite volume fractions. The Mg^{2+} concentration was 26.8 ± 0.3 mg/L, 32 ± 1 mg/L, 36 ± 1 mg/L, and 43 ± 1 mg/L for the Fe-5Ak, Fe-10Ak, Fe-15Ak, and Fe-20Ak specimens, respectively. The corresponding values of the Si^{+} concentration were 44 ± 1 mg/L, 59 ± 2 mg/L, 60 ± 2 mg/L, and 66 ± 1 mg/L, respectively. Unlike Ca^{2+} and Fe^{2+} , higher concentrations of Mg^{2+} and Si^{+} were observed for the extracts of the specimens with higher volume fractions of akermanite.

6.3.7 Proliferation of cells and their morphology

From day 7 of the cell culture, the preosteoblasts cultured on the porous Fe-10Ak, Fe-15Ak, and Fe-20Ak specimens showed significantly higher proliferation as compared to that of the Fe-5Ak specimens (Figure 6.8c). A higher viable cell count was measured for the specimens with a higher volume fraction of akermanite. However, the preosteoblasts did not proliferate on the Fe-5Ak composite. In addition, a lower cell viability was observed, indicating that these specimens were cytotoxic. Therefore, this group was excluded from the osteogenic assays. At day 7 of cell culture, the numbers of preosteoblasts corresponding to the Fe-10Ak, Fe-15Ak, and Fe-20Ak specimens were not significantly different from the number of cells measured for the Ti-6Al-4V specimens. At day 28 of cell culture, the cells grew more on Ti-6Al-4V than on all the porous iron-akermanite scaffolds ($p < 0.0001$). Nevertheless, the number of

preosteoblasts present on the composite scaffolds exhibited a 30-fold increase within the same period of time (Figure 6.8c).

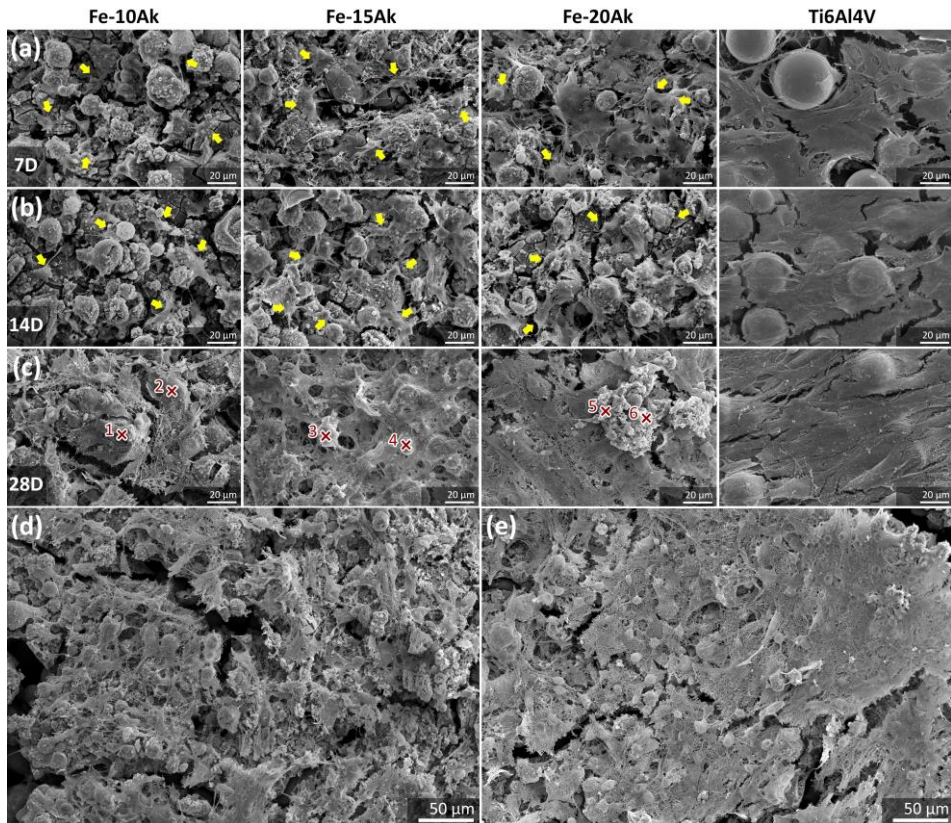


Figure 6.9. The morphologies of the preosteoblasts after (a) 7 d, (b) 14 d, and (c) 28 d of culture on the Fe-10Ak, Fe-15Ak, and Fe-20Ak composite scaffolds. At a lower magnification, the formation of fibrous extracellular matrix on the periphery of the (d) Fe-10Ak and (e) Fe-20Ak composites.

The fluorescent images revealed the morphologies and distributions of preosteoblasts after 7 d (Figure 6.8d), 14 d (Figure 6.8e), and 28 d (Figure 6.8f) of culture on the porous Fe-10Ak, Fe-15Ak, and Fe-20Ak composites and Ti-6Al-4V specimens. High-density, well-adherent cells were evident on the iron-akermanite composites with almost no differences from the cells residing to the Ti-6Al-4V specimens, save for the Fe-5Ak scaffolds (Figure S6.7). On the SEM micrographs captured at days 7 (Figure 6.9a) and 14 (Figure 6.9b), the preosteoblasts were elongated and had developed extended poly-directional filopodia on the tested porous composite specimens (*i.e.*, Fe-10Ak, Fe-15Ak, and Fe-20Ak). By day 28, the preosteoblasts were integrated into fibrous matrix

layers on the surface of the porous composite specimens (Figure 6.9c). The preosteoblasts present on the Ti-6Al-4V specimens proliferated well and formed multiple cellular layers by the end of the cell culture period. But such a fibrous-like layer was not observed on the Ti-6Al-4V specimens. Preosteoblasts on the Fe-20Ak composite developed the densest fibrous matrix layer (Figure 6.9d-e). On this matrix, the precipitation of minerals containing high Ca/P mass percentages, corresponding to the Ca/P atomic ratios in the range of 0.47 to 0.88 was identified (Table 6.3).

Table 6.3. Chemical compositions of the precipitated compounds (wt%) on the periphery of the porous Fe-Ak scaffolds after being cultured with preosteoblasts for 28 d, determined by EDS analysis.

EDS point		C	O	Na	Mg	Cl	P	K	Ca	Fe
Fe-10Ak	1	19.99	36.43	7.13	-	0.67	5.97	0.81	5.27	23.72
	2	14.34	27.62	6.57	-	0.97	9.57	1.14	7.68	32.11
Fe-15Ak	3	39.45	28.52	7.59	-	0.85	5.73	0.87	2.93	14.06
	4	32.63	28.57	6.04	-	-	8.30	0.75	3.90	19.81
Fe-20Ak	5	15.31	15.82	3.30	0.38	0.84	13.04	1.46	8.99	40.86
	6	16.24	16.45	5.02	-	0.85	12.72	1.98	8.29	38.45

6.3.8 Collagen type-1 staining, Ca/P deposition, and ALP activity

Preosteoblasts cultured on the porous iron-akermanite composites demonstrated the initial cues of osteogenic differentiation. The fibrous matrix observed on the SEM micrographs (Figure 6.9) was confirmed to be made of collagen type-1 (Figure 6.10). At the 7th d of cell culture, the collagen type-1 staining on the composites was more profound on the Fe-20Ak scaffolds than on the Fe-15Ak and Fe-10Ak scaffolds (Figure 6.10a). The collagen type-1 matrix further intensified over 14 d of cell culture (Figure 6.10b). At day 28, the matrix covered the struts of the Fe-15Ak and Fe-20Ak specimens (Figure 6.10c). The porous iron-akermanite composites clearly induced more collagen secretion than the Ti-6Al-4V specimens. In addition, the variation of the Ca²⁺ concentrations in the cell culture medium of the iron-akermanite composites with time was also measured (Figure 6.10d). At day 7, the Ca²⁺ concentrations were 146.9 ± 5.3 mg/L, 155.6 ± 7.4 mg/L, and 169.4 ± 4.2 mg/L for the Fe-10Ak, Fe-15Ak, and

Fe-20Ak groups, respectively. At days 14 and 28, the Ca^{2+} concentrations decreased to 127.0 ± 3.1 mg/L and 113.2 ± 6.8 mg/L for Fe-10Ak, 147.8 ± 2.4 mg/L and 97.0 ± 2.6 mg/L for Fe-15Ak, and 154.2 ± 4.2 mg/L and 104.9 ± 3.3 mg/L for Fe-20Ak.

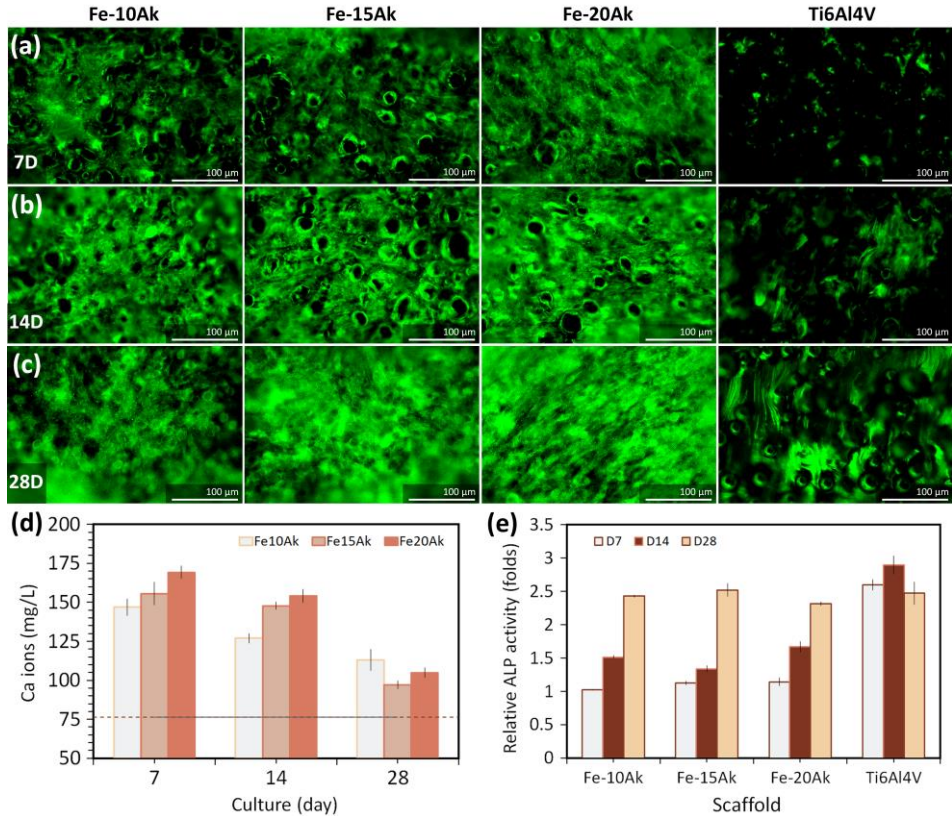


Figure 6.10. Collagen type-1 staining on the porous Fe-10Ak, Fe-15Ak, and Fe-20Ak composite scaffolds after culture with preosteoblasts for (a) 7 d, (b) 14 d, and (c) 28 d. (d) The variations of the Ca ion concentration in the cell culture medium during the cell culture period. (e) The ALP activity values of the preosteoblasts at a number of selected time points.

Furthermore, at day 7, the ALP activity values of the preosteoblasts on the Fe-10Ak, Fe-15Ak, Fe-20Ak and Ti6Al4V specimens were 1.0-fold, 1.1-fold, 1.1-fold, and 2.6-fold higher than the negative control groups, respectively. At day 14, the ALP activity values were 1.5-fold, 1.3-fold, 1.7-fold, and 2.9-fold higher than the negative control groups, respectively. At day 28, the ALP activity values of the preosteoblasts cultured on the composite specimens (*i.e.*, Fe-10Ak, Fe-15Ak, Fe-20Ak) were 2.4-fold, 2.5-fold, and 2.3-fold higher than the negative control

groups. The values were almost comparable to the Ti-6Al-4V specimens cultured in the osteogenic medium (*i.e.*, 2.5-fold higher than the negative control groups).

6.4 Discussion

The results of this study show the potential of iron-akermanite composite scaffolds fabricated using extrusion-based 3D printing for enhancing the performance of iron-based bone substitutes. The developed biomaterials successfully addressed both challenges associated with iron-based bone substitutes, namely their low rates of biodegradation and limited bioactivity. The biodegradation rates (*i.e.*, 0.08–0.13 mm/y 28 d *in vitro*) were significantly enhanced due to the addition of 5–20 vol% akermanite to iron. Despite the intensified biodegradation, the porous composites maintained their mechanical properties (*i.e.*, $E = 0.13\text{--}0.24$ GPa and $\sigma_y = 0.8\text{--}4.3$ MPa) high enough to be in the range of the values reported for the cancellous bone [56]. Furthermore, the composite scaffolds provided a favorable environment for the adhesion, proliferation, and osteogenic differentiation of preosteoblasts. These findings further advance the development of additively manufactured porous biodegradable iron for application as bone substitutes, encouraging further *in vivo* research to bring them closer to clinical applications.

6.4.1 Extrusion-based 3D printing of the porous iron-akermanite scaffolds

Extrusion-based 3D printing, followed by debinding and sintering, accomplished the additive manufacturing of porous iron-akermanite composite scaffolds. We created iron-akermanite-containing inks that could be simply extruded into 3D porous architecture at ambient temperature. Here, the choice of binder is of critical importance, *e.g.*, hypromellose polymer (Figure S6.2) being able to provide the inks with the shear-thinning properties that are required to enable smooth flow without clogging at the nozzle tip [57–60]. The printing pressure was the only variable that was altered during the 3D printing of the inks. A higher printing pressure was required for a more viscous iron-akermanite ink (Figure S6.2). The viscosity values of the inks differed due to the hydrophilic behavior of akermanite [61], which increased with the volume fraction of akermanite suspended in the ink. Upon extrusion, the inks quickly solidified, meaning that the shape of the scaffolds could be well maintained. The green-bodies were robust (Figure S6.1) and could be immediately transformed into porous iron-akermanite composites through the debinding and sintering process steps (Figure 6.1).

The composite scaffolds contained well-defined macropores that conformed to the original design (Figure 6.1d). The choice of the sintering parameters (*i.e.*, temperature = 1200 °C and time = 6 h) allowed iron and akermanite powder

particles to be partially sintered, resulting in minimal shrinkage. The partially sintered iron-akermanite powders provided random micropores in the struts (Figure 6.1e-h), thereby increasing the total porosity of the final scaffolds beyond the initially designed values (with solid struts). Iron particles appeared to have been coated with Ca, Mg, and Si (Figure 6.1i), which was due to the water-based binder in the ink that promoted the dissolution of akermanite particles during the ink preparation and the 3D printing process (Figure S6.3). This coating could be beneficial for the adhesion and proliferation of osteoprogenitor cells to promote osseointegration [62,63]. The iron-akermanite composite scaffolds exhibited a large pore interconnectivity (*i.e.*, 97-99%, Figure 6.2a). A highly interconnected porous scaffold has been suggested to be beneficial for tissue regeneration [64], as it allows for improved cell migration, nutrition, and oxygenation throughout the scaffolds.

Furthermore, the composite scaffolds only contained the α -Fe and akermanite phases (Figure 6.2c), indicating that the two materials maintained their individual characteristics even after exposure to the high temperature during sintering at 1200 °C for 6 h. However, at the interfaces, iron had diffused into the akermanite phase (Figure 6.2d). Such an event has been also observed in other studies on iron-based composites prepared by using the sintering technique [26,28,29]. Proper interfacial bonding between both material types is of importance, as poorly bonded interfaces often cause premature failure when applied stress exceeds certain thresholds [65–67]. Such interface diffusion between the iron matrix and the akermanite phase may strengthen the mechanical integrity of the composite scaffold for its intended use and assist with the bone regeneration process.

6.4.2 Biodegradation

Porous iron-akermanite composites demonstrated significant increases in their rates of *in vitro* biodegradation (*i.e.*, from 1.6 to 2.6 times at day 28) as compared to porous monolithic iron scaffolds [19]. The higher solubility of akermanite in the physiological solution (as compared to iron) led to a higher mass loss during the initial 4 days of biodegradation for all the scaffolds (Figure 6.3b), which is in line with the biodegradation mechanisms of typical iron-bioceramic composites described in the literature [22,28,29]. The mass loss values dropped on day 7 and progressed with even lower rates for the later time points (*i.e.*, days 14 and 28) of the biodegradation tests. Such variations in mass loss were a result of the precipitated biodegradation products that influenced the corrosion process. Indeed, the addition of akermanite enhanced the biodegradation of the composites. This was further confirmed by the continuous release of Ca^{2+} , Mg^{2+} , and Si^{+} into the immersion medium (Figure 6.4). Besides

its favorable solubility, the dissolution of akermanite is expected to have also created available micro-channels for r-SBF to be in contact with more iron surfaces for biodegradation.

As corrosion naturally occurred during the immersion tests, the degradation products precipitated all over the surfaces of the composite scaffolds (Figure 6.5, S6.4-6.6). In general, the dense Fe-based corrosion products are known to promote the passivation of the substrate, thereby slowing down biodegradation at the later time points of the immersion period (Figure 6.3c). The principal phase in the degradation products was identified to be γ -FeOOH (Figure 6.3d-e). This is similar to other biodegraded Fe scaffolds [17].

Ca-based biodegradation products were also identified. The precipitation of Ca-based degradation products can be related to the total Ca^{2+} concentration in the immersion medium (Figure 6.4). The concentration of Ca^{2+} released from akermanite into SBF was reported to be approximately 5 times higher than its initial concentration in the medium after 20 days of *in vitro* biodegradation [68]. After 28 d of biodegradation, however, the Ca^{2+} concentrations in the immersion media of the Fe-15Ak and Fe-20Ak specimens were only 1.2-1.3 times higher than the initial concentration in the r-SBF medium (Figure 6.4b). For the specimens with a lower akermanite volume fraction (*i.e.*, Fe-5Ak or Fe-10Ak), Ca^{2+} released from the akermanite phase was merely sufficient to maintain the ion concentration close to the original value in r-SBF for 7 days. At the later time points of immersion, the Ca^{2+} concentration even dropped (Figure 4b). These imply that the Ca^{2+} released from the composite scaffolds mostly participated in the formation of the biodegradation products. However, the expected calcium phosphate compounds were not detected, despite the significant decline in the concentration of the PO_4^{3-} in the immersion medium (Figure 6.4e). The P element was scarcely observed in the other biodegradation products (Table 6.2, S6.1-6.3). Instead, CaCO_3 formed on the composite scaffolds as early as day 4 of the immersion test (Figure 6.3d-e). This is likely because the biodegradation process took place in a 5% CO_2 atmosphere, which maintained the HCO_3^- concentration in the immersion medium, allowing CaCO_3 to form [69].

The CaCO_3 phase is stable in the presence of Mg and Si [70–72]. Given that we observed the CaCO_3 phase in the biodegradation products up to the end of the immersion test period (*i.e.*, 28 d), the stabilization stage must have occurred due to the readily accessible Mg^{2+} and Si^+ in the immersion medium (Figure 6.4c-d). The Mg^{2+} and Si^+ concentrations continuously increased over the immersion period (Figure 6.4c-d). The Mg-based biodegradation products (*e.g.*, $\text{Mg}(\text{OH})_2$) are known to be stable in environments with $\text{pH} \geq 11.5$ [73]. The absence of Mg- or Si-based biodegradation products is, therefore, not unexpected, given that the biodegradation takes place under relatively stable pH conditions with a pH value

of up to 7.65. In addition, for calcium phosphate formation in CaO-SiO₂-based compounds, such as akermanite, a negatively charged surface made of a hydrated silica-rich layer is required for apatite nucleation [68]. The unavailability of Si-based biodegradation products can further explain the delay in the growth of bony apatite on the struts of the scaffolds. A favorable property of the CaCO₃ phase is that it is a precursor material for the carbonate apatite mineral [74–76]. CaCO₃ is well-known for its biodegradability and bioactivity and is clinically used as a bone filler [77]. The addition of CaCO₃ to the biodegradation products is, therefore, expected to improve the cytocompatibility of the developed bone substitutes.

The precipitation of the biodegradation products influences the electrochemical responses of the specimens. The stable OCP values (Figure 6.6a) suggest that the iron-akermanite composite scaffolds preserved their susceptibility to biodegradation over time and that their associated biodegradation products did not passivate the base materials (Figure 6.6b). The modulus of the impedance at low frequencies, indicative of the charge transfer and hence corrosion resistance, shows a reducing trend with time (Figure 6.6c-f), which is similar to the R_p results (Figure 6.6b). In addition, the impedance modulus values at mid-frequency range (*e.g.*, 100 Hz), indicative of the evolution of the corrosion products [52–54], were relatively stable over time (Figure 6.6c-f), albeit that some ongoing corrosion product formation is suggested by the trend of the peak start of the Bode plot phase angle at low-to-mid frequencies to shift from a higher frequency to a lower frequency as a function of time of exposure [78]. All in all, the EIS data analysis indicates that the intrinsic integrity and protectiveness of the biodegradation products are relatively limited. The decreasing resistivity and the evolution of the corrosion process can also be explained by the formation and maturation of CaCO₃ on the surfaces of the specimen struts. Despite its dense coverage on the surfaces, the biodegradability of CaCO₃ [77] means that corrosion can continuously progress into the base material.

In general, the *in vitro* biodegradation rates of the iron-akermanite composite scaffolds are comparable with those reported in the literature (Table 6.4). However, the Fe-based composites were mostly studied in the bulk form and contained different types or compositions of bioceramics, which makes direct comparison challenging. Several factors are of importance to consider when one compares the biodegradation rates of Fe-based composites. Firstly, the addition of bioceramics with a high volume fraction to the Fe matrix improves the biodegradability of the composites. For example, akermanite biodegraded faster than TCP [41,43], but the bulk Fe composites with higher TCP volume fractions (*i.e.*, 25–50 vol% [25,27]) biodegraded more rapidly than our composite scaffolds

with lower akermanite volume fractions (*i.e.*, 5–20 vol%). Secondly, bioceramics are often selected, based on their own biodegradation profiles. For example, bredigite has a higher biodegradation rate than akermanite [79]. The addition of 5 and 7.5 wt% bredigite to the Fe matrix [33] led to much higher rates of biodegradation than our scaffolds made of Fe-15Ak (= 6.2 wt% Ak) and Fe-20Ak (= 8.6 wt% Ak). However, this can be further tuned by the design of the composite structure (*e.g.*, open porosity or intricate porous design). For instance, CaSiO₃ is known for its superior biodegradability [43,80], but the bulk Fe-based composites containing 20–30 wt% CaSiO₃ did not biodegrade faster, as compared to porous Fe-20Ak (= 8.6 wt% Ak) composite scaffolds [28,29]. The high interconnected porosity of the iron-akermanite composite scaffolds clearly enhances their biodegradation rates, even though the dissolution rate of akermanite is lower than that of CaSiO₃ [43].

In addition, the fabrication processes applied to a composite material can alter its biodegradation profile too. A powder metallurgy technique that includes ball milling can create a much refined microstructure of the resulting powder particles, which often results in an enhanced biodegradation rate of the composite. The bulk Fe composite containing 5 wt% HA did not show a faster biodegradation rate compared to the bulk pure Fe [22]. When the HA particles were milled into various smaller sizes, the biodegradation rate of Fe-5 wt% HA composites increased up to 5 times [24]. A similar event was also reported for the Fe-Mg₂Si composites [30–32], given in Table 6.4.

Furthermore, the immersion solution influences the biodegradation rates. We used the r-SBF medium that has the same ion concentrations as the blood plasma. Other available solutions (*e.g.*, SBF or modified Hank's Balanced Salts) contain a higher concentration of Cl⁻ that can accelerate the biodegradation of iron. Moreover, the addition of proteins to the solution has been reported to affect the corrosion profile of iron [81]. Finally, and most importantly, the corrosion profile of Fe-based composites should be styled for sustainable biodegradation, while maintaining the mechanical integrity of the bone substitutes.

6.4.3 Mechanical behavior

When loading is applied to a composite scaffold, the load will be transferred from the iron matrix to the reinforcing phase across many interfaces [21]. Therefore, good interfacial bonding between iron and akermanite is of importance to ensure that high strength is achieved and the mechanical integrity of the composite material is preserved. Our iron-akermanite composite scaffolds were capable of maintaining their mechanical properties (*i.e.*, $E = 0.13\text{--}0.24$ GPa and $\sigma_y = 0.8\text{--}4.3$ MPa) in the range of those of the cancellous bone [56], even after 28 days of biodegradation and did not exhibit any signs of premature failure

(Figure 6.7). The addition of 10 vol% akermanite to the iron matrix led to the highest Young's modulus value (Figure 6.7b). As for the yield strength, adding akermanite did not improve the value. The mechanical properties of the composite scaffolds were much lower than those of the porous monolithic iron ($E = 0.6$ GPa and $\sigma_y = 7.2$ MPa) [19]. This could be attributed to the intrinsically brittle nature of akermanite and its low fracture toughness [82].

Biodegradation usually reduces the mechanical properties of the biomaterials. The change in the mechanical properties should be tailored to match the rate of bone tissue regeneration to ensure that the required mechanical support continues to be available. The yield strength decreased with biodegradation time for all the porous iron-akermanite scaffolds. Similar trends have been also observed for Fe-TCP composites (with 30–40 vol% TCP) after 56 days of biodegradation [25]. Interestingly, the Young's moduli of the composite scaffolds increased at the later time points of biodegradation (Figure 6.7b-c).

The changes in the mechanical properties can be explained by the interactions between the composite scaffold and its biodegradation products during mechanical loading. The bonding between the biodegradation products and the strut surfaces and pores of the composite scaffolds is due to the van der Waals forces. When subjected to small levels of compressive strain, this weak bonding can share the load between the composite matrix and the degradation products, hence increasing Young's modulus. The improvement in Young's modulus after biodegradation is likely due to the strengthening effect of precipitation and the growth of the biodegradation product phases and has been observed in other studies as well [83,84]. At the higher levels of strain (*e.g.*, reaching the yield strain), however, such load transfer will fail. From there on, the mechanical strength will only depend on the biodegraded base materials, which is why the yield strength decreases with immersion time. It is important to note that the inclusion of up to 20 vol% akermanite in the composite did not make the composite material brittle. The iron-akermanite scaffolds exhibited a ductile behavior despite biodegradation (Figure 6.7), which is important for enduring cyclic loading when used as load-bearing bone substitutes.

6.4.4 Cytocompatibility and osteogenic properties

Limited bioactivity is one of the major challenges hampering the clinical use of biodegradable Fe-based materials. The response of the cells to biodegradable materials is strongly conditioned by the concentrations of the ions released into the medium and the formation of the biodegradation products. In the present work, the iron-akermanite composite scaffolds (with 10–20 vol% akermanite) received a high metabolic response from the preosteoblasts MC3T3-E1 cell line (Figure 6.8). The composite scaffolds were favored by the cells for adhesion and

proliferation over the entire period of the cell culture experiments (Figure 6.8). The specimens also allowed the deposition of collagen type-1 (Figure 6.9) and the formation of initial bone minerals *in vitro* (Figure 6.10).

First, we evaluated the metabolic activity of preosteoblasts using the iron-akermanite extracts. A higher volume fraction of akermanite in the composite scaffold resulted in lower concentrations of Ca^{2+} and Fe^{2+} released into the medium (Figure 6.8b). The reduced Ca^{2+} concentration in the extracts corresponded to the formation of Ca/P compounds on the composite scaffolds during the immersion in the cell culture medium (Figure S6.8, Table S6.4). The Fe^{2+} depletion could be due to its precipitation in the formation of other degradation products (*e.g.*, made of carbonates). The cytocompatibility of the Fe-based composite scaffolds is mainly limited by the high concentration of released Fe^{2+} , which catalyzes the formation of radical compounds that are harmful to cells [85]. However, the Fe^{2+} concentration values in all the extracts were much lower than the inhibitory concentration (IC_{50}) reported for preosteoblasts [20]. This implies that the inhibition of the metabolic activity by 100% extracts may be due to other factors, such as the highly ionic environment in the medium that could induce cell death [86]. With a slight dilution (*i.e.*, $1.3\times$), the preosteoblasts turned highly active in the Fe-10Ak, Fe-15Ak and Fe-20Ak extracts. These results were very much improved, compared to those of monolithic iron scaffolds [19].

Furthermore, we studied the adhesion, proliferation, and osteogenic differentiation of the preosteoblasts directly cultured on the composite scaffolds with a high medium amount to minimize the local build-up of metal ions and better mimic the *in vivo* conditions (*e.g.*, in the presence of *in vivo* fluid circulation). The Fe-5Ak composite scaffold was found to exhibit a similar cytotoxic response to the pure iron scaffold (as reported elsewhere [19]). The Fe-5Ak group released a higher concentration of Fe^{2+} , as compared to the other composite scaffold groups (Figure 6.8b), which must have contributed to the cytotoxicity of the material. In other words, the 95 vol% iron content in the composite appeared to be still too high to provide a cytocompatible and bioactive environment for the cells. Conversely, the preosteoblasts were viable and proliferated on the Fe-10Ak, Fe-15Ak, and Fe-20Ak composites (Figure 6.8c). The proliferation rates of the cells cultured with the composite scaffolds (with 10 – 20 vol% Akermanite) were comparable to the values measured for Ti-6Al-4V (the reference) during the first 7 days but somewhat decreased over time. Nevertheless, the preosteoblasts were actively growing over time (Figure 6.8c), which is a strong indicator for the cytocompatibility of the Fe-based composite scaffolds for these cells. In addition, the preosteoblasts well adhered to the composite surfaces (Figure 6.8d-f) with an elongated shape and poly-directional filopodia (Figure 6.9a-b). Despite the enhanced biodegradation rates, all the

hallmarks of cytocompatibility were observed in the responses of the preosteoblasts to the composite scaffolds. This is caused by the addition of akermanite to the Fe matrix [41–43]. Similar levels of cytocompatibility have been also observed for other types of Fe-based composites (*e.g.*, Fe-TCP [22], Fe-CaSiO₃ [28,29], and Fe-Bredigite [33]).

The composite scaffolds (containing 10–20 vol% akermanite) further evidenced their ability to induce osteogenic differentiation without the use of any osteogenic reagent (*i.e.*, ascorbic acid or β -glycerophosphate) during the cell culture experiments. At the later time points (*i.e.*, from day 7 and onwards), the preosteoblasts secreted a fibrous-like matrix (Figure 6.9) that was recognized as collagen type-1 (Figure 6.10a-c). Collagen substrate has been shown to facilitate the precipitation of minerals and support osteogenic differentiation [87,88]. We observed large amounts of Ca/P elements (Table 6.3) in the minerals deposited on the collagen layer (Figure 6.9c) along with other molecules (*e.g.*, carbonate-based precipitates). On the contrary, the formation of Ca/P compounds on the scaffolds immersed in the cell culture medium without cells (Figure S6.8, Table S6.4) only occurred on the surfaces of akermanite particles, but not on Fe particles. Finally, the composite scaffolds enhanced the ALP activity of the cells from day 14 towards a level comparable with that of the cells cultured on Ti-6Al-4V scaffolds under the osteogenic conditions at day 28 (Figure 6.10e). Akermanite was previously found to promote the osteogenic differentiation of rat bone marrow stem cells [42] and of human bone marrow stem cells [89] even without any need for osteogenic supplements [90]. Taken together, our *in vitro* results show the potential of the iron-akermanite composite scaffolds as osteoinductive biomaterials to assist bone regeneration.

6.5 Conclusion

We used extrusion-based 3D printing to fabricate, for the first time ever, porous iron-akermanite composite scaffolds. We then studied the characteristics of the porous composite scaffolds, aiming to bring Fe-based biomaterials closer to meeting the clinical requirements for bone substitution. The iron-akermanite composites possessed a highly interconnected porous structure. The *in vitro* biodegradation rates of the composite scaffolds were enhanced due to the presence of akermanite in the α -Fe matrix. The biodegradation process and its associated product formation on the composite scaffolds influenced the mechanical properties of the composites. However, the yield strengths and elastic moduli of the specimens stayed in the range of those reported for the cancellous bone even after 28 days of biodegradation. Indirect cell culture showed the enhanced cytocompatibility of the composites for preosteoblasts as compared to similarly processed pure iron, which was most likely caused by the presence of Ca²⁺, Mg²⁺, and Si⁺ in the culture medium. In direct cell cultures, the

preosteoblasts well adhered to the composite specimens (containing 10-20 vol% akermanite), proliferated over time, and secreted the collagen type-1 matrix that stimulated bony-like mineralization. In terms of ALP activity, the composite specimens (containing 10-20 vol% akermanite) were not significantly different from the positive control (*i.e.*, Ti6Al4V specimens), when subjected to the cell culture under osteogenic conditions. Taken together, the results of this study clearly show the exceptional potential of the developed porous composite scaffolds for application as bone substitutes and motivate further research into their *in vivo* performance.

6.6 Supplementary material

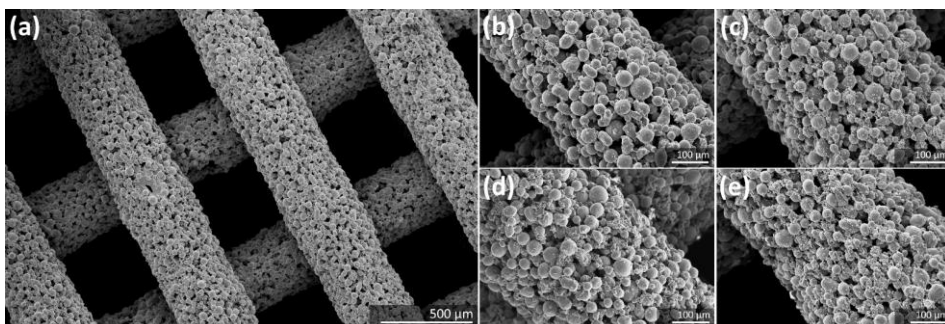


Figure S6.1. (a) Morphology of the green-body porous iron-akermanite composite scaffolds, and the strut morphologies of the (b) Fe-5Ak, (c) Fe-10Ak, (d) Fe-15Ak, and (e) Fe-20Ak composites at a higher magnification.

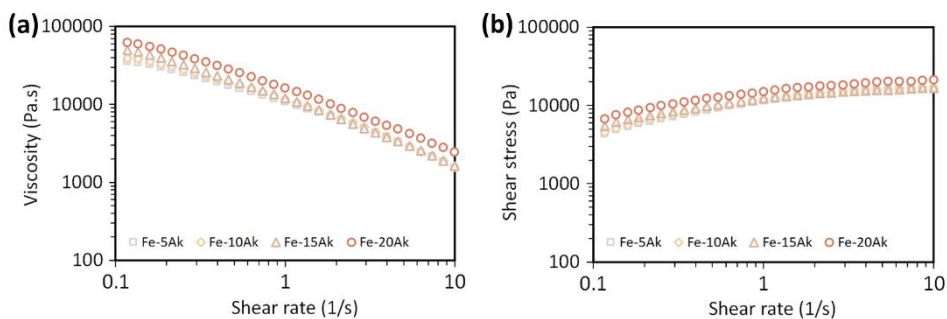


Figure S6.2. The rheology properties of the iron-akermanite-containing inks: (a) the viscosity curves and (b) the shear stress values as a function of shear rate.

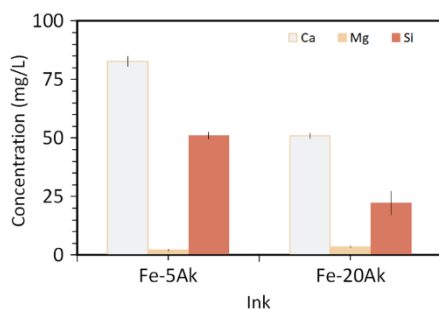


Figure S6.3. Concentrations of Ca, Mg, Si ions released to the iron-akermanite-containing inks during ink preparation and 3D printing.

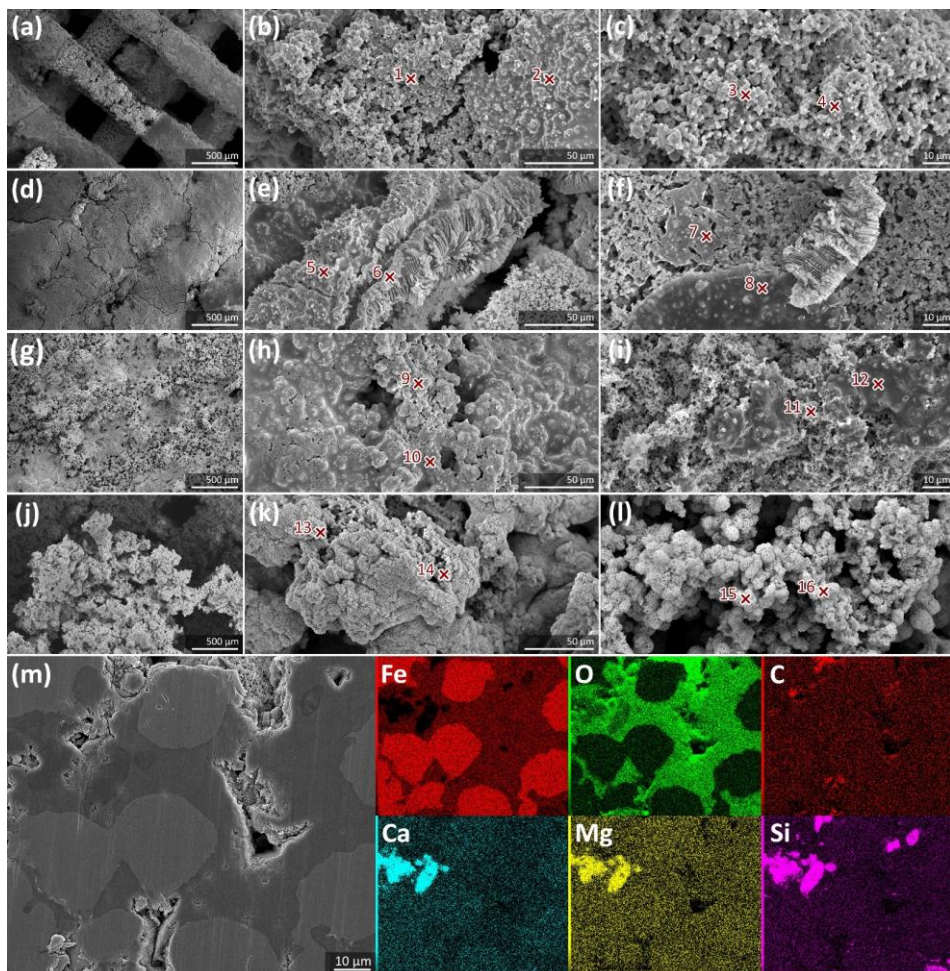


Figure S6.4. The morphologies of the *in vitro* biodegradation products formed on the porous Fe-15Ak scaffolds: on the periphery after (a, b, c) 4 d, (d, e, f) 7 d, (g, h, i) 14 d and (j, k, l) 28 d of biodegradation, and (m) at the center of the scaffolds after 28 d of biodegradation. The cross marks with numbers indicate the location of EDS analyses, whose results are presented in Table S6.1.

Table S6.1. Chemical compositions of the *in vitro* biodegradation products on the periphery of the porous Fe-15Ak scaffolds, determined by EDS analysis.

Fe-15Ak	EDS point	C	O	Na	Mg	Si	Cl	P	Ca	Fe
4 d	1	5.36	26.11	-	-	-	0.68	-	0.60	67.26
	2	10.39	24.41	-	-	-	-	-	1.48	63.72
	3	7.79	21.09	-	-	-	1.81	-	2.90	66.40
	4	8.03	37.30	-	0.70	-	-	-	45.51	8.46
7 d	5	13.85	44.84	-	1.76	-	2.33	-	31.56	5.66
	6	-	19.16	2.66	1.03	-	-	5.52	28.96	42.68
	7	10.49	27.16	-	-	-	2.17	7.31	5.55	47.33
	8	12.48	33.53	-	-	-	2.03	-	5.10	46.87
14 d	9	10.88	32.75	9.38	-	-	-	7.02	7.00	32.96
	10	3.06	19.10	-	-	-	-	-	55.64	22.20
	11	13.88	33.30	11.20	-	-	-	-	1.47	40.16
	12	10.07	26.24	9.36	-	-	-	-	1.55	52.79
28 d	13	8.57	14.62	-	-	-	-	-	7.58	69.24
	14	19.39	15.43	-	-	-	-	-	5.65	59.53
	15	25.57	16.84	-	-	-	-	-	2.79	54.79
	16	18.63	7.41	-	-	-	-	-	1.00	72.96

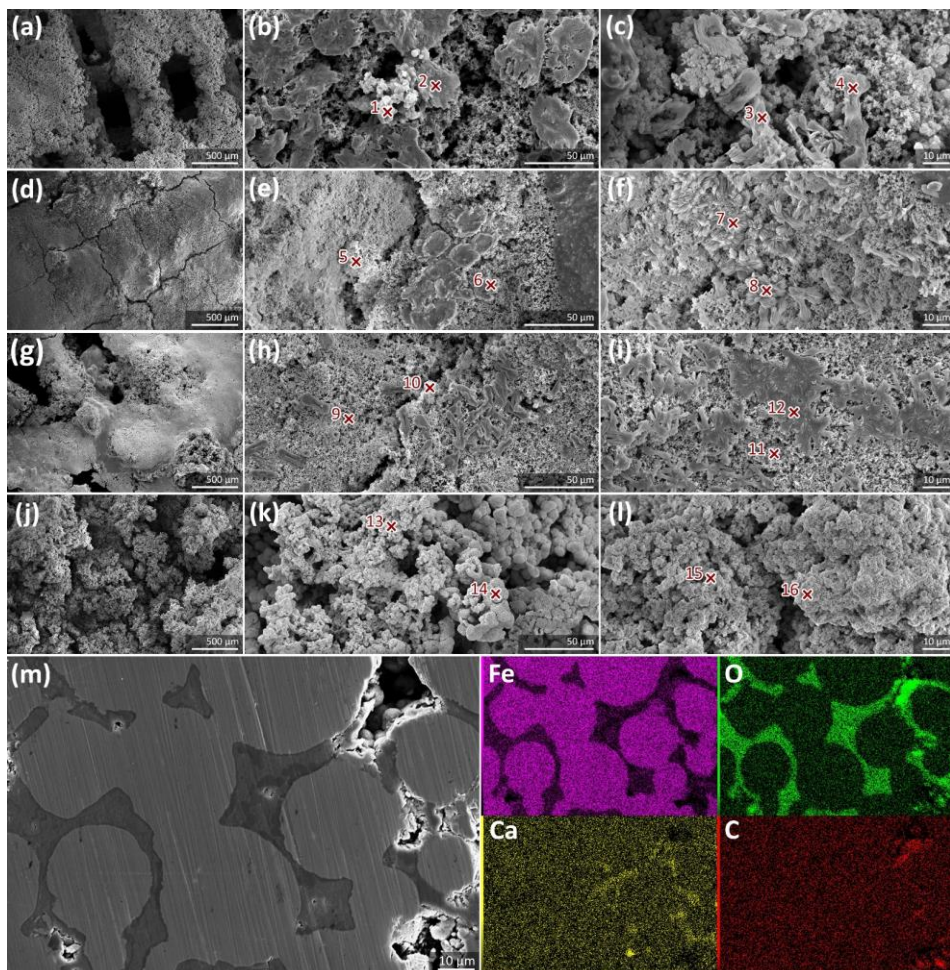


Figure S6.5. The morphologies of the *in vitro* biodegradation products formed on the porous Fe-10Ak scaffolds: on the periphery after (a, b, c) 4 d, (d, e, f) 7 d, (g, h, i) 14 d and (j, k, l) 28 d of biodegradation, and (m) at the center of the scaffolds after 28 d of biodegradation. The cross marks with numbers indicate the location of EDS analyses, whose results are presented in Table S6.2.

Table S6.2. Chemical compositions of the *in vitro* biodegradation products on the periphery of the porous Fe-10Ak scaffolds, determined by EDS analysis.

Fe-10Ak	EDS point	C	O	Na	Mg	Si	Cl	P	Ca	Fe
4 d	1	17.67	38.72	6.06	-	-	-	-	12.07	25.47
	2	9.89	39.83	1.28	0.69	-	-	-	45.62	2.69
	3	12.81	27.55	-	-	-	3.21	4.40	1.62	50.41
	4	16.23	35.18	-	-	-	2.51	3.07	1.18	41.83
7 d	5	11.25	32.59	2.24	1.42	-	-	-	38.61	13.88
	6	15.70	43.72	1.26	1.01	-	1.23	-	29.24	7.83
	7	8.21	16.97	-	-	-	-	-	26.16	48.66
	8	7.79	29.95	1.50	0.93	-	-	-	50.69	9.15
14 d	9	14.04	29.21	-	-	-	-	-	8.46	48.29
	10	6.53	24.85	4.16	-	-	-	2.69	6.36	35.01
	11	-	16.00	-	-	-	-	-	12.60	71.40
	12	21.78	23.30	2.09	2.09	-	-	-	34.30	16.45
28 d	13	3.85	3.19	-	-	-	-	-	9.39	83.56
	14	26.59	7.34	-	-	-	-	-	2.28	63.80
	15	41.77	9.85	-	-	-	-	-	3.63	44.75
	16	45.20	6.52	-	-	-	-	-	2.85	45.42

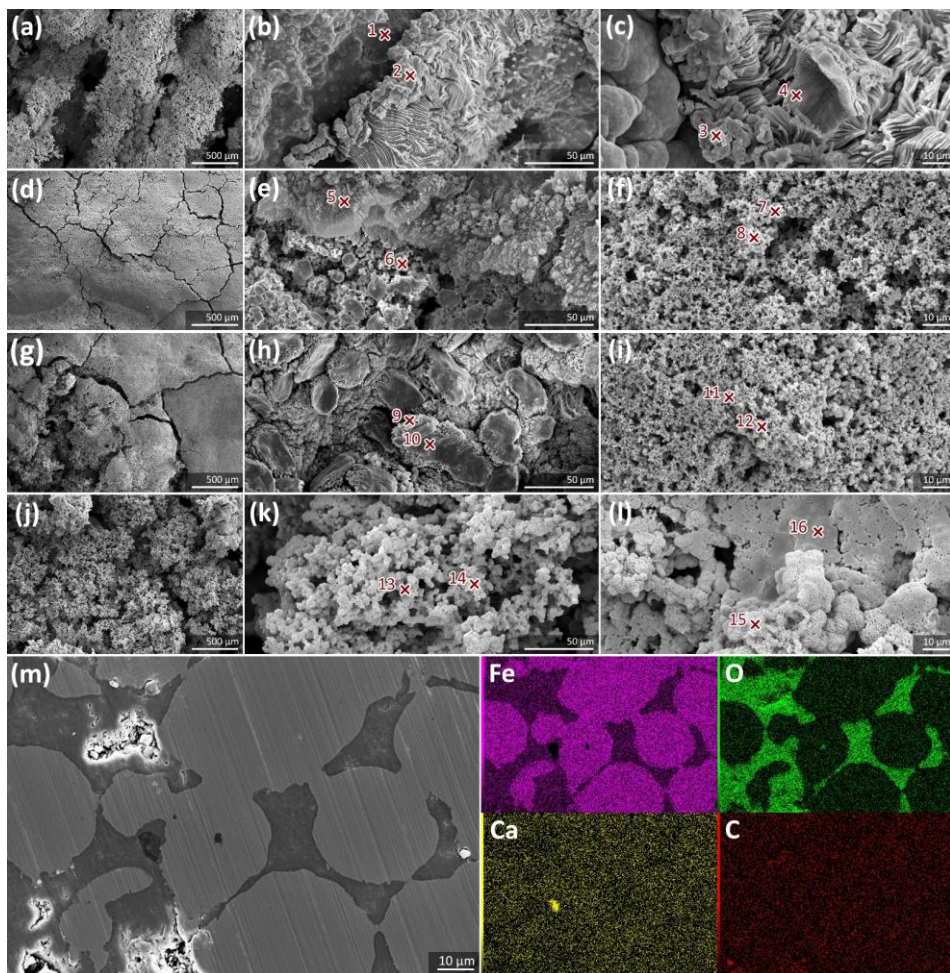


Figure S6.6. The morphologies of the *in vitro* biodegradation products formed on the porous Fe-5Ak scaffolds: on the periphery after (a, b, c) 4 d, (d, e, f) 7 d, (g, h, i) 14 d and (j, k, l) 28 d of biodegradation, and (m) at the center of the scaffolds after 28 d of biodegradation. The cross marks with numbers indicate the location of EDS analyses, whose results are presented in Table S6.3.

Table S6.3. Chemical compositions of the *in vitro* biodegradation products on the periphery of the porous Fe-5Ak scaffolds, determined by EDS analysis.

Fe-5Ak	EDS point	C	O	Na	Mg	Si	Cl	P	Ca	Fe
4 d	1	1.91	12.12	-	-	-	-	1.34	2.05	82.58
	2	1.60	7.26	-	-	-	-	-	1.00	90.15
	3	1.46	8.33	-	-	-	-	-	0.95	89.26
	4	8.66	33.15	1.67	-	-	-	1.59	2.19	52.74
7 d	5	9.11	18.80	-	-	-	3.34	-	9.63	59.12
	6	14.08	48.22	-	1.46	-	-	-	23.21	13.04
	7	14.87	18.93	-	-	-	4.68	-	8.54	52.98
	8	14.14	36.28	-	-	-	-	-	38.62	10.96
14 d	9	8.39	23.51	-	-	-	-	-	-	68.10
	10	6.07	24.09	-	-	-	-	-	-	69.84
	11	11.55	34.53	3.55	0.70	-	-	6.42	8.67	34.58
	12	13.00	45.39	2.57	0.47	-	-	1.70	17.82	19.05
28 d	13	11.92	14.02	3.59	-	-	-	-	10.76	59.72
	14	30.88	25.11	4.83	-	-	-	-	5.64	33.54
	15	20.59	10.97	-	-	-	-	-	-	68.44
	16	10.41	17.85	-	-	-	-	-	3.01	68.73

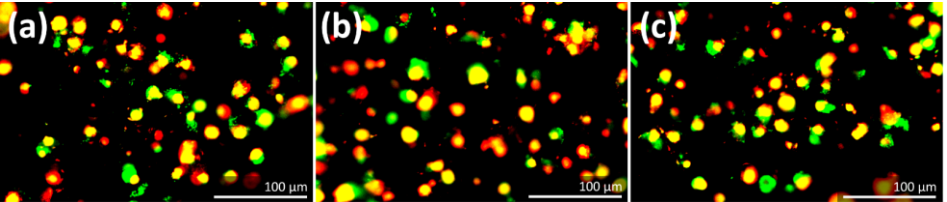


Figure S6.7. Live dead staining of preosteoblasts on the porous Fe-5Ak composite scaffolds after (a) 7 d, (b) 14 d, and (c) 28 d of culture.

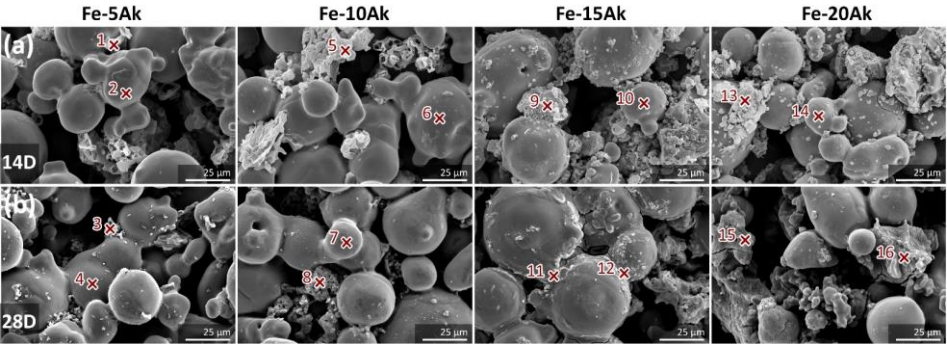


Figure S6.8. The morphologies of the *in vitro* biodegradation products and struts morphologies of the porous iron-akermanite scaffolds after (a) 14 d and (b) 28 d in the cell culture medium. The cross mark with number indicates the location of EDS analysis, whose results are given in Table S6.4.

Table S6.4. Chemical compositions of the *in vitro* biodegradation products on the porous iron-akermanite scaffolds in the cell culture medium, determined by EDS analysis.

Samples	EDS point	C	O	Na	Mg	Si	P	Ca	Fe
Fe-5Ak D14	1	17.56	29.75	6.42	-	-	-	7.77	38.49
	2	3.52	1.98	1.11	-	-	-	1.44	91.95
Fe-5Ak D28	3	17.97	19.21	7.39	1.19	-	2.04	11.47	40.74
	4	7.01	2.14	-	-	-	-	0.91	89.94
Fe-10Ak D14	5	18.46	38.19	7.32	2.57	-	3.41	12.89	17.16
	6	4.07	4.31	-	-	-	-	1.13	90.50
Fe-10Ak D28	7	4.69	1.32	-	-	-	-	2.45	91.54
	8	7.34	12.59	3.97	2.10	-	3.08	28.47	42.44
Fe-15Ak D14	9	10.58	31.04	6.81	1.32	-	7.37	21.98	20.91
	10	5.86	3.27	0.85	-	-	-	1.11	88.91
Fe-15Ak D28	11	-	8.36	3.20	2.12	-	-	35.57	50.74
	12	7.72	10.05	4.16	2.02	-	-	21.56	54.48
Fe-20Ak D14	13	8.10	20.29	3.64	1.75	-	13.26	30.49	22.47
	14	4.30	2.78	1.36	-	-	-	1.29	90.27
Fe-20Ak D28	15	3.17	6.90	-	1.51	8.67	2.78	22.47	54.50
	16	22.36	22.36	-	5.80	19.02	-	13.17	17.29

Bibliography

- [1] Y.F. Zheng, X.N. Gu, F. Witte, Biodegradable metals, *Mater. Sci. Eng. R Reports*. 77 (2014) 1–34. <https://doi.org/10.1016/j.mser.2014.01.001>.
- [2] J. He, F.L. He, D.W. Li, Y.L. Liu, Y.Y. Liu, Y.J. Ye, D.C. Yin, Advances in Fe-based biodegradable metallic materials, *RSC Adv.* 6 (2016) 112819–112838. <https://doi.org/10.1039/C6RA20594A>.
- [3] H. Hermawan, Updates on the research and development of absorbable metals for biomedical applications, *Prog. Biomater.* 7 (2018) 93–110. <https://doi.org/10.1007/s40204-018-0091-4>.
- [4] R. Gorejová, L. Haverová, R. Oriňáková, A. Oriňák, M. Oriňák, Recent advancements in Fe-based biodegradable materials for bone repair, *J. Mater. Sci.* 54 (2019) 1913–1947. <https://doi.org/10.1007/s10853-018-3011-z>.
- [5] A. Sharipova, S.K. Swain, I. Gotman, D. Starosvetsky, S.G. Psakhie, R. Unger, E.Y. Gutmanas, Mechanical, degradation and drug-release behavior of nano-grained Fe-Ag composites for biomedical applications, *J. Mech. Behav. Biomed. Mater.* 86 (2018) 240–249. <https://doi.org/10.1016/j.jmbbm.2018.06.037>.
- [6] A. Sharipova, I. Gotman, S.G. Psakhie, E.Y. Gutmanas, Biodegradable nanocomposite Fe-Ag load-bearing scaffolds for bone healing, *J. Mech. Behav. Biomed. Mater.* 98 (2019) 246–254. <https://doi.org/10.1016/j.jmbbm.2019.06.033>.
- [7] Y.P. Feng, N. Gaztelumendi, J. Fornell, H.Y. Zhang, P. Solsona, M.D. Baró, S. Suriñach, E. Ibáñez, L. Barrios, E. Pellicer, C. Nogués, J. Sort, Mechanical properties, corrosion performance and cell viability studies on newly developed porous Fe-Mn-Si-Pd alloys, *J. Alloys Compd.* 724 (2017) 1046–1056. <https://doi.org/10.1016/j.jallcom.2017.07.112>.
- [8] M.S. Dargusch, A. Dehghan-Manshadi, M. Shahbazi, J. Venezuela, X. Tran, J. Song, N. Liu, C. Xu, Q. Ye, C. Wen, Exploring the role of manganese on the microstructure, mechanical properties, biodegradability, and biocompatibility of porous iron-based scaffolds, *ACS Biomater. Sci. Eng.* 5 (2019) 1686–1702. <https://doi.org/10.1021/acsbiomaterials.8b01497>.
- [9] C. Shuai, W. Yang, Y. Yang, H. Pan, C. He, F. Qi, D. Xie, H. Liang, Selective laser melted Fe-Mn bone scaffold: Microstructure, corrosion behavior and cell response, *Mater. Res. Express*. 7 (2019) 015404. <https://doi.org/10.1088/2053-1591/ab62f5>.
- [10] P. Liu, D. Zhang, Y. Dai, J. Lin, Y. Li, C. Wen, Microstructure, mechanical properties, degradation behavior, and biocompatibility of porous Fe-Mn alloys fabricated by sponge impregnation and sintering techniques, *Acta Biomater.* 114 (2020) 485–496. <https://doi.org/10.1016/j.actbio.2020.07.048>.
- [11] N.E. Putra, M.A. Leeflang, P. Taheri, L.E. Fratila-Apachitei, J.M.C. Mol, J. Zhou, A.A. Zadpoor, Extrusion-based 3D printing of *ex situ*-alloyed highly biodegradable MRI-friendly porous iron-manganese scaffolds, *Acta Biomater.* 134 (2021) 774–790. <https://doi.org/10.1016/j.actbio.2021.07.042>.
- [12] P. Sotoudehbagha, S. Sheibani, M. Khakbiz, S. Ebrahimi-Barough, H. Hermawan, Novel antibacterial biodegradable Fe-Mn-Ag alloys produced by mechanical alloying, *Mater. Sci. Eng. C*. 88 (2018) 88–94. <https://doi.org/10.1016/j.msec.2018.03.005>.
- [13] M. Caligari Conti, B. Mallia, E. Sinagra, P. Schembri Wismayer, J. Buhagiar, D. Vella, The effect of alloying elements on the properties of pressed and non-pressed biodegradable Fe-Mn-Ag powder metallurgy alloys, *Heliyon*. 5 (2019) e02522. <https://doi.org/10.1016/j.heliyon.2019.e02522>.
- [14] P. Sotoudeh Bagha, M. Khakbiz, S. Sheibani, H. Hermawan, Design and characterization of nano and bimodal structured biodegradable Fe-Mn-Ag alloy with accelerated corrosion rate, *J. Alloys Compd.* 767 (2018) 955–965. <https://doi.org/10.1016/j.jallcom.2018.07.206>.
- [15] T. Huang, J. Cheng, Y.F. Zheng, *In vitro* degradation and biocompatibility of Fe-Pd and Fe-Pt composites fabricated by spark plasma sintering, *Mater. Sci. Eng. C*. 35 (2014) 43–53. <https://doi.org/10.1016/j.msec.2013.10.023>.
- [16] J. Čapek, Š. Msallamová, E. Jablonská, J. Lipov, D. Vojtěch, A novel high-strength and highly corrosive biodegradable Fe-Pd alloy: Structural, mechanical and *in vitro* corrosion and cytotoxicity study, *Mater. Sci. Eng. C*. 79 (2017) 550–562. <https://doi.org/10.1016/j.msec.2017.05.100>.
- [17] Y. Li, H. Jahr, P. Pavanram, F.S.L. Bobbert, U. Puggi, X.Y. Zhang, B. Pouran, M.A. Leeflang, H. Weinans, J. Zhou, A.A. Zadpoor, Additively manufactured functionally graded biodegradable porous iron, *Acta Biomater.* 96 (2019) 646–661. <https://doi.org/10.1016/j.actbio.2019.07.013>.

- [18] Y. Li, H. Jahr, K. Lietaert, P. Pavanram, A. Yilmaz, L.I. Fockaert, M.A. Leeflang, B. Pouran, Y. Gonzalez-Garcia, H. Weinans, J.M.C. Mol, J. Zhou, A.A. Zadpoor, Additively manufactured biodegradable porous iron, *Acta Biomater.* 77 (2018) 380–393. <https://doi.org/10.1016/j.actbio.2018.07.011>.
- [19] N.E. Putra, M.A. Leeflang, M. Minneboo, P. Taheri, L.E. Fratila-Apachitei, J.M.C. Mol, J. Zhou, A.A. Zadpoor, Extrusion-based 3D printed biodegradable porous iron, *Acta Biomater.* 121 (2021) 741–756. <https://doi.org/10.1016/j.actbio.2020.11.022>.
- [20] A. Yamamoto, R. Honma, M. Sumita, Cytotoxicity evaluation of 43 metal salts using murine fibroblasts and osteoblastic cells, *J. Biomed. Mater. Res.* 39 (1998) 331–40. [https://doi.org/10.1002/\(SICI\)1097-4636\(199802\)39:2<331::AID-JBM22>3.0.CO;2-E](https://doi.org/10.1002/(SICI)1097-4636(199802)39:2<331::AID-JBM22>3.0.CO;2-E).
- [21] C. Gao, M. Yao, C. Shuai, P. Feng, S. Peng, Advances in bioceramics for bone implant applications, *Bio-Design Manuf.* 3 (2020) 307–330. <https://doi.org/10.1007/s42242-020-00087-3>.
- [22] M.F. Ulum, A. Arafat, D. Noviana, A.H. Yusop, A.K. Nasution, M.R. Abdul Kadir, H. Hermawan, *In vitro* and *in vivo* degradation evaluation of novel iron-bioceramic composites for bone implant applications, *Mater. Sci. Eng. C.* 36 (2014) 336–344. <https://doi.org/10.1016/j.msec.2013.12.022>.
- [23] M.F. Ulum, A.K. Nasution, A.H. Yusop, A. Arafat, M.R.A. Kadir, V. Juniantito, D. Noviana, H. Hermawan, Evidences of *in vivo* bioactivity of Fe-bioceramic composites for temporary bone implants, *J. Biomed. Mater. Res. - Part B Appl. Biomater.* 103 (2015) 1354–1365. <https://doi.org/10.1002/jbm.b.33315>.
- [24] M. Dehestani, E. Adolfsson, L.A. Stanciu, Mechanical properties and corrosion behavior of powder metallurgy iron-hydroxyapatite composites for biodegradable implant applications, *Mater. Des.* 109 (2016) 556–569. <https://doi.org/10.1016/j.matdes.2016.07.092>.
- [25] A. Reindl, R. Borowsky, S.B. Hein, J. Geis-Gerstorf, P. Imgrund, F. Petzoldt, Degradation behavior of novel Fe/ β -TCP composites produced by powder injection molding for cortical bone replacement, *J. Mater. Sci.* 49 (2014) 8234–8243. <https://doi.org/10.1007/s10853-014-8532-5>.
- [26] F. He, G. Qian, W. Ren, J. Ke, P. Fan, X. Shi, Y. Cheng, S. Wu, X. Deng, J. Ye, Preparation and characterization of iron/ β -tricalcium phosphate bio-ceramics for load-bearing bone substitutes, *Ceram. Int.* 43 (2017) 8348–8355. <https://doi.org/10.1016/j.ceramint.2017.03.173>.
- [27] E.B. Montufar, M. Casas-Luna, M. Horynová, S. Tkachenko, Z. Fohlerová, S. Diaz-de-la-Torre, K. Dvořák, L. Čelko, J. Kaiser, High strength, biodegradable and cytocompatible alpha tricalcium phosphate-iron composites for temporal reduction of bone fractures, *Acta Biomater.* 70 (2018) 293–303. <https://doi.org/10.1016/j.actbio.2018.02.002>.
- [28] S. Wang, Y. Xu, J. Zhou, H. Li, J. Chang, Z. Huan, *In vitro* degradation and surface bioactivity of iron-matrix composites containing silicate-based bioceramic, *Bioact. Mater.* 2 (2017) 10–18. <https://doi.org/10.1016/j.bioactmat.2016.12.001>.
- [29] H. Ma, T. Li, Z. Huan, M. Zhang, Z. Yang, J. Wang, J. Chang, C. Wu, 3D printing of high-strength bioscaffolds for the synergistic treatment of bone cancer, *NPG Asia Mater.* 10 (2018) 31–44. <https://doi.org/10.1038/s41427-018-0015-8>.
- [30] M. Sikora-Jasinska, C. Paternoster, E. Mostaed, R. Tolouei, R. Casati, M. Vedani, D. Mantovani, Synthesis, mechanical properties and corrosion behavior of powder metallurgy processed Fe/Mg₂Si composites for biodegradable implant applications, *Mater. Sci. Eng. C.* 81 (2017) 511–521. <https://doi.org/10.1016/j.msec.2017.07.049>.
- [31] M. Sikora-Jasinska, P. Chevallier, S. Turgeon, C. Paternoster, E. Mostaed, M. Vedani, D. Mantovani, Long-term *in vitro* degradation behaviour of Fe and Fe/Mg₂Si composites for biodegradable implant applications, *RSC Adv.* 8 (2018) 9627–9639. <https://doi.org/10.1039/c8ra00404h>.
- [32] M. Sikora-Jasinska, P. Chevallier, S. Turgeon, C. Paternoster, E. Mostaed, M. Vedani, D. Mantovani, Understanding the effect of the reinforcement addition on corrosion behavior of Fe/Mg₂Si composites for biodegradable implant applications, *Mater. Chem. Phys.* 223 (2019) 771–778. <https://doi.org/10.1016/j.matchemphys.2018.11.068>.
- [33] C. Shuai, Y. Li, Y. Yang, S. Peng, W. Yang, F. Qi, S. Xiong, H. Liang, L. Shen, Bioceramic enhances the degradation and bioactivity of iron bone implant, *Mater. Res. Express.* 6 (2019) 115401. <https://doi.org/10.1088/2053-1591/ab45b9>.
- [34] C. Gao, M. Yao, S. Li, P. Feng, S. Peng, C. Shuai, Highly biodegradable and bioactive Fe-Pd-bredigite biocomposites prepared by selective laser melting, *J. Adv. Res.* 20 (2019) 91–104. <https://doi.org/10.1016/j.jare.2019.06.001>.

- [35] M. Diba, O.M. Goudouri, F. Tapia, A.R. Boccaccini, Magnesium-containing bioactive polycrystalline silicate-based ceramics and glass-ceramics for biomedical applications, *Curr. Opin. Solid State Mater. Sci.* 18 (2014) 147–167. <https://doi.org/10.1016/j.cossms.2014.02.004>.
- [36] K. Bavya Devi, S.K. Nandi, M. Roy, Magnesium silicate bioceramics for bone regeneration: A review, *J. Indian Inst. Sci.* 99 (2019) 261–288. <https://doi.org/10.1007/s41745-019-00119-7>.
- [37] S. Yoshizawa, A. Brown, A. Barchowsky, C. Sfeir, Magnesium ion stimulation of bone marrow stromal cells enhances osteogenic activity, simulating the effect of magnesium alloy degradation, *Acta Biomater.* 10 (2014) 2834–2842. <https://doi.org/10.1016/j.actbio.2014.02.002>.
- [38] M.Q. Cheng, T. Wahafu, G.F. Jiang, W. Liu, Y.Q. Qiao, X.C. Peng, T. Cheng, X.L. Zhang, G. He, X.Y. Liu, A novel open-porous magnesium scaffold with controllable microstructures and properties for bone regeneration, *Sci. Rep.* 6 (2016) 1–14. <https://doi.org/10.1038/srep24134>.
- [39] K. Szurkowska, J. Kolmas, Hydroxyapatites enriched in silicon – Bioceramic materials for biomedical and pharmaceutical applications, *Prog. Nat. Sci. Mater. Int.* 27 (2017) 401–409. <https://doi.org/10.1016/j.pnsc.2017.08.009>.
- [40] A.F. Khan, M. Saleem, A. Afzal, A. Ali, A. Khan, A.R. Khan, Bioactive behavior of silicon substituted calcium phosphate based bioceramics for bone regeneration, *Mater. Sci. Eng. C.* 35 (2014) 245–252. <https://doi.org/10.1016/j.msec.2013.11.013>.
- [41] Y. Huang, X. Jin, X. Zhang, H. Sun, J. Tu, T. Tang, J. Chang, K. Dai, *In vitro* and *in vivo* evaluation of akermanite bioceramics for bone regeneration, *Biomaterials.* 30 (2009) 5041–5048. <https://doi.org/10.1016/j.biomaterials.2009.05.077>.
- [42] L. Xia, Z. Yin, L. Mao, X. Wang, J. Liu, X. Jiang, Z. Zhang, K. Lin, J. Chang, B. Fang, Akermanite bioceramics promote osteogenesis, angiogenesis and suppress osteoclastogenesis for osteoporotic bone regeneration, *Sci. Rep.* 6 (2016) 1–17. <https://doi.org/10.1038/srep22005>.
- [43] W. Liu, T. Wang, X. Zhao, X. Dan, W.W. Lu, H. Pan, Akermanite used as an alkaline biodegradable implants for the treatment of osteoporotic bone defect, *Bioact. Mater.* 1 (2016) 151–159. <https://doi.org/10.1016/j.bioactmat.2016.11.004>.
- [44] Y. Huang, C. Wu, X. Zhang, J. Chang, K. Dai, Regulation of immune response by bioactive ions released from silicate bioceramics for bone regeneration, *Acta Biomater.* 66 (2018) 81–92. <https://doi.org/10.1016/j.actbio.2017.08.044>.
- [45] C. Wu, J. Chang, Synthesis and apatite-formation ability of akermanite, *Mater. Lett.* 58 (2004) 2415–2417. <https://doi.org/10.1016/j.matlet.2004.02.039>.
- [46] ASTM B963-17, Standard test methods for oil content, oil-impregnation efficiency, and surface-connected porosity of sintered powder metallurgy (PM) products using Archimedes' principle, ASTM International, 2017. <https://doi.org/10.1520/B0963-14>.
- [47] A. Oyane, H.M. Kim, T. Furuya, T. Kokubo, T. Miyazaki, T. Nakamura, Preparation and assessment of revised simulated body fluids, *J. Biomed. Mater. Res. - Part A.* 65 (2003) 188–195. <https://doi.org/10.1002/jbm.a.10482>.
- [48] L. Yang, E. Zhang, Biocorrosion behavior of magnesium alloy in different simulated fluids for biomedical application, *Mater. Sci. Eng. C.* 29 (2009) 1691–1696. <https://doi.org/10.1016/j.msec.2009.01.014>.
- [49] ASTM G1-03, Standard practice for preparing, cleaning, and evaluating corrosion test specimens, ASTM International, (2017). <https://doi.org/10.1520/G0001-03R17E01.2>.
- [50] ASTM G32-72, Standard practice for laboratory immersion corrosion testing of metals., ASTM International, (2004). <https://doi.org/10.1520/G0031-72R04.2>.
- [51] ISO 13314, Mechanical testing of metals - Ductility testing - Compression test for porous and cellular metals, International Organization for Standardization, 2011. <https://doi.org/ISO 13314:2011>.
- [52] C. Valero, A. Igual, Electrochemical aspects in biomedical alloy characterization: Electrochemical impedance spectroscopy, in: *Biomedical Engineering, Trends in Materials Science*, 2011: pp. 283–306. <https://doi.org/10.5772/13039>.
- [53] J. Tedim, M.L. Zheludkevich, A.C. Bastos, A.N. Salak, A.D. Lisenkov, M.G.S. Ferreira, Influence of preparation conditions of layered double hydroxide conversion films on corrosion protection, *Electrochim. Acta.* 117 (2014) 164–171. <https://doi.org/10.1016/j.electacta.2013.11.111>.
- [54] B. Van der Linden, H. Terryn, J. Vereecken, Investigation of anodic aluminium oxide layers

- by electrochemical impedance spectroscopy, *J. Appl. Electrochem.* 20 (1990) 798–803. <https://doi.org/10.1007/BF01094309>.
- [55] ISO 10993-5, Tests for *in vitro* cytotoxicity, International Organization for Standardization, 2009. <https://doi.org/10.1021/es0620181>.
- [56] E.F. Morgan, G.U. Unnikrisnan, A.I. Hussein, Bone mechanical properties in healthy and diseased states, *Annu. Rev. Biomed. Eng.* 20 (2018) 119–43. <https://doi.org/10.1146/annurev-bioeng-062117-121139>.
- [57] A. Ribeiro, M.M. Blokzijl, R. Levato, C.W. Visser, M. Castilho, W.E. Hennink, T. Vermonden, J. Malda, Assessing bioink shape fidelity to aid material development in 3D bioprinting, *Biofabrication.* 10 (2018) 014102. <https://doi.org/10.1088/1758-5090/aa90e2>.
- [58] C. Duty, C. Ajinjeru, V. Kishore, B. Compton, N. Hmeidat, X. Chen, P. Liu, A.A. Hassen, J. Lindahl, V. Kunc, What makes a material printable? A viscoelastic model for extrusion-based 3D printing of polymers, *J. Manuf. Process.* 35 (2018) 526–537. <https://doi.org/10.1016/j.jmapro.2018.08.008>.
- [59] A.F. Bonatti, I. Chiesa, G. Vozzi, C. De Maria, Open-source CAD-CAM simulator of the extrusion-based bioprinting process, *Bioprinting.* 24 (2021) e00172. <https://doi.org/10.1016/j.bprint.2021.e00172>.
- [60] N. Paxton, W. Smolan, T. Böck, F. Melchels, J. Groll, T. Jungst, Proposal to assess printability of bioinks for extrusion-based bioprinting and evaluation of rheological properties governing bioprintability, *Biofabrication.* 9 (2017) 044107. <https://doi.org/10.1088/1758-5090/aa8dd8>.
- [61] R. Marunaka, M. Kawaguchi, Rheological behavior of hydrophobic fumed silica suspensions in aromatic dispersion media, *J. Dispers. Sci. Technol.* 38 (2017) 223–228. <https://doi.org/10.1080/01932691.2016.1155154>.
- [62] C. Yang, Z. Huan, X. Wang, C. Wu, J. Chang 3D printed Fe scaffolds with HA nanocoating for bone regeneration, *ACS Biomater. Sci. Eng.* 4 (2018) 608–616. <https://doi.org/10.1021/acsbomaterials.7b00885>.
- [63] J. He, H. Ye, Y. Li, J. Fang, Q. Mei, X. Lu, F. Ren, Cancellous-bone-like porous iron scaffold coated with strontium incorporated octacalcium phosphate nanowhiskers for bone regeneration, *ACS Biomater. Sci. Eng.* 5 (2019) 509–518. <https://doi.org/10.1021/acsbomaterials.8b01188>.
- [64] M.C. Ratri, A.I. Brilian, A. Setiawati, H.T. Nguyen, V. Soum, K. Shin, Recent advances in regenerative tissue fabrication: tools, materials, and microenvironment in hierarchical aspects, *Adv. NanoBiomed Res.* 1 (2021) 2000088. <https://doi.org/10.1002/anbr.202000088>.
- [65] S. Debnath, R. Ranade, S.L. Wunder, J. McCool, K. Boberick, G. Baran, Interface effects on mechanical properties of particle-reinforced composites, *Dent. Mater.* 20 (2004) 677–686. <https://doi.org/10.1016/j.dental.2003.12.001>.
- [66] S.Y. Fu, X.Q. Feng, B. Lauke, Y.W. Mai, Effects of particle size, particle/matrix interface adhesion and particle loading on mechanical properties of particulate-polymer composites, *Compos. Part B Eng.* 39 (2008) 933–961. <https://doi.org/10.1016/j.compositesb.2008.01.002>.
- [67] Y. Su, Q. Ouyang, W. Zhang, Z. Li, Q. Guo, G. Fan, D. Zhang, Composite structure modeling and mechanical behavior of particle reinforced metal matrix composites, *Mater. Sci. Eng. A.* 597 (2014) 359–369. <https://doi.org/10.1016/j.msea.2014.01.024>.
- [68] C. Wu, J. Chang, S. Ni, J. Wang, *In vitro* bioactivity of akermanite ceramics, *J. Biomed. Mater. Res. - Part A.* 76 (2006) 73–80. <https://doi.org/10.1002/jbm.a.30496>.
- [69] E. Mouzou, C. Paternoster, R. Tolouei, P. Chevallier, C.A. Biffi, A. Tuissi, D. Mantovani, CO₂-rich atmosphere strongly affects the degradation of Fe-21Mn-1C for biodegradable metallic implants, *Mater. Lett.* 181 (2016) 362–366. <https://doi.org/10.1016/j.matlet.2016.06.017>.
- [70] S.Y. Yang, H.H. Chang, C.J. Lin, S.J. Huang, J.C.C. Chan, Is Mg-stabilized amorphous calcium carbonate a homogeneous mixture of amorphous magnesium carbonate and amorphous calcium carbonate?, *Chem. Commun.* 52 (2016) 11527–11530. <https://doi.org/10.1039/c6cc04522g>.
- [71] J. Zhang, C. Dong, Y. Sun, J. Yu, Mechanism of magnesium's influence on calcium carbonate crystallization: Kinetically controlled multistep crystallization, *Cryst. Res. Technol.* 53 (2018) 1–8. <https://doi.org/10.1002/crat.201800075>.
- [72] M. Kellermeier, E. Melero-García, F. Glaab, R. Klein, M. Drechsler, R. Rachel, J.M. García-

- Ruiz, W. Kunz, Stabilization of amorphous calcium carbonate in inorganic silica-rich environments, *J. Am. Chem. Soc.* 132 (2010) 17859–17866. <https://doi.org/10.1021/ja106959p>.
- [73] F. Witte, V. Kaese, H. Haferkamp, E. Switzer, A. Meyer-Lindenberg, C.J. Wirth, H. Windhagen, *In vivo* corrosion of four magnesium alloys and the associated bone response, *Biomaterials*. 26 (2005) 3557–3563. <https://doi.org/10.1016/j.biomaterials.2004.09.049>.
- [74] C.J.S. Ibsen, D. Chernyshov, H. Birkedal, Apatite formation from amorphous calcium phosphate and mixed amorphous calcium phosphate/amorphous calcium carbonate, *Chem. - A Eur. J.* 22 (2016) 12347–12357. <https://doi.org/10.1002/chem.201601280>.
- [75] K. Ishikawa, K. Hayashi, Carbonate apatite artificial bone, *Sci. Technol. Adv. Mater.* 22 (2021) 683–694. <https://doi.org/10.1080/14686996.2021.1947120>.
- [76] P. Opitz, L. Besch, M. Panthöfer, A. Kabelitz, R.E. Unger, F. Emmerling, M. Mondeshki, W. Tremel, Insights into the *in vitro* formation of apatite from Mg-stabilized amorphous calcium carbonate, *Adv. Funct. Mater.* 31 (2021) 2007830. <https://doi.org/10.1002/adfm.202007830>.
- [77] M. Mozafari, S. Banijamali, F. Baines, S. Kargozar, R.G. Hill, Calcium carbonate: Adored and ignored in bioactivity assessment, *Acta Biomater.* 91 (2019) 35–47. <https://doi.org/10.1016/j.actbio.2019.04.039>.
- [78] A. Xu, F. Zhang, F. Jin, R. Zhang, B. Luo, T. Zhang, The evaluation of coating performance by analyzing the intersection of Bode plots, *Int. J. Electrochem. Sci.* 9 (2014) 5125.
- [79] C. Wu, J. Chang, Degradation, bioactivity, and cytocompatibility of diopside, akermanite, and bredigite ceramics, *J. Biomed. Mater. Res.* 83 (2007) 153–160. <https://doi.org/10.1002/jbmb>.
- [80] S. Ni, J. Chang, *In vitro* degradation, bioactivity, and cytocompatibility of calcium silicate, dimagnesium silicate, and tricalcium phosphate bioceramics, *J. Biomater. Appl.* 24 (2009) 139–158. <https://doi.org/10.1177/0885328208094745>.
- [81] R. Oriňáková, R. Gorejová, Z.O. Králová, A. Oriňák, I. Shepa, J. Hovancová, A. Kovalčíková, Z.L. Bujňáková, N. Király, M. Kaňuchová, M. Baláž, M. Strečková, M. Kupková, M. Hrubovčáková, F. Kaľavský, M. Oriňák, Influence of albumin interaction on corrosion resistance of sintered iron biomaterials with polyethyleneimine coating, *Appl. Surf. Sci.* 509 (2020) 145379. <https://doi.org/10.1016/j.apsusc.2020.145379>.
- [82] P. Feng, C. Gao, C. Shuai, S. Peng, Toughening and strengthening mechanisms of porous akermanite scaffolds reinforced with nano-titania, *RSC Adv.* 5 (2015) 3498–3507. <https://doi.org/10.1039/c4ra12095g>.
- [83] Y. Lin, H. Chen, C.M. Chan, J. Wu, High impact toughness polypropylene/CaCO₃ nanocomposites and the toughening mechanism, *Macromolecules*. 41 (2008) 9204–9213. <https://doi.org/10.1021/ma801095d>.
- [84] S. Menbari, F. Ashenai Ghasemi, I. Ghasemi, Simultaneous improvement in the strength and toughness of polypropylene by incorporating hybrid graphene/CaCO₃ reinforcement, *Polym. Test.* 54 (2016) 281–287. <https://doi.org/10.1016/j.polymertesting.2016.07.026>.
- [85] Y.F. He, Y. Ma, C. Gao, G.Y. Zhao, L.L. Zhang, G.F. Li, Y.Z. Pan, K. Li, Y.J. Xu, Iron overload inhibits osteoblast biological activity through oxidative stress, *Biol. Trace Elem. Res.* 152 (2013) 292–296. <https://doi.org/10.1007/s12011-013-9605-z>.
- [86] Y.B. Wang, X.H. Xie, H.F. Li, X.L. Wang, M.Z. Zhao, E.W. Zhang, Y.J. Bai, Y.F. Zheng, L. Qin, Biodegradable CaMgZn bulk metallic glass for potential skeletal application, *Acta Biomater.* 7 (2011) 3196–3208. <https://doi.org/10.1016/j.actbio.2011.04.027>.
- [87] T. Kihara, M. Hirose, A. Oshima, H. Ohgushi, Exogenous type I collagen facilitates osteogenic differentiation and acts as a substrate for mineralization of rat marrow mesenchymal stem cells *in vitro*, *Biochem. Biophys. Res. Commun.* 341 (2006) 1029–1035. <https://doi.org/10.1016/j.bbrc.2006.01.059>.
- [88] Z. Xu, K.G. Neoh, A. Kishen, A biomimetic strategy to form calcium phosphate crystals on type I collagen substrate, *Mater. Sci. Eng. C*. 30 (2010) 822–826. <https://doi.org/10.1016/j.msec.2010.03.014>.
- [89] Q. Liu, L. Cen, S. Yin, L. Chen, G. Liu, J. Chang, L. Cui, A comparative study of proliferation and osteogenic differentiation of adipose-derived stem cells on akermanite and β -TCP ceramics, *Biomaterials*. 29 (2008) 4792–4799. <https://doi.org/10.1016/j.biomaterials.2008.08.039>.
- [90] H. Sun, C. Wu, K. Dai, J. Chang, T. Tang, Proliferation and osteoblastic differentiation of human bone marrow-derived stromal cells on akermanite-bioactive ceramics, *Biomaterials*. 27 (2006) 5651–5657. <https://doi.org/10.1016/j.biomaterials.2006.07.027>.

Highly biodegradable MRI-friendly osteogenic porous Fe-Mn-Akermanite

The development of Fe-based materials as biodegradable bone implants has advanced a great deal in the recent years. Yet not all the challenges have been overcome. Here, we present porous FeMn-akermanite composite scaffolds fabricated by extrusion-based 3D printing to address the unmet clinical needs associated with Fe-based biomaterials for bone regeneration. We developed novel inks containing Fe, 35 wt% Mn, and 20 or 30 vol% akermanite powder mixtures. The 3D printing step was optimized together with the debinding and sintering steps to obtain scaffolds with interconnected porosity of 69%. The metal matrix in the composites contained the γ -FeMn phase and nesosilicate phases. The former made the composites weakly paramagnetic and, thus, MRI-friendly. The *in vitro* biodegradation rates of the composites with 20 and 30 vol% akermanite were respectively 0.24 and 0.27 mm/y (in the ideal range of biodegradation rates for bone substitutes). The yield strengths and elastic moduli of the composites stayed within the range of the values of the trabecular bone, despite *in vitro* biodegradation for 28 d. All the scaffolds favored the adhesion and proliferation of preosteoblasts MC3T3-E1 and allowed the osteogenic differentiation of the cells comparable to Ti6Al4V. The presence of the osteopontin matrix on the composite scaffolds hallmarked the initiation of *in vitro* biomineralization. Altogether, these results show the remarkable potential of the composites in fulfilling all the requirements of porous biodegradable bone substitutes, motivating future research to evaluate their performance *in vivo*.

Putra, N.E., Dong, J., Leeflang, M.A., Klimopoulou, M., Taheri, P., Huan, Z., Fratila-Apachitei, L.E., Mol, J.M.C., Chang, J., Zhou, J. and Zadpoor A.A., 2023. Extrusion-based 3D printing of biodegradable, osteogenic, paramagnetic, and porous FeMn-akermanite bone substitutes. *Under review*.

7.1 Introduction

In the recent years, remarkable progress has been made in the development of biodegradable Fe-based metals to assist in the regeneration of critical-size bony defects. In particular, researchers have tried to address some key challenges and find viable solutions to speed up the clinical adoption of such metals [1]. The first challenge concerns the slow degradation rate of pure Fe *in vivo* [2]. To improve their biodegradation profile, Fe implants have been recently designed to possess a geometrically ordered porous structure, which are then realized through additive manufacturing (AM) [3]. Such hierarchical porous Fe structures have, indeed, exhibited enhanced rates of biodegradation *in vitro* [4–6]. The second challenge concerns the inherent ferromagnetic behavior of Fe, which hinders its use in patients who may need magnetic resonance imaging (MRI) during their treatments. Alloying Fe with >28 wt% Mn has been shown to make Fe antiferromagnetic [7] while also increasing its biodegradation rate [8,9]. In addition, the mechanical properties of FeMn alloys have been shown to be tunable by varying the porosity, pore shape, and pore sizes so as to match the mechanical properties of the trabecular bone [10–12] as well as those of the cortical bone [13–15].

Despite all these developments, the biocompatibility and bioactivity of FeMn alloys remain limited, potentially hindering the progress of the bone tissue regeneration. Porosity has been generally found to dictate the biodegradation profile and, thus, the biological response of Fe-based metals. For porosities < 40 vol%, several studies have found FeMn alloys to be compatible with such cell types as mouse preosteoblasts MC3T3-E1 [16–18], mouse fibroblasts (3T3 [19], L929 [20]), and mouse bone marrow stromal cells (BMSCs) [10]. FeMn alloys with higher porosities (*e.g.*, 60 vol% [10] and 69 vol% [11]), however, have presented *in vitro* cytotoxicity against mouse BMSCs [10] and preosteoblasts MC3T3-E1 [11]. That said, one study has reported good *in vitro* cytocompatibility between MC3T3-E1 and 85 vol% porous FeMn alloy structures [12]. The picture regarding the biological performance of porous FeMn alloys is incomplete because most of the findings regarding their *in vitro* cytocompatibility is based on short-term *in vitro* tests (*i.e.*, up to 7 days), while their osteogenic potential is hardly studied.

The biodegradation rates of FeMn alloys have been reported to be lower *in vivo* than *in vitro* [21]. A selective laser-melted Fe₂₅Mn alloy (with 66.7% porosity [13]) and Fe₃₅Mn alloy (with 42.6% porosity [14]) have presented *in vitro* biodegradation rates of 0.25 mm/y and 0.42 mm/y, respectively. *In vivo*, another selective laser-melted Fe₃₀Mn alloy (with a porosity range of 37.9–47.2%) has shown a volume loss of 10.1–20.9% after 48 weeks of implantation

[15], corresponding to the degradation rates of 0.04 to 0.11 mm/y, which falls outside the desired range of biodegradation rates (*i.e.*, 0.2–0.5 mm/y [22]). A slower biodegradation rate typically translates to improved biocompatibility of FeMn alloys, due to the decreased amounts of metallic ions released per unit time.

A broad spectrum of biocompatibility is one of the most important prerequisites for biomaterials to be utilized in clinical settings [23]. The concerns regarding the biological response of porous FeMn alloys may delay their clinical adoption, despite the positive results of a number of *in vivo* studies [14,15]. To address this concern, FeMn alloys have been enriched with Ca [17], Cu [24], Si-Ca [25], and hydroxyapatite [26] to reduce the combined release of Fe and Mn ions and their effects on cells. In addition to Ca, Mg/Si-based bioactive ceramics (*e.g.*, akermanite and bredigite) have shown promise in improving the biological properties of pure Fe [27,28]. The magnesium content of these bioceramics can stimulate the osteogenic differentiation of cells [29], while silicon helps in the synthesis of collagen matrix and bone mineralization [30,31]. Indeed, adding akermanite (20 vol%) to pure Fe has been shown to enable continuous proliferation of bone cell and the secretion of collagen for biomineralization [28]. However, all these results pertain to pure iron and not FeMn alloys, for which the potential benefits of adding akermanite are unknown.

Here, we propose 3D printed geometrically ordered porous FeMn-akermanite composite to address all the abovementioned challenges regarding Fe-based biodegradable metals, including (i) a low rate of biodegradation, (ii) MRI incompatibility, (iii) uncertain biocompatibility, and (iv) a lack of bioactivity for bone regeneration. We developed an extrusion-based 3D printing technique *via* an *ex situ* AM route [32] to fabricate porous FeMn-akermanite composites, which have never been reported in the literature. Furthermore, we comprehensively evaluated the *in vitro* properties of the new composites, including their biodegradation behavior, electrochemical response, magnetic properties, mechanical performance before and after *in vitro* biodegradation, *in vitro* cytocompatibility with MC3T3-E1 cells, and their osteogenic potential assessed using Runx2 and osteopontin assays.

7.2 Materials and methods

7.2.1 FeMn-akermanite ink preparation

Fe powder (purity = 99.88 wt%; spherical morphology; particle sizes < 63 μm , Figure 7.1a) and Mn powder (purity = 99.86 wt%; irregular morphology; particle sizes < 45 μm , Figure 7.1b) were purchased from Material Technology Innovations Co. Ltd., China. Akermanite powder ($\text{Ca}_2\text{MgSi}_2\text{O}_7$; containing 8.92 wt% Mg; irregular morphology; particle sizes < 45 μm , Figure 7.1c) was produced

from tetraethyl orthosilicate $[(C_2H_5O)_4Si]$, magnesium nitrate hexahydrate $[Mg(NO_3)_2 \cdot 6H_2O]$, and calcium nitrate tetrahydrate $[Ca(NO_3)_2 \cdot 4H_2O]$ with a sol-gel method, followed by calcination at 1300 °C for 3 h [33].



Figure 7.1. The morphologies of (a) iron, (b) manganese, and (c) akermanite powders.

Fe, Mn, and akermanite powder mixtures with 35 wt% Mn and either 20 or 30 vol% akermanite, hereafter referred as Fe35Mn-20Ak and Fe35Mn-30Ak, respectively, were prepared using a roller mixer (CAT Zipperer GmbH, Germany) at 80 rpm for 18 h. The powder mixtures were blended with a hydro-ethanol binder containing 5 wt% hydroxypropyl methylcellulose (hypromellose $M_w \sim 86$ kDa, Sigma Aldrich, Germany) [11]. The powder mixture in the inks corresponded to a volume ratio of 47.45%. The rheological characteristics of the inks were determined using an MCR302 rheometer (Anton Paar GmbH, Germany).

7.2.2 Extrusion-based 3D printing, debinding and sintering

The FeMn-Ak inks were extruded using a 3D BioScaffolder 3.2 printer (GeSiM Bio-instruments and Microfluidics, Germany) in a lay-down pattern design of 0° and 90° switching every other layer to build cylindrical porous specimens ($\phi = 10$ mm, $h = 10.5$ mm). The porous scaffolds were designed with a strut size of 410 μm, a strut spacing of 400 μm, a surface area of 40.4 cm², and a relative porosity of 50% (Figure 7.2a). The extrusion-based 3D printing was performed under a printing speed of 3.5 mm/s under the printing pressures of 325 kPa and 360 kPa for the Fe35Mn-20Ak and Fe35Mn-30Ak inks, respectively. After 3D printing, the green bodies were heat-treated, following the procedure described in Chapter 5, section 5.2.2.

7.2.3 Characterization of microstructure, porosity, and phase composition

The dimensional changes caused by the sintering process were determined by measuring the diameters and heights of the specimens before and after. The porous morphology of the FeMn-Ak scaffolds was observed using a scanning electron microscope (SEM, JEOL JSM-IT100, Japan) and their strut characteristics (*i.e.*, strut size and strut spacing) were measured. The chemical composition of the struts was determined using energy dispersive X-ray

spectroscopy (EDS, JEOL JSM-IT100, Japan). The cross sections of the as-sintered Fe₃₅Mn-30Ak struts were observed using SEM and the elemental compositions were determined using EDS map and EDS line analyses (JEOL JSM-IT100, Japan). In addition, the phases present in the composite scaffolds were identified using an X-ray diffractometer (XRD, D8 Advance, Bruker, USA) following the parameters described in Chapter 4, section 4.2.4.

The absolute porosity values of the FeMn-Ak composites were determined, using dry weighing as described in Chapter 3 with Equation (3.2) and (3.3). The interconnected porosity of the scaffolds was determined by using the oil-impregnation technique and calculated using Equation (3.4), following the ASTM standard B963-13 [34]. The theoretical density of the FeMn-Ak composites ($\rho_{\text{FeMn-Ak}}$) is 6.68 g/cm³ for Fe₃₅Mn-20Ak and 6.22 g/cm³ for Fe₃₅Mn-30Ak.

7.2.4 Measurement of magnetic susceptibility

The magnetic behavior of porous FeMn-Ak specimens (in triplicate, before and after 28 d of *in vitro* biodegradation) was assessed by exposing the specimens to a 2 T magnetic field in a vibrating sample magnetometer (VSM 7307, Lake Shore, USA). Geometrically similar porous pure Fe specimens were tested as the control group. Magnetic hysteresis loops were obtained and analyzed to determine the saturated and residual magnetization values, as well as the magnetic susceptibility of the specimens.

7.2.5 Biodegradation tests

Static immersion and characterization of the biodegradation products

The FeMn-Ak composites were immersed in the revised simulated body fluid (r-SBF) solution [35] with a medium volume of 6.7 mL per 1 cm² of the scaffold surface area [36] and an initial pH of 7.40 for 1, 4, 7, 14, and 28 d. The immersion tests were conducted under the conditions as described in Chapter 3, section 3.2.4. During the immersion tests, the pH value of the medium was monitored using a pH electrode (InLab Expert Pro-ISM, METTLER TOLEDO, Switzerland). In addition, Fe²⁺, Mn²⁺, Ca²⁺, Mg²⁺, Si⁴⁺, and PO₄³⁻ ion concentrations in the medium were measured at various time points using inductively coupled plasma-optical emission spectrometry (ICP-OES, iCAP 6500 Duo, Thermo Scientific, USA).

At the designated time points, the specimens were retrieved to characterize their morphology and determine the chemical composition of their biodegradation products using SEM and EDS (JEOL JSM-IT100, Japan). The phases present in the biodegradation products after immersion for 28 d were identified using XRD (D8 Advance, Bruker, USA). Furthermore, the biodegradation rates of the FeMn-Ak composites at the selected time points were

determined using mass loss measurements as described in Chapter 3, section 3.2.4, following the ASTM standard G1-03 [37]. The remaining scaffold material was weighed and the average biodegradation rate was calculated with Equation (3.5), based on the ASTM standard G31-72 [38].

Electrochemical tests

The electrochemical characteristics of the porous FeMn-Ak composites were studied using a Bio-Logic SP-200 potentiostat (Bio-Logic Science Instruments, France). The potentiostat was connected to a setup consisting of three electrodes, including an Ag/AgCl electrode as the reference electrode, a graphite bar as the counter electrode, and the porous specimen partially embedded in an acrylic resin as the working electrode. The biodegradation medium was r-SBF [35] with an initial pH of 7.40. The temperature was maintained at 37 ± 0.5 °C. The exposed surface area of the specimens was calculated, based on their initial designs. The three-electrode system was stabilized for 1 h to a steady open circuit potential (OCP). Then, linear polarization resistance (LPR) and electrochemical impedance spectroscopy (EIS) measurements were performed for up to 28 d, following the parameters described in Chapter 3, section 3.2.6.

7.2.6 Mechanical characterization

The compressive mechanical properties of the porous FeMn-Ak composites were evaluated before and after *in vitro* biodegradation tests (in triplicate) using a universal mechanical testing machine with a 100 kN load cell (Zwick Z100, Germany). The compression tests were conducted, following the ISO standard 13314:2011 [39], at a crosshead speed of 3 mm/s. Based on the stress-strain curves, the compressive 0.2% offset stress (referred as the yield strength) and the quasi elastic gradient (referred as the Young's modulus) were determined, as described in Chapter 3, section 3.2.7.

7.2.7 Cytocompatibility evaluation

Preculture of preosteoblasts

Murine preosteoblasts (MC3T3-E1, Sigma Aldrich, Germany) were cultured in a flask in a cell culture incubator (temperature = 37 ± 0.5 °C, relative humidity (RH) = 95%, CO₂ content = 5%). The cell culture medium contained the α -minimum essential medium (α -MEM) supplemented with 10% fetal bovine serum (FBS) and 1% penicillin/streptomycin (p/s). The cell culture medium components were purchased from Thermo Fisher Scientific, USA.

Extracts of FeMn-Ak composites

The extracts of the composite specimens were obtained by incubating the sterile specimens ($\phi = 10.2$ mm, $h = 10.6$ mm) in the cell culture medium (with a

ratio of 1 mL per 5 cm² specimen surface area) for 72 h [40]. The surface area of the composites was calculated, using their initial design. Thereafter, the extracts were retrieved and filtered through a 0.22 µm pore (Merck Millipore, Germany). The concentrations of Fe²⁺, Mn²⁺, Ca²⁺, Mg²⁺, and Si⁴⁺ ions in the extracts were measured using ICP-OES (iCAP 6500 Duo, Thermo Scientific, USA).

PrestoBlue assay

Murine preosteoblasts (MC3T3-E1, 1×10^4 cells per well) were cultured in triplicate in a 48-well plate containing 200 µL of the above-described extracts. Preosteoblasts cultured in the normal cell culture medium were used as the negative control. After 1, 3, and 7 d of cell culture, the PrestoBlue reagent (Thermo Fisher Scientific, USA) was used to evaluate the metabolic activity of the cells, following the procedure described in Chapter 3, section 3.2.8, and calculated with Equation (3.7).

Live-dead staining and SEM imaging

Murine preosteoblasts (MC3T3-E1, 5×10^4 cells per specimen) were cultured on the FeMn-Ak specimens ($\phi = 7.0$ mm and $h = 0.6$ mm) in 6-well plates containing 8 mL of the cell culture medium (made of α -MEM, supplemented with 10% FBS, 1% p/s, 1:1000 ascorbic acid, and 1:500 β -glycerophosphate). The specimens were cultured for 7 and 21 d (in triplicate for each time point). The viability of the preosteoblasts on the composite specimens was determined using calcein and ethidium homodimer-1 staining (Thermo Fisher Scientific, USA). The morphology of the cells was observed using SEM (JEOL JSM-IT100, Japan). Geometrically alike porous Ti6Al4V specimens were used as the controls for the cell morphology evaluation at the selected time points.

Immunostaining of osteogenic markers

The immunostaining of the preosteoblasts MC3T3-E1 cultured on the composite specimens was performed at day 14 for Runt-related transcription factor 2 (Runx2) and at day 21 for osteopontin (OPN). At the designated time points, the specimens were washed with phosphate buffer saline (PBS) and were fixated using 4% paraformaldehyde for 15 min, followed by permeabilization using 0.5% Triton/PBS (Sigma Aldrich, Germany). Consecutively, the specimens were individually incubated in well-plates containing 1% bovine serum albumin (BSA)/PBS with primary antibodies of anti-Runx2 anti-rabbit (1:250 per specimen, Abcam, UK) and anti-OPN anti-mouse (1:100 per specimen, Santa Cruz Biotechnology, USA). Thereafter, the specimens were washed using 0.5% Tween/PBS (Sigma Aldrich, Germany), followed by an incubation step in 1% BSA/PBS containing conjugated secondary antibodies of Alexa Fluor 488 anti-rabbit (1:200, Thermo Fischer Scientific, USA) and Alexa Fluor 594 anti-mouse

(1:100, Thermo Fischer Scientific, USA). Subsequently, the specimens were washed using 0.5% Tween/PBS prior to imaging using a microscope (ZOE cell imager, Bio-Rad, USA). Geometrically alike porous Ti6Al4V specimens were used as controls for the Runx2 staining at day 14.

7.2.8 Statistical analysis

The statistical analysis of the PrestoBlue results was performed using a two-way ANOVA, followed by a Tukey multiple comparison *post hoc* test (**** = $p < 0.0001$, *** = $p < 0.001$, ** = $p < 0.01$, and * = $p < 0.05$, n.s. = not significant).

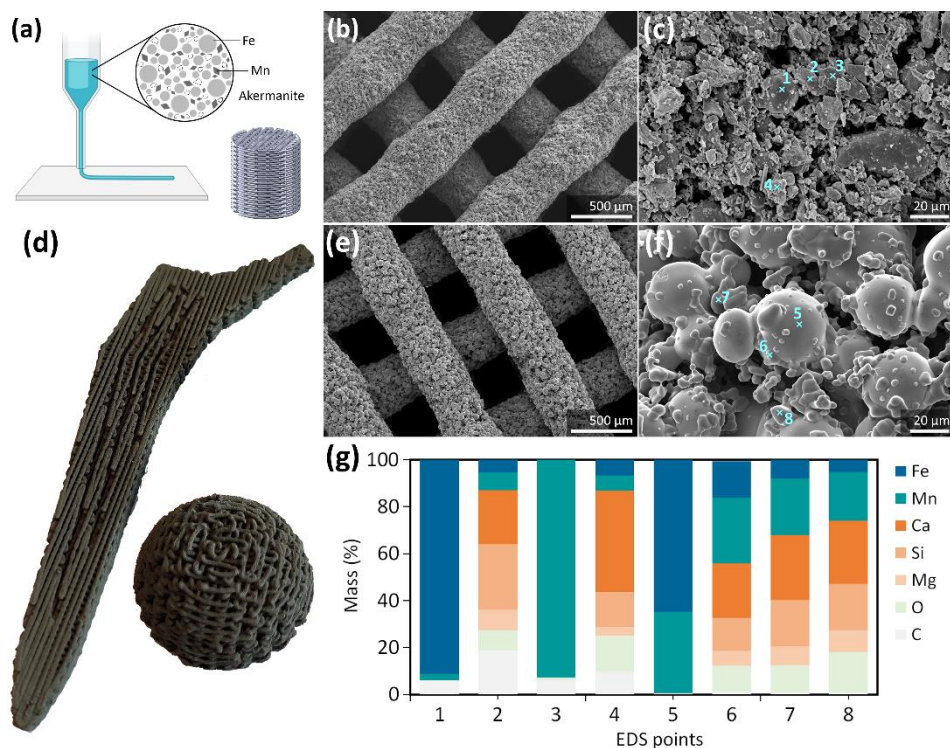


Figure 7.2. (a) An illustration of extrusion-based 3D printing and the scaffold design. (b) The morphology of the as-printed Fe₃₅Mn-30Ak specimens and (c) powder particle distribution on the struts. (d) An extrusion-based 3D-printed hip stem as well as a similarly produced acetabular cup. (e) The morphology of the as-sintered Fe₃₅Mn-30Ak specimens and (f) powder particle distribution on the struts. (g) The chemical compositions of the scaffold struts obtained by EDS analysis. The cross signs with a number indicate the location of the EDS point analyses.

7.3 Results

7.3.1 Characteristics of the porous FeMn-Ak composite scaffolds

Extrusion-based 3D printing was successful in fabricating porous FeMn-Ak scaffolds (Figure 7.2a). The design of the lay-down pattern was such that the struts bridged above the underlying layers at 0° and 90° angles (Figure 7.2b, S7.2). In addition to the cylindrical specimens, the extrusion-based 3D printing was capable of fabricating geometrically complex implants (*e.g.*, hip stem and acetabular components (Figure 7.2d)). Given that the success in 3D printing strongly depends on adequate powder loading in the ink as well as its rheological behavior (*i.e.*, shear-thinning, Figure S7.1). On the struts of the green-body scaffolds (Figure 7.2b), individual powder particles (*i.e.*, Fe, Mn, and akermanite) could still be discerned (Figure 7.2c), together with a relatively high mass% of carbon from the hypromellose binder (*i.e.*, 6–19%, Figure 7.2g, EDS points 1–4).

After debinding and sintering, the FeMn-Ak composite scaffolds maintained the original geometrical design (Figure 7.2e, S7.2) with minimal expansions of 1–1.5% in height and 1.4–1.8% in diameter. The measured mean values of the strut size and strut spacing are listed in Table 7.1. The struts of the specimens featured an open micro-porous architecture with absolute porosities of 69% and 70% ($\pm 3\%$) for Fe₃₅Mn-20Ak and Fe₃₅Mn-30Ak, respectively. The interconnected porosity of both types of composite scaffolds was 69% \pm 1%. The spherical particles found on the periphery of the Fe₃₅Mn-30Ak struts were composed of Fe and Mn (EDS point 5 in Figure 7.2f–g). These spherical powder particles were decorated and occasionally connected by irregularly shaped particles that were mainly composed of Ca, Mg, Si, and O, in addition to traces of Fe and Mn (Figure 7.2f–g, EDS points 6 to 8). Similar observations were made for the Fe₃₅Mn-20Ak specimens (Figure S7.2). After sintering, the mass percentages of carbon on the struts of both types of scaffolds (*i.e.*, 0.6–1.2%, Figure 7.2g, EDS points 5 to 8) were significantly decreased as compared to the green bodies.

Table 7.1. The geometric characteristics of the extrusion-based 3D printed FeMn-Ak composite scaffolds.

Sample group	Strut width (μm)	Strut spacing (μm)
Fe ₃₅ Mn-20Ak	419 \pm 3	391 \pm 3
Fe ₃₅ Mn-30Ak	414 \pm 3	395 \pm 4

On the cross-sections of the Fe₃₅Mn-30Ak specimens, EDS mapping analysis indicated the diffusion of Fe and Mn into the akermanite particles (highlighted by boxes in Figure 7.3a). The depths of the elemental diffusion of Fe and Mn into the akermanite phase were measured to be $\approx 4.9 \mu\text{m}$ and $> 28 \mu\text{m}$, respectively (Figure 7.3b). XRD analysis revealed the presence of the γ -FeMn phase in the specimens, thereby confirming the successful *in situ* alloying of Fe with Mn during sintering (Figure 7.4a). In addition, the nesosilicate crystalline phases, including kirschsteinite (Ca(Fe)SiO_4), glaucocroite (Ca(Mn)SiO_4), and monticellite (Ca(Mg)SiO_4), were identified (Figure 7.4a). The intensities of the nesosilicate phases were higher in the specimens containing with more akermanite.

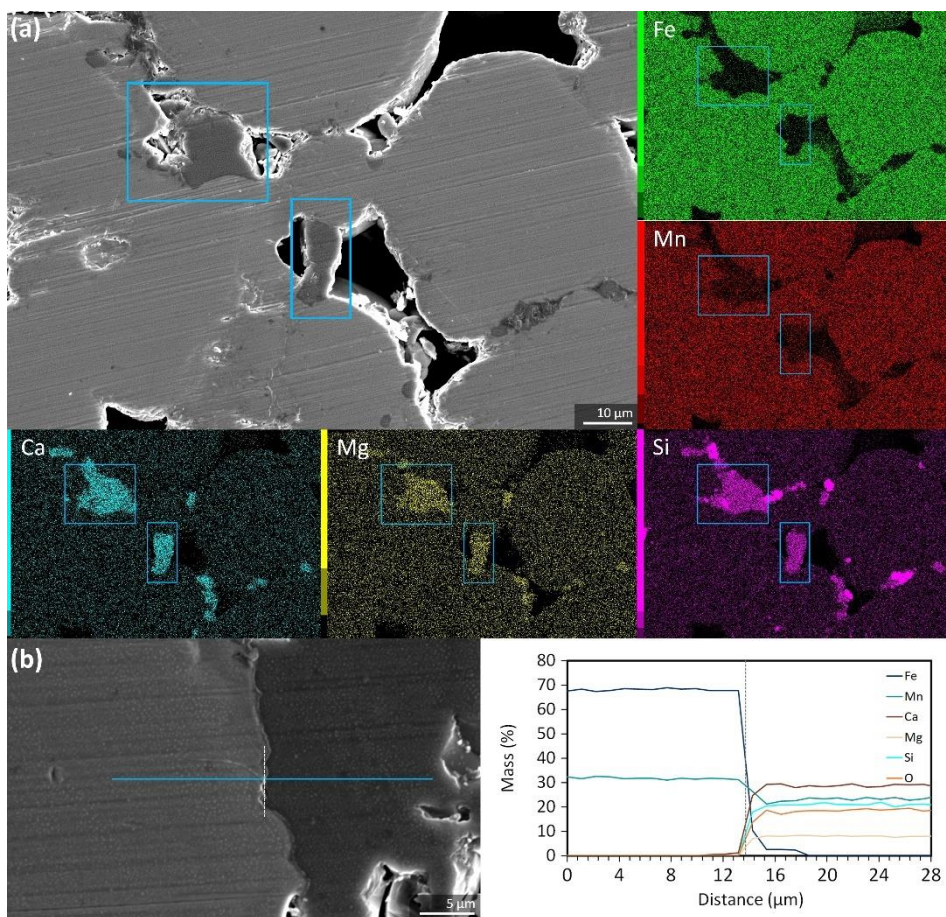


Figure 7.3. The cross-sections of the composite struts: (a) EDS map analysis in the region of interest, and (b) EDS line analysis across the interface of the FeMn alloy and the bioceramic.

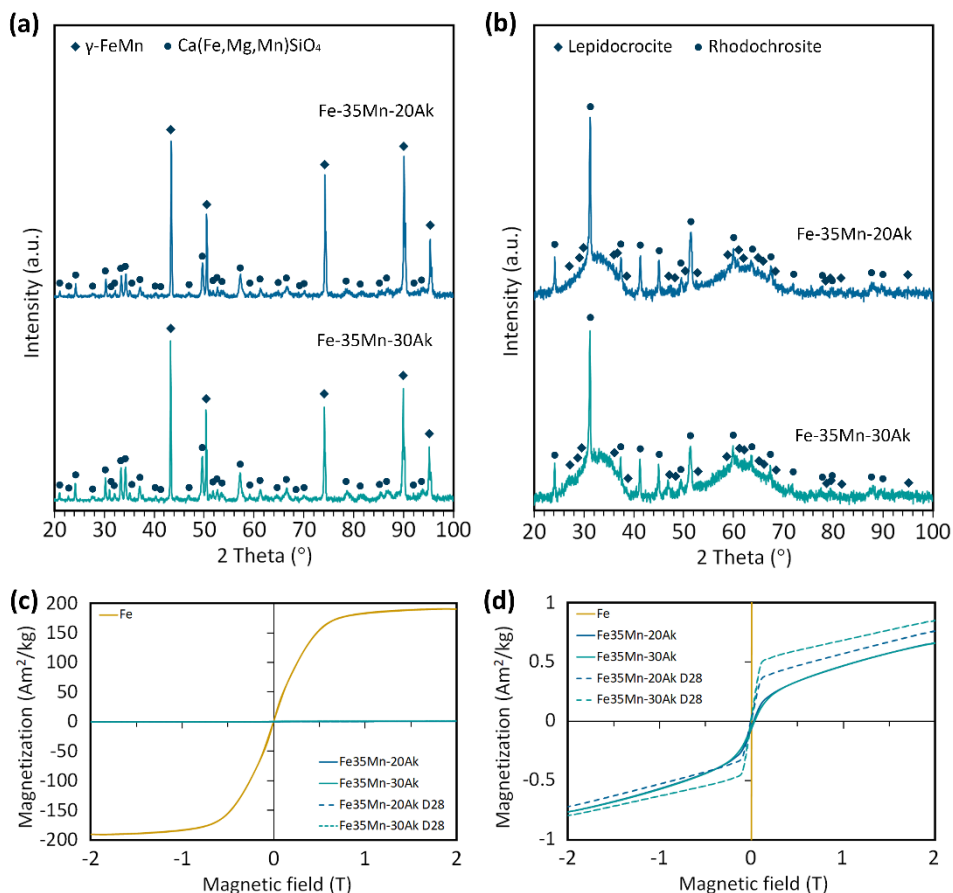


Figure 7.4. The phase compositions of the composite scaffolds: (a) as-sintered and (b) after *in vitro* biodegradation for 28 d. (c, d) The magnetization curves of the FeMn-Ak specimens (as-sintered and after *in vitro* biodegradation for 28 d) at different graph scales in comparison with pure Fe.

7.3.2 Magnetic properties

The saturated magnetization of the FeMn-Ak composites in the presence of 2 T magnetic field (*i.e.*, 0.64 Am^2/kg for Fe₃₅Mn-20Ak and 0.71 Am^2/kg for Fe₃₅Mn-30Ak, Figure 7.4c), was 2–3 orders of magnitude lower than that of comparable pure Fe scaffolds (*i.e.*, 190 Am^2/kg). The residual magnetism values of the porous composites were low too (*i.e.*, 0.05 and 0.06 Am^2/kg for Fe₃₅Mn-20Ak and Fe₃₅Mn-30Ak, respectively). After 28 d of biodegradation (Figure 7.4d), the saturation magnetization values of the porous FeMn-Ak scaffolds only slightly increased (to 0.9 Am^2/kg) but, nevertheless, remained multiple orders of magnitude below that of pure Fe. Along with *in vitro* biodegradation, the residual magnetism values of the porous composites decreased to 0.03 and 0.02 Am^2/kg ,

respectively. The magnetic susceptibility values of the porous composites were $3.6 \pm 0.2 (\times 10^{-3})$ for Fe₃₅Mn-20Ak and $3.7 \pm 0.4 (\times 10^{-3})$ for Fe₃₅Mn-30Ak. After 28 d of biodegradation, the values remained low (*i.e.*, $4.0 \pm 0.4 (\times 10^{-3})$ and $4.5 \pm 0.9 (\times 10^{-3})$ for Fe₃₅Mn-20Ak and Fe₃₅Mn-30Ak, respectively). As for the ferromagnetic pure Fe, the magnetic susceptibility value was 5.08 ± 0.05 , which was three orders of magnitude higher than the values of the porous composites scaffolds.

7.3.3 Biodegradability and the characteristics of the biodegradation products

During the *in vitro* biodegradation tests, the typical yellow-brownish layer of Fe-based biodegradation products formed on the specimens (Figure 7.5a). Initially (*i.e.*, at day 4), the scaffolds exhibited a high biodegradability, with corrosion rates of 1.27 ± 0.01 mm/y for Fe₃₅Mn-20Ak and 1.36 ± 0.06 mm/y for Fe₃₅Mn-30Ak. By day 28, the *in vitro* biodegradation rates of the porous composites had reduced to 0.24 ± 0.01 mm/y and 0.27 ± 0.04 mm/y, for Fe₃₅Mn-20Ak and Fe₃₅Mn-30Ak, respectively (Figure 7.5b). Until the end of the immersion tests (28 d), the global pH values of the r-SBF medium remained between 7.64 and 7.68, due to the controlled 5% CO₂ atmosphere in the incubator.

SEM (Figure 7.5c-e) revealed that the struts of the composite scaffolds were encapsulated by the degradation products that accumulated over the immersion time. The morphologies of the biodegradation products on the periphery could be discerned from a particulate structure to a denser phase over time. The biodegradation products were composed of a mixture of Fe, Mn, C, and O elements (Figure 7.5f-h, S7.3). In addition, the biodegradation products on the struts of Fe₃₅Mn-30Ak specimens contained Ca and P at all time points (Figure 7.5f-h). In the degradation products of the Fe₃₅Mn-20Ak scaffolds, however, only Ca was detected (Figure S7.3). The phases present in the biodegradation products of the porous specimens after 28 d of immersion were lepidocrocite (γ -FeOOH) and rhodochrosite (MnCO₃, Figure 7.4b), which corresponded to the main chemical compositions identified by EDS. At the center of the composite scaffolds (Figure 7.5i, S7.3), the biodegradation products had formed over the pore networks of the struts and were largely composed of oxides. After biodegradation, the initially spherical Fe-Mn particles were decorated by irregularly shaped nesosilicate particles (Figure 7.2f) and exhibited rough particle surface characteristics, indicating localized corrosion that occurred on the interfaces of the powder particles (indicated by arrows in Figure 7.5i). Overall, the nesosilicate particles (mainly composed of Ca, Mg, Si, and O) could still be identified at the center of the composites (Figure 7.5i, S7.3).

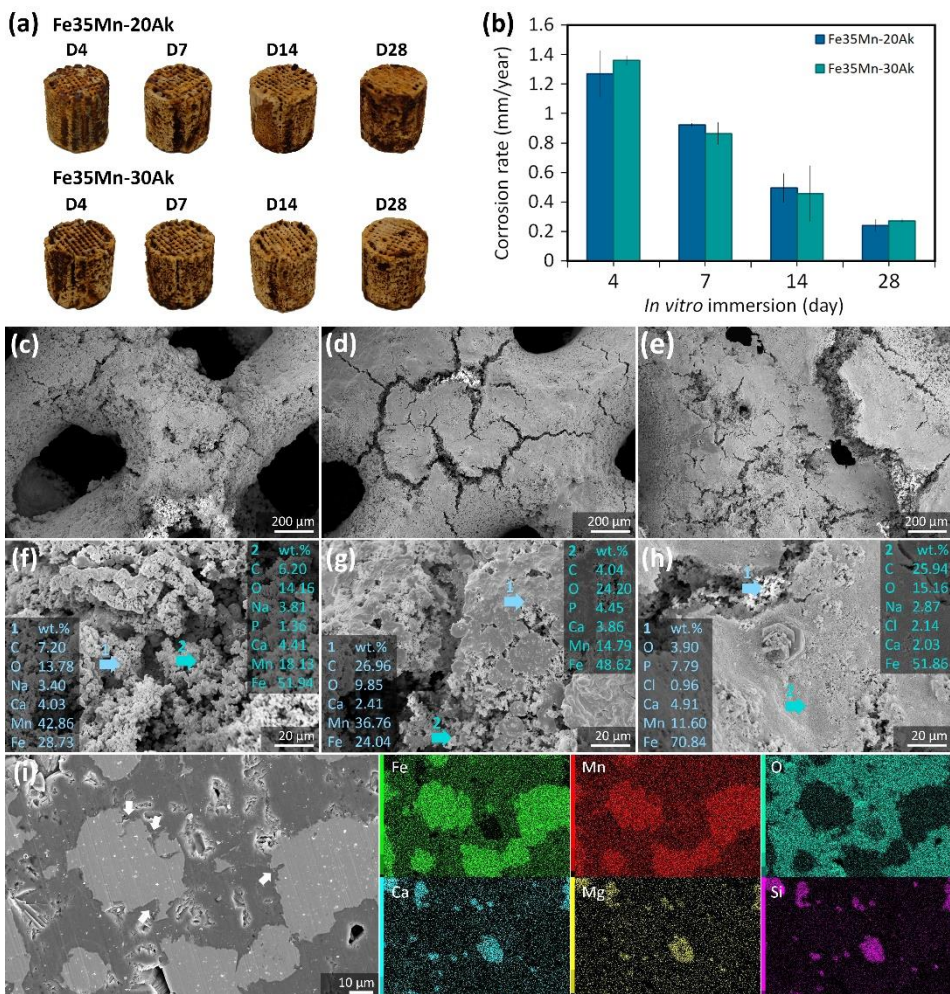


Figure 7.5. The *in vitro* biodegradation characteristics of the porous composite scaffolds: (a) The visual inspection of the scaffolds after *in vitro* biodegradation at different time points and (b) the corresponding corrosion rates. (c-e) The morphologies and (f-h) chemical compositions of the biodegradation products on the periphery of the Fe35Mn-30Ak specimens after (c, f) 4, (d, g) 7, and (e, h) 28 d of biodegradation as well as (i) at the center of the specimens after 28 d of biodegradation.

The concentrations of Fe^{2+} , Mn^{2+} , Ca^{2+} , PO_4^{3-} , Mg^{2+} , and Si^{4+} ions in the r-SBF medium along were measured during the course of the immersion tests (Figure 7.6). Fe^{2+} ions were steadily released from both the Fe35Mn-20Ak and Fe35Mn-30Ak specimens over time (*i.e.*, from 0.23 ± 0.02 mg/L and 0.34 ± 0.02 mg/L at day 4 to 0.90 ± 0.02 mg/L and 0.93 ± 0.06 mg/L at day 28, respectively, Figure 7.6a). The concentration of the Mn^{2+} ions released from the Fe35Mn-30Ak specimens was the highest at day 7 (*i.e.*, 11.0 ± 0.3 mg/L) followed by decreasing

trend towards the end of the immersion tests at day 28 (*i.e.*, 9.4 ± 0.4 mg/L). Mn^{2+} ions were continuously released from the Fe35Mn-20Ak specimens and the concentration increased from 6.2 ± 0.1 mg/L at day 4 up to 11.4 ± 0.3 mg/L at day 28 (Figure 7.6b).

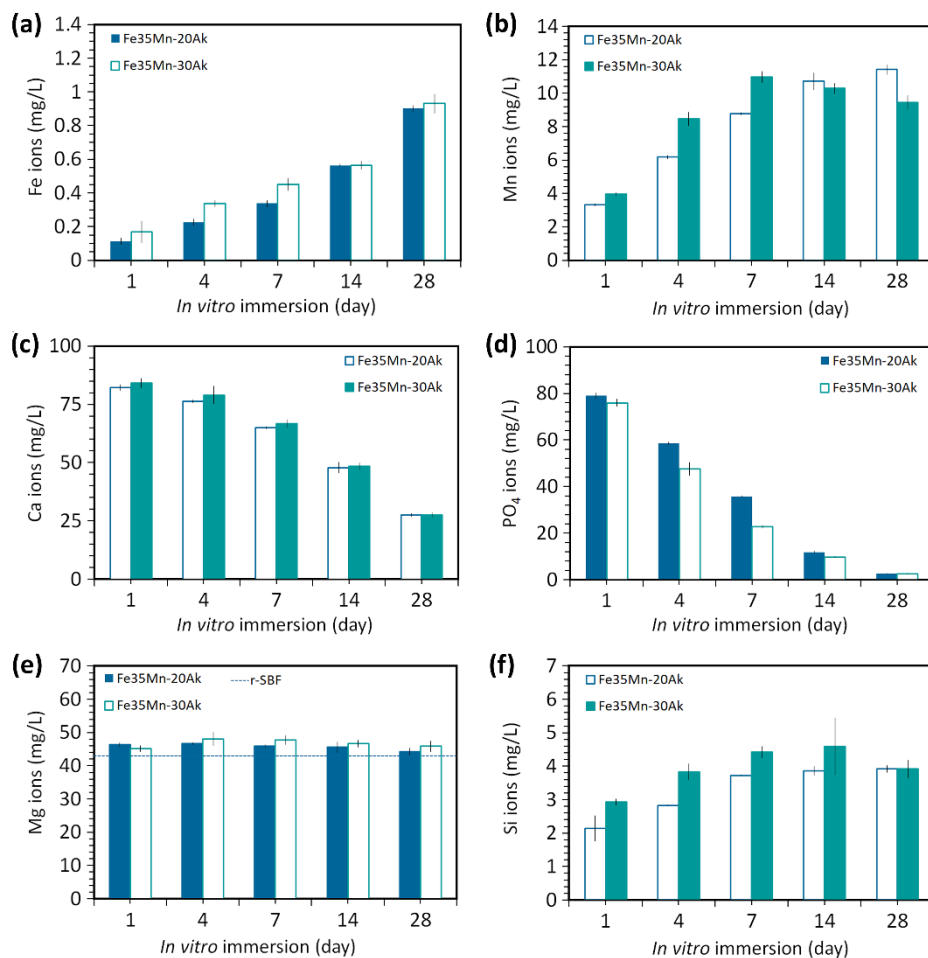


Figure 7.6. The concentrations of (a) Fe, (b) Mn, (c) Ca, (d) PO_4 , (e) Mg, and (f) Si ions in the r-SBF medium over biodegradation time. The dotted line indicates the initial concentration of Mg ions in the medium.

The Ca^{2+} ion concentrations in the r-SBF medium decreased throughout the immersion period for all the composite specimens similarly (*i.e.*, from 76 ± 1 mg/L and 79 ± 4 mg/L at day 4 to 28 ± 1 mg/L at day 28, Figure 7.6c). In a similar trend, the PO_4^{3-} ion concentration decreased over time, with a larger reduction

observed for the Fe₃₅Mn-30Ak specimens during the first 7 days of immersion (Figure 7.6d). Moreover, the Mg²⁺ ion concentration in the r-SBF medium marginally increased over time, with the highest Mg²⁺ ion concentrations registered at day 4 (*i.e.*, 46.7 ± 0.3 mg/L for Fe₃₅Mn-20Ak and 48 ± 2 mg/L for Fe₃₅Mn-30Ak, Figure 7.6e). The concentration of Si⁴⁺ ion increased from 2.83 ± 0.3 mg/L and 3.8 ± 0.2 mg/L at day 4 to 3.9 ± 0.1 mg/L and 3.9 ± 0.3 mg/L at day 28 for the Fe₃₅Mn-20Ak and Fe₃₅Mn-30Ak specimens, respectively (Figure 7.6f).

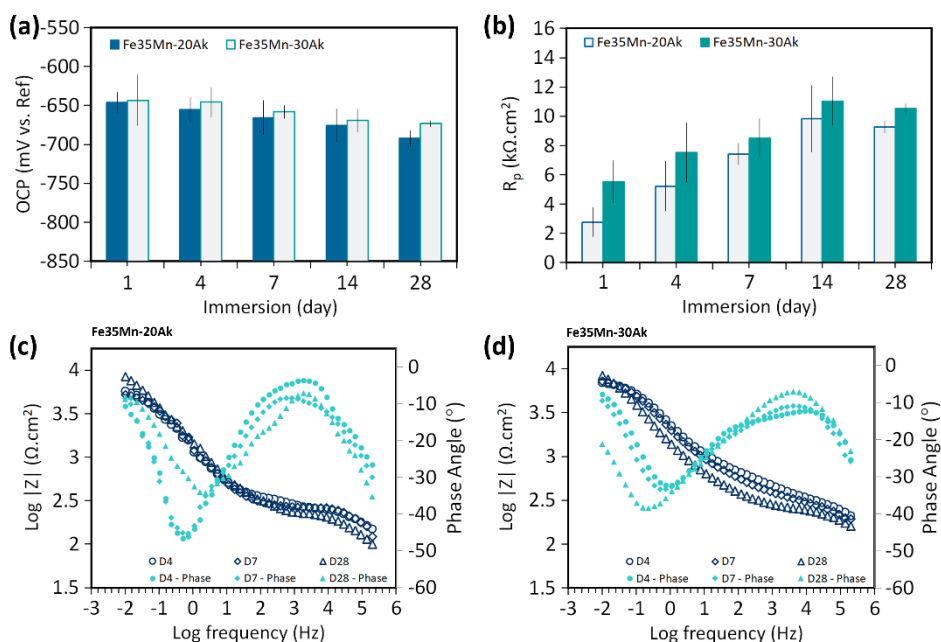


Figure 7.7. The electrochemical responses of the porous composite scaffolds during 28 d of biodegradation: (a) OCP and (b) R_p values from the LPR tests. The Bode impedance and phase angles at the selected time points for the (c) Fe₃₅Mn-20Ak and Fe₃₅Mn-30Ak scaffolds.

7.3.4 Electrochemical measurements

Both the porous FeMn-Ak composites demonstrated decreasing OCP values during the 28 d of biodegradation (Figure 7.7a). At day 1, the OCP values were -646 ± 9 mV for Fe₃₅Mn-20Ak and -643 ± 23 mV for Fe₃₅Mn-30Ak. At day 28, the OCP values decreased to -692 ± 7 mV and -673 ± 3 mV for the Fe₃₅Mn-20Ak and Fe₃₅Mn-30Ak specimens, respectively. The polarization resistance (R_p) values of the porous composites were 5 ± 2 kΩ.cm² for Fe₃₅Mn-20Ak and 8 ± 2 kΩ.cm² for Fe₃₅Mn-30Ak at day 4 of immersion, which then increased to

$10 \pm 2 \text{ k}\Omega\cdot\text{cm}^2$ and $11 \pm 2 \text{ k}\Omega\cdot\text{cm}^2$ at day 14 of immersion, respectively (Figure 7.7b). At day 28, R_p stabilized at the values of $9.3 \pm 0.4 \text{ k}\Omega\cdot\text{cm}^2$ and $10.5 \pm 0.4 \text{ k}\Omega\cdot\text{cm}^2$, respectively, for the Fe₃₅Mn-20Ak and Fe₃₅Mn-30Ak specimens. The Bode impedance values of the porous composites at a low frequency of 0.01 Hz slightly increased over the immersion period (Figure 7.7c-d). At day 4, the impedance magnitudes were $3.7 \pm 0.3 \text{ k}\Omega\cdot\text{cm}^2$ and $3.8 \pm 0.9 \text{ k}\Omega\cdot\text{cm}^2$ for the Fe₃₅Mn-20Ak and Fe₃₅Mn-30Ak specimens, respectively. At day 28, the impedance magnitudes marginally increased to $3.9 \pm 0.1 \text{ k}\Omega\cdot\text{cm}^2$ for both types of composites. At the mid-frequency of 100 Hz, the Bode impedance values of the Fe₃₅Mn-20Ak specimens were relatively stable (*i.e.*, $2.5 \pm 0.1 \text{ k}\Omega\cdot\text{cm}^2$ at day 4 and $2.5 \pm 0.2 \text{ k}\Omega\cdot\text{cm}^2$ at day 28 of immersion, Figure 7.7c). However, the Bode impedance values of the Fe₃₅Mn-30Ak specimens at the mid-frequency of 100 Hz slightly decreased over time from $2.82 \pm 0.05 \text{ k}\Omega\cdot\text{cm}^2$ at day 4 to $2.57 \pm 0.03 \text{ k}\Omega\cdot\text{cm}^2$ at day 28 of immersion (Figure 7.7d). Furthermore, the peak of the Bode plot phase angle did not shift during the biodegradation tests of the Fe₃₅Mn-20Ak and Fe₃₅Mn-30Ak specimens, and remained in the high frequency region (*e.g.*, 1–10 kHz) (Figure 7.7c-d). The Bode plot phase angles at high frequencies (*e.g.*, 10 kHz) were relatively stable between -8° to -12° for the Fe₃₅Mn-20Ak and Fe₃₅Mn-30Ak specimens over the entire period of the immersion tests.

7.3.5 Mechanical properties

The composite scaffolds exhibited stress-strain curves with an initial linear elastic deformation, followed by plastic deformation, resembling the typical strain-hardening behavior of such materials (Figure 7.8a-b). The composite scaffolds (*i.e.*, Fe₃₅Mn-20Ak and Fe₃₅Mn-30Ak) had yield strengths of $8.3 \pm 0.6 \text{ MPa}$ and $3.1 \pm 0.4 \text{ MPa}$, respectively. The Young's modulus values were $0.53 \pm 0.03 \text{ GPa}$ and $0.25 \pm 0.04 \text{ GPa}$, respectively. Due to biodegradation, the yield strength of the Fe₃₅Mn-20Ak specimens reduced to $4.1 \pm 0.7 \text{ MPa}$ at day 7, and to $1.8 \pm 0.6 \text{ MPa}$ at day 28 (Figure 7.8c). The Young's modulus of the Fe₃₅Mn-20Ak specimens also decreased to $0.17 \pm 0.02 \text{ GPa}$ at day 7, and to $0.09 \pm 0.01 \text{ GPa}$ at day 28 (Figure 7.8d). For the Fe₃₅Mn-30Ak specimens, the yield strength and Young's modulus decreased to $2.5 \pm 0.7 \text{ MPa}$ and $0.17 \pm 0.06 \text{ GPa}$ after 7 days. The Fe₃₅Mn-30Ak scaffolds did not exhibit strain-hardening after 14 and 28 d of biodegradation (Figure 7.8b). The compressive strength values were $4.5 \pm 0.3 \text{ MPa}$ at day 14 which decreased to $3.9 \pm 0.9 \text{ MPa}$ at day 28 (Figure 7.8c) while the Young's modulus values were reduced to $0.057 \pm 0.005 \text{ GPa}$ at day 14 and $0.034 \pm 0.009 \text{ GPa}$ at day 28 (Figure 7.8d).

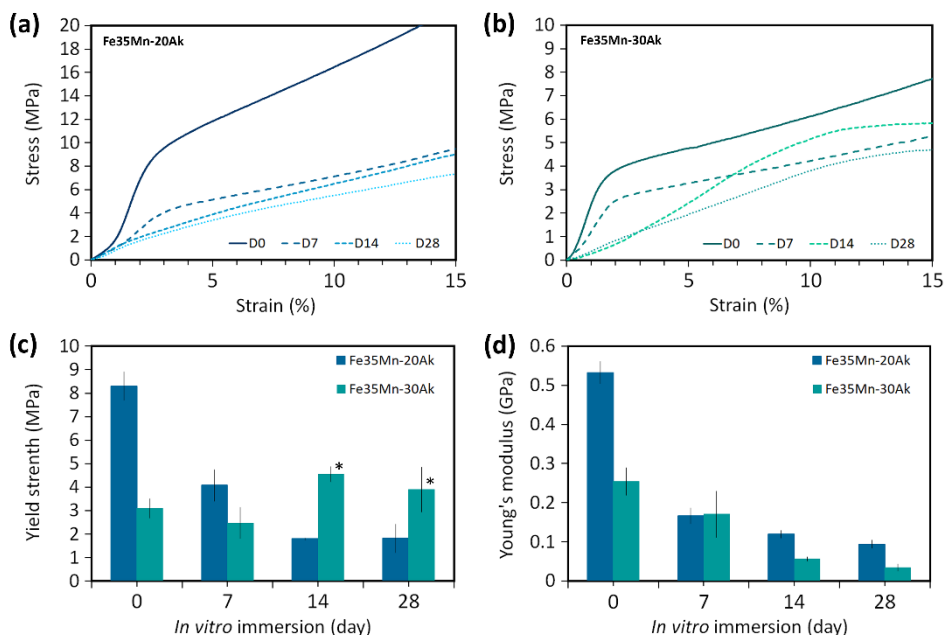


Figure 7.8. The compressive mechanical properties of the porous composite scaffolds: the stress-strain curves of the (a) Fe35Mn-20Ak and (b) Fe35Mn-30Ak scaffolds, and variations in the (c) yield strength and (d) Young's modulus with biodegradation time. The asterisk symbols indicate the compressive strength values of the Fe35Mn-30Ak scaffolds after 14 and 28 d of biodegradation.

7.3.6 Metabolic activity of cells cultured with the extracts of the composites

The Fe35Mn-20Ak extracts contained 61 ± 2 mg/L of Fe^{2+} ions, 35.3 ± 0.6 mg/L of Mn^{2+} ions, 73.3 ± 0.6 mg/L of Ca^{2+} ions, 40.7 ± 0.6 mg/L of Mg^{2+} ions, and 6 ± 1 mg/L of Si^{4+} ions. In the Fe35Mn-30Ak extracts, the ionic concentrations were 68.7 ± 1.2 mg/L of Fe^{2+} , 30.3 ± 0.6 mg/L of Mn^{2+} , 104 ± 2 mg/L of Ca^{2+} , 36.3 ± 0.6 mg/L of Mg^{2+} , and 7.3 ± 0.1 mg/L Si^{4+} . The preosteoblasts were metabolically active (grade 1, non-toxic [41]) in the composite extracts of 25% and 50% (Figure 7.9a-b). In the 75% extracts of Fe35Mn-20Ak (Figure 7.9a), the preosteoblasts showed a decline in their metabolic activity (grade 2, fairly reactive [41]). However, in the 75% extracts of Fe35Mn-30Ak, the cells were still metabolically active (Figure 7.9b, grade 1, non-toxic [41]). The cellular metabolic activities were suppressed (grade 4, severely reactive [41]) only when cultured with the 100% extracts.

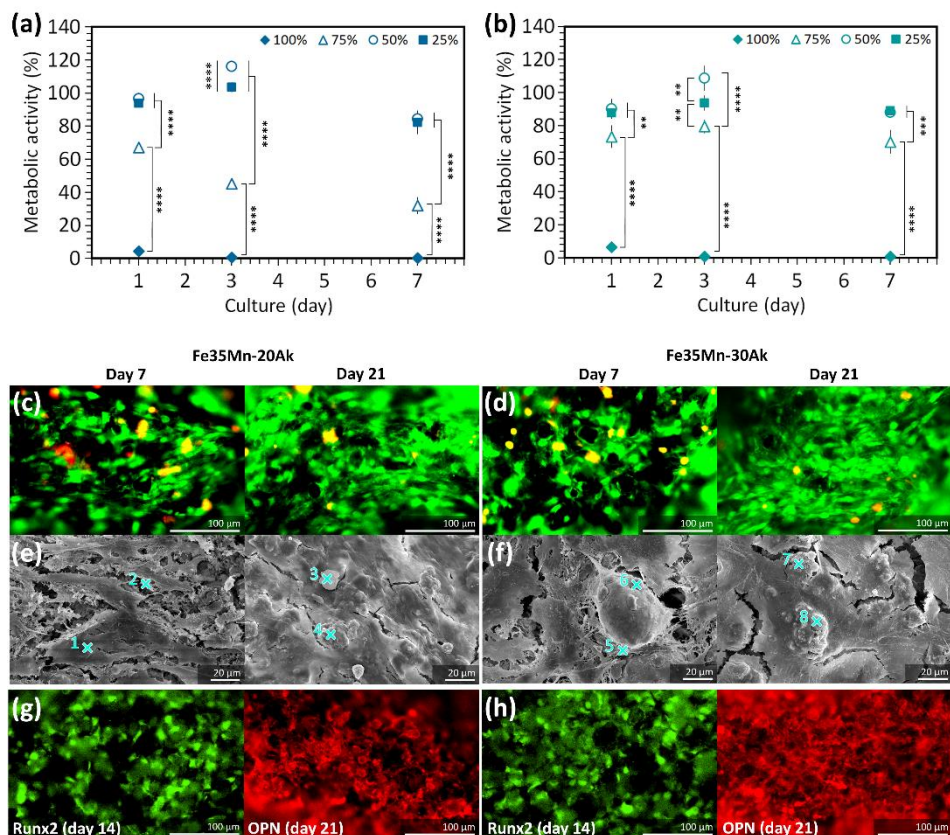


Figure 7.9. The cytocompatibility and bioactivity of the porous composite scaffolds assessed using the MC3T3-E1 preosteoblasts: the metabolic activity of the cells after culture with the extracts of the (a) Fe35Mn-20Ak and (b) Fe35Mn-30Ak specimens. The live/dead staining and morphology of the cells cultured on the (c, d) Fe35Mn-20Ak and (e, f) Fe35Mn-30Ak specimens at day 7 and 21. (g-h) The immunostaining of Runx2 at day 14 and OPN at day 21. **** = $p < 0.0001$, *** = $p < 0.001$, and ** = $p < 0.01$

7.3.7 Morphology and osteogenic differentiation of cells on the composites

Live/dead fluorescent images showed the viability of the preosteoblasts cultured on the composite specimens after 7 and 21 d (Figure 7.9c-d). The preosteoblasts adhered on the surfaces of the composites and exhibited elongated cell morphologies and extended filopodia. A monolayer of cells had formed at day 7, covering the struts of the specimens (Figure 7.9e-f). The cell layer thickened at day 21 (Figure 7.9e-f), showing that cells proliferated over time on the composite specimens, which was comparable to those observed on Ti6Al4V specimens (Figure S7.4). Moreover, the preosteoblasts cultured on the FeMn-Ak composite specimens exhibited cues of osteogenic differentiation. The Runx2 proteins were

expressed at day 14, showing that the osteogenic differentiation of the cells had occurred (Figure 7.9g-h) comparable to the levels observed for the Ti6Al4V specimens (Figure S7.4). The cells were surrounded by precipitates, which were more clearly visible on day 21. The precipitates were integrated into the cell layers and contained Ca and P (Table 7.2), which may indicate an initial stage of *in vitro* biomineralization. This observation was confirmed by the visualization of OPN proteins at day 21, indicating biomineralization (Figure 7.9g-h). A higher intensity of OPN proteins could be observed on the Fe35Mn-30Ak specimens than on the Fe35Mn-20Ak.

Table 7.2. The chemical compositions of the biodegradation products on the composites during cell culture as determined by EDS analysis.

EDS points		C	O	Na	P	K	Ca	Mn	Fe
Fe35Mn-20Ak D7	1	19.38	18.68	6.29	13.58	-	10.30	7.21	24.56
	2	16.25	28.11	8.80	8.53	1.38	8.98	6.97	20.97
Fe35Mn-20Ak D21	3	23.09	34.84	1.58	5.08	0.43	4.96	9.26	20.75
	4	12.15	31.19	1.54	9.04	0.73	6.64	8.44	30.20
Fe35Mn-30Ak D7	5	11.79	26.67	9.85	11.60	-	8.30	5.88	25.90
	6	10.53	25.84	8.73	12.78	1.63	9.21	5.46	25.81
Fe35Mn-30Ak D21	7	7.28	9.45	9.34	13.94	1.40	9.42	6.10	43.07
	8	16.42	30.07	6.29	7.49	0.91	5.27	7.42	26.12

7.4 Discussion

The newly developed porous biomaterials made of Fe, Mn, and akermanite successfully satisfied all the requirements of porous biodegradable Fe-based scaffolds for bone substitution. The FeMn-Ak composite scaffolds produced by extrusion-based 3D printing demonstrated (i) enhanced biodegradability at the rates of 0.24–0.27 mm/y that are in the suggested range of suitable biodegradation rates for ideal bone substitutes (*i.e.*, 0.2–0.5 mm/y [22]); (ii) a very low saturated magnetization and magnetic susceptibility, confirming the MRI-compatibility of the composite materials; (iii) sufficient mechanical properties even after 28 d of biodegradation (*i.e.* $\sigma_y = 1.8$ –8.3 MPa and $E = 0.03$ –

0.53 GPa) which mimicked the mechanical properties of the trabecular bone [42]; and (iv) a functional environment for the adhesion, proliferation, and osteogenic differentiation of preosteoblasts MC3T3-E1. The combined effect of such favorable properties puts the porous composites developed here as one of the top-rank AM Fe-based bone substitutes and encourages *in vivo* studies on such biomaterials.

7.4.1 Extrusion-based 3D printing of the composite scaffolds

Extrusion-based 3D printing is a viable fabrication technique to produce geometrically complex structures suitable for orthopedic applications [43,44]. Here, we demonstrated the capability of 3D printing to fabricate prototype hip stem and acetabular cup (Figure 7.2d) in addition to the cylindrical specimens. The success in extrusion-based 3D printing essentially relies on the choice of a binder that possesses suitable viscoelastic properties. We made choice of a binder made of hypromellose for its shear thinning property (Figure S7.1) to enable the smooth extrusion of the FeMn-Ak-containing inks (Figure 7.2). Hypromellose polymers have been utilized for extrusion-based 3D printing of various metal/ceramic-based inks [45–47]. In addition to the binder, the chemical interactions between the powder particles and binder must be considered. For example, the viscosity of the FeMn-Ak ink increased as the akermanite content increased to 30 vol% (Figure S7.1). Akermanite powder is hydrophilic [48], meaning that powder particles can tightly adhere to the hypromellose binder. Consequently, a higher 3D printing pressure was required for the Fe₃₅Mn-30Ak ink as compared to Fe₃₅Mn-20Ak. A sufficient powder-to-binder ratio is another important parameter to ensure the stability of the extruded struts, enabling the fabrication of the scaffolds with a high aspect ratio.

Robust green bodies of the FeMn-Ak scaffolds were successfully constructed during the 3D printing of the metal-ceramic inks (Figure 7.2b-c). After 3D printing, the green bodies were subjected to debinding at the temperature where the hypromellose binder decomposed (*i.e.*, at 350 °C) [11]. Subsequently, the brown bodies were sintered to form the composites. The as-sintered FeMn-Ak composite scaffolds preserved the original macro-pore design with a laydown pattern of 0°/90° angle (Figure 7.2e). Such a scaffold architecture has been found to perform well *in vivo* in critical-size rat skull and sheep tibia defects [49,50]. In addition to the macro-pores, the struts of the composites possessed open micro-pores (Figure 7.2e-f), which increased the total interconnectivity of the pore networks to 99%.

We supplemented Fe with a 35 wt% Mn to ensure the formation of the γ -austenite Fe-Mn phase, thereby ensuring the anti-ferromagnetic behavior of the *in situ* formed alloy [7]. The inclusion of 20–30 vol% akermanite was aimed to

provide bioactive properties. In addition, interfacial bonding between Fe, Mn, and akermanite is of equal importance for obtaining bone-substituting scaffolds with sufficiently high mechanical performance. Sintering (*i.e.*, at 1200 °C) facilitated multiple diffusion processes, which was an effective way to engage every component in the multi-material scaffolds, realizing the intended material biofunctionalities.

The occurrence of diffusion was clearly observed in the cross-sectional analyses of the composite scaffolds (Figure 7.3). At a high temperature, Mn is known to be volatile [51]. The compact configuration of the as-printed scaffold struts (Figure 7.2b-c) allowed volatile Mn to diffuse into Fe and the akermanite particles. Overall, the diffusion of Mn into Fe appeared to be homogenous (Figure 7.3a), resulting in the formation of the γ -austenite Fe-Mn phase in the scaffolds (Figure 7.4a). Near the interface of the Fe-Mn alloy to the akermanite phase, the mass% value of Mn in the Fe matrix decreased to about 31–32 wt%. This is expected because Mn diffuses into the neighboring bioceramic particles (Figure 7.3b).

In addition to the diffusion of Mn into Fe and that of Mn into the bioceramic, Fe dispersed into the bioceramic particles. The diffusion of Fe into silicate-based bioceramics has been reported at the interface of both materials, without new phases forming [27,52]. In the present composite scaffolds, an intense level of diffusion of Fe into the bioceramic phase was observed (Figure 7.3b). Fe diffused approximately 3.2 μm deeper into the akermanite phase than what was previously observed in Fe-Ak composite scaffolds [28]. During the formation of the Fe-Mn solid solution, the α -Fe crystal structure (*i.e.*, body-centered cubic) had transformed into a γ -FeMn crystal structure (*i.e.*, face-centered cubic) that provides more atomic packing, hence enabling more Fe diffusion into the bioceramic phase.

In addition to the γ -austenite Fe-Mn phase in the scaffolds (Figure 7.4a), the diffusion of Fe and Mn into akermanite displaced the locations of Ca, Mg, and O in the lattice structure. Consequently, a mixture of nesosilicate crystalline phases, including kirschsteinite (Ca(Fe)SiO_4), glaucocroite (Ca(Mn)SiO_4), and monticellite (Ca(Mg)SiO_4), was formed (Figure 7.4a). The XRD peaks of the nesosilicate phases could not be easily distinguished, since these phases have the same crystal structure (*i.e.*, orthorhombic). The presence of these nesosilicate phases could still be beneficial for bone regeneration. The monticellite phase has been reported to stimulate the adhesion and proliferation of osteoblasts [53]. Moreover, the penetration of Fe into akermanite tends to enhance the apatite-forming ability of the material [54]. Finally, Mn-doped calcium silicate is reported to promote bone regeneration *in vivo* [55].

7.4.2 Magnetic characteristics of the composite scaffolds

To have MRI compatibility of the first kind, the magnetic susceptibility value of a bone-substituting material under the hydrated condition must be $< 10^{-2}$ [56]. The magnetic susceptibility values of the porous composites were 3.6 and 4.5×10^{-3} before and after *in vitro* biodegradation, respectively, confirming that the developed biomaterials are paramagnetic and MRI-friendly. The γ -austenite Fe-Mn phase formed during sintering guaranteed the anti-ferromagnetic property of the composite scaffolds (Figure 7.4) [57]. The magnetic properties of the scaffolds were comparable to the values found in the literature [11,16,57,58]. Our results showed that the FeMn-Ak composites fall into the same category of magnetic compatibility as Ti6Al4V and non-magnetic stainless steel [56]. While such materials do not react strongly to the applied magnetic field of MRI (*i.e.*, at 2 T), some MRI image artefacts may be present. Such image interference is almost inevitable for most paramagnetic implantable medical devices during MRI imaging. This is due to the huge differences between the magnetic susceptibility of the paramagnetic medical devices (*i.e.*, magnetic susceptibility values of 10^{-5} – 10^{-2}) and the surrounding tissue that is mostly diamagnetic (*e.g.*, magnetic susceptibility value -9×10^{-6}) [56,59]. Nonetheless, the volume of MRI image artefacts can be reduced by introducing a porous geometry design into the implant material [60,61].

7.4.3 Biodegradation behavior of the composite scaffolds

The FeMn-Ak composite scaffolds biodegraded at the rates of 0.24 – 0.27 mm/y that are within the suggested range of biodegradation rates suitable for ideal bone substitutes (*i.e.*, 0.2 – 0.5 mm/y [22]). The biodegradation rates of the composite scaffolds are, indeed, much higher than those of pure Fe [6], Fe-Mn alloys [11], and Fe-Ak composites [28] previously fabricated by extrusion-based 3D printing, and are comparable to those of porous Fe₃₀Mn-hydroxyapatite fabricated by applying the space holder technique [26]. The enhanced biodegradability of the materials is mainly due to the alloying of Mn into the Fe matrix and the addition of akermanite powder particles. In addition, the composite scaffolds had a high pore interconnectivity that provided a large surface area for the initiation of biodegradation.

The γ -FeMn phase in the composite scaffolds lowers their standard electrode potential, thus increasing their tendency to corrode [16]. The nesosilicate phases formed in the composite scaffolds also influenced the biodegradation behavior. In general, silicate-based bioceramics are known for their favorable biodegradability [62,63]. Monticellite has a similar solubility to diopside [64], while the solubilities of the kirschsteinite and glaucocroite phases in the physiological condition are yet to be investigated. In the scaffold struts, the

nesosilicates particles were randomly distributed and decorated the surfaces of Fe-Mn alloy particles (Figure 7.2f). The bonding of the materials with multiphases (*i.e.*, γ -FeMn and nesosilicate phases) may promote local galvanic corrosion, which was, indeed, observed on the cross-section of the biodegraded specimens. The Fe-Mn alloy particles exhibited typical pitting corrosion characteristics on their surface (as indicated by arrows in Figure 7.5i).

During biodegradation, Fe, Mn, Ca, Si, and Mg ions were released from the composite scaffolds (Figure 7.6). The ions reacted with the components in the r-SBF medium and formed precipitates (Figure 7.5). The biodegradation precipitates on the composite scaffolds were predominantly made of lepidocrocite (γ -FeOOH) and rhodochrosite (MnCO_3 , Figure 7.4b). These degradation by-products are expected, as Fe and Mn are the two main constituents in the material composition of the scaffolds. The γ -FeOOH and MnCO_3 degradation products are identified in other studies on Fe-Mn alloys as well [65–68]. Despite the formation of Fe- and Mn-based precipitates (Figure 7.5), the increasing concentration of Fe^{2+} ions over time and the high concentration of Mn^{2+} ions in the medium collected over the 28 days of immersion showed the good biodegradability of the specimens (Figure 7.6a–b). The concentration of Mn^{2+} ions reached values up to 30 times higher than that of Fe^{2+} ions after only 1 day of immersion. The values remained up to 13 times higher by day 28 (Figure 7.6b). The higher concentration of Mn^{2+} ions as compared to Fe^{2+} ions implies that the precipitation of Fe-based biodegradation products was favored (Figure 7.4b). Such excessive release of Mn^{2+} ions has also been reported in previous studies and is strongly correlated to the 5% CO_2 atmospheric condition and the availability of bicarbonate ions (HCO_3^-) in the biodegradation medium [66,67,69].

The Ca-based precipitates were vastly present on the periphery of the composite scaffolds too (Figure 7.5f–h). Unlike Fe-Ak composite scaffolds [28], however, crystalline Ca-based products were not identified. This may be because the concentration of the Ca^{2+} ions released from the nesosilicate phases in the FeMn-Ak scaffolds has been inadequate to form a stable CaCO_3 phase (Figure 7.6c). Moreover, the release of Mn^{2+} ions was substantial throughout the immersion period (Figure 7.6b). The precipitation of the MnCO_3 phase has, therefore, been thermodynamically more favorable than the CaCO_3 phase [70]. Despite the absence of crystalline Ca-based precipitates, the Ca^{2+} and PO_4^{3-} ions in the r-SBF medium decreased over time (Figure 7.6c–d), which suggested the potential formation of amorphous calcium phosphate or calcium carbonate, as biodegradation occurred in the 5% CO_2 environment. The amorphous Ca-based degradation products have been reported to be beneficial for the regeneration of bone tissue [71–74].

Mg- and Si-containing biodegradation products were not observed on the periphery of the biodegradation products (Figure 7.5f-h). That is because the concentrations of the Mg^{2+} and Si^{4+} ions released from the FeMn-Ak specimens on day 28 (Figure 7.6e-f) were, respectively, 2 and 6 times lower than those reported during the biodegradation of Fe-Ak composite scaffolds [28]. Our results imply that the nesosilicate bioceramic phases are more stable than pure akermanite, which is in line with the literature [54,55]. When Fe^{3+} had partially substituted the crystal lattice of akermanite, the release of Ca^{2+} , Mg^{2+} , and Si^{4+} ions during biodegradation was lower than the values reported for pure akermanite [54]. A decreasing ion release profile was also reported, when Mn^{2+} diffused into calcium silicate [55]. Nevertheless, the slower dissolution of the nesosilicate phases means that the bioceramic particles could stay longer in the matrix (Figure 7.5i) and provide silica-rich surfaces that act as nucleation sites for apatite formation [63], encouraging osteoconductivity.

The observed biodegradation behavior is intimately linked to the electrochemical responses of the composite scaffolds over time. The decreasing OCP values during the immersion tests (Figure 7.7a) indicate that the base material of the FeMn-Ak composites has been susceptible to corrosion, despite the thickening of the biodegradation products. The biodegradation precipitates moderately limited the mass transport of material during corrosion, which could be recognized from the decrease in the rate of biodegradation (Figure 7.4b) and the marginal increase in the R_p value over time (Figure 7.7b). The Bode impedance modulus in the low frequency region, which are indicative of the corrosion resistance of the material, exhibited a slight increasing trend similar to the ones seen for the R_p values (Figure 7.7c-d). On the other hand, the values of the Bode impedance modulus in the mid-frequency region, which are indicative of the evolution of the corrosion products, were relatively stable over time. The peak of the Bode plots phase angles did not shift from a higher frequency to a lower frequency when exposed to r-SBF for 28 d (Figure 7.7c-d), which suggests that the partial growth and dissolution of the corrosion products is near-equivalent. Corresponding to the trend of OCP values, the peaks of the Bode plot phase angle at high frequencies (*e.g.*, 10 kHz) remained close to 0° , indicating that the material had a propensity to corrode [75,76]. Altogether, our results demonstrated that the rate and mechanism of biodegradability of the composite scaffolds developed here, and the associated biodegradation products supported their intended use as temporary bone substitutes.

7.4.4 Mechanical properties of the composite scaffolds

The structural integrity of biodegradable implants is of great importance and should be maintained until newly formed bone takes over the role of mechanical

support. As compared to geometrically similar scaffolds made from Fe₃₅Mn alloy [11], the Fe₃₅Mn-20Ak composite scaffolds developed here exhibited a higher yield strength and elastic modulus. However, the Fe₃₅Mn-30Ak composite scaffolds exhibited lower mechanical properties than the Fe₃₅Mn alloy scaffolds [11]. Increasing the content of the reinforcing akermanite particles from 20 to 30 vol% decreased the yield strength and the elastic modulus of the resulting biomaterial (Figure 7.8). This is likely due to the embrittlement effect of the bioceramic phase on the metal matrix [77–79]. Nevertheless, both the FeMn-Ak composite scaffolds developed in this study exhibited trabecular bone-mimicking mechanical properties [42] (*i.e.*, $\sigma_y = 3.1\text{--}8.3$ MPa and $E = 0.3\text{--}0.5$ GPa) even after 28 d of biodegradation.

For any scaffolds containing multiple materials, strong bonding at the interface of the materials is required to ensure smooth load transfer from the matrix to the reinforcing phases so as to prevent premature failure of the material. On the other hand, the interfacial bonding of the phases can act as the initiation sites for localized corrosion, which may adversely influence the mechanical integrity of the material during biodegradation. In the FeMn-Ak composites, the diffusion of Fe and Mn into the bioceramic phase was clearly observed along with the newly formed bioceramic phases (Figure 7.3, 7.4a). The diffusion resulted in strong bonding of the multi-material phases, thus leading to the higher yield strength and elastic modulus of the Fe₃₅Mn-20Ak scaffolds as compared to those of the Fe-20Ak specimens [28].

During biodegradation, the mechanical properties of the FeMn-20Ak specimens decreased with time, as has been the case for Fe-Ak [28] and Fe-TCP [80] composites. The Fe₃₅Mn-30Ak specimens turned brittle. Given the deteriorating effects of 28 d of biodegradation and the negligible strengthening effects of the precipitated degradation products, the mechanical properties of the Fe₃₅Mn-30Ak scaffolds were expected to decrease. It should, however, be noted that the composite scaffolds did not fail prematurely despite their fast biodegradation over a period of 28 d.

7.4.5 Cytocompatibility and osteogenic potential of the composite scaffolds

In the development of osteoregenerative biodegradable materials, cytocompatibility and osteogenic responses are of great importance. The FeMn-Ak composite scaffolds developed here enabled the preosteoblasts MC3T3-E1 to be metabolically active (Figure 7.9a-b) while supporting their adherence to the specimens and their proliferation on the surface of the specimen struts (Figure 7.9c-f). In addition, the precipitated minerals, which could be a combination of biodegradation products and apatite, integrated well into the cellular matrix (Figure 7.9e-f, Table 7.2). The composite scaffolds enabled the osteogenic

differentiation of the cells, as evidenced by the expression of Runx2. At the later time points, the visualized OPN matrix indicated the occurrence of *in vitro* biomineralization (Figure 7.9g-h).

Initially, we studied the metabolic behavior of the MC3T3-E1 preosteoblasts cultured with the extracts of the composite specimens. The inhibition of the preosteoblasts growth (IC_{50}) has been reported at 53 mg/L Fe ions and 5 mg/L Mn ions [81]. We observed that the preosteoblasts metabolic activity declined in the extracts of the composite scaffolds with high concentrations (Figure 7.9a-b). In the 100% extracts, the concentration of Fe^{2+} ions alone would be high enough to inhibit the metabolic activity of the cells. While the concentration of Fe^{2+} ions reduced to a safe value in the 75% extracts, the concentration of Mn^{2+} ions in both extracts remained high enough to adversely affect cell activity, as observed in the 75% Fe₃₅Mn-20Ak extracts (Figure 7.9a). Interestingly, the high concentration of Mn^{2+} ions in the 75% Fe₃₅Mn-30Ak extracts did not negatively influence the metabolic activity of the preosteoblasts (Figure 7.9b). This could be due to the presence of a higher concentration of bioactive ions released from the silicate-based ceramics in the Fe₃₅Mn-30Ak specimens. When further diluted (*i.e.*, 2× and more), the preosteoblasts were metabolically active despite the fact that the concentration of Mn ions (*i.e.*, 15–18 mg/L) was still higher than the reported IC_{50} value. Bone tissue is known to have a large amount of Mn reserve [82], which may explain the cytocompatibility of the preosteoblasts in the 50% and 25% FeMn-Ak extracts.

Furthermore, we evaluated the growth of the preosteoblasts directly cultured on the specimens. We used a high ratio of the cell culture medium to the surface area of the specimen to more closely mimic the conditions experienced by the specimens in the human body. Our results demonstrated the adhesion and proliferation of cells on both types of composite scaffolds (**Figure 7.9c-f**), which were comparable to one of the currently most widely used materials for permanent bone implants (*i.e.*, Ti6Al4V, **Figure S7.4**) and bioactive Fe-Ak [28]. The *in vitro* biological responses of the cells on the composites were improved as compared to the cell responses observed on geometrically similar Fe [6] and Fe-35Mn alloy specimens [11]. These comparisons confirm that the enhanced cytocompatibility of the developed biomaterials is due to the addition of the silicate-based bioceramics into their matrix. The direct cell culture results did not show any visual differences in the cell proliferation on the composite specimens, unlike the results from the indirect cell culture. This is most likely because the cells were continuously exposed to the FeMn-Ak extracts in the indirect cell tests, while the cells received a fresh cell culture medium in the direct cell tests. The metallic ions, therefore, did not accumulate to cause cytotoxicity.

In addition to cell proliferation, enabling the osteogenic differentiation of cells is an essential biofunctionality for bone substitutes. Osteoblasts are responsible for the synthesis of proteins and the secretion of the matrix (*e.g.*, OPN) to generate *de novo* bone [83]. Our scaffolds allowed for the differentiation of preosteoblasts, expressed by Runx2 proteins (Figure 7.9g-h), similar to the observation on Ti6Al4V (Figure S7.4). Then, the OPN proteins were deposited on the composite specimens in a matrix-like structure (Figure 7.9g-h). OPN is often expressed by mineralized tissue [84], suggesting that *in vitro* biomineralization occurred on the composites. We also observed the precipitation of minerals integrated into the cell layers, which strengthened the evidence of the occurrence of the biomineralization (Figure 7.9e-f, Table 7.2). Overall, the *in vitro* biological performance of FeMn-Ak composite specimens was comparable to that of Fe-Ak composites [28], despite the fact that akermanite in the FeMn-Ak specimens was transformed into nesosilicate crystalline phases. Taken together, our findings demonstrate the potential of the developed 3D printed FeMn-Ak porous biomaterials for use as osseointegrative bone substitutes.

7.5 Conclusion

We developed two novel types of bone-substituting 3D printed biodegradable FeMn-akermanite composite scaffolds. Our thorough characterization of these biomaterials showed that they offer suitable rates of biodegradability, are MRI-friendly and osteogenic, and mimic the trabecular bone in terms of mechanical properties. The porosity and pore interconnectivity of the composites were both high to meet their functional requirements. The *in vitro* biodegradation rates of the composites fell into the range of the desired values for ideal bone substitution. The γ -FeMn phase in the composite matrix made the biomaterials weakly paramagnetic, allowing the composites to be classified as first kind MRI-friendly biomaterials. The mechanical properties of the porous composite remained in the range of the mechanical properties of the trabecular bone, despite the decreasing trend due to *in vitro* biodegradation. The preosteoblast MC3T3-E1 cell line showed a positive *in vitro* biological response to the composite materials, as evidenced by the good adhesion and proliferation of the cells. Furthermore, the composites allowed the cells to differentiate and exhibit the hallmarks of biomineralization. Altogether, our results evidently show the remarkable potential of the FeMn-Ak composites in fulfilling all the requirements of porous biodegradable bone substitutes, encouraging further research towards their clinical translation.

7.6 Supplementary material

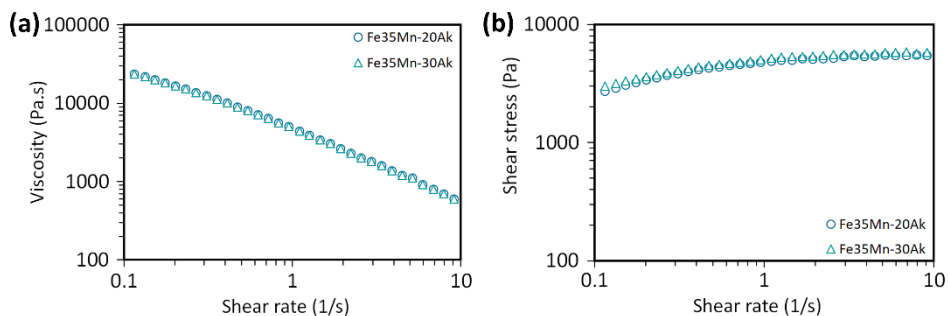


Figure S7.1. Rheological properties of the FeMn-akermanite-containing inks: (a) the viscosity and (b) shear stress as a function of shear rate.

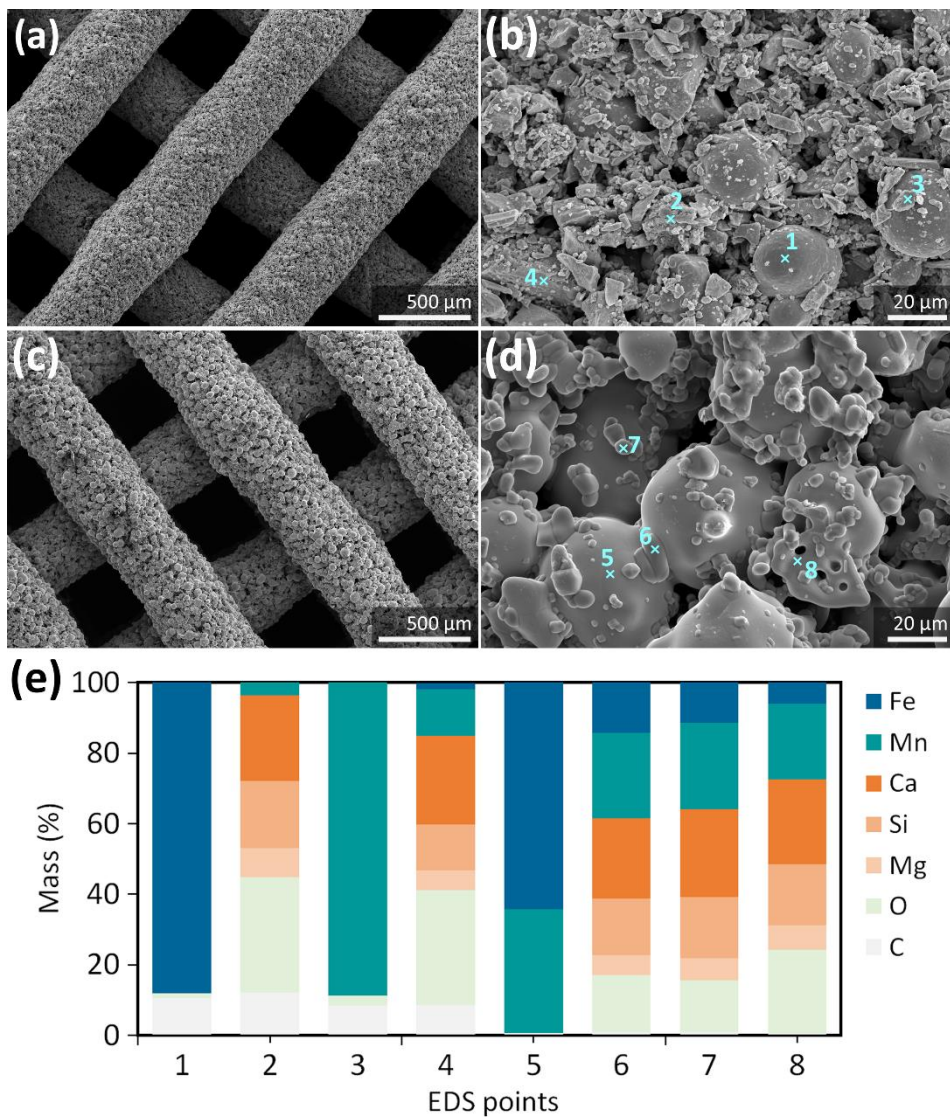


Figure S7.2. (a) The morphology of the as-printed Fe₃₅Mn-20Ak specimens and (b) powder particle distribution on the struts. (c) The morphology of the as-sintered Fe₃₅Mn-20Ak specimens and (d) powder particle distribution on the struts. (e) The chemical compositions of scaffold struts obtained by EDS. The cross signs with a number indicate the location of the EDS point analyses.

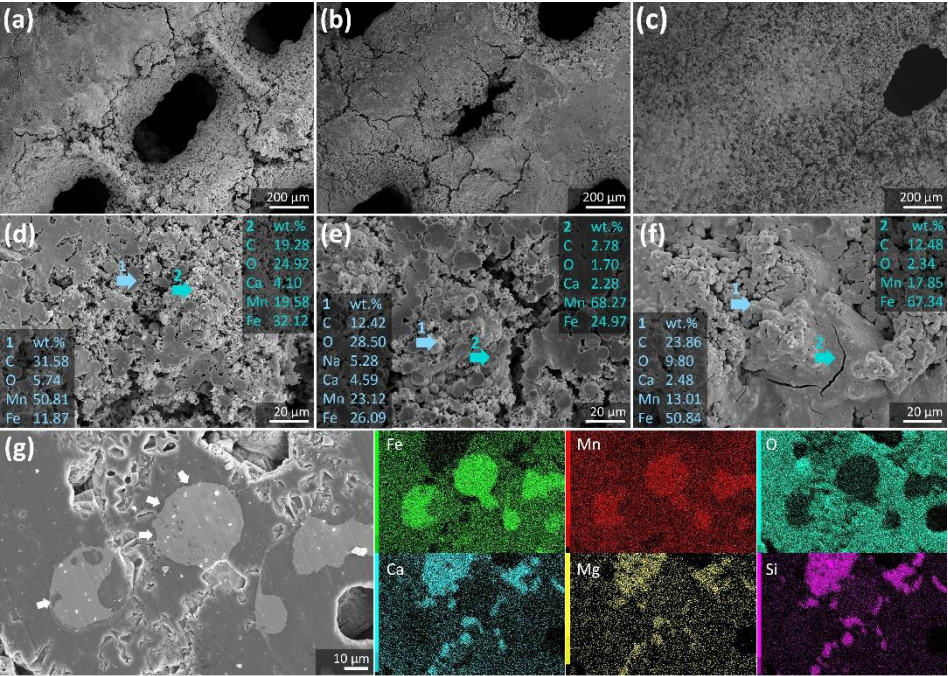


Figure S7.3. (a-c) The morphologies and (d-f) chemical compositions of the biodegradation products on the periphery of Fe₃₅Mn-20Ak specimens after (a, d) 4, (b, e) 7, and (c, f) 28 d of biodegradation as well as (g) at the center of the specimens after 28 d of biodegradation.

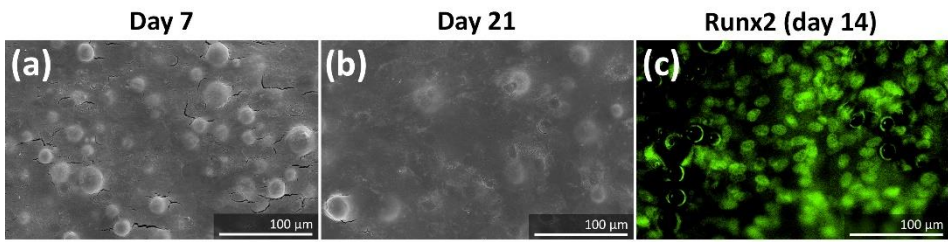


Figure S7.4. The morphologies of the cells on the Ti6Al4V scaffolds at (a) day 7 and (b) day 21, and (c) Runx2 immunostaining at day 14.

Bibliography

- [1] A.H. Md Yusop, M.F. Ulum, A. Al Sakka, D. Hartanto, H. Nur, Insight into the bioabsorption of Fe-based materials and their current developments in bone applications, *Biotechnol. J.* 16 (2021). <https://doi.org/10.1002/biot.202100255>.
- [2] R. Gorejová, L. Haverová, R. Oriňáková, A. Oriňák, M. Oriňák, Recent advancements in Fe-based biodegradable materials for bone repair, *J. Mater. Sci.* 54 (2019) 1913–1947. <https://doi.org/10.1007/s10853-018-3011-z>.
- [3] A.H. Md Yusop, A. Al Sakka, H. Nur, Modifications on porous absorbable Fe-based scaffolds for bone applications: A review from corrosion and biocompatibility viewpoints, *J. Biomed. Mater. Res. - Part B Appl. Biomater.* 110 (2022) 18–44. <https://doi.org/10.1002/jbm.b.34893>.
- [4] Y. Li, H. Jahr, K. Lietaert, P. Pavanram, A. Yilmaz, L.I. Fockaert, M.A. Leeftang, B. Pouran, Y. Gonzalez-Garcia, H. Weinans, J.M.C. Mol, J. Zhou, A.A. Zadpoor, Additively manufactured biodegradable porous iron, *Acta Biomater.* 77 (2018) 380–393. <https://doi.org/10.1016/j.actbio.2018.07.011>.
- [5] Y. Li, H. Jahr, P. Pavanram, F.S.L. Bobbert, U. Puggi, X.Y. Zhang, B. Pouran, M.A. Leeftang, H. Weinans, J. Zhou, A.A. Zadpoor, Additively manufactured functionally graded biodegradable porous iron, *Acta Biomater.* 96 (2019) 646–661. <https://doi.org/10.1016/j.actbio.2019.07.013>.
- [6] N.E. Putra, M.A. Leeftang, M. Minneboo, P. Taheri, L.E. Fratila-Apachitei, J.M.C. Mol, J. Zhou, A.A. Zadpoor, Extrusion-based 3D printed biodegradable porous iron, *Acta Biomater.* 121 (2021) 741–756. <https://doi.org/10.1016/j.actbio.2020.11.022>.
- [7] J. Martínez, S.M. Cotes, A.F. Cabrera, J. Desimoni, A. Fernández Guillermet, On the relative fraction of ϵ martensite in γ -Fe-Mn alloys, *Mater. Sci. Eng. A.* 408 (2005) 26–32. <https://doi.org/10.1016/j.msea.2005.06.019>.
- [8] H. Hermawan, H. Alamdari, D. Mantovani, D. Dubé, Iron-manganese: New class of metallic degradable biomaterials prepared by powder metallurgy, *Powder Metall.* 51 (2008) 38–45. <https://doi.org/10.1179/174329008X284868>.
- [9] M. Schinhammer, A.C. Hänzli, J.F. Löffler, P.J. Uggowitzer, Design strategy for biodegradable Fe-based alloys for medical applications, *Acta Biomater.* 6 (2010) 1705–1713. <https://doi.org/10.1016/j.actbio.2009.07.039>.
- [10] S.M. Huang, E.A. Nauman, L.A. Stanciu, Investigation of porosity on mechanical properties, degradation and in-vitro cytotoxicity limit of Fe₃₀Mn using space holder technique, *Mater. Sci. Eng. C.* 99 (2019) 1048–1057. <https://doi.org/10.1016/j.msec.2019.02.055>.
- [11] N.E. Putra, M.A. Leeftang, P. Taheri, L.E. Fratila-Apachitei, J.M.C. Mol, J. Zhou, A.A. Zadpoor, Extrusion-based 3D printing of ex situ-alloyed highly biodegradable MRI-friendly porous iron-manganese scaffolds, *Acta Biomater.* 134 (2021) 774–790. <https://doi.org/10.1016/j.actbio.2021.07.042>.
- [12] P. Liu, D. Zhang, Y. Dai, J. Lin, Y. Li, C. Wen, Microstructure, mechanical properties, degradation behavior, and biocompatibility of porous Fe-Mn alloys fabricated by sponge impregnation and sintering techniques, *Acta Biomater.* 114 (2020) 485–496. <https://doi.org/10.1016/j.actbio.2020.07.048>.
- [13] C. Shuai, W. Yang, Y. Yang, H. Pan, C. He, F. Qi, D. Xie, H. Liang, Selective laser melted Fe-Mn bone scaffold: Microstructure, corrosion behavior and cell response, *Mater. Res. Express.* 7 (2019) 015404. <https://doi.org/10.1088/2053-1591/ab62f5>.
- [14] D. Carluccio, C. Xu, J. Venezuela, Y. Cao, D. Kent, M. Bermingham, A.G. Demir, B. Previtali, Q. Ye, M. Dargusch, Additively manufactured iron-manganese for biodegradable porous load-bearing bone scaffold applications, *Acta Biomater.* 103 (2020) 346–360. <https://doi.org/10.1016/j.actbio.2019.12.018>.
- [15] Y. Nie, G. Chen, H. Peng, S. Tang, Z. Zhou, F. Pei, B. Shen, In vitro and 48 weeks in vivo performances of 3D printed porous Fe-30Mn biodegradable scaffolds, *Acta Biomater.* 121 (2021) 724–740. <https://doi.org/10.1016/j.actbio.2020.12.028>.
- [16] M.S. Dargusch, A. Dehghan-Manshadi, M. Shahbazi, J. Venezuela, X. Tran, J. Song, N. Liu, C. Xu, Q. Ye, C. Wen, Exploring the role of manganese on the microstructure, mechanical properties, biodegradability, and biocompatibility of porous iron-based scaffolds, *ACS Biomater. Sci. Eng.* 5 (2019) 1686–1702. <https://doi.org/10.1021/acsbomaterials.8b01497>.

- [17] D. Hong, D.T. Chou, O.I. Velikokhatnyi, A. Roy, B. Lee, I. Swink, I. Issaev, H.A. Kuhn, P.N. Kumta, Binder-jetting 3D printing and alloy development of new biodegradable Fe-Mn-Ca/Mg alloys, *Acta Biomater.* 45 (2016) 375–386. <https://doi.org/10.1016/j.actbio.2016.08.032>.
- [18] D.T. Chou, D. Wells, D. Hong, B. Lee, H. Kuhn, P.N. Kumta, Novel processing of iron-manganese alloy-based biomaterials by inkjet 3-D printing, *Acta Biomater.* 9 (2013) 8593–8603. <https://doi.org/10.1016/j.actbio.2013.04.016>.
- [19] H. Hermawan, A. Purnama, D. Dube, J. Couet, D. Mantovani, Fe-Mn alloys for metallic biodegradable stents: Degradation and cell viability studies, *Acta Biomater.* 6 (2010) 1852–1860. <https://doi.org/10.1016/j.actbio.2009.11.025>.
- [20] J. Capek, J. Kubásek, D. Vojtěch, E. Jablonská, J. Lipov, T. Ruml, Microstructural, mechanical, corrosion and cytotoxicity characterization of the hot forged FeMn30(wt.%) alloy, *Mater. Sci. Eng. C.* 58 (2016) 900–908. <https://doi.org/10.1016/j.msec.2015.09.049>.
- [21] J. Venezuela, M.S. Dargusch, Addressing the slow corrosion rate of biodegradable Fe-Mn: Current approaches and future trends, *Curr. Opin. Solid State Mater. Sci.* 24 (2020) 100822. <https://doi.org/10.1016/j.cossms.2020.100822>.
- [22] C. Shuai, S. Li, S. Peng, P. Feng, Y. Lai, C. Gao, Biodegradable metallic bone implants, *Mater. Chem. Front.* 3 (2019) 544–62. <https://doi.org/10.1039/c8qm00507a>.
- [23] B. Huzum, B. Puha, R. Necoara, S. Gheorghevi, G. Puha, A. Filip, P. Sirbu, O. Alexa, Biocompatibility assessment of biomaterials used in orthopedic devices: An overview (Review), *Exp. Ther. Med.* 22 (2021) 1–9. <https://doi.org/10.3892/etm.2021.10750>.
- [24] S. Mandal, V. Kishore, M. Bose, S.K. Nandi, M. Roy, In vitro and in vivo degradability, biocompatibility and antimicrobial characteristics of Cu added iron-manganese alloy, *J. Mater. Sci. Technol.* 84 (2021) 159–172. <https://doi.org/10.1016/j.jmst.2020.12.029>.
- [25] L.C. Trincă, L. Burtan, D. Mareci, B.M. Fernández-Pérez, I. Stoleriu, T. Stanciu, S. Stanciu, C. Solcan, J. Izquierdo, R.M. Souto, Evaluation of in vitro corrosion resistance and in vivo osseointegration properties of a FeMnSiCa alloy as potential degradable implant biomaterial, *Mater. Sci. Eng. C.* 118 (2021) 111436. <https://doi.org/10.1016/j.msec.2020.111436>.
- [26] M. Heiden, E. Nauman, L. Stanciu, Bioresorbable Fe–Mn and Fe–Mn–HA materials for orthopedic implantation: Enhancing degradation through porosity control, *Adv. Healthc. Mater.* 6 (2017) 1–12. <https://doi.org/10.1002/adhm.201700120>.
- [27] C. Shuai, Y. Li, Y. Yang, S. Peng, W. Yang, F. Qi, S. Xiong, H. Liang, L. Shen, Bioceramic enhances the degradation and bioactivity of iron bone implant, *Mater. Res. Express.* 6 (2019) 115401. <https://doi.org/10.1088/2053-1591/ab45b9>.
- [28] N.E. Putra, K.G.N. Borg, P.J. Diaz-Payno, M.A. Leeftang, M. Klimopoulou, P. Taheri, J.M.C. Mol, L.E. Fratila-Apachitei, Z. Huan, J. Chang, J. Zhou, A.A. Zadpoor, Additive manufacturing of bioactive and biodegradable porous iron-akermanite composites for bone regeneration, *Acta Biomater.* 148 (2022) 355–373. <https://doi.org/10.1016/j.actbio.2022.06.009>.
- [29] S. Yoshizawa, A. Brown, A. Barchowsky, C. Sfeir, Magnesium ion stimulation of bone marrow stromal cells enhances osteogenic activity, simulating the effect of magnesium alloy degradation, *Acta Biomater.* 10 (2014) 2834–2842. <https://doi.org/10.1016/j.actbio.2014.02.002>.
- [30] A.F. Khan, M. Saleem, A. Afzal, A. Ali, A. Khan, A.R. Khan, Bioactive behavior of silicon substituted calcium phosphate based bioceramics for bone regeneration, *Mater. Sci. Eng. C.* 35 (2014) 245–252. <https://doi.org/10.1016/j.msec.2013.11.013>.
- [31] K. Szurkowska, J. Kolmas, Hydroxyapatites enriched in silicon – Bioceramic materials for biomedical and pharmaceutical applications, *Prog. Nat. Sci. Mater. Int.* 27 (2017) 401–409. <https://doi.org/10.1016/j.pnsc.2017.08.009>.
- [32] N.E. Putra, M.J. Mirzaali, I. Apachitei, J. Zhou, A.A. Zadpoor, Multi-material additive manufacturing technologies for Ti-, Mg-, and Fe-based biomaterials for bone substitution, *Acta Biomater.* 109 (2020) 1–20. <https://doi.org/10.1016/j.actbio.2020.03.037>.
- [33] C. Wu, J. Chang, Synthesis and apatite-formation ability of akermanite, *Mater. Lett.* 58 (2004) 2415–2417. <https://doi.org/10.1016/j.matlet.2004.02.039>.
- [34] ASTM B963-17, Standard test methods for oil content, oil-impregnation efficiency, and surface-connected porosity of sintered powder metallurgy (PM) products using Archimedes' principle, ASTM International, 2017. <https://doi.org/10.1520/B0963-14>.

- [35] A. Oyane, H.M. Kim, T. Furuya, T. Kokubo, T. Miyazaki, T. Nakamura, Preparation and assessment of revised simulated body fluids, *J. Biomed. Mater. Res. - Part A*. 65 (2003) 188–195. <https://doi.org/10.1002/jbm.a.10482>.
- [36] L. Yang, E. Zhang, Biocorrosion behavior of magnesium alloy in different simulated fluids for biomedical application, *Mater. Sci. Eng. C*. 29 (2009) 1691–1696. <https://doi.org/10.1016/j.msec.2009.01.014>.
- [37] ASTM G1-03, Standard practice for preparing, cleaning, and evaluating corrosion test specimens, ASTM International. (2017). <https://doi.org/10.1520/G0001-03R17E01.2>.
- [38] ASTM G32-72, Standard practice for laboratory immersion corrosion testing of metals., ASTM International. (2004). <https://doi.org/10.1520/G0031-72R04.2>.
- [39] ISO 13314, Mechanical testing of metals - Ductility testing - Compression test for porous and cellular metals, International Organization for Standardization, 2011. <https://doi.org/ISO 13314:2011>.
- [40] ISO 10993-12, Biological evaluation of medical devices - Part 12: Sample preparation and reference materials, International Organization for Standardization 2012. [https://doi.org/10.1016/S0080-8784\(08\)60069-1](https://doi.org/10.1016/S0080-8784(08)60069-1).
- [41] ISO 10993-5, Tests for in vitro cytotoxicity, International Organization for Standardization, 2009. <https://doi.org/10.1021/es0620181>.
- [42] E.F. Morgan, G.U. Unnikrisnan, A.I. Hussein, Bone mechanical properties in healthy and diseased states, *Annu. Rev. Biomed. Eng.* 20 (2018) 119–43. <https://doi.org/10.1146/annurev-bioeng-062117-121139>.
- [43] J.P. Li, J.R. De Wijn, C.A. Van Blitterswijk, K. De Groot, The effect of scaffold architecture on properties of direct 3D fiber deposition of porous Ti6Al4V for orthopedic implants, *J. Biomed. Mater. Res. - Part A*. 92 (2010) 33–42. <https://doi.org/10.1002/jbm.a.32330>.
- [44] J.P. Li, P. Habibovic, M. van den Doel, C.E. Wilson, J.R. de Wijn, C.A. van Blitterswijk, K. de Groot, Bone ingrowth in porous titanium implants produced by 3D fiber deposition, *Biomaterials*. 28 (2007) 2810–2820. <https://doi.org/10.1016/j.biomaterials.2007.02.020>.
- [45] S.B. Li, J.X. Xie, Fabrication of thin-walled 316L stainless steel seamless pipes by extrusion technology, *J. Mater. Process. Technol.* 183 (2007) 57–61. <https://doi.org/10.1016/j.jmatprotec.2006.09.024>.
- [46] M.W. Sa, B.N.B. Nguyen, R.A. Moriarty, T. Kamaltdinov, J.P. Fisher, J.Y. Kim, Fabrication and evaluation of 3D printed BCP scaffolds reinforced with ZrO₂ for bone tissue applications, *Biotechnol. Bioeng.* 115 (2018) 989–999. <https://doi.org/10.1002/bit.26514>.
- [47] C.F. Marques, F.H. Perera, A. Marote, S. Ferreira, S.I. Vieira, S. Olhero, P. Miranda, J.M.F. Ferreira, Biphasic calcium phosphate scaffolds fabricated by direct write assembly: Mechanical, anti-microbial and osteoblastic properties, *J. Eur. Ceram. Soc.* 37 (2017) 359–368. <https://doi.org/10.1016/j.jeurceramsoc.2016.08.018>.
- [48] R. Marunaka, M. Kawaguchi, Rheological behavior of hydrophobic fumed silica suspensions in aromatic dispersion media, *J. Dispers. Sci. Technol.* 38 (2017) 223–228. <https://doi.org/10.1080/01932691.2016.1155154>.
- [49] A. Berner, M.A. Woodruff, C.X.F. Lam, M.T. Arafat, S. Saifzadeh, R. Steck, J. Ren, M. Nerlich, A.K. Ekaputra, I. Gibson, D.W. Hutmacher, Effects of scaffold architecture on cranial bone healing, *Int. J. Oral Maxillofac. Surg.* 43 (2014) 506–513. <https://doi.org/10.1016/j.ijom.2013.05.008>.
- [50] M. Paris, A. Götz, I. Hettrich, C.M. Bidan, J.W.C. Dunlop, H. Razi, I. Zizak, D.W. Hutmacher, P. Fratzl, G.N. Duda, W. Wagermaier, A. Cipitria, Scaffold curvature-mediated novel biomineralization process originates a continuous soft tissue-to-bone interface, *Acta Biomater.* 60 (2017) 64–80. <https://doi.org/10.1016/j.actbio.2017.07.029>.
- [51] A. Šalak, M. Selecká, R. Bureš, Manganese in ferrous powder metallurgy, *Powder Metall. Prog.* 1 (2001) 41–58.
- [52] H. Ma, T. Li, Z. Huan, M. Zhang, Z. Yang, J. Wang, J. Chang, C. Wu, 3D printing of high-strength bioscaffolds for the synergistic treatment of bone cancer, *NPG Asia Mater.* 10 (2018) 31–44. <https://doi.org/10.1038/s41427-018-0015-8>.
- [53] X. Chen, J. Ou, Y. Kang, Z. Huang, H. Zhu, G. Yin, H. Wen, Synthesis and characteristics of monticellite bioactive ceramic, *J. Mater. Sci. Mater. Med.* 19 (2008) 1257–1263. <https://doi.org/10.1007/s10856-007-3233-0>.
- [54] M. Myat-Htun, A.F. Mohd Noor, M. Kawashita, Y.M. Baba Ismail, Tailoring mechanical and in vitro biological properties of calcium-silicate based bioceramic through iron

- doping in developing future material, *J. Mech. Behav. Biomed. Mater.* 128 (2022) 105122. <https://doi.org/10.1016/j.jmbbm.2022.105122>.
- [55] Z. Du, H. Leng, L. Guo, Y. Huang, T. Zheng, Z. Zhao, X. Liu, X. Zhang, Q. Cai, X. Yang, Calcium silicate scaffolds promoting bone regeneration via the doping of Mg^{2+} or Mn^{2+} ion, *Compos. Part B Eng.* 190 (2020) 107937. <https://doi.org/10.1016/j.compositesb.2020.107937>.
- [56] J.F. Schenck, The role of magnetic susceptibility in magnetic resonance imaging: MRI magnetic compatibility of the first and second kinds, *Med. Phys.* 23 (1996) 815–850. <https://doi.org/10.1118/1.597854>.
- [57] H. Hermawan, D. Dubé, D. Mantovani, Degradable metallic biomaterials: Design and development of Fe-Mn alloys for stents, *J. Biomed. Mater. Res. - Part A* 93 (2010) 1–11. <https://doi.org/10.1002/jbm.a.32224>.
- [58] Y.P. Feng, A. Blanquer, J. Fornell, H. Zhang, P. Solsona, M.D. Baró, S. Suriñach, E. Ibáñez, E. García-Lecina, X. Wei, R. Li, L. Barrios, E. Pellicer, C. Nogués, J. Sort, Novel Fe-Mn-Si-Pd alloys: Insights into mechanical, magnetic, corrosion resistance and biocompatibility performances, *J. Mater. Chem. B* 4 (2016) 6402–6412. <https://doi.org/10.1039/c6tb01951j>.
- [59] P.M. Jungmann, C.A. Agten, C.W. Pfirrmann, R. Sutter, Advances in MRI around metal, *J. Magn. Reson. Imaging* 46 (2017) 972–991. <https://doi.org/10.1002/jmri.25708>.
- [60] F.G. Shellock, S. Valencina, Septal repair implants: Evaluation of magnetic resonance imaging safety at 3 T, *Magn. Reson. Imaging* 23 (2005) 1021–1025. <https://doi.org/10.1016/j.mri.2005.10.010>.
- [61] L.N. Carter, O. Addison, N. Naji, P. Seres, A.H. Wilman, D.E.T. Shepherd, L. Grover, S. Cox, Reducing MRI susceptibility artefacts in implants using additively manufactured porous Ti-6Al-4V structures, *Acta Biomater.* 107 (2020) 338–348. <https://doi.org/10.1016/j.actbio.2020.02.038>.
- [62] K. Bayya Devi, S.K. Nandi, M. Roy, Magnesium silicate bioceramics for bone regeneration: A review, *J. Indian Inst. Sci.* 99 (2019) 261–288. <https://doi.org/10.1007/s41745-019-00119-7>.
- [63] P. Srinath, P. Abdul Azeem, K. Venugopal Reddy, Review on calcium silicate-based bioceramics in bone tissue engineering, *Int. J. Appl. Ceram. Technol.* 17 (2020) 2450–2464. <https://doi.org/10.1111/ijac.13577>.
- [64] S.K. Venkatraman, R. Choudhary, G. Krishnamurthy, H.R. Balaji Raghavendran, M.R. Murali, T. Kamarul, A. Suresh, J. Abraham, S. Praharaj, S. Swamiappan, Comparative investigation on antibacterial, biological and mechanical behaviour of monticellite and diopside derived from biowaste for bone regeneration, *Mater. Chem. Phys.* 286 (2022) 126157. <https://doi.org/10.1016/j.matchemphys.2022.126157>.
- [65] M. Schinhammer, P. Steiger, F. Moszner, J.F. Löffler, P.J. Uggowitzer, Degradation performance of biodegradable FeMnC(Pd) alloys, *Mater. Sci. Eng. C* 33 (2013) 1882–1893. <https://doi.org/10.1016/j.msec.2012.10.013>.
- [66] E. Mouzou, C. Paternoster, R. Tolouei, A. Purnama, P. Chevallier, D. Dubé, F. Prima, D. Mantovani, In vitro degradation behavior of Fe-20Mn-1.2C alloy in three different pseudo-physiological solutions, *Mater. Sci. Eng. C* 61 (2016) 564–573. <https://doi.org/10.1016/j.msec.2015.12.092>.
- [67] S. Gambaro, C. Paternoster, B. Occhionero, J. Fiocchi, C.A. Biffi, A. Tuissi, D. Mantovani, Mechanical and degradation behavior of three Fe-Mn-C alloys for potential biomedical applications, *Mater. Today Commun.* 27 (2021) 102250. <https://doi.org/10.1016/j.mtcomm.2021.102250>.
- [68] E. Mouzou, C. Paternoster, R. Tolouei, P. Chevallier, C.A. Biffi, A. Tuissi, D. Mantovani, CO₂-rich atmosphere strongly affects the degradation of Fe-21Mn-1C for biodegradable metallic implants, *Mater. Lett.* 181 (2016) 362–366. <https://doi.org/10.1016/j.matlet.2016.06.017>.
- [69] M. Schinhammer, I. Gerber, A.C. Hänzli, P.J. Uggowitzer, On the cytocompatibility of biodegradable Fe-based alloys, *Mater. Sci. Eng. C* 33 (2013) 782–789. <https://doi.org/10.1016/j.msec.2012.11.002>.
- [70] J.G. Speight, *Lange's handbook of chemistry*, McGraw-hill, New York, 2005.
- [71] X. Wang, M. Ackermann, S. Wang, E. Tolba, M. Neufurth, Q. Feng, H.C. Schröder, W.E.G. Müller, Amorphous polyphosphate/amorphous calcium carbonate implant material with enhanced bone healing efficacy in a critical-size defect in rats, *Biomed. Mater.* 11 (2016). <https://doi.org/10.1088/1748-6041/11/3/035005>.

- [72] W.E.G. Müller, M. Neufurth, S. Wang, M. Ackermann, R. Muñoz-Espí, Q. Feng, Q. Lu, H.C. Schröder, X. Wang, Amorphous, smart, and bioinspired polyphosphate nano/microparticles: A biomaterial for regeneration and repair of osteo-articular impairments in-situ, *Int. J. Mol. Sci.* 19 (2018). <https://doi.org/10.3390/ijms19020427>.
- [73] E. Tolba, W.E.G. Müller, B.M. Abd El-Hady, M. Neufurth, F. Wurm, S. Wang, H.C. Schröder, X. Wang, High biocompatibility and improved osteogenic potential of amorphous calcium carbonate/vaterite, *J. Mater. Chem. B* 4 (2016) 376–386. <https://doi.org/10.1039/c5tb02228b>.
- [74] J.R. Popp, K.E. Laflin, B.J. Love, A.S. Goldstein, In vitro evaluation of osteoblastic differentiation on amorphous calcium phosphate-decorated poly(lactic-co-glycolic acid) scaffolds, *J. Tissue Eng. Regen. Med.* 5 (2011) 780–789. <https://doi.org/10.1002/term>.
- [75] M. Mahdavian, M.M. Attar, Another approach in analysis of paint coatings with EIS measurement: Phase angle at high frequencies, *Corros. Sci.* 48 (2006) 4152–4157. <https://doi.org/10.1016/j.corsci.2006.03.012>.
- [76] Y. Zuo, R. Pang, W. Li, J.P. Xiong, Y.M. Tang, The evaluation of coating performance by the variations of phase angles in middle and high frequency domains of EIS, *Corros. Sci.* 50 (2008) 3322–3328. <https://doi.org/10.1016/j.corsci.2008.08.049>.
- [77] M. Dehestani, E. Adolfsson, L.A. Stanciu, Mechanical properties and corrosion behavior of powder metallurgy iron-hydroxyapatite composites for biodegradable implant applications, *Mater. Des.* 109 (2016) 556–569. <https://doi.org/10.1016/j.matdes.2016.07.092>.
- [78] E.B. Montufar, M. Casas-Luna, M. Horynová, S. Tkachenko, Z. Fohlerová, S. Diaz-de-la-Torre, K. Dvořák, L. Čelko, J. Kaiser, High strength, biodegradable and cytocompatible alpha tricalcium phosphate-iron composites for temporal reduction of bone fractures, *Acta Biomater.* 70 (2018) 293–303. <https://doi.org/10.1016/j.actbio.2018.02.002>.
- [79] P. Feng, C. Gao, C. Shuai, S. Peng, Toughening and strengthening mechanisms of porous akermanite scaffolds reinforced with nano-titania, *RSC Adv.* 5 (2015) 3498–3507. <https://doi.org/10.1039/c4ra12095g>.
- [80] A. Reindl, R. Borowsky, S.B. Hein, J. Geis-Gerstorfer, P. Imgrund, F. Petzoldt, Degradation behavior of novel Fe/β-TCP composites produced by powder injection molding for cortical bone replacement, *J. Mater. Sci.* 49 (2014) 8234–8243. <https://doi.org/10.1007/s10853-014-8532-5>.
- [81] A. Yamamoto, R. Honma, M. Sumita, Cytotoxicity evaluation of 43 metal salts using murine fibroblasts and osteoblastic cells, *J. Biomed. Mater. Res.* 39 (1998) 331–40. [https://doi.org/10.1002/\(SICI\)1097-4636\(199802\)39:2<331::AID-JBM22>3.0.CO;2-E](https://doi.org/10.1002/(SICI)1097-4636(199802)39:2<331::AID-JBM22>3.0.CO;2-E).
- [82] P. Chen, J. Bornhorst, M. Aschner, Manganese metabolism in humans, *Front. Biosci. - Landmark* 23 (2018) 1655–1679. <https://doi.org/10.2741/4665>.
- [83] Z.Y. Qiu, Y. Cui, X.M. Wang, Chapter 1 - Natural bone tissue and its biomimetic, *Mineralized collagen Bone Graft Substitutes*, Elsevier Ltd, 2019. <https://doi.org/10.1016/B978-0-08-102717-2.00001-1>.
- [84] E. Holm, J.S. Gleberzon, Y. Liao, E.S. Sørensen, F. Beier, G.K. Hunter, H.A. Goldberg, Osteopontin mediates mineralization and not osteogenic cell development in vitro, *Biochem. J.* 464 (2014) 355–364. <https://doi.org/10.1042/BJ20140702>.

8

Concluding remarks

*“Vaya Dhamma Sankhara. Appamadena sampadetha:
It is the nature of all conditioned things to perish.
Accomplish all your duties with mindfulness.”*

Buddha Gautama

8.1 Main findings

In this thesis project, we developed porous biodegradable Fe-based scaffolds fabricated through extrusion-based 3D printing technology and comprehensively studied their characteristics, while progressively approaching the destination of fulfilling all the requirements for bone substitution. The overall aim was to bring Fe-based biomaterials closer to their orthopedic application. We first fabricated porous pure Fe scaffolds and thoroughly examined the characteristics of their porous structure upon 3D printing and sintering. We then investigated their *in vitro* biodegradation behavior, electrochemical responses, uniaxial compressive mechanical properties along with *in vitro* biodegradation, and cytocompatibility. We recognized the strong need to enhance the degradation rate further and improve the biocompatibility of Fe-based biomaterials. Then, we applied a non-biodegradable coating onto the Fe scaffolds and compared the characteristics and properties of the scaffolds with and without the coating. In the meantime, we felt the necessity for modifying the material chemistry to resolve the issues of pure Fe scaffolds concerning their ferromagnetic behavior and lack of bioactivity. We then implemented the multi-material additive manufacturing (AM) strategy by alloying Fe with Mn and reinforcing Fe with akermanite and thoroughly evaluated the performance of the scaffolds, including the magnetic behavior and osteogenic potential. With the expected benefits gained individually from alloying and compositing, we developed the FeMn-akermanite composite scaffolds, taking advantage of the multi-material capacity of extrusion-based 3D printing. Our results clearly demonstrated that the extrusion-based 3D printed porous FeMn-akermanite scaffolds could fulfill all the requirements for bone substitution *in vitro*. Here, we summarize the main findings of this thesis project:

1. Extrusion-based 3D printing can be used to fabricate porous Fe-based scaffold materials. The porous structure is fully interconnected, including precisely controlled macropores as well as randomly distributed micropores in the struts.
2. Porous Fe alone is not suited for use as a biodegradable bone implant material.
3. A non-biodegradable polymer coating on the surface of porous Fe alters the morphology and chemistry of the biodegradation products and improves the biodegradation profile of pure Fe scaffolds. However, the PEtOx coating cannot provide the coated scaffold material with bioactive properties needed for bone substitution.

4. *Ex situ* alloying of Fe with Mn results in FeMn alloys containing the γ -FeMn phase that is paramagnetic and MRI-friendly, even after 4 weeks of *in vitro* biodegradation. The same paramagnetic behavior is present in the FeMn-Ak composite scaffolds as well.
5. Porous FeMn alloys (with 30–35 wt% Mn) and Fe₃₅Mn-Ak composites (with 20 or 30 vol% akermanite) exhibit the biodegradation rates that are in the range of the desired values for ideal bone substitution.

The *in vitro* biodegradation rates of the Fe-based scaffolds can be improved to a great extent, depending on the material chemistry. Porous Fe has the slowest biodegradation rate (*i.e.*, 0.05 mm/y). The PEtOx coating improves the biodegradation rate to 0.13 mm/y. Alloying Fe with 30 and 35 wt% Mn speeds up the biodegradation of the pure Fe scaffolds to the rates of 0.20 and 0.23 mm/y, respectively. Reinforcing porous Fe with 20 vol% akermanite increases the biodegradation rate to 0.14 mm/y. Combining 35 wt% Mn with 20 vol% or 30 vol% akermanite in Fe enhances the biodegradation rate to 0.24 mm/y or 0.27 mm/y, respectively.

6. The mechanical properties of all the Fe-based scaffolds investigated are sufficiently high to provide mechanical support during the initial stage of bone regeneration. The mechanical property values of the scaffolds are within the range of the values reported for the cancellous bone. With the same design of porous structures, the Fe₃₅Mn-20Ak composite has the highest yield strength. Both the Fe₃₅Mn-20Ak and Fe scaffolds have similarly high elastic modulus values, while the Fe-20Ak composite has the lowest yield strength and elastic modulus.

After 4 weeks of *in vitro* biodegradation, the yield strength and elastic modulus of the porous Fe scaffolds increase by 24% and 19%, respectively, due to the very slow biodegradation and the strong adhesion of the degradation products. During this period, however, the yield strength and elastic modulus values of the PEtOx-coated Fe scaffolds decrease by 15% and 11%, respectively; the yield strength and elastic modulus values of the Fe-Mn alloys (with 25–30 wt% Mn) decrease by up to 57% and 54%, respectively; the yield strength and elastic modulus values of the Fe-Ak composites (with 5–20 vol% akermanite) decrease by up to 72% and 26%, respectively; the yield strength and elastic modulus values of the Fe₃₅Mn-20Ak composites decrease by 78% and 83%, respectively. For the Fe₃₅Mn-30Ak composite scaffolds, the material becomes brittle after 4 weeks of *in vitro*

biodegradation due to the high rate of biodegradation. It should be noted that none of the Fe-based scaffolds developed in this thesis fails prematurely.

7. The AM porous Fe and FeMn scaffolds developed here exhibit *in vitro* cytotoxicity towards the preosteoblasts MC3T3-E1. Substituting at least 10 vol% of Fe and 20 vol% of Fe₃₅Mn alloy with akermanite significantly enhances the cytocompatibility of these materials towards the preosteoblasts and results in the appearance of an osteogenic behavior.

These findings motivate further research into the *in vivo* performance of the Fe-based scaffold biomaterials to treat large-size bone defects.

8.2 General discussion

This thesis project covers a broad scope of 3D printing process development, material design, and comprehensive evaluation of the Fe-based biomaterials developed so as to take up all the challenges currently faced in using such biodegradable materials for bone substitution. Here, we reflect upon the relevance of our findings to the target application and discuss the new challenges ahead.

On the fabrication of Fe-based biomaterials for bone substitution

Advanced AM technologies address the need to fabricate geometrically complex structures containing multiple material components. Extrusion-based 3D printing is one of the AM technologies that has been continuously developed to turn design ideas to real structures [1,2]. In this research, we demonstrated the capability of extrusion-based 3D printing to fabricate and reproduce biodegradable Fe-based scaffolds with well controlled macropores and randomly distributed micropores in the struts. We also showed that extrusion-based 3D printing is, indeed, a straightforward multi-material AM technology, allowing us to add alloying elements or supplementing the primary material, *i.e.*, pure Fe, with additional components. Each of the added components was chosen based on the rational needs for functionality to make Fe-based biomaterials viable bone implants (*i.e.*, Mn for paramagnetic behavior and enhanced biodegradability, and akermanite for bioactivity and fast dissolution in bodily fluids). We chose the water-based hypromellose binder to carry Fe, Mn, and akermanite powder particles through the nozzle during 3D printing. In addition to its shear-thinning property, the hypromellose binder has little propensity to react with Fe, Mn, and akermanite particles during the preparation of the inks and 3D printing. After 3D printing, the as-printed scaffolds were post-processed through debinding and sintering. The debinding step was optimized for complete binder removal. The

sintering parameters were optimized for a low shrinkage value to retain the open pore feature of the scaffolds, as well as for the alloying and for the diffusion of the elements in the reinforcing component into the Fe matrix.

Extrusion-based 3D printing, utilizing a flowable paste (or colloidal slurry) highly loaded with nano- to micron-size particles, has been developed over decades to fabricate the structures of diverse materials (*e.g.*, polymer, metals, composites) for various applications from biomedical, to food, electronics and energy [3,4], including 4D printing [5]. Different types of binders are available today, *e.g.*, water-based, solvent-based, thermo-sensitive, or UV-curable polymers. Depending on the choice of the binder and powder components, the 3D printable ink can be tuned to achieve geometrically complex 3D structures containing multiple materials. However, the versatility of extrusion-based 3D printing is yet to be explored further for the development of AM porous metals intended for load-bearing orthopedic applications and many technological challenges are ahead to go beyond the current limits.

The first aspect concerns the 3D printing resolution for the fabrication of complex porous structures with thin struts. Extrusion-based 3D printing relies on nozzles with different sizes to achieve the finest possible resolution, which is related to the choice of the starting powder particle sizes. For example, in this thesis project, we used a nozzle size of 410 μm with Fe powder particle sizes < 63 μm and Mn and akermanite powder particle sizes < 45 μm . For a higher resolution, smaller powder particles (*e.g.*, in the nano-size range) are required. However, handling nano-size powder particles for 3D printing can be highly challenging due to the strong tendency of agglomeration and even volatility. The post-AM processing must be carefully fine-tuned too.

The second aspect concerns the choice of the binder and its rheological behavior. Multi-component binders are often formulated and used for extrusion-based 3D printing of complex structures, for example those involving curvatures. In addition to the main polymer component, elastomers, waxes, or plasticizers are often added to disperse powder particles homogeneously in the ink. However, binder complexity may negatively impact the post-processing stage (*i.e.*, debinding or sintering) of the as-printed scaffolds [6]. Debinding to remove a compact polymeric binder may generate entrapped gases that can create internal stresses and defects inside the scaffolds. If the binder is not totally decomposed, carbon residue may manifest as impurity added to the scaffold material composition. Furthermore, it is important to ensure minimal or no interaction of the chosen binder with the powder particles in the 3D printing feedstock. Such a reaction can, for example, create an oxide layer on particle surfaces, preventing the subsequent sintering step to progress. In this thesis project, we utilized hypromellose as the backbone polymer and water (and ethanol) as the solvent.

Since the solvent easily evaporates, the remaining hypromellose back bone can be decomposed easily during thermal debinding. Despite the benefits of the post-processing of the scaffolds, the complexity of the hypromellose binder is low, which limits the 3D printable design to the lay-down patterns. With the understanding of material compositions to create multi-functional Fe-based bone substitutes, further research can be carried out to explore various types of binder for 3D printing of Fe-based scaffolds with geometrically complex designs that will lead to the further improvements of the biodegradation profile and mechanical properties.

The third aspect concerns the influence of sintering on the properties of metallic scaffolds [7]. Sintering at a low temperature or with an insufficiently long holding time can result in insufficient bonding of powder particles. On the other hand, sintering at a high temperature or over a long holding time can result in high-density scaffold struts, in addition to grain growth. Grain size is known to influence the functionalities of metals, including Fe-based scaffolds. Not only the mechanical properties but also the biodegradation profile of the material will, thus, be affected [8]. For extrusion-based 3D printed scaffolds, the initial grain size or grain boundary area can be adjusted, based on the choice of the starting powder particle sizes. However, coarsening of grains during sintering is inevitable. Therefore, it is of great importance to choose the right sintering process parameters to ensure the powder particles sufficiently bonded without substantially diminishing the material properties. In this thesis project, we optimized the sintering parameters of the Fe-based scaffolds to achieve the biofunctionalities required for biodegradable bone substitution. Fine-tuning is still needed to reach an optimum balance for other Fe-based materials that will be developed in the future.

On the biodegradability of Fe-based bone substitutes

Speeding up the biodegradation of Fe-based biomaterials is one of the challenges that has been encountered [9]. Numerous efforts have been made *via* (i) making Fe implant structure porous, (ii) applying polymer coating, (iii) alloying Fe with other elements, and (iv) adding bioceramics into the Fe matrix.

Porous Fe biodegrades faster, as compared to the bulk counterpart [10]. In Chapter 3, we have shown an increased biodegradation rate of the extrusion-based 3D printed porous Fe with hierarchical macropores and random micropores in the struts. However, the rate is still quite low, considering the requirement that the biodegradable implant is fully absorbed within 2 years [11]. It is now clear that a mere increase in the surface area of Fe is not sufficient to achieve continuous biodegradation of Fe over time, since the naturally

passivating biodegradation products (made of Fe oxide-hydroxide, Fe oxides and Fe phosphate) will prevent the underlying substrate from degrading further.

Another effort to enhance the biodegradation rate of Fe has been made by applying polymer coating to the Fe surface. In the literature, biodegradable polymer coating is often used. The polymer is expected to hydrolyze and create a local acidic environment to enhance the corrosion process of Fe [12]. The enhancement is likely to be temporary only and will diminish once the polymer coating is completely dissolved. In Chapter 4, we have presented a non-biodegradable polymer coating to assist the biodegradation of porous Fe, as the thin polymer layer can transform the morphology and chemical composition of the biodegradation products into being more porous and only composed of Fe oxide-hydroxide. This improves the biodegradation profile as the corrosion products tend to be less passivating. Despite the positive *in vitro* outcome, we realize that applying coating is unlikely to be the solution to all the challenges of Fe-based bone substitutes, as the coating cannot change the magnetic behavior of such biomaterials or provide the coated material with sufficient bioactivity.

Alloying Fe with noble elements (*e.g.*, Ag, Au, or Pd) has been tried to increase the biodegradation rate of Fe [13]. The alloyed Fe contains intermetallic phases with a higher standard electrode potential than the Fe matrix, which induces micro-galvanic corrosion at the interface [14]. Other than the noble metals, alloying Fe with Mn has been considered to be more promising, as Fe-Mn solid solutions have overall lower standard electrode potential values, which means that these alloys will have a higher tendency to biodegrade [15,16]. Moreover, FeMn alloys with > 28 wt% Mn are paramagnetic [17]. In Chapter 5, we have presented MRI-friendly and highly biodegradable porous FeMn scaffolds whose biodegradation rates fall into the range of the values of ideal bone substitutes. Nevertheless, the cytotoxicity of the alloying elements (including Mn) is still a crucial concern for the application of such biomaterials.

Bioceramic reinforcement in the Fe matrix has been taken as an effective strategy to improve the biocompatibility of Fe-based implant materials [18]. The composites can also benefit from the fast dissolution of the bioceramic component, which increases the overall biodegradation rate. In Chapter 6, we have demonstrated the improved biodegradability of the extrusion-based 3D printed porous Fe-akermanite composites, as compared to the monolithic Fe. Even so, the Fe-bioceramic composites have a drawback. The Fe matrix in the composite is preserved in the α -Fe single phase [19–21]. This means that, once the bioceramic component is completely dissolved, a larger volume of Fe will remain and become a slowly biodegrading material.

The improvement of the initial biodegradation rate of Fe can certainly be achieved. However, sustaining the improved biodegradation rate over time until the whole Fe-based implant is fully biodegraded remains a huge challenge. Of all the abovementioned efforts, changing the phase composition of pure Fe, *i.e.*, by alloying Fe with Mn, seems the best option. The γ -FeMn phase indeed ensures an enhanced biodegradability over a longer period of time. This is because the biodegradation products of the FeMn alloys are less passivating due to the changed surface chemical components with Fe-based and Mn-based corrosion products combined [22,23]. Regarding the biofunctionality and osteogenic property, the FeMn alloys can be reinforced with bioceramics (as we have demonstrated in Chapter 7 and in other study [24]) or coated with natural bioactive polymer (*e.g.*, collagen [25]).

On the magnetic behavior of Fe-based bone substitutes

Magnetic behavior and MRI safety of implantable medical devices have been one of the major concerns with using Fe-based biodegradable materials, because of the intrinsic ferromagnetism of the α -Fe phase. It is of importance to ensure the MRI safety of Fe-based bone implants for the patients who may need MRI scan during their treatment. The magnet strength depends on the volume of the implanted material. Pure Fe with the α -Fe single phase can be categorized as MRI-conditional, when fabricated into a stent with a strut thickness of 53 μm [26]. Unfortunately, for load-bearing bone substitution, the volume of an Fe-based implant is usually much larger than that used for cardiovascular purpose. In such a case, changing the ferromagnetism of Fe is a requisite for its clinical application.

In Chapter 5 and 7, we have demonstrated the paramagnetic and MRI-friendly FeMn scaffolds and FeMn-akermanite composites with the presence of the γ -Fe phase. In addition to measuring the intrinsic magnetization performance, visualizing the image artefacts caused by FeMn alloys *in vitro* and *in vivo* during MRI scan should be performed. These results will provide further understanding on the scaffold volume and structural design for minimizing the MRI artefacts and should be tailored to the other required biofunctionalities of Fe-based bone implants. Furthermore, the research on Fe-based biomaterials for bone substitution should consider using FeMn alloys as the starting materials. This will ensure the MRI-friendly behavior, while optimizing other biofunctionalities (*i.e.*, biodegradation, mechanical properties, and bioactivity).

On the mechanical properties of Fe-based bone substitutes

Mechanical properties are one of the requirements for the biomaterials intended for load-bearing bone substitution. As presented in this thesis, all the

porous Fe-based scaffolds developed by using extrusion-based 3D printing (with 67–71% porosity) exhibit the compressive yield strength and elastic modulus values in the range of the values of the cancellous bone, even after 4 weeks of *in vitro* biodegradation.

Bulk Fe-based biomaterials have much higher mechanical properties than the cortical bone [22]. To reduce the excess mechanical properties and aim for the values closest to those of the native bone, the Fe-based biomaterials can be designed and fabricated as porous structures. For example, porous Fe₃₀Mn alloy scaffolds (with porosity = 37.9–47.8%) have been reported to have the mechanical properties in the range of the cortical bone even after 48 weeks *in vivo* [27]. With an increasing porosity value, the FeMn alloy scaffolds can be tuned to match the mechanical properties of the cancellous bone [16,28].

Porosity, including the pore size and pore shape, plays an important role in determining the mechanical properties of AM porous biomaterials. For Fe-based biomaterials, the porosity should be optimized not only to achieve bone-mimicking mechanical properties but also to facilitate biodegradation, to ensure the mechanical integrity during biodegradation and simultaneously allow bone to regenerate and replace the gradually degrading implant material.

On the biocompatibility of Fe-based bone substitutes

The biocompatibility of porous Fe and FeMn alloy bone substitutes is still debatable. The extrusion-based 3D printed Fe (in Chapter 3, porosity = 67%) and FeMn alloys (in Chapter 5, porosity = 69%) developed in this thesis project exhibit cytotoxicity towards mouse MC3T3-E1 preosteoblasts. Likewise, a reduction in cell viability has been reported for Fe (porosity = 67.5%) [29], the Fe₃₀Mn alloy (porosity = 60%) [30], and the Fe₃₀Mn₆Si₁Pd alloy (porosity = 40%) [31]. However, there are several reports on the *in vitro* cytocompatibility of the Fe₃₅Mn alloy (porosity = 39.3%) [32], Fe₂₅Mn (porosity = 66.7%) [33], and Fe₃₀Mn alloy (porosity = 85%) [28]. In Chapters 6 and 7, we have presented akermanite as the reinforcing component of porous Fe and FeMn alloys to improve their biological properties. By substituting at least 10 vol% of Fe and 20 vol% Fe₃₅Mn alloy with akermanite, the Fe-based scaffolds exhibit an osteogenic behavior. In addition, the composite scaffolds exhibit increased biodegradation rates without changing much of the cancellous bone-mimicking mechanical properties.

The recent *in vivo* studies on porous FeMn alloys (porosity = <50%) have demonstrated osseointegration and bone regeneration [27,34]. Nevertheless, it is difficult to translate the *in vitro* results into predictable *in vivo* performance of the Fe and FeMn alloys. It is of great importance to understand the relationship between porosity, biodegradation profile, and mechanical properties, as well as

the influences of porosity and biodegradation on bone regeneration. More systematic *in vitro* and *in vivo* studies are urgently needed to evaluate the *in vivo* performance of such materials in order to move closer to the clinical application of Fe-based bone substitutes.

8.3 Recommendations and outlook of future research

While this thesis has contributed to designing biodegradable Fe-based scaffolds material configurations and developing associated fabrication technology with a focus placed on achieving an appropriate biodegradation rate, paramagnetic behavior, mimicking trabecular bone mechanical properties, and osteogenic all at once, there are still many outstanding challenges towards clinical applications. In this section, we make a number of recommendations and suggest potential future research directions.

1. Extrusion-based 3D printing of Fe-based biomaterials should aim at multi-material fabrication of porous structures with complex geometries, other than the lay-down pattern design. This will not only allow the engineering of Fe-based material configuration for trabecular bone tissue repair as demonstrated in this thesis, but also the creation of Fe-based bone implants with complex porous geometry that may possess mechanical properties close to those of the cortical bone, while retaining a sufficient biodegradation rate and osteosynthesis ability. Scaffolds with other 3D architectures should be possible to achieve by carefully tuning the powder loading and the choice of binder, by using a sacrificial ink as removable supports [35], or by modifying the printer with additional laser assistance for *in situ* selective laser debinding and sintering [36].
2. Future studies should consider the paramagnetic FeMn alloys [16,22,37] as the starting materials of Fe-based scaffolds intended for bone repair. In this thesis, we have demonstrated that Fe-based alloys containing a sufficient amount of Mn are indeed paramagnetic and theoretically MRI-friendly. However, excessive release of Mn ions as a result of the biodegradation of FeMn alloys may raise cytotoxic and neurotoxic concerns. The MRI safety of Fe-based bone substitutes should therefore be studied in more detail, *e.g.*, displacement or torque induced by the magnetic field of a given strength, heat induced by radio frequency, and MRI image artefact [26]. It is essential to ensure the safety of Fe-based bone implants for the patients who may need MRI scan during their treatment, and in the meantime the biocompatibility of such implants.
3. Regarding the biodegradation behavior, there is a large gap between the *in vitro* and *in vivo* biodegradation rates of Fe-based materials, as found out by

a number of researchers [9,27,38,39]. The reported *in vivo* biodegradation of Fe₃₀Mn implants is actually slower than the *in vitro* electrochemical prediction [27]. In the literature, *in vitro* immersion setup in the static environment has been used by most of the researchers, while others have developed immersion tests under fluid flow and cyclic mechanical loading conditions to reveal the corrosion fatigue behavior [40] and reported faster biodegradation rates. Some have even simulated the inflammatory conditions at the early stage of implantation by adding H₂O₂ at various concentrations [41], or incorporated proteins into the immersion solution [42] in order to present an *in vitro* environment closer to the *in vivo* one.

To date, there have been limited *in vivo* studies on AM porous Fe-based bone substitutes [27,34]. More *in vivo* studies are needed to understand the actual biodegradation behavior of AM porous Fe-based implants. As a start, the *in vivo* bone defect model in small animal, *e.g.*, in rat [34] or rabbit [27], can be performed to understand the biodegradation behavior. The next step will be using a large animal model to understand the influence of mechanical loading on the biodegradation behavior. For example, sheep model [43,44] has a body weight similar to that of adult human, a bone macrostructure similar to that of human bones, and suitable long bone dimensions for testing human bone implants. With the comprehension of the *in vivo* biodegradation behavior, the correct and standardized *in vitro* immersion setup can be developed to study the biodegradable Fe-based biomaterials that will provide reliable results for the translation into clinical use.

4. In addition to the biodegradation behavior, the *in vivo* studies on AM porous Fe-based implants in small-animal bone defect models can enrich our knowledge on the biological responses to Fe-based materials [27,34]. This knowledge is important for understanding the bone formation and in-growth in large-animal models. The *in vivo* studies will also support the development of standardized *in vitro* cytocompatibility tests for biodegradable metals. Until today, the *in vitro* cytocompatibility tests for biodegradable metals have followed the standards established for bioinert materials [45,46]. As a result, the *in vitro* cell culture outcome of Fe-based scaffolds is debatable [8,16,28,33,34]. Following the interpretation of the *in vivo* biocompatibility results, the correct volume ratio of the cell culture medium to the surface area of the AM biodegradable Fe-based materials can be standardized. This will enable the comparison between various Fe-based materials for bone implants in *in vitro* cell culture and a reliable translation of results.
5. Mechanical properties of the retrieved AM porous Fe-based bone implant samples after *in vivo* implantation in animal bone defect models should be measured [27]. The small-animal model will provide preliminary data on the

mechanical properties influenced by *in vivo* biodegradation, while the large-animal model will include an additional variable of the mechanical loading effect. The results will enable the translation of the initially designed AM porous biodegradable Fe-based implants into those required *in vivo* and for clinical application.

6. Once a better understanding of the *in vivo* performance of AM porous Fe-based bone substitutes and the development of the standards for *in vitro* tests have been achieved, developing the *in vitro* co-culture of multiple cell types relevant to bone tissue on AM porous Fe-based implants should be considered. This will be the next step for the biocompatibility screening of any novel biodegradable materials, prior to the *in vivo* test that can be costly. Performing *in vitro* co-culture of cells can better mimic *in vivo* conditions due to the crosstalk between cell types, *e.g.*, an orchestra of osteogenic, angiogenic and osteoimmunomodulatory properties at once [47–49].
7. In parallel to the development of biodegradable Fe-based materials for bone substitution, AM biodegradable Fe-based scaffolds should also be explored further for bone cancer therapy by making use of the magnetic heating capacity of Fe [50].
8. The success in developing AM porous biodegradable Fe-based bone implants towards clinical adoption requires extensive evaluation of many performance indexes of the implants. Comprehensive and large-scale experiments are time-consuming and costly. With standardized *in vitro* tests of biodegradable metals, *in silico* studies can provide complementary data to the experimental data so as to speed up the understanding of the performance and biofunctionalities of such biomaterials. For example, *in silico* model can be developed and used to optimize the porous structure design of a bone implant to achieve an optimum balance in mechanical, physical, chemical and osteoinductive properties, in addition to biodegradability [51].

Taken together, the research presented in this thesis demonstrates the remarkable potential of the extrusion-based 3D printing and Fe-based biomaterials for bone substitution. The results from the research motivate further research to evaluate the *in vivo* performance of the extrusion-based 3D printed Fe-based bone implant materials.

Bibliography

- [1] J.A. Lewis, G.M. Gratson, Direct writing in three dimensions, *Mater. Today*. 7 (2004) 32–39. [https://doi.org/10.1016/S1369-7021\(04\)00344-X](https://doi.org/10.1016/S1369-7021(04)00344-X).
- [2] J.A. Lewis, Direct ink writing of 3D functional materials, *Adv. Funct. Mater.* 16 (2006) 2193–2204. <https://doi.org/10.1002/adfm.200600434>.
- [3] N.E. Putra, M.J. Mirzaali, I. Apachitei, J. Zhou, A.A. Zadpoor, Multi-material additive manufacturing technologies for Ti-, Mg-, and Fe-based biomaterials for bone substitution, *Acta Biomater.* 109 (2020) 1–20. <https://doi.org/10.1016/j.actbio.2020.03.037>.
- [4] M.A.S.R. Saadi, A. Maguire, N.T. Pottackal, M.S.H. Thakur, M.M. Ikram, A.J. Hart, P.M. Ajayan, M.M. Rahman, Direct ink writing: A 3D printing technology for diverse materials, *Adv. Mater.* 34 (2022) 2108855. <https://doi.org/10.1002/adma.202108855>.
- [5] X. Wan, L. Luo, Y. Liu, J. Leng, Direct ink writing based 4D printing of materials and their applications, *Adv. Sci.* 7 (2020) 1–29. <https://doi.org/10.1002/advs.202001000>.
- [6] S. Banerjee, C.J. Joens, Debinding and sintering of metal injection molding (MIM) components, in *Handbook of Metal Injection Molding*, The 2nd Ed, Elsevier Ltd., 2019. <https://doi.org/10.1016/B978-0-08-102152-1.00009-X>.
- [7] D.K. Mishra, P.M. Pandey, Effect of sintering parameters on the microstructure and compressive mechanical properties of porous Fe scaffold fabricated using 3D printing and pressure less microwave sintering, *Proc. Inst. Mech. Eng. Part C J. Mech. Eng. Sci.* 234 (2020) 4305–4320. <https://doi.org/10.1177/0954406220921416>.
- [8] Y. Li, H. Jahr, K. Lietaert, P. Pavanram, A. Yilmaz, L.I. Fockaert, M.A. Leeflang, B. Pouran, Y. Gonzalez-Garcia, H. Weinans, J.M.C. Mol, J. Zhou, A.A. Zadpoor, Additively manufactured biodegradable porous iron, *Acta Biomater.* 77 (2018) 380–393. <https://doi.org/10.1016/j.actbio.2018.07.011>.
- [9] T. Kraus, F. Moszner, S. Fischerauer, M. Fiedler, E. Martinelli, J. Eichler, F. Witte, E. Willbold, M. Schinhammer, M. Meischel, P.J. Uggowitzer, J.F. Löffler, A. Weinberg, Biodegradable Fe-based alloys for use in osteosynthesis: Outcome of an in vivo study after 52 weeks, *Acta Biomater.* 10 (2014) 3346–3353. <https://doi.org/10.1016/j.actbio.2014.04.007>.
- [10] Y. Qin, P. Wen, H. Guo, D. Xia, Y. Zheng, L. Jauer, R. Poprawe, M. Voshage, J.H. Schleifenbaum, Additive manufacturing of biodegradable metals: Current research status and future perspectives, *Acta Biomater.* 98 (2019) 3–22. <https://doi.org/10.1016/j.actbio.2019.04.046>.
- [11] C. Shuai, S. Li, S. Peng, P. Feng, Y. Lai, C. Gao, Biodegradable metallic bone implants, *Mater. Chem. Front.* 3 (2019) 544–62. <https://doi.org/10.1039/c8qm00507a>.
- [12] R. Orináková, R. Gorejová, Z. Orságová Králová, A. Oriňak, Surface modifications of biodegradable metallic foams for medical applications, *Coatings*. 10 (2020) 819. <https://doi.org/10.3390/coatings10090819>.
- [13] M. Schinhammer, A.C. Hänzi, J.F. Löffler, P.J. Uggowitzer, Design strategy for biodegradable Fe-based alloys for medical applications, *Acta Biomater.* 6 (2010) 1705–1713. <https://doi.org/10.1016/j.actbio.2009.07.039>.
- [14] C. Gao, M. Yao, S. Li, P. Feng, S. Peng, C. Shuai, Highly biodegradable and bioactive Fe-Pd-bredigite biocomposites prepared by selective laser melting, *J. Adv. Res.* 20 (2019) 91–104. <https://doi.org/10.1016/j.jare.2019.06.001>.
- [15] H. Hermawan, H. Alamdari, D. Mantovani, D. Dubé, Iron-manganese: New class of metallic degradable biomaterials prepared by powder metallurgy, *Powder Metall.* 51 (2008) 38–45. <https://doi.org/10.1179/174329008X284868>.
- [16] N.E. Putra, M.A. Leeflang, P. Taheri, L.E. Fratila-Apachitei, J.M.C. Mol, J. Zhou, A.A. Zadpoor, Extrusion-based 3D printing of ex situ-alloyed highly biodegradable MRI-friendly porous iron-manganese scaffolds, *Acta Biomater.* 134 (2021) 774–790. <https://doi.org/10.1016/j.actbio.2021.07.042>.
- [17] Y. Ishikawa, Y. Endoh, Antiferromagnetism of γ -FeMn alloys, *J. Appl. Phys.* 39 (1968) 1318–1319. <https://doi.org/10.1063/1.1656274>.

-
- [18] C. Gao, M. Yao, C. Shuai, P. Feng, S. Peng, Advances in bioceramics for bone implant applications, *Bio-Design Manuf.* 3 (2020) 307–330. <https://doi.org/10.1007/s42242-020-00087-3>.
- [19] C. Shuai, Y. Li, Y. Yang, S. Peng, W. Yang, F. Qi, S. Xiong, H. Liang, L. Shen, Bioceramic enhances the degradation and bioactivity of iron bone implant, *Mater. Res. Express.* 6 (2019) 115401. <https://doi.org/10.1088/2053-1591/ab45b9>.
- [20] M. Sikora-Jasinska, C. Paternoster, E. Mostaed, R. Tolouei, R. Casati, M. Vedani, D. Mantovani, Synthesis, mechanical properties and corrosion behavior of powder metallurgy processed Fe/Mg₂Si composites for biodegradable implant applications, *Mater. Sci. Eng. C.* 81 (2017) 511–521. <https://doi.org/10.1016/j.msec.2017.07.049>.
- [21] N.E. Putra, K.G.N. Borg, P.J. Diaz-Payno, M.A. Leeflang, M. Klimopoulou, P. Taheri, J.M.C. Mol, L.E. Fratila-Apachitei, Z. Huan, J. Chang, J. Zhou, A.A. Zadpoor, Additive manufacturing of bioactive and biodegradable porous iron-akermanite composites for bone regeneration, *Acta Biomater.* 148 (2022) 355–373. <https://doi.org/10.1016/j.actbio.2022.06.009>.
- [22] M.S. Dargusch, A. Dehghan-Manshadi, M. Shahbazi, J. Venezuela, X. Tran, J. Song, N. Liu, C. Xu, Q. Ye, C. Wen, Exploring the role of manganese on the microstructure, mechanical properties, biodegradability, and biocompatibility of porous iron-based scaffolds, *ACS Biomater. Sci. Eng.* 5 (2019) 1686–1702. <https://doi.org/10.1021/acsbiomaterials.8b01497>.
- [23] M. Heiden, E. Walker, E. Nauman, L. Stanciu, Evolution of novel bioresorbable iron-manganese implant surfaces and their degradation behaviors in vitro, *J. Biomed. Mater. Res. - Part A* 103 (2015) 185–193. <https://doi.org/10.1002/jbm.a.35155>.
- [24] M. Heiden, E. Nauman, L. Stanciu, Bioresorbable Fe–Mn and Fe–Mn–HA materials for orthopedic implantation: Enhancing degradation through porosity control, *Adv. Healthc. Mater.* 6 (2017) 1–12. <https://doi.org/10.1002/adhm.201700120>.
- [25] S. Huang, A. Ulloa, E. Nauman, L. Stanciu, Collagen coating effects on Fe–Mn bioresorbable alloys, *J. Orthop. Res.* 38 (2020) 523–535. <https://doi.org/10.1002/jor.24492>.
- [26] D. Bian, L. Qin, W. Lin, D. Shen, H. Qi, X. Shi, G. Zhang, H. Liu, H. Yang, J. Wang, D. Zhang, Y. Zheng, Magnetic resonance (MR) safety and compatibility of a novel iron bioresorbable scaffold, *Bioact. Mater.* 5 (2020) 260–274. <https://doi.org/10.1016/j.bioactmat.2020.02.011>.
- [27] Y. Nie, G. Chen, H. Peng, S. Tang, Z. Zhou, F. Pei, B. Shen, In vitro and 48 weeks in vivo performances of 3D printed porous Fe-30Mn biodegradable scaffolds, *Acta Biomater.* 121 (2021) 724–740. <https://doi.org/10.1016/j.actbio.2020.12.028>.
- [28] P. Liu, D. Zhang, Y. Dai, J. Lin, Y. Li, C. Wen, Microstructure, mechanical properties, degradation behavior, and biocompatibility of porous Fe–Mn alloys fabricated by sponge impregnation and sintering techniques, *Acta Biomater.* 114 (2020) 485–496. <https://doi.org/10.1016/j.actbio.2020.07.048>.
- [29] C. Yang, Z. Huan, X. Wang, C. Wu, J. Chang, 3D printed Fe scaffolds with HA nanocoating for bone regeneration, *ACS Biomater. Sci. Eng.* 4 (2018) 608–616. <https://doi.org/10.1021/acsbiomaterials.7b00885>.
- [30] S.M. Huang, E.A. Nauman, L.A. Stanciu, Investigation of porosity on mechanical properties, degradation and in-vitro cytotoxicity limit of Fe₃₀Mn using space holder technique, *Mater. Sci. Eng. C.* 99 (2019) 1048–1057. <https://doi.org/10.1016/j.msec.2019.02.055>.
- [31] Y.P. Feng, N. Gaztelumendi, J. Fornell, H.Y. Zhang, P. Solsona, M.D. Baró, S. Suriñach, E. Ibáñez, L. Barrios, E. Pellicer, C. Nogués, J. Sort, Mechanical properties, corrosion performance and cell viability studies on newly developed porous Fe–Mn–Si–Pd alloys, *J. Alloys Compd.* 724 (2017) 1046–1056. <https://doi.org/10.1016/j.jallcom.2017.07.112>.
- [32] D. Hong, D.T. Chou, O.I. Velikokhatnyi, A. Roy, B. Lee, I. Swink, I. Issaev, H.A. Kuhn, P.N. Kumta, Binder-jetting 3D printing and alloy development of new biodegradable Fe–Mn–Ca/Mg alloys, *Acta Biomater.* 45 (2016) 375–386. <https://doi.org/10.1016/j.actbio.2016.08.032>.
- [33] C. Shuai, W. Yang, Y. Yang, H. Pan, C. He, F. Qi, D. Xie, H. Liang, Selective laser melted Fe–

- Mn bone scaffold: Microstructure, corrosion behavior and cell response, *Mater. Res. Express*. 7 (2019) 015404. <https://doi.org/10.1088/2053-1591/ab62f5>.
- [34] D. Carluccio, C. Xu, J. Venezuela, Y. Cao, D. Kent, M. Bermingham, A.G. Demir, B. Previtali, Q. Ye, M. Dargusch, Additively manufactured iron-manganese for biodegradable porous load-bearing bone scaffold applications, *Acta Biomater*. 103 (2020) 346–360. <https://doi.org/10.1016/j.actbio.2019.12.018>.
- [35] C. Xu, B. Quinn, L.L. Lebel, D. Therriault, G. L'espérance, Multi-material direct ink writing (DIW) for complex 3D metallic structures with removable supports, *ACS Appl. Mater. Interfaces*. 11 (2019) 8499–8506. <https://doi.org/10.1021/acsami.8b19986>.
- [36] M.A. Skylar-Scott, S. Gunasekaran, J.A. Lewis, Laser-assisted direct ink writing of planar and 3D metal architectures, *Proc. Natl. Acad. Sci. U. S. A.* 113 (2016) 6137–6142. <https://doi.org/10.1073/pnas.1525131113>.
- [37] Y.P. Feng, A. Blanquer, J. Fornell, H. Zhang, P. Solsona, M.D. Baró, S. Suriñach, E. Ibáñez, E. García-Lecina, X. Wei, R. Li, L. Barrios, E. Pellicer, C. Nogués, J. Sort, Novel Fe-Mn-Si-Pd alloys: Insights into mechanical, magnetic, corrosion resistance and biocompatibility performances, *J. Mater. Chem. B*. 4 (2016) 6402–6412. <https://doi.org/10.1039/c6tb01951j>.
- [38] Y. Li, K. Lietaert, W. Li, X.Y. Zhang, M.A. Leeftang, J. Zhou, A.A. Zadpoor, Corrosion fatigue behavior of additively manufactured biodegradable porous iron, *Corros. Sci.* 156 (2019) 106–116. <https://doi.org/10.1016/j.corsci.2019.05.003>.
- [39] X. Liu, W. Li, Y. Cheng, Y. Zheng, The effect of simulated inflammatory conditions on the corrosion of Mg, Fe and CoCrMo, *Mater. Lett.* 308 (2022) 131197. <https://doi.org/10.1016/j.matlet.2021.131197>.
- [40] R. Oriňáková, R. Gorejová, Z.O. Králová, A. Oriňák, I. Shepa, J. Hovancová, A. Kovalčíková, Z.L. Bujňáková, N. Király, M. Kaňuchová, M. Baláž, M. Strečková, M. Kupková, M. Hrubovčáková, F. Kaľavský, M. Oriňák, Influence of albumin interaction on corrosion resistance of sintered iron biomaterials with polyethyleneimine coating, *Appl. Surf. Sci.* 509 (2020) 145379. <https://doi.org/10.1016/j.apsusc.2020.145379>.
- [41] Z. Chen, T. Klein, R.Z. Murray, R. Crawford, J. Chang, C. Wu, Y. Xiao, Osteoimmunomodulation for the development of advanced bone biomaterials, *Mater. Today*. 19 (2016) 304–321. <https://doi.org/10.1016/j.mattod.2015.11.004>.
- [42] Z. Chen, X. Mao, L. Tan, T. Friis, C. Wu, R. Crawford, Y. Xiao, Osteoimmunomodulatory properties of magnesium scaffolds coated with β -tricalcium phosphate, *Biomaterials*. 35 (2014) 8553–8565. <https://doi.org/10.1016/j.biomaterials.2014.06.038>.
- [43] L. Bai, P. Chen, Y. Zhao, R. Hang, X. Yao, B. Tang, C. Liu, Y. Xiao, R. Hang, A micro/nano-biomimetic coating on titanium orchestrates osteo/angio-genesis and osteoimmunomodulation for advanced osseointegration, *Biomaterials*. 278 (2021) 121162. <https://doi.org/10.1016/j.biomaterials.2021.121162>.
- [44] H. Ma, T. Li, Z. Huan, M. Zhang, Z. Yang, J. Wang, J. Chang, C. Wu, 3D printing of high-strength bioscaffolds for the synergistic treatment of bone cancer, *NPG Asia Mater.* 10 (2018) 31–44. <https://doi.org/10.1038/s41427-018-0015-8>.
- [45] D. Van hede, B. Liang, S. Anania, M. Barzegari, B. Verlé, G. Nolens, J. Pirson, L. Geris, F. Lambert, 3D-printed synthetic hydroxyapatite scaffold with in silico optimized macrostructure enhances bone formation in vivo, *Adv. Funct. Mater.* 32 (2022) 2105002. <https://doi.org/10.1002/adfm.202105002>.

Acknowledgements

I am very grateful to **Amir** and **Jie** for giving me the opportunity to work on this PhD project. **Amir**, thank you for letting me know about the project vacancy at my master's graduation ceremony. I still remember how excited I was that day! You inspire me with your out-of-the-box approach and always encourage me to set a high standard for the outcome of my research. **Jie**, I reached out to you after learning about the vacancy. We had a nice chat during the interview, which you paid special attention to my daily life. That day, I learned that it is important to have a balanced life so that I can stay focused on doing something I love. **Jie** and **Amir**, thank you for always challenging me to become a better researcher. I really appreciate your availability to answer my questions or having discussions anytime. One thing that makes other PhDs jealous is your amazing ability to review my manuscripts in the shortest possible time. I admire your dedication to research and education and your ability to make your students feel that their work and themselves matter.

Dear **Iulian** and **Lidy**, your passion for research inspires me to have one of my own. While the PhD project is largely about biodegradable iron implants, **Iulian**, we managed to produce antibacterial surfaces using iron nanoparticles. Thank you for your support and guidance, and I am looking forward to our next projects in the DARTBAC consortium. **Lidy**, I am very happy to be part of your CCB lab team. Thank you for your support and guidance in all the cell-related experiments. I always enjoy being in the team to supervise students in the Regenerative Medicine course.

Every PhD project would not have run smoothly without the support of the technical experts and the administration team. Thank you, **Sander**, for always being positive in the lab. Your design and engineering expertise has been invaluable for our project. It has always been my pleasure to work with you. Dear **Michelle** and **Maria**, today I would not have been able to culture cells without the training you provided me. Thank you for making the CCB lab very enjoyable to work in. And Kudos to **Angelique**, **Marjolijn**, **Sabrina**, and **Amanda** for

managing all the department administrations. Moreover, I also would like to sincerely thank my colleagues from the Materials Science department. I greatly appreciate **Arjan Mol** for providing me with the convenience to work in the corrosion lab, which has been a pleasant collaboration that enriched my research with more comprehensive insights. Thank you **Agnieszka** and **Peyman**, for helping me with the electrochemical experiments, **Ruud** for the XRD analysis, **Michel** for the ICP analysis, **Nico** for the magnetic measurements, and **Sander** for metallographic characterization trainings. Thank you **Elise**, **Kevork**, **Sean**, and **Ton** for your swift availability to assist me in mechanical tests. Apart from learning a lot of new skills from all of you, I enjoyed our chats and casual encounters in the lab.

Collaboration makes a PhD project more inclusive and meaningful. I would like to genuinely thank the collaborators from the 3DMed project and beyond. Thank you, **Ali**, **Suzan**, and **Victor**, for sharing your knowledge about polymers, which has been very helpful to our project. Thank you, **Sandra** and **Cathy**, for managing the work-packages smoothly. Special shout-outs to **Karl**, **Verena**, and **Viorica**, without your genuine help for the microbiology tests during the Covid (lockdown) time, we would never have completed the research.

During my PhD projects, I have had the opportunity to supervise students for their internship and master's thesis projects. **Carlos**, you were a very discipline student and you did a very good job, even publishing a review article. **Karl**, you worked independently in the lab and managed your thesis project very well. I am glad that now you are pursuing a PhD in Malta. **Leo**, you were very skilled in design and theoretical modeling. I wish you the best in your second master's study. All of you have taught me invaluable lessons on how to communicate, teach, and supervise projects, and I surely learned that not everything works for everyone.

The most important part of doing a PhD is having fun both in science and socially. My PhD journey would not have been memorable without the company and discussion with many brilliant people: **Anneke**, **Anton**, **Bart**, **Chunfeng**, **Costanza**, **Daniel**, **Dirk**, **Ebrahim**, **Edwin**, **Eline**, **Esther**, **Evelien**, **Fabian**, **Françoise**, **Gerwin**, **Helda**, **Ingmar**, **Jake**, **Jelle**, **Jette**, **Jiahui**, **Jinlai**, **Jon**, **Judith**, **Katerina**, **Keyu**, **Khashayar** and **Sara**, **Kirsten**, **Lorenzo**, **Lucy**, **Mahdiyeh**, **Mahya**, **Marit**, **Martijn**, **Mauricio**, **Merle**,

Mohammad, Monika, Mostafa, Nazli, Paul, Pier, Pedro, Robin, Sebastien, Shahram, Suzanne, Teddy, Teunis, Vahid, Vera, Yageng, and Yujiang. I enjoyed getting to know all of you during coffee breaks, cake time, lunch, or at faculty events.

Eline, Ingmar, Khashayar, Mahya, Sebastien, and Yageng, your high standard for your PhDs have inspired me to strive for the same in my own research. You have also shown that team work and collaboration are essential and that success can be achieved together. For that, I am very thankful. **Jiahui,** I am grateful that we started about the same time with a similar research topic. I appreciate all the time we spent in brainstorming, discussion and collaboration, also chats over life in China. To my office mates **Ebrahim, Jiahui, Jelle, Helda, Khashayar, Mahdiyeh, Pedro,** and **Vahid,** sharing the working space with you have been very enjoyable and amusing. Thank you for all the nice memories.

I am grateful to have gotten to know some of you better and to have you as my dearest friends. **Kirsten,** you are a good listener and I really appreciate your support. It is amazing to see how you went through two surgeries, delivered a baby, and managed to be a successful PhD. I am very proud of you! **Francoise,** your kindness creates a sense of community. Thank you for making me feel connected to the group when I started. I really appreciate all the social activities you organized, from the movie nights, laser tag game, to BBQs and the *rissoles* workshop. I am looking forward to more of our *dim sum* time. **Costanza,** I definitely miss your presence in the office hallway. You are always full of energy, enthusiastic, and you bring the PhD community to life. Thank you for teaching us how to make pasta like a true Italian. **Ingmar,** you always appear calm despite any frustrating lab work. I will always remember the time we spent working on those pile of agar plates. It was a memorable experience that I believe getting me to this PhD position. Thank you for being a great mentor.

Khashayar and **Sara,** you are very approachable and friendly, thank you for introducing me to your culture and invited us for BBQs and the Iranian cuisine. **Dirk,** our friendship was forged over shared appreciation for special Belgian beers. I truly appreciate that you took the time to introduce me to your circle of Dutch friends, and of course I am proud you nailed cooking *Soto ayam*. **Merle,** you are a respected friend to me, *not joking*. Our vegan lunches have been

very pleasant. I am glad that we witnessed the rare bloom of *Amorphophallus titanium* in *hortus* Leiden. My PhD would not be fun without the *Fishtank* **Pier** captain and the members **Katerina, Judith, Anneke, Chunfeng, Jon,** and **Mauricio**. We spent so much time together, sometimes way too much. Thank you for the great times and especially for keeping up with my obsession for food and plants.

Our first PhD outing since lockdown was a sailing trip in Friesland. That trip definitely brought me closer to several people. **Suzanne**, our casual get-togethers have been enjoyable. I never thought I would be swimming at *de Schie*, but it was definitely a great time and we should do it again. **Lucy**, you are very energetic and have a lively personality. We had a lot of fun at *Bebop*, especially with *Ziggy*. And I never would have guessed that I would make friends at the 3me faculty drinks! **Jake**, it has been great connecting with you. I am looking forward to more hang outs with more *ramen* and beers. Finally, to our new PhD members, **Ludovica, Sara, Federica,** and **Christoph**, your personality have brought joy in the department. I wish you all the best for your PhD.

Living abroad makes you appreciate each and every moment you can spend with your long-life, long-distance, dearest friends: **Callista, Angela, Natalia, Shelly, Erica, Haryanto, Wira, Lauren, Audrey,** and **Fiona**. Thank you for all the unforgettable moments. Last but not least, I am deeply grateful for all your unconditional love **Mom, Dad,** and **Vito**, and of course **Ruud**.

List of publications

Putra, N.E., Dong, J., Leeﬂang, M.A., Klimopoulou, M., Taheri, P., Huan, Z., Fratila-Apachitei, L.E., Mol, J.M.C., Chang, J., Zhou, J. and Zadpoor A.A., 2023. Extrusion-based 3D printing of biodegradable, osteogenic, paramagnetic, and porous FeMn-akermanite bone substitutes. *Under review*.

Putra, N.E., Leeﬂang, M.A., Ducret, V., Patrilea, V., Fratila-Apachitei, L.E., Perron, K., Ye, H., Zhou, J., Apachitei, I. and Zadpoor, A.A., 2022. Preventing antibiotic-resistant infections: Additively manufactured porous titanium biofunctionalized with Ag and Fe nanoparticles. *International Journal of Molecular Sciences*, 23, p.13239

Putra, N.E., Borg, K.G.N., Diaz-Payno, P.J., Leeﬂang, M.A., Klimopoulou, M., Taheri, P., Mol, J.M.C., Fratila-Apachitei, L.E., Huan, Z., Chang, J., Zhou, J. and Zadpoor, A.A., 2022. Additive manufacturing of bioactive and biodegradable porous iron-akermanite composites for bone regeneration. *Acta Biomaterialia*, 148, pp.355-373.

Dong, J., Lin, P., **Putra, N.E.**, Tümer, N., Leeﬂang, M.A., Huan, Z., Fratila-Apachitei, L.E., Chang, J., Zadpoor, A.A. and Zhou, J., 2022. Extrusion-based additive manufacturing of Mg-Zn/bioceramic composite scaffolds. *Acta Biomaterialia*.

Putra, N.E., Tigrine, A., Aksakal, S., de la Rosa, V.R., Taheri, P., Fratila-Apachitei, L.E., Mol, J.M.C., Zhou, J. and Zadpoor, A.A., 2022. Poly (2-ethyl-2-oxazoline) coating of additively manufactured biodegradable porous iron. *Biomaterials Advances*, 133, p.112617.

Pitta Kruize, C., Panahkhahi, S., **Putra, N.E.**, Diaz-Payno, P., Van Osch, G., Zadpoor, A.A. and Mirzaali, M.J., 2021. Biomimetic Approaches for the Design and Fabrication of Bone-to-Soft Tissue Interfaces. *ACS Biomaterials Science & Engineering*.

Putra, N.E., Leeﬂang, M.A., Taheri, P., Fratila-Apachitei, L.E., Mol, J.M.C., Zhou, J. and Zadpoor, A.A., 2021. Extrusion-based 3D printing of *ex situ*-alloyed highly biodegradable MRI-friendly porous iron-manganese scaffolds. *Acta Biomaterialia*, 134, pp.774-790.

Dong, J., Tümer, N., **Putra, N.E.**, Zhu, J., Li, Y., Leeftang, M.A., Taheri, P., Fratila-Apachitei, L.E., Mol, J.M.C., Zadpoor, A.A. and Zhou, J., 2021. Extrusion-based 3D printed magnesium scaffolds with multifunctional MgF_2 and MgF_2 -CaP coatings. *Biomaterials Science*, 9(21), pp.7159-7182.

Putra, N.E., Leeftang, M.A., Minneboo, M., Taheri, P., Fratila-Apachitei, L.E., Mol, J.M.C., Zhou, J. and Zadpoor, A.A., 2021. Extrusion-based 3D printed biodegradable porous iron. *Acta Biomaterialia*, 121, pp.741-756.

Putra, N.E., Mirzaali, M.J., Apachitei, I., Zhou, J. and Zadpoor, A.A., 2020. Multi-material additive manufacturing technologies for Ti-, Mg-, and Fe-based biomaterials for bone substitution. *Acta biomaterialia*, 109, pp.1-20.

Van Hengel, I.A.J., **Putra, N.E.**, Tierolf, M.W.A.M., Minneboo, M., Fluit, A.C., Fratila-Apachitei, L.E., Apachitei, I. and Zadpoor, A.A., 2020. Biofunctionalization of selective laser melted porous titanium using silver and zinc nanoparticles to prevent infections by antibiotic-resistant bacteria. *Acta biomaterialia*, 107, pp.325-337.

Putra, N.E., Fendra, Y., Nurdin, D. and Purwasasmita, B.S., 2016. Synthesize and characterization Zr-Al-Si post through eggshell membrane strengthening with PMMA matrix. *Key Engineering Materials*, 696, pp. 85-88.

Curriculum Vitae

Niko Eka Putra was born on March 16, 1994 in Medan, Indonesia. In high school, he developed a great interest in physics, medicine and biology. In 2011, he attended Institut Teknologi Bandung. He was active in various social services organized by the local and Buddhist communities in Bandung. He combined his interest in medicine and his engineering background into research in the field of biomaterials. He performed his end-year bachelor project at Advanced Materials Processing Lab, fabricating dental implants. His work was presented at the Bioceramics 27 symposium in Bali, 2015. At the same year, he gained his BSc degree in Engineering Physics.

Niko worked in Indonesia Corruption Watch in Jakarta. In 2016, he was awarded for the Indonesia Endowment Fund for Education to pursue a master degree at Technische Universiteit (TU) Delft. At the Biomaterials and Tissue Biomechanics research group, he developed skills in surface biofunctionalization of titanium bone implants with nanoparticles to prevent antibiotic-resistant bacteria infections. He worked under the supervision of Ingmar A.J. van Hengel and Iulian Apachitei. In 2018, he gained his MSc degree in Biomedical Engineering.

Niko followed his interest in biomaterials as a PhD candidate under Jie Zhou and Amir A. Zadpoor. His PhD project was a part of the 3DMed consortium funded by Interreg 2 Seas program and European Regional Development Fund. During his PhD, he developed biodegradable iron-based scaffolds for bone substitution using extrusion-based 3D printing. In 2023, he will continue his research as a post-doctoral researcher in the Dutch Antimicrobial Resistance Technology development and Biofilm Assessment (DARTBAC) consortium.

